UNIVERSITÄT HAMBURG
Department PHYSIK

Measurement of the $W \to \tau\nu_\tau$ cross section in proton-proton collisions at ATLAS and the development of the HepMCAnalysis Tool

Dissertation
zur Erlangung des Doktorgrades
des Department Physik
der Universität Hamburg

vorgelegt von

Dipl.-Phys. Sebastian Johnert

aus Hamburg

Hamburg

2012

Gutachter der Dissertation:	Dr. Philip Bechtle
	Prof. Dr. Johannes Haller
Gutachter der Disputation:	Dr. Philip Bechtle
	Prof. Dr. Peter Schleper
Datum der Disputation:	15.03.2012
Vorsitzender des Prüfungsausschusses:	Dr. Michael Martins
Vorsitzender des Promotionsausschusses:	Prof. Dr. Peter Hauschildt
Leiterin des Fachbereichs Physik:	Prof. Dr. Daniela Pfannkuche
Dekan der MIN-Fakultät:	Prof. Dr. Heinrich Graener

Abstract

The goal of modern particle physics experiments is the most precise measurement of known phenomena and the discovery of new physics. The complexity of these experiments requires dedicated tools to ensure the correct functionality of every part of the experiment and the analyses. One of these tools is the HepMCAnalysis Tool, a software framework for Monte Carlo (MC) generator validation and comparisons, using the generator independent HepMC event record. In this thesis, the development of the HepMCAnalysis Tool is presented. Its wide range of applications extends from validation and regression tests at the ATLAS experiment, over generator level studies and preparations of analyses, up to histogram based validation in the Generator Services Project. Examples of its applications are given.

In November 2009, the Large Hadron Collider (LHC) started operation and the ATLAS detector, the largest of the four LHC experiments, began taking data. Many Standard Model (SM) processes can already be rediscovered and are used to optimise the detector performance. Amongst those SM processes, processes involving particles from the third generation, like τ leptons, play an important role e.g. in the decay of the Higgs boson. Also in models of new physics like supersymmetry (SUSY), third generation particles, especially τ leptons, can be found in the final state. An accurate understanding of underlying SM processes with τ leptons is therefore one of the keys for the search of new physics. Among these, one of the most important processes is the $W \to \tau\nu_\tau$ decay. In the second part of this thesis, the cross section measurement of $W \to \tau\nu_\tau$ decays in proton-proton collisions at a center-of-mass energy of $\sqrt{s} = 7\,\text{TeV}$ with the ATLAS experiment is presented. This was measured to be $\sigma^{\text{tot}}_{W\to\tau\nu_\tau} = (11.1 \pm 0.3\ (\text{stat.}) \pm 1.7\ (\text{syst.}) \pm 0.4\ (\text{lumi.}))\,\text{nb}$. This result is in agreement with the NNLO prediction of $(10.46 \pm 0.52)\,\text{nb}$. Furthermore, the $W \to \tau\nu_\tau$ branching ratio was determined, using a total W boson production cross section of 100 nb with an uncertainty of 5%, to be $(11.1 \pm 0.3\ (\text{stat.}) \pm 1.8\ (\text{syst.}) \pm 0.4\ (\text{lumi.}))\%$, also in agreement with the SM expectation of 10.83%.

Zusammenfassung

Das Ziel moderner Teilchenphysikexperimente ist die präzise Vermessung bekannter Phänomene und die Entdeckung neuer Physik. Die Komplexität dieser Experimente erfordert fortgeschrittene Programme um die richtige Funktionalität jedes einzelnen Teils des Detektors sowie jedes einzelnen Analyseabschnitts zu gewährleisten. Eines dieser Programme ist das HepMCAnalysis Tool, ein Softwareframework für Monte Carlo (MC) Generatorvalidierung und -vergleiche, das das generatorunabhängige HepMC Format verwendet. In dieser Arbeit wird die Entwicklung des HepMCAnalysis Tools vorgestellt. Seine Anwendungsbereiche reichen von Validierungen und Regressionstests am ATLAS Experiment über Generatorstudien und vorbereitenden Studien physikalischer Analysen bis hin zur histogrammbasierten Validierung im Generator Services Project. Anwendungsbeispiele werden kurz erläutert.

November 2009 fing die Datennahme am Large Hadron Collider (LHC) und dem ATLAS Experiment, dem größten der vier LHC Experimente, an. Viele Standardmodellereignisse (SM) können bereits wieder entdeckt werden und werden für die Optimierung der Detektoreigenschaften genutzt. In diesen SM Ereignissen haben Ereignisse mit Teilchen der dritten Generation (z.B. τ Leptonen) u.a. im Zerfall des Higgs Bosons eine bedeutende Rolle. Teilchen der dritten Generation, insbesondere τ Leptonen, können aber auch im Endzustand vieler Modelle neuer Physik (z.B. Supersymmetrie (SUSY)) gefunden werden. Daher ist ein genaues Verständnis von SM Ereignissen mit τ Leptonen einer der Schlüssel bei der Suche nach neuer Physik. Einer der wichtigsten Prozesse bildet dabei der $W \to \tau\nu_\tau$ Zerfall. Im zweiten Teil dieser Arbeit wird die Messung des $W \to \tau\nu_\tau$ Wirkungsquerschnitts in Proton-Proton-Kollisionen bei einer Schwerpunktsenergie von $\sqrt{s} = 7\,\text{TeV}$ am ATLAS Experiment vorgestellt. Der ermittelte Wirkungsquerschnitt $\sigma^{\text{tot}}_{W\to\tau\nu_\tau} = (11.1 \pm 0.3\ (\text{stat.}) \pm 1.7\ (\text{syst.}) \pm 0.4\ (\text{lumi.}))\,\text{nb}$ stimmt mit der NNLO Vorhersage von $(10.46 \pm 0.52)\,\text{nb}$ überein. Des Weiteren wurde das $W \to \tau\nu_\tau$ Verzweigungsverhältnis bestimmt. Bei einem gesamten W Boson Produktionswirkungsquerschnitt von 100 nb mit einer fünfprozentigen Unsicherheit, ergibt sich ein Wert von $(11.1 \pm 0.3\ (\text{stat.}) \pm 1.8\ (\text{syst.}) \pm 0.4\ (\text{lumi.}))\%$, der wiederum mit der SM Erwartung von 10.83% übereinstimmt.

Das schönste Glück des denkenden Menschen ist,
das Erforschliche erforscht zu haben
und das Unerforschliche zu verehren.

Johann Wolfgang von Goethe

Contents

1 Introduction

Since time immemorial, mankind has tried to answer questions about the content of the universe, the elemental forces, and the origin of matter. Particle physics concentrates on these questions and studies the fundamental constituents of matter and their fundamental forces. The current theory of elementary particles is called the Standard Model (SM). It describes all known elementary particles and their interactions. The SM has been successfully tested at many experiments. Nevertheless, the SM has a number of limitations, of a theoretical as well as experimental and cosmological nature. It cannot explain, why the SM particles cover only 4% of the energy and matter content of the universe, why there is an asymmetry between matter and antimatter, and why there are a number of free parameters which cannot be calculated and have to be measured in experiments, to name only a few. Furthermore, the Higgs boson, the particle that explains how particles get mass, has not yet been found convincingly.

All these problems have led particle physicists to suppose that there must be a more fundamental theory, and the search for physics beyond the SM is underway. The third generation of the SM plays an important role for the Higgs sector and many extensions of the SM. Third generation particles, like the τ lepton, can be found in the final states of many supersymmetric scenarios as well as in the final states of Higgs bosons with light Higgs masses. Currently, there are some indications that point to a light Higgs boson with a mass around 126 GeV [1]. In this case, τ leptons would become very important.

Therefore, an exact understanding of τ leptons coming from SM processes is the key being able to identify τ leptons coming from processes beyond the SM. One of the most important SM processes with τ leptons in the final state is the $W \to \tau\nu_\tau$ decay due to a high cross section. Its cross section is ten times higher than the cross section for the $Z \to \tau\tau$ decay. Furthermore, it has a similar event signature as the event signature of a charged Higgs boson decaying into a τ lepton and the corresponding neutrino ν_τ, as well as the event signature of a $H \to \tau\tau$ decay in which one of the τ leptons is not reconstructed.

Studies of particles and their decays at highest energies are performed by experiments at high-energy particle colliders like the Large Hadron Collider (LHC), which started taking data in November 2009. Searching for physics beyond the SM, searching for the Higgs boson, and precision measurements of SM parameters are three of the main reasons for the construction of the LHC and its experiments.

In this thesis, the measurement of the $W \to \tau\nu_\tau$ cross section in proton-proton collisions at a center-of-mass energy of $\sqrt{s} = 7\,\text{TeV}$ at ATLAS is presented using 2010 ATLAS data. The ATLAS experiment is the largest of the LHC experiments. Repeating measurements of known SM processes is important to demonstrate that ATLAS works as expected. Furthermore, the $W \to \tau\nu_\tau$ branching ratio has to be remeasured because its average value was found to be 2.2σ outside of the SM expectation at the Large Electron Positron (LEP) collider (see Sec. 7.3) [2–5].

The experiments used to perform particle physics measurements are in general very complex. Very precise descriptions of MC events are needed in order to check the expectations of what will be measured in the detector and to optimise the detector performance. Such a description

performed in a MC simulation comprises the MC event generation (including the hard process, the parton shower, the hadronisation, the decay of particles, and the underlying event), a detector simulation, and particle reconstruction. Sophisticated tools are needed to check and ensure that the simulations work well. One of these tools is the HepMCAnalysis Tool, a framework for MC generator validation and comparisons. A description of its development and a discussion of its wide range of applications will be presented in this thesis.

This thesis covers two topics: the $W \to \tau\nu_\tau$ cross section measurement in proton-proton collisions at a center-of-mass energy of $\sqrt{s} = 7\,\text{TeV}$ at ATLAS and the development of the HepMCAnalysis Tool including its applications.
Chapter 2 describes theoretical aspects of particle physics. It gives an introduction to the SM, describes the main aspects of physics in proton-proton collisions, provides a brief overview of supersymmetry as an example of physics beyond the SM, and discusses the role of τ leptons in the context of new physics. This is followed by a description of the LHC and the ATLAS experiment in Chapter 3. Data taking at ATLAS, the ATLAS software framework Athena and object reconstruction at ATLAS are covered in Chapter 4. Afterwards, a general overview of Monte Carlo (MC) event generation and MC generators is given in Chapter 5. Chapter 6 illustrates the HepMCAnalysis Tool and its wide range of applications. The HepMC event record, a generator independent event record, is also introduced. The physics of the W boson and the τ lepton, as well as expectations of $W \to \tau\nu_\tau$ events in proton-proton collisions are covered in Chapter 7, followed by the measurement of the $W \to \tau\nu_\tau$ cross section in proton-proton collisions at $\sqrt{s} = 7\,\text{TeV}$ with the ATLAS experiment in Chapter 8. Chapter 9 summarises the main aspects discussed in this thesis.

2 Theoretical introduction

One of the goals in elementary particle physics is to explain and understand the constitution, the interactions, and the origin of matter.

There are four fundamental forces (interactions) that play a role in physics processes. Physicists would like to unify these four forces to one elemental force, described in a Theory of Everything (see Fig. 2.1).

A successful description is the Standard Model of particle physics (SM) [6–10] which summarises the today's knowledge in particle physics. According to the SM there are matter particles (fermions) as well as interaction particles (gauge bosons).

In the following, the SM and its main attributes are shortly described. Its particles and interactions are explained, as well as its limitations, supersymmetry (SUSY) as a possible extension of the SM and the role of τ leptons in this context. The main basics of proton-proton collisions, the structure of the proton and the τ lepton and the W boson are discussed in more detail. In Chap. 7, general aspects of $pp \to W + \mathrm{X} \to \tau\nu_\tau + \mathrm{X}$ events are discussed.

2.1 Standard Model of particle physics

The SM describes all known elementary particles which can participate in fundamental interactions due to the exchange of gauge bosons. Mathematically, the SM is based on a relativistic quantum field theory formulated within the Lagrangian formalism. The most important properties are described below.

2.1.1 Particles and interactions

The particles can be divided into two parts: fermions and bosons. Fermions, particles with half-integer spin, are the fundamental components of matter. Bosons are all particles with integer spin. For instance all exchange particles, the gauge bosons, belong to the bosons.

Fermions

The fermions can be divided further into two subgroups: quarks (up u, down d, charm c, strange s, top t, bottom b) and leptons (electron e, muon μ, tau τ and the corresponding neutrinos ν_e, ν_μ, ν_τ). All fermions, the quarks and the leptons, are sorted in three generations (families) as illustrated in Tab. 2.1. Each generation consists of two quarks (an up- and a down-type quark), a lepton and the corresponding neutrino. The mass range of these particles starts from a few eV and ends in the order of hundred GeV. From the first to the third generation the masses of the particles increases. The mass can not be calculated in the SM and has to be measured by experiments (see Sec. 2.1.2). Properties of these particles are listed in Tab. 2.2. A corresponding anti-particle is assigned to each of these twelve particles. By doing so, all quantities (e.g. mass) keep their value except the charged based quantities; they switch their sign. Mathematically,

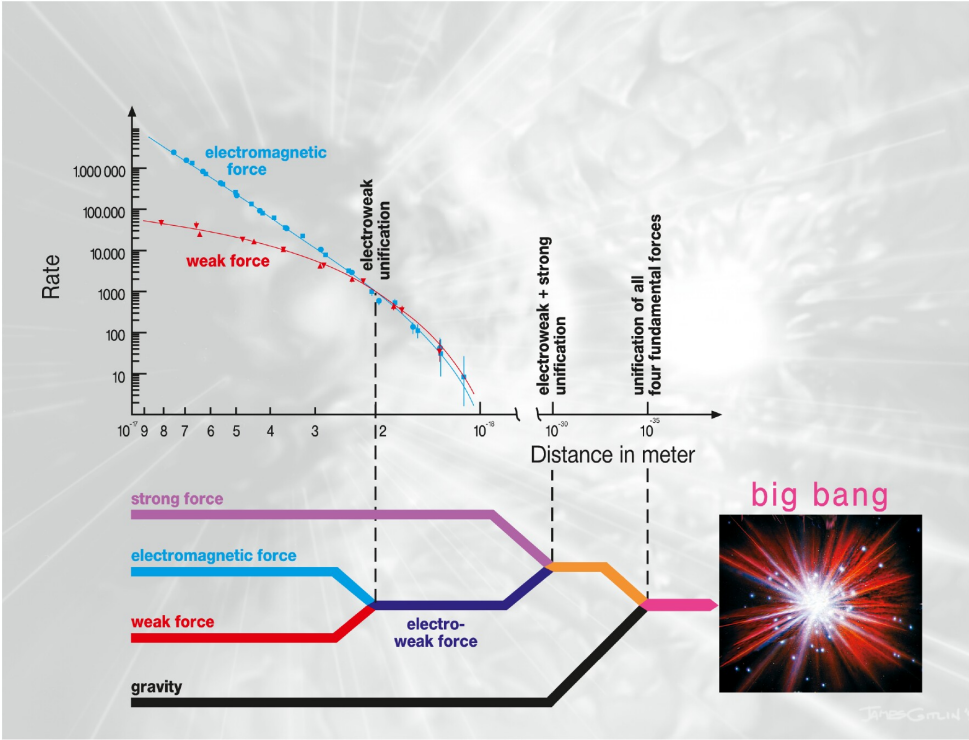

Figure 2.1: Unification of fundamental forces [11].

fermion \ generation	1	2	3
quark	u d	c s	t b
lepton	ν_e e	ν_μ μ	ν_τ τ

Table 2.1: Fermions of the Standard Model of particle physics.

all these fermions are described by spinors, so that they have a left-handed and a right-handed part, except of the neutrinos which are assumed to exist as left-handed particles only in the SM.

Interactions

The four fundamental forces/interactions - electromagnetic, weak, and the strong interaction, as well as gravity - and their properties are summarised in Tab. 2.3. Gravity does not belong to the SM. It is only listed here for completeness.

In order that particles interact, they need a fundamental charge. Additionally to the electrical charge in the electromagnetic interaction, it is the weak charge in the weak and the colour charge in the strong interaction. The mathematical description of the three interactions of the SM is done by an invariant $SU(3)_C \otimes SU(2)_L \otimes U(1)_Y$ gauge theory, which can be divided into two parts:

fermion \ property		electrical charge [e]	mass	interaction
quarks	u	$\frac{2}{3}$	$(1.7 - 3.1)\,\mathrm{MeV}$	em, strong, weak
	d	$-\frac{1}{3}$	$(4.1 - 5.7)\,\mathrm{MeV}$	
	c	$\frac{2}{3}$	$1.29^{+0.05}_{-0.11}\,\mathrm{GeV}$	em, strong, weak
	s	$-\frac{1}{3}$	$100^{+30}_{-20}\,\mathrm{MeV}$	
	t	$\frac{2}{3}$	$(172.9 \pm 0.6 \pm 0.9)\,\mathrm{GeV}$	em, strong, weak
	b	$-\frac{1}{3}$	$4.19^{+0.185}_{-0.06}\,\mathrm{GeV}$	
leptons	ν_e	0	$< 2\,\mathrm{eV}$	weak
	e	-1	$511\,\mathrm{keV}$	em, weak
	ν_μ	0	$< 0.19\,\mathrm{MeV}$	weak
	μ	-1	$105.658\,\mathrm{MeV}$	em, weak
	ν_τ	0	$< 18.2\,\mathrm{MeV}$	weak
	τ	-1	$1.777\,\mathrm{GeV}$	em, weak

Table 2.2: Properties of the fermions in the SM; the error for the mass of e, μ and τ is less than one per mill, so it is not mentioned here [12].

interaction	gauge boson	range	charge	mass [GeV]	relative force
electro-magnetic	photon γ	∞	0 electrical charge	0	10^{-2}
weak	$W^\pm$ Z^0	$10^{-18}\,\mathrm{m}$	± 1 0 weak charge	$(80,399 \pm 0,023)$ $(91,1876 \pm 0,0021)$	10^{-6}
strong	gluon g	$10^{-15}\,\mathrm{m}$	0 colour charge	0	1
gravity	graviton G	∞	0	0	10^{-40}

Table 2.3: Interactions and gauge bosons of the SM and their properties, gravity is listed in addition [12, 13].

- $SU(3)_C$[1], the symmetry of Quantum Chromodynamics (QCD) [9], describes the strong interaction between colour charged particles like quarks by coupling them to eight massless also coloured gluons which can interact/couple themselves, see Sec. 2.1.3.

- $SU(2)_L \otimes U(1)_Y$ specifies the electroweak interaction, the unification of the electromagnetic [14, 15] and weak [7, 8] force. The electroweak symmetry introduces three gauge bosons coming from $SU(2)_L$, the $W^{0,1,2}$, and one from $U(1)_Y$, the B^0, which all mix to the $W^\pm$ and Z^0 bosons and the massless photon γ. These four bosons couple to left-handed fermions (and right-handed antifermions) via the weak isospin I_3 and the weak hypercharge Y.

The fermions are sorted into multiplets which are summarised in Tab. 2.4. The left-handed fermions (and right-handed antifermions) form weak isospin doublets, while the right-handed fermions (and left-handed antifermions) are singlets.

[1]The subscript C stands for the colour charge.

			I_3	Y	Q
$\begin{pmatrix}\nu_e\\ e\end{pmatrix}_L$	$\begin{pmatrix}\nu_\mu\\ \mu\end{pmatrix}_L$	$\begin{pmatrix}\nu_\tau\\ \tau\end{pmatrix}_L$	$\begin{pmatrix}1/2\\ -1/2\end{pmatrix}$	$\begin{pmatrix}-1\\ -1\end{pmatrix}$	$\begin{pmatrix}0\\ -1\end{pmatrix}$
$\begin{pmatrix}u\\ d\end{pmatrix}_L$	$\begin{pmatrix}c\\ s\end{pmatrix}_L$	$\begin{pmatrix}t\\ b\end{pmatrix}_L$	$\begin{pmatrix}+1/2\\ -1/2\end{pmatrix}$	$\begin{pmatrix}1/3\\ 1/3\end{pmatrix}$	$\begin{pmatrix}+2/3\\ -1/3\end{pmatrix}$
e_R	μ_R	τ_R	0	-2	-1
u_R	c_R	t_R	0	+4/3	+2/3
d'_R	s'_R	b'_R	0	-2/3	-1/3

Table 2.4: $SU(2)_L$ doublets and $U(1)_Y$ singlets and corresponding electroweak quantum numbers and electromagnetic charge of fermions and antifermions, respectively.

The electric charge Q can be calculated from the weak isospin I_3 and the weak hypercharge Y

$$Q = I_3 + \frac{Y}{2}. \tag{2.1}$$

As mentioned above, the electroweak symmetry introduces in total 4 gauge bosons which are formed by four massless vector boson fields $W^{0,1,2}$ and B^0. The W^0 and W^1 fields build the two charged W bosons

$$W^{\pm} = \frac{1}{\sqrt{2}}\left(W^0 \mp iW^1\right) \tag{2.2}$$

and the B^0 and W^2 fields the neutral Z^0 boson and the photon A/γ

$$\begin{pmatrix}Z^0\\ A\end{pmatrix} = \begin{pmatrix}\cos(\theta_W) & -\sin(\theta_W)\\ \sin(\theta_W) & \cos(\theta_W)\end{pmatrix}\begin{pmatrix}W^2\\ B^0\end{pmatrix}. \tag{2.3}$$

The angle θ_W is the electroweak mixing angle with the value of $\sin^2(\theta_W) \approx 0.231$. The electroweak mixing angle θ_W describes the connection between the coupling constants of the electromagnetic force e and of the $SU(2)_L \otimes U(1)_Y$ model g and g'[2]

$$e = g\sin(\theta_W) = g'\cos(\theta_W). \tag{2.4}$$

The quark mass eigenstates also differ from their weak eigenstates, due to the Yukawa couplings

$$\mathcal{L}_Y = -Y^d_{ij}\overline{Q}_{L,i}\phi d_{R,j} - Y^u_{ij}\overline{Q}_{L,i}\epsilon\phi^* u_{R,j} + \text{h.c.} \tag{2.5}$$

with $Y^{u,d}$ as complex 3×3 matrix, ϕ as the Higgs field, i, j as generation labels and ϵ as the anti-symmetric 2×2 tensor. Q_L are left-handed quark doublets and d_R and u_R right-handed down- and up-type quark singlets, respectively.

2.1.2 The Higgs mechanism

The origin of the mass of particles is one of the fundamental problems in the SM. The problem is that the electroweak symmetry must be broken

$$SU(2)_L \otimes U(1)_Y \rightarrow U(1)_{em}. \tag{2.6}$$

[2]The coupling constant e comes out of the $U(1)_{em}$, g of $U(1)_Y$ and g' of $SU(2)_L$.

This is done by introducing the Higgs mechanism [16, 17].

The Higgs field is a scalar complex doublet

$$\phi = \frac{1}{\sqrt{2}} \begin{pmatrix} \phi_1 + i\phi_2 \\ \phi_3 + i\phi_4 \end{pmatrix} = \begin{pmatrix} \phi^+ \\ \phi^0 \end{pmatrix} \tag{2.7}$$

with four degrees of freedom. The Lagrangian of this Higgs field is

$$\mathcal{L} = \frac{1}{2} \left(\partial_\mu \phi\right) \left(\partial^\mu \phi\right) - V\left(\phi\right) \tag{2.8}$$

with

$$V\left(\phi\right) = \mu^2 \phi^\dagger \phi + \lambda \left(\phi^\dagger \phi\right)^2 \tag{2.9}$$

as the Higgs potential and μ^2 and λ being constants. $V \to \infty$ should apply for $\phi \to \pm\infty$, so λ has to be positive. The minimum of the potential lies at

$$|\phi_0| = \sqrt{\frac{-\mu^2}{\lambda}} = v \tag{2.10}$$

for $\mu^2 \leq 0$. For $\mu^2 < 0$, the ground state is no longer $SU(2)_L$ symmetric, which is called spontaneous symmetry breaking. Although the potential V with the parameter v, the vacuum expectation value, is still symmetric in $SU(2)_L$, every ground state breaks this symmetry. By choosing a specific ground state with $\phi_1 = \phi_2 = \phi_4 = 0$ and by expanding ϕ around the minimum

$$\phi = \frac{1}{\sqrt{2}} \begin{pmatrix} \xi_1\left(x\right) + i\xi_2\left(x\right) \\ v + h\left(x\right) + i\xi_3\left(x\right) \end{pmatrix} \tag{2.11}$$

with $h\left(x\right)$ and $\xi_{1,2,3}\left(x\right)$ as real scalar fields, one gets a mass term $m_h = \sqrt{2}\mu$ for h. The massless fields $\xi_{1,2,3}\left(x\right)$ are known as Goldstone bosons, which are absorbed by the gauge bosons and create mass terms:

$$m_W = \frac{1}{2} g v, \tag{2.12}$$

$$m_Z = \frac{1}{2} v \sqrt{g^2 + g'^2} \tag{2.13}$$

and

$$m_\gamma = 0. \tag{2.14}$$

Thereby the masses of the W and Z bosons are coupled via

$$m_W = m_Z \cos\left(\theta_W\right). \tag{2.15}$$

With Eqs. (2.12), (2.13), (2.14), (2.15) and (2.4) as well as the measurements of m_W, m_Z and θ_W, the vacuum expectation value v can be estimated to be

$$v \approx 246 \text{ GeV}. \tag{2.16}$$

In addition to the gauge boson mass terms, all fermions get masses by the Higgs mechanism

$$m_f = \lambda_f \frac{v}{\sqrt{2}}, \tag{2.17}$$

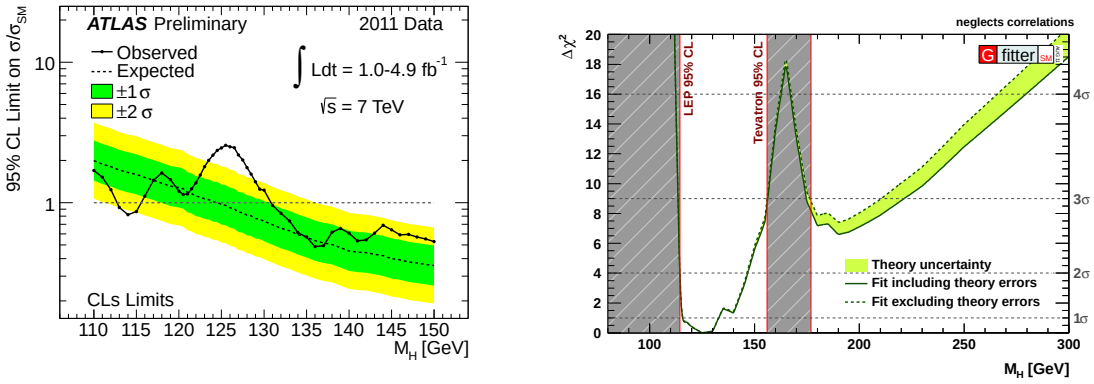

(a) (b)

Figure 2.2: (a) Combined upper limit on the measured SM Higgs boson production cross section divided by the SM expectation as a function of the Higgs boson mass m_H [1] and (b) indirect determination of the Higgs boson mass: $\Delta\chi^2$ as a function of M_H for the complete fit including direct Higgs searches results with data from LEP, TEVATRON, and 2010 LHC data [19].

where λ_f is the coupling constant depending on the fermion.

The mass of the Higgs boson, which has not yet been discovered, is a free parameter of the model which can only be determined by measurements. Many experiments at LEP and TEVATRON have searched for the Higgs boson, but could only set limits on its mass range. The Higgs boson has a mass in the range of (116 – 130) GeV (ATLAS), respectively (115 – 127) GeV (CMS) [18]. Figure 2.2(a) shows the upper limit on the SM cross section over the SM expectation as a function of the Higgs boson mass at the ATLAS experiment [1]. An indirect determination including LEP, TEVATRON, and 2010 LHC data of the Higgs boson mass is shown in Fig. 2.2(b) with a possible Higgs boson mass in the same mass range [19].

2.1.3 Quantum Chromodynamics

Quantum Chromodynamics (QCD) [9] is the gauge theory, based on the $SU(3)_C$ gauge group, of the strong interaction and describes the interaction between quarks and gluons. The gluons are massless and the gauge bosons of QCD. Analogous to the electric charge, there is the colour charge in QCD with three different colours: red, blue and green. The quarks as well as the gluons are coloured, whereas the quarks carry three different colours[3] and the gluons a colour and an anticolour. In total there are nine colour combinations for the gluons, but only eight are realised in nature and described by the $SU(3)_C$ colour octet.

Interactions in particle physics can be described by Feynman diagrams, while the calculations are often performed by Taylor expanding the Lagrangian. Every term of the Taylor series corresponds to a specific Feynman diagram. These diagrams also contain closed internal particle loops. These loops can be arbitrarily massive, so these diagrams can become divergent, which results also in divergencies of the calculations – an infinite scattering amplitude. A method called renormalisation is needed to avoid this. A scale Λ^2_{QCD} is introduced. This scale limits the energy in the loop and every divergent diagram is corrected by a counterterm.

[3] Accordingly, antiquarks carry three different anticolours.

This scale Λ^2_{QCD} goes into the (running) strong coupling constant α_s which is also dependent on the momentum transfer Q^2. At leading order, α_s can be described as

$$\alpha_s\left(Q^2\right) = \frac{4\pi}{\beta_0 \ln\left(Q^2/\Lambda^2_{\mathrm{QCD}}\right)} \tag{2.18}$$

with Λ^2_{QCD} as the so-called QCD scale ($\sim 217\,\mathrm{MeV}$) and $\beta_0 = 11 - \frac{2}{3}n_f$ (n_f is the number of quark flavours which contributes) as a constant which is called the QFT beta-function in which the running of the coupling parameter is included. The strong coupling constant α_s is large at small values of Q^2 and decreases up to ≈ 0 for high values of Q^2. This behaviour is called asymptotic freedom and confinement. Asymptotic freedom means that at short distances (high Q^2) quarks and gluons are quasi-free particles, while for small Q^2 and therefore large distances, quarks are coupled together (confinement) and build hadrons.

2.1.4 Proton-proton collisions and proton structure

Hadrons consist of gluons and two kinds of quarks, valence quarks and sea quarks. In the simplest description, a proton is made up of two up- and one down-quark, the valence quarks, but to be more detailed there are further quark-antiquark pairs, the sea quarks, and gluons. There is a permanent flux of gluons emitting quark-antiquark pairs and quark-antiquark pairs annihilating to gluons. All constituent parts of the proton, the partons[4], carry the total momentum of the proton. The fractional momentum of each parton is given by the parton distribution functions (PDFs) [20–28], which are determined experimentally, for example in deep inelastic scattering (DIS) experiments at the HERA accelerator, more details see below.

The detailed knowledge of the proton structure is important in proton-proton collisions [29], where several processes contribute, visualised in Fig. 2.3, like the partonic hard scattering process including initial state radiation (ISR, gluon radiation from the initial state partons) and final state radiation (FSR, gluon radiation from the final state partons), the multiple parton interactions (MPI) and the underlying event (UE) which are all activities in the event not affected by the hard scattering process. Though, there are hard as well as soft scattering processes in a proton-proton collision which can be predicted with different techniques. The underlying theory for such processes is the QCD.

The hard interaction can be calculated with a perturbative expansion of the QCD (perturbative QCD, pQCD) through leading order (LO) and next-to-leading order (NLO) calculations of the cross section. LO cross section calculations contains contributions of $\mathcal{O}\left(\alpha_s\right)$ while at NLO calculations contributions up to $\mathcal{O}\left(\alpha_s^2\right)$ are included. The distribution of quarks and gluons in the proton has to be considered for the calculation of soft processes. They can not be calculated with pQCD [29]. For an exact calculation of a proton-proton collision, pQCD and non-perturbative calculations are needed which can be separated in the factorisation theorem. The short-distance, process-dependent parton cross section is calculated using pQCD while the long-distance functions (hadronisation, parton distribution functions, models of multi parton interactions) are determined empirically.

The factorisation theorem was formulated by Drell and Yan [30] and assumes that the cross section of a process (σ_{AB}) can be reduced to the partonic cross section ($\hat{\sigma}_{ab\to X}$) with the PDFs

[4] Partons are the valence and sea quarks as well as the gluons, though all constituent parts of the proton.

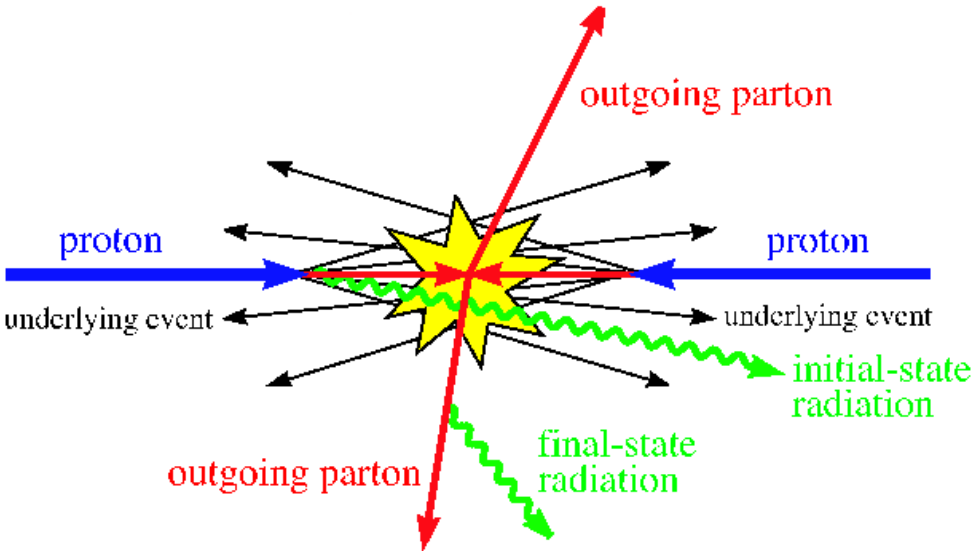

Figure 2.3: Schematic cartoon of a $2 \rightarrow 2$ hard scattering event [29].

of the protons A and B ($f_{a/A}\left(x_a, \mu_F^2\right)$, $f_{b/B}\left(x_b, \mu_F^2\right)$)

$$\sigma_{AB} = \int dx_a dx_b f_{a/A}\left(x_a, \mu_F^2\right) f_{b/B}\left(x_b, \mu_F^2\right) \times \left[\hat{\sigma}_0 + \alpha_s\left(\mu_R^2\right)\hat{\sigma}_1 + \cdots\right]_{ab\rightarrow X} \tag{2.19}$$

with μ_F as factorization scale, which can be thought of as the scale separating the long- and short-distance physics, and μ_R as renormalisation scale for the running coupling constant α_s. The factorization scale μ_F is similar to the renormalisation scale μ_R and needed to deal with the divergencies.

The partonic cross section in Eq. (2.19) is given by integrating the squared matrix element (amplitude of the interaction) over the appropriate phase space, which is often done numerically. To avoid divergencies, corresponding regions of the phase space are simply excluded from the calculation.

The parton distribution functions describe the distribution of quarks and gluons by parametrising the parton momentum as a function of the fraction x of the total proton momentum and the momentum transfer Q^2. Figure 2.4 shows the combined results from H1 and Zeus for the valence quarks xu_v and xd_v, the gluons xg as well the sea quarks xS at $Q^2 = 10\,\mathrm{GeV}^2$ [28]. It is illustrated that valence quarks are dominated at high x values while at low x values there is an increase of the gluon and sea quarks densities.

Parton distribution functions are evoluted with different evolution methods in such a way that they delete the divergencies in the partonic cross section calculation. Several groups, for example CTEQ [20], MRST/MSTW [21, 22], Alekhin [23], and groups at HERA [24–28], have produced sets of PDFs based on data from HERA and the TEVATRON.

One of the evolution methods are the Dokshitzer-Gribov-Lipatov-Altarelli-Parisi (DGLAP) equations [31–34] which start from an initial distribution at a measured predefined scale

$$\frac{df_{a|p}\left(x, Q^2\right)}{dlogQ^2} = \frac{\alpha_s\left(Q^2\right)}{2\pi}\int_x^1 \frac{dz}{z}\left\{P_{aa'}\left(z, \alpha_s\left(Q^2\right)\right) f_{a'|p}\left(\frac{x}{z}, Q^2\right)\right\} \tag{2.20}$$

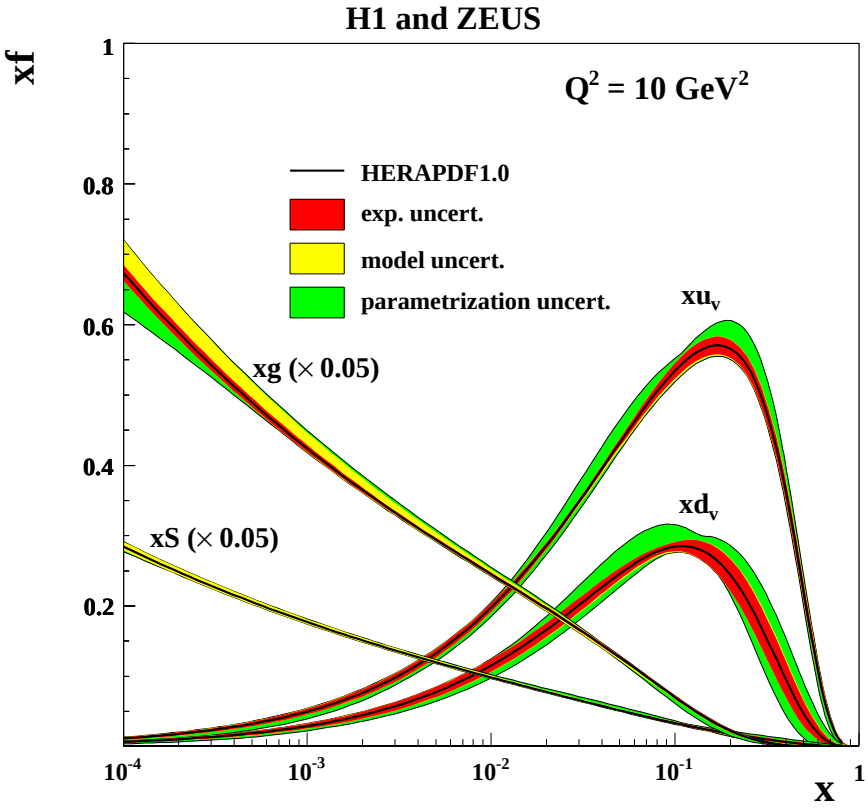

Figure 2.4: The parton distribution functions from HERAPDF1.0, $xu_v, xd_v, xS = 2x(\bar{U}+\bar{D}), xg$, at $Q^2 = 10$ GeV^2. The gluon and sea quark distributions are scaled down by a factor 20 [28].

with $P_{aa'}\left(z, \alpha_s\left(Q^2\right)\right)$ as Altarelli-Parisi splitting functions which give the probability that a parton a with the momentum fraction z emits another parton a' with the momentum fraction x

$$P_{aa'}\left(z, \alpha_s\left(Q^2\right)\right) = P^0_{aa'}(z) + \frac{\alpha_s\left(Q^2\right)}{2\pi} P^1_{aa'}(z) + \left(\frac{\alpha_s\left(Q^2\right)}{2\pi}\right)^2 P^2_{aa'}(z) + \ldots . \tag{2.21}$$

The superscript 0, 1, 2, ... corresponds to the order of the calculation. In the DGLAP equations, the partons are ordered by their transverse momentum k_T with

$$Q^2 \gg k^2_{T_n} \gg \cdots \gg k^2_{T_2} \gg k^2_{T_1}, \tag{2.22}$$

which is only valid for large Q^2 and large x with $\alpha_s\left(Q^2\right) \ln\left(\frac{1}{x}\right) \ll \alpha_s\left(Q^2\right) \ln Q^2$. At low x the Balitsky-Faden-Kuraev-Lipatov (BFKL) equations [35–38] are used. The BFKL method orders the partons by their momentum fraction and the ordering in k_T is not longer used. The Ciafaloni-Cantani-Fiorani-Marchesini (CCFM) scheme [39, 40] is an attempt to combine the two evolution methods (DGLAP for high and BFKL for low x).

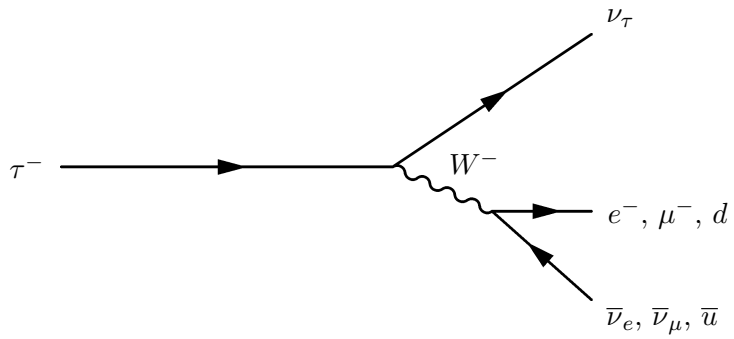

Figure 2.5: Illustration of a feynman diagram of a τ^- lepton decay via the production of a virtual W^- boson.

2.1.5 The τ lepton and W boson

The decay $W \rightarrow \tau\nu_\tau$ in proton-proton collisions is studied in this thesis. Therefore, the most important characteristics of the τ lepton and the W boson are discussed here, while the physics of the τ lepton and the W boson at the Large Hadron Collider (LHC) is discussed in Chap. 7.

The τ lepton has been discovered 1975 at the electron-positron storage ring SPEAR at the Stanford Linear Accelerator (SLAC) in Stanford [41]. It belongs to the third generation of the leptons, is negatively charged, underlies the electroweak interaction and is the heaviest lepton with a mass of $(1776.82 \pm 0.16)\,\text{MeV}$ [12]. Due to its rather short lifetime of $(2.906 \pm 0.010) \times 10^{-13}\,\text{s}$ [12], it decays instantaneously in the detector of collision experiments and can only be detected via its decay products. Due to its large mass, the τ lepton is able to decay into leptons and hadrons and has a high number of decay products. A τ lepton decay is illustrated in Fig. 2.5. The most important decay channels are listed in Tab. 2.5. As it can be seen, there is always at least one neutrino in the τ lepton decay which leads to missing transverse momentum in the detector. Tau leptons decay leptonically in around 35.21% of the cases. These τ leptons can not be easily distinguished from prompt electrons or muons and though can not be reconstructed directly. All other τ leptons decay hadronically, mainly to pions. These τ lepton decays are sorted by the number of charged decay particles, the so-called '1-prong', '3-prong' and '5-prong' τ leptons. Hadronically decaying τ leptons are difficult to detect due to their similarity to QCD jets. The shape difference of a hadronic τ lepton decay and a QCD jet is due to the colour flow of these two objects. The τ lepton decays colour neutral via a W boson (see Fig. 2.5) which means that the maximum Q^2 of the decay is m_τ^2 resulting in a narrow cone compared to a QCD jet (see Sec. 4.4.2). Compared to this, a QCD jet, consisting of quarks and gluons, is not a colour neutral object. The colour field in such a jet can have enough energy, so that new quark-antiquark pairs are produced resulting in colour neutral hadrons during the fragmentation. There is no energy limit in the colour field of a jet, which is why the jet shape expands compared to a hadronically decaying τ lepton.

The τ neutrino is present in all decay channels. It was discovered in the year 2 000 at the DONUT experiment located at FERMILAB [42]. High-energy protons have been accelerated and collided with a tungsten block to produce τ neutrinos and other particles. Its mass is less than 18.2 MeV [12].

The positively and the negatively charged W bosons are together with the Z^0 boson the gauge bosons of the weak theory. They have been predicted by Glashow, Salam and Weinberg

	decay cannel	branching fraction
	$\tau \rightarrow$ hadrons	64.79%
	$\tau \rightarrow$ leptons	35.21%
leptonic	$\tau^- \rightarrow \mu^- \overline{\nu}_\mu \nu_\tau$	$(17.39 \pm 0.04)\,\%$
	$\tau^- \rightarrow e^- \overline{\nu}_e \nu_\tau$	$(17.82 \pm 0.04)\,\%$
hadronic 1-prong	$\tau^- \rightarrow \pi^- \nu_\tau$	$(10.91 \pm 0.07)\,\%$
	$\tau^- \rightarrow \pi^- \pi^0 \nu_\tau$	$(25.51 \pm 0.09)\,\%$
	$\tau^- \rightarrow \pi^- 2\pi^0 \nu_\tau$	$(9.29 \pm 0.11)\,\%$
	$\tau^- \rightarrow \pi^- 3\pi^0 \nu_\tau$	$(1.04 \pm 0.07)\,\%$
	$\tau^- \rightarrow K^- \nu_\tau$	$(0.696 \pm 0.023)\,\%$
	$\tau^- \rightarrow K^- \pi^0 \nu_\tau$	$(0.429 \pm 0.015)\,\%$
	$\tau^- \rightarrow K^- 2\pi^0 \nu_\tau$	$(0.065 \pm 0.023)\,\%$
	$\tau^- \rightarrow K^- 2\pi^0 \nu_\tau$	$(0.049 \pm 0.022)\,\%$
hadronic 3-prong	$\tau^- \rightarrow \pi^- \pi^+ \pi^- \nu_\tau$	$(9.31 \pm 0.06)\,\%$
	$\tau^- \rightarrow \pi^- \pi^+ \pi^- \pi^0 \nu_\tau$	$(4.61 \pm 0.06)\,\%$

Table 2.5: Overview of the most probable τ lepton decay channels and their branching fractions [12].

	decay cannel	branching fraction
	$W \rightarrow$ hadrons	67.6%
	$W \rightarrow$ leptons	32.4%
leptonic	$W^+ \rightarrow e^+ \nu_e$	$(10.75 \pm 0.13)\,\%$
	$W^+ \rightarrow \mu^+ \nu_\mu$	$(10.57 \pm 0.15)\,\%$
	$W^+ \rightarrow \tau^+ \nu_\tau$	$(11.25 \pm 0.20)\,\%$
hadronic	$W^+ \rightarrow c\mathrm{X}$	$(33.4 \pm 2.6)\,\%$
	$W^+ \rightarrow c\overline{s}$	$\left(31\ {}^{+13}_{-11}\right)\,\%$

Table 2.6: Overview of the most probable W boson decay channels and their branching fractions [12].

in the sixties of the 20th century [6–8] and observed 1983 by the UA1 and UA2 Collaborations at the proton-antiproton collider Sp$\overline{\text{p}}$S at CERN [43, 44]. The W bosons mediate the weak interaction between leptons and quarks and change the flavour of the particles. Their properties are measured in detail by the LEP experiments via W pair production $e^+e^- \rightarrow W^+W^-$ [45]. The W bosons have a mass of $(80.399 \pm 0.023)\,\text{GeV}$ and decay 67.6% hadronically and 32.4% leptonically [12]. The most common decay channels are listed in Tab. 2.6.

2.1.6 Problems of the Standard Model of particle physics

Although the Standard Model of particle physics is a successful theory, there are still some open issues. Together with some experimental problems of cosmological nature (e.g. dark matter, matter-antimatter asymmetry), there are also unsolved problems in the theoretical formalism of the SM (e.g. parameter problem, hierarchy problem). Some of these problems will be shortly illustrated here.

There are a lot of free parameters in the SM which can not be calculated within the model. Furthermore the running coupling constants of the electroweak and the strong interaction do not unify as this is done for the electromagnetic and weak interaction. A possible solution for such a unification could be Grand Unified Theories (GUTs) [46], in which the SM could be embedded, and supersymmetric extensions of the Standard Model [47–49].

Another limitation of the SM studies the question why only 4% of the energy/matter content of the universe can be described by the SM. 76% is filled up with so-called dark energy which is responsible for the accelerated expansion of the universe. The remaining 20% of the universe content consists of dark matter [50] which interacts only weakly and can be observed by astrophysical measurements and gravitational effects. Due to its small mass, the neutrino is excluded as the only candidate of dark matter in the SM. Supersymmetric theories, which introduce many dark matter candidates depending on the model, could provide a solution for this problem.

There is also a matter-antimatter asymmetry in the universe which can not be explained only by the complex phase in the CKM matrix as source of CP violation [51–53]. Additional complex phases in supersymmetric extensions could solve this problem [54].

The Higgs mechanism explains how particles get mass. But enormous quantum corrections from loop effects of every particle coupling to the Higgs boson increase the Higgs boson mass quadratically with the cutoff scale Λ. This is known as the hierarchy problem

$$\Delta M_H^2 = -\frac{|\lambda_t|^2}{8\pi^2}\Lambda^2 + \mathcal{O}\left(\ln\frac{\Lambda}{m_f}\right) + \dots . \tag{2.23}$$

These mathematical divergencies can only be avoided by a finetuning of the cutoff scale.

As last limitation, it should be mentioned that gravity is not included in particle physics. The gravitational force is weak enough that it can be neglected in collider physics. But at energies at the Planck scale the strength of the SM forces and gravity are of the same order of magnitude. This is why a fundamental theory including gravity and the SM is needed.

2.2 Supersymmetry as a possible extension of the Standard Model

Due to the limitations of the SM, it is believed that the SM is only a part of a more fundamental theory. There are lots of such theories which solve the limitations of the SM. The basic idea of one of the most studied extensions, supersymmetry (SUSY), will be briefly sketched here, just to give one example for physics beyond the SM, where the third generation of the SM plays an important role.

Supersymmetry (SUSY) is an extension of the SM which can unify the three running coupling constants (electromagnetic, weak and strong) in one point at around $10^{16}\,\text{GeV}$ (see Fig. 2.6). SUSY is a symmetry which transforms bosons into fermions and vice versa

$$\begin{aligned} Q\,|\text{fermion}\rangle &= |\text{boson}\rangle \\ Q\,|\text{boson}\rangle &= |\text{fermion}\rangle \end{aligned}\,', \tag{2.24}$$

where Q is a transformation operator. The supersymmetric partner particles of the SM particles, listed in Tab. 2.7, are called sfermions (squarks, sleptons) for the SM fermions and gauginos for the SM gauge bosons.

This fermion-boson symmetry provides a solution for the hierarchy problem (see Eq. (2.23))

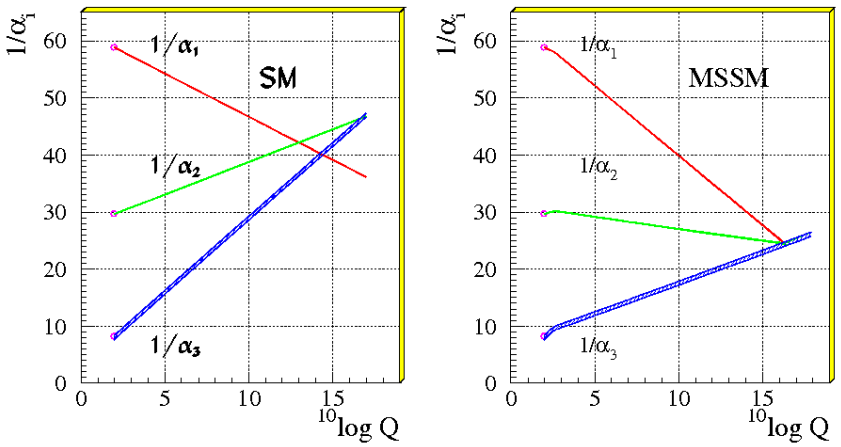

Figure 2.6: The unification of the running coupling constants in the SM and the Minimal Supersymmetric Standard Model (MSSM) [55].

	SM particle	SUSY particle
fermion/sfermion	e, μ, τ ν_e, ν_μ, ν_τ	$\widetilde{e}$, $\widetilde{\mu}$, $\widetilde{\tau}$ $\widetilde{\nu}_e$, $\widetilde{\nu}_\mu$, $\widetilde{\nu}_\tau$
quark/squark	u, c, t d, s, b	$\widetilde{u}$, $\widetilde{c}$, $\widetilde{t}$ $\widetilde{d}$, $\widetilde{s}$, $\widetilde{b}$
gauge bosons/gauginos	γ, g, Z^0, $W^\pm$, $H^{0,\pm}$	$\widetilde{\gamma}$, $\widetilde{g}$, $\widetilde{Z}^0$, $\widetilde{W}^\pm$, $\widetilde{H}^{0,\pm}$

Table 2.7: SM particles and their supersymmetric partner particles.

by introducing quantum corrections of scalar particles that cancel the divergencies of the SM fermions.

All quantum numbers of SM and SUSY particles except the spin of the particle are the same if there were an exact symmetry between these two types of particles. The consequence of an exact symmetry would be that the masses of SUSY particles are the same as for SM particles. But so far, no supersymmetric particle has been found in nature, so SUSY has to be broken (like the electroweak symmetry) which is achieved by extending the Lagrangian with non-supersymmetric terms.

In SUSY an additional quantum number is defined, the R-parity

$$P_R = (-1)^{3(B-L)+2s} \tag{2.25}$$

with B as baryon number, L as lepton number and s as the spin of the particle. SM particles have an R-parity of $P_R = 1$ and SUSY particles of $P_R = -1$. If R-parity is conserved, SUSY particles are only produced in pairs and the lightest supersymmetric particle (LSP) has to be stable. Therefore the LSP would be a good candidate for dark matter.

There are several supersymmetric models. The Minimal Supersymmetric Standard Model (MSSM) has 105 additional free parameters in comparison to the SM. Using assumptions for the SUSY breaking mechanism the number of free parameters can be reduced to five parameters in minimal Supergravity (mSugra) and six parameters in the Gauge Mediated SUSY Breaking

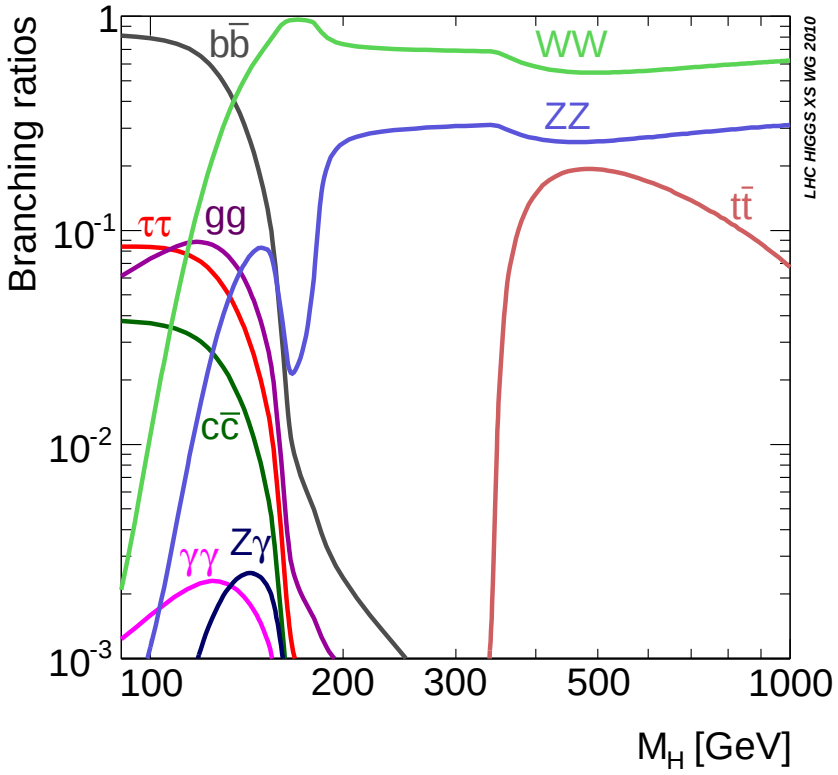

Figure 2.7: Branching ratios of a SM Higgs boson [60].

(GMSB).

Further information on supersymmetric theories can be found in [47–49].

2.3 Tau leptons in context of new physics

Tau leptons play an important role in the context of new physics. They are often final state particles of SUSY scenarios and can be found in the Higgs boson decay.

Higgs searches

Tau leptons are fundamental decay products of the Higgs boson. Figure 2.7 shows the branching ratio of the SM Higgs boson as a function of its mass for different Higgs decay channels. It can be seen that the third generation fermions are quite useful for the search of the Higgs boson. In addition to the decay into gauge bosons, the Higgs boson often decays to heavier fermions. For light Higgs boson masses the decays $H \to b\bar{b}$ and $H \to \tau^+\tau^-$ become dominant. Due to the fact that $H \to b\bar{b}$ is difficult to measure at the LHC [56–58], the decay $H \to \tau^+\tau^-$ is an important final state for the Higgs search. There is also the Higgs boson decay into two photons (no third generation particles), which can be measured precisely [59], but the branching ratio of $H \to \tau\tau$ processes is substantial (see Fig. 2.7). The production of a Higgs boson decaying into two τ leptons is illustrated in Fig. 2.8.

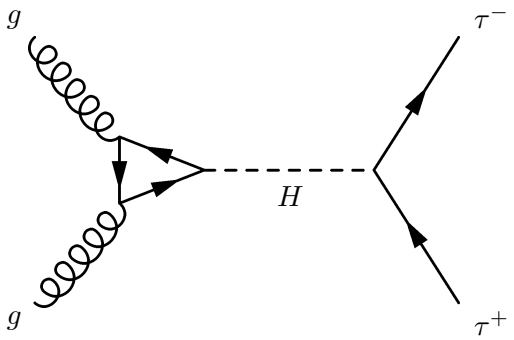

Figure 2.8: Production process of a Higgs boson decaying into two τ leptons.

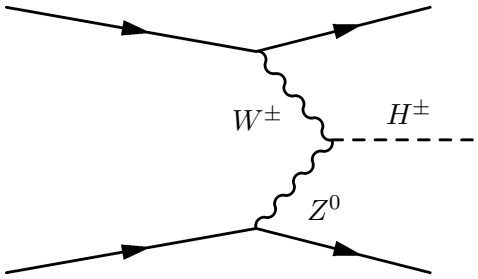

Figure 2.9: Production of a charged Higgs boson via vector boson fusion.

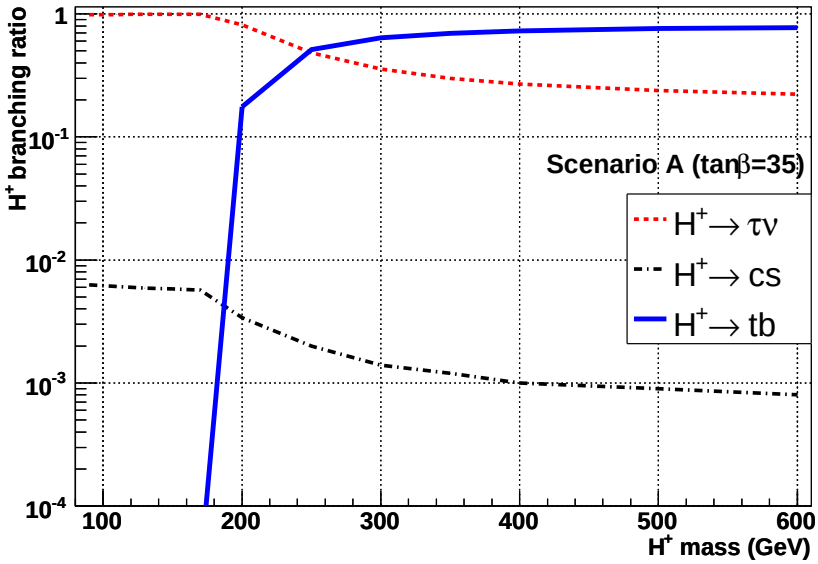

Figure 2.10: Expected branching ratios of a charged Higgs boson H^+ in the MSSM [61]. Scenario A is one of the scenarios in the MSSM, in which the free parameters get particular values described in [61]. $\tan\beta$ is the ratio of the vacuum expectation values of the Higgs fields.

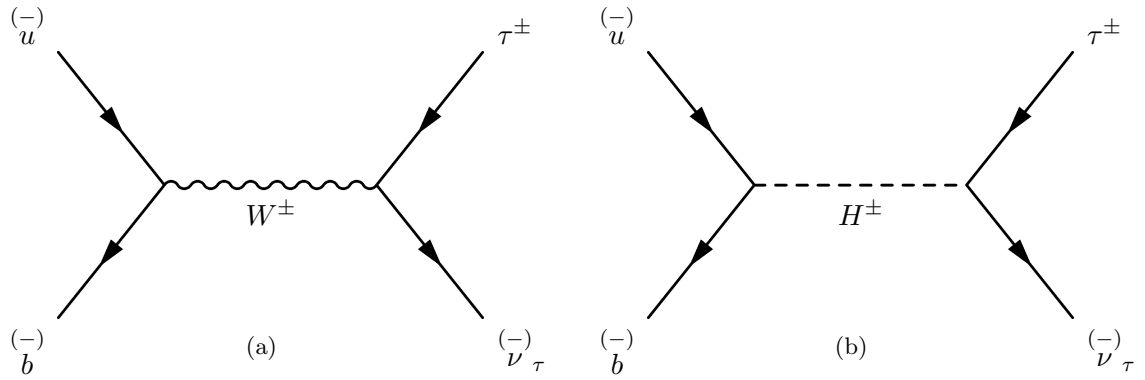

Figure 2.11: (a) $W^{\pm}$ boson and (b) $H^{\pm}$ boson decay via a τ lepton and a τ neutrino.

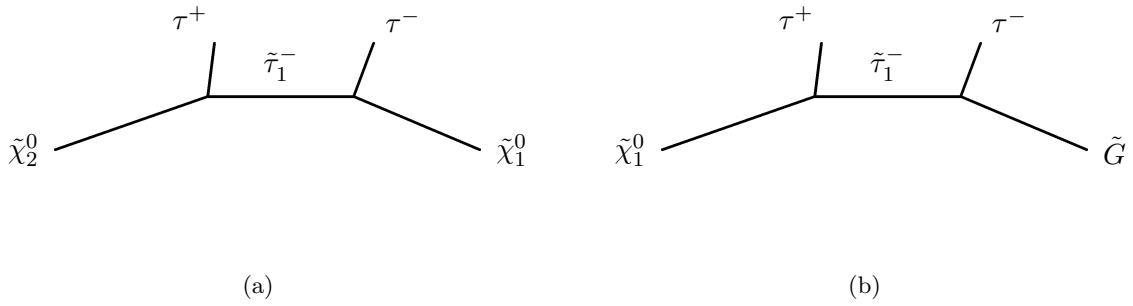

Figure 2.12: Two SUSY decay chains with τ leptons in the final state for (a) mSugra and (b) GMSB.

Furthermore, the understanding of τ leptons is required due to the production of charged Higgs bosons in SUSY models via vector boson fusion [62, 63] (see Fig. 2.9). Its branching ratios are given in Fig. 2.10. One can see that the most dominant process is the charged Higgs boson decay into a τ lepton and a τ neutrino for light Higgs masses. These decays are similar to the signature of $W \to \tau\nu_\tau$ events as illustrated in Fig. 2.11. This is why a deep comprehension of the behaviour of τ leptons is fundamental.

SUSY search

Tau leptons can often be found in the final state of supersymmetric scenarios. According to the electroweak breaking, a left and right handed sfermion mixing appears in the SUSY breaking, which results in a mixture of left and right handed components for the mass eigenstates. The result is that sfermions of the first and second generation have large masses in many SUSY models, while the mass of the $\tilde{\tau}_{1,2}$ slepton, the supersymmetric partners of the τ lepton, is relative small.[5] As a consequence, the branching ratios for e.g. $\tilde{\chi}_2^0 \to \tilde{\tau}_1\tau$ are in specific SUSY scenarios larger than for electrons or muons in the final state of the SUSY decay chain. Figure 2.12 shows two SUSY scenarios with τ leptons in the final state. The understanding of the τ leptons is so fundamental in these cases because they provide information for e.g. $\tilde{\tau}$ masses. So, τ leptons are important for the discovery of SUSY particles. The decay channels $W \to \tau\nu_\tau$ and $Z \to \tau\tau$ are for such a discovery one of the most important backgrounds.

[5]The mass for the $\tilde{\tau}_1$ slepton is by definition smaller than for the $\tilde{\tau}_2$ slepton.

3 The LHC and the ATLAS detector

The Large Hadron Collider (LHC) is designed to solve the problems of the Standard Model, which were described in Chap. 2. The LHC and the ATLAS detector is illustrated in this chapter. At the beginning, the LHC is shortly introduced. Afterwards, the design of the detector is described. Next, the coordinate system used at ATLAS, the magnet system, the inner detector, the calorimeter system, and the muon spectrometer are presented. At the end, the ATLAS trigger is discussed which is responsible for reducing the event rate from 40 MHz to around 200 Hz. Finally, the τ lepton and missing transverse momentum $E_{\mathrm{T}}^{\mathrm{miss}}$ performance of the ATLAS detector, relevant to the analysed decay $W \to \tau\nu_\tau$ in proton-proton collissions (see Chaps. 7 and 8), is shown.

Unless otherwise specified, the explanations are based on [64] and [58].

3.1 The Large Hadron Collider

The Large Hadron Collider (LHC) is a two ring superconducting hadron accelerator and collider located at CERN[1], near Geneva in Switzerland. The accelerator was built in the former LEP[2] tunnel, is between 45 m and 170 m below the surface, and has a circumference of 26.7 km.
Fig. 3.1 shows a schematic view of the LHC with its four major experiments. ATLAS[3] and CMS[4] are multipurpose detectors designed to search for new physics such as the Higgs boson, supersymmetry, mini black holes, extra dimensions etc., while the two other detectors are more specialised. LHCb[5] is a B-physics experiment, focusing on CP-violating and rare decays with the hope of explaining the universes baryonic asymmetry. And last but not least the ALICE [6] experiment is designed to study the quark-gluon plasma in heavy ion collisions.

The LHC is filled with protons, lead (Pb) ions, or gold (Au) ions via the LINAC2, the Proton Synchrotron Booster (PSB, Booster), the Proton Synchrotron (PS) and the Super Proton Synchrotron (SPS) as shown in Fig. 3.2.
After cooling down the machine to an operating temperature of 1.9 K, the LHC was successfully switched on on September 10th 2008, but on September 19th 2008 there was an incident which damaged an electrical connection between two magnets and resulted in a large helium leak into the tunnel which destroyed several magnets [65–68].

Finally, after a repair time of approximately one year, the LHC started data taking in November 2009. First proton-proton-collisions at 450 GeV - the injection energy of the SPS - took place from November 23rd 2009 to December 18th 2009 [69, 70]. After a Christmas break and a short shutdown, on March 30th 2010 there were the first proton-proton collisions with a beam energy of 3.5 TeV resulting in a center-of-mass energy of 7 TeV [71]. From November 7th 2010 until the winter shut down in December 2010 heavy lead ions collided in the LHC [72].

[1] Conseil Européen pour la Recherche Nucléaire
[2] Large Electron Positron (collider)
[3] **A** **T**oroidal **L**HC **A**pparatu**S**
[4] **C**ompact **M**uon **S**olenoid
[5] **L**arge **H**adron **C**ollider **b**eauty
[6] **A** **L**arge **I**on **C**ollider **E**xperiment

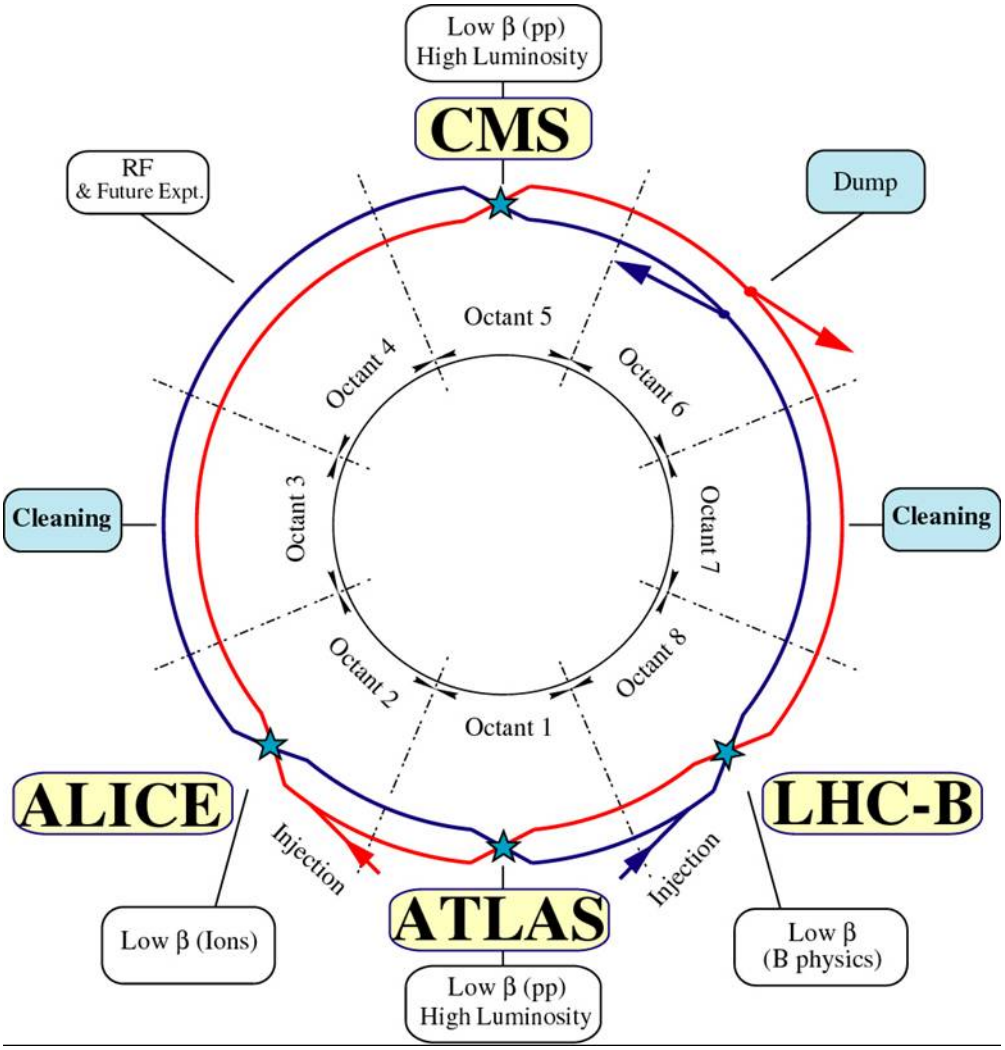

Figure 3.1: Schematic view of the LHC with its four major experiments [64].

It is foreseen that the LHC will run with a center-of-mass energy of 7 TeV until the end of 2012 [73]. Afterwards during a longer shut down, the LHC will be prepared to run with its designed center-of-mass energy of 14 TeV [64, 73].

The LHC collects a huge amount of data. The number of events per second in LHC collisions is calculated by

$$N_{\text{event}} = \mathcal{L} \cdot \sigma_{\text{event}}, \tag{3.1}$$

where σ_{event} is the cross section for the event under study and $\mathcal{L}$ the machine luminosity which depends on beam parameters and is written as[7]:

$$\mathcal{L} = \frac{N_b^2 n_b f_{rev} \gamma_r}{4\pi\epsilon_n \beta_*} F \tag{3.2}$$

[7] for a Gaussian beam distribution

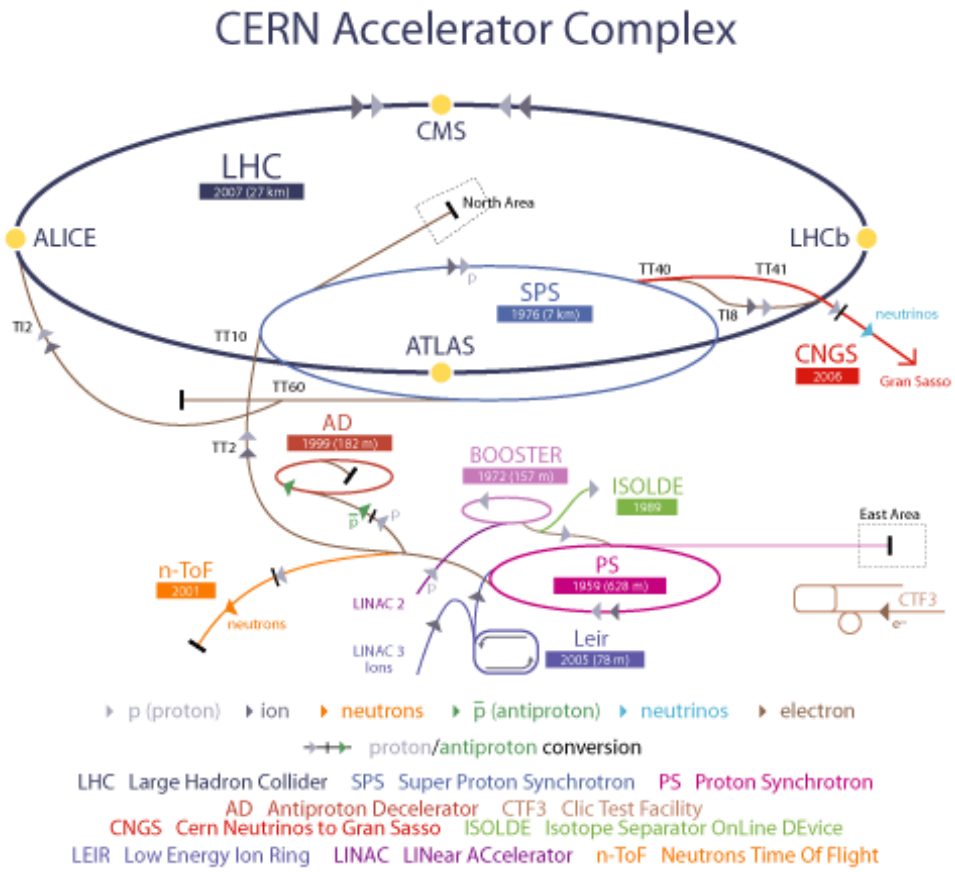

Figure 3.2: Accelerator complex at CERN, preaccelators of the LHC: LINAC2, Proton Synchrotron Booster (PSB, Booster), Proton Synchrotron (PS), Super Proton Synchrotron (SPS) [74].

with N_b as the number of particles per bunch, n_b the number of bunches per beam, f_{rev} the revolution frequency, γ_r the relativistic gamma factor, ϵ_n the normalised transverse beam emittance, β^* the beta function at the collision point and F the geometric luminosity reduction factor[8] due to the crossing at the interaction point.

The cross sections of different processes in proton-proton collisions at the LHC and proton-antiproton collisions at the Tevatron are given in Fig. 3.3. The cross section σ in nanobarn and the number of events per second for a luminosity of $10^{33}\,\mathrm{cm}^{-2}\mathrm{s}^{-1}$ are plotted against the center-of-mass energy $\sqrt{s}$. One can see that the LHC is mainly dominated by events with b-quarks. In comparison, the cross sections for other events are several magnitudes smaller than for b-quark-events. For instance, the cross section for a Higgs boson with a mass of 150 GeV is 10 000 000 magnitudes smaller than the cross section for b-quarks. This means, to find these rare events, the LHC needs a high beam energy, a high number of interactions per bunch crossing, and therefore a high luminosity.

Therefore, the LHC design parameters are a center-of-mass energy of 14 TeV and a luminosity of $10^{34}\mathrm{cm}^{-2}\mathrm{s}^{-1}$ for proton-proton collisions. The LHC has a large number of bunches (2808

[8] $F = \left(1 + \left(\frac{\theta_c \sigma_z}{2\sigma^*}\right)^2\right)^{-1/2}$

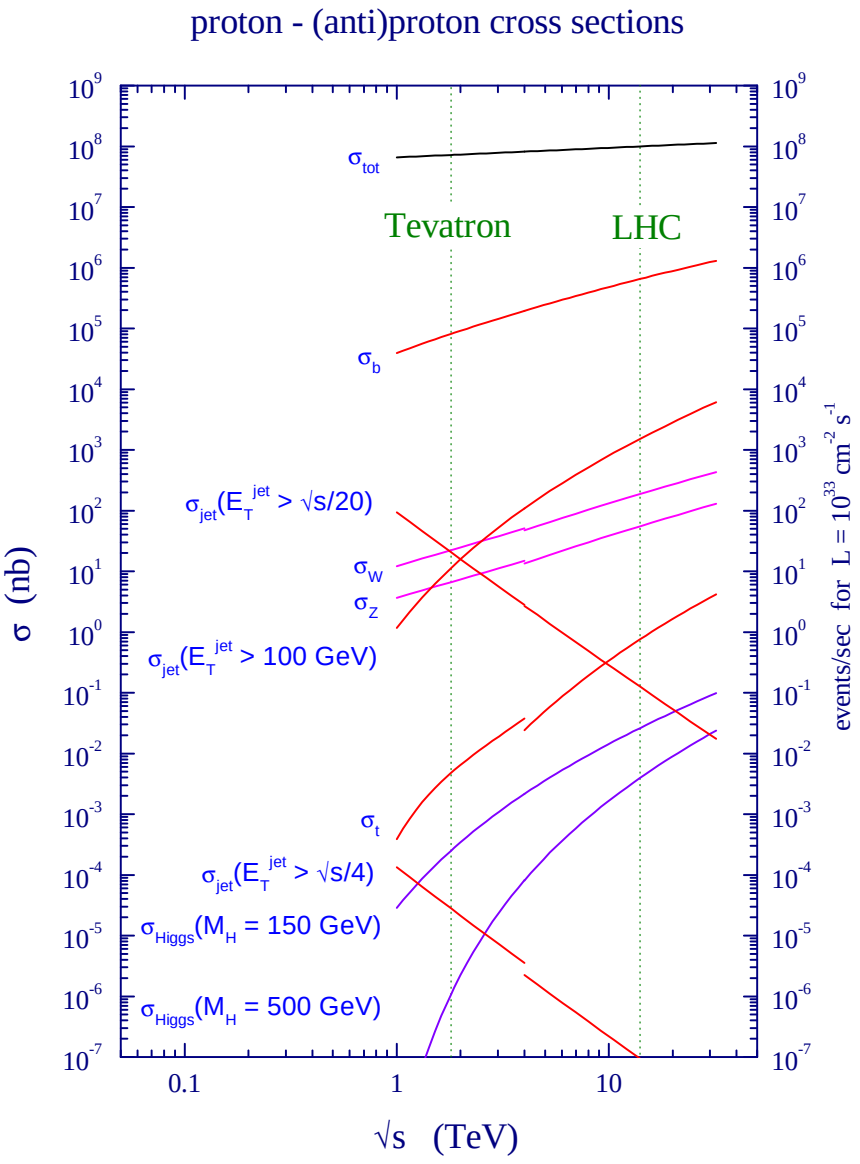

Figure 3.3: Cross sections for some Standard Model processes at the Tevatron and the LHC [29].

Energy	[TeV]	7.0
Dipole field	[T]	8.33
Luminosity	$\mathrm{cm}^{-2}\mathrm{s}^{-1}$	10^{34}
Beam-beam parameter		0.0032
Injection energy	[GeV]	450
Circulating current/beam	[A]	0.53
Bunch spacing	[ns]	25
Particles per bunch		$1.15 \cdot 10^{11}$
Stored beam energy	[MJ]	332
Normalised transverse emittance	[μm]	3.75
R.m.s. bunch length	[m]	0.075
Beta values at I.P.	[m]	0.5
Crossing angle	[μrad]	200
Beam lifetime	[h]	22
Luminosity lifetime	[h]	10
Energy loss per turn	[keV]	6.9
Critical photon energy	[eV]	45.6
Total radiated power per beam	[kW]	3.7

Table 3.1: LHC main parameters [65].

bunches per proton beam) with $1.15 \cdot 10^{11}$ protons per bunch and a bunch spacing of 25 ns.[9] To keep the protons in the beam, strong magnets are needed which provide a magnetic field of 8.33 T [65].

An overview of main design parameters of the LHC is given in Tab. 3.1.

3.2 The ATLAS detector

The ATLAS detector is a multipurpose detector and the largest of the LHC experiments. A schematic view of the detector with its subdetectors is given in Fig. 3.4. It has a height of 25 m, a length of 44 m and its overall weight is approximately 7 000 tonnes.

The main goals of the ATLAS detector are the discovery of the Higgs boson or new physics, but due to the high luminosity and increased cross sections at the LHC (see Fig. 3.3), it is also planned to do high-precision measurements for the Standard Model. These include high-precision tests of QCD, electroweak interactions and flavour physics, for instance the top couplings and spin. The LHC gives a good opportunity to test these parameters because the top quark is produced at a rate of a few tens per second.

Furthermore, it is also expected that ATLAS will be able to measure the top and the W boson mass with an accuracy of $1\,\mathrm{GeV/c^2}$ and $15\,\mathrm{MeV/c^2}$, respectively [75].

This is relevant for Higgs searches because for different Higgs masses there are different production and decay mechanisms. The branching ratio against the Higgs mass for different Higgs decays was given in Fig. 2.7. All these different Higgs decays have to be covered by ATLAS and its subsystems, so a good performace for each of the systems is needed. For light Higgs masses

[9] This corresponds to 40 million proton-proton collisions per second and counts for ATLAS and CMS. LHCb is a low luminosity experiment and has a peak luminosity of $10^{32}\mathrm{cm}^{-2}\mathrm{s}^{-1}$. ALICE is an ion experiment for lead-lead ion collisions with a luminosity of $10^{27}\mathrm{cm}^{-2}\mathrm{s}^{-1}$ and an energy of 2.75 TeV per nuclei [58, 65].

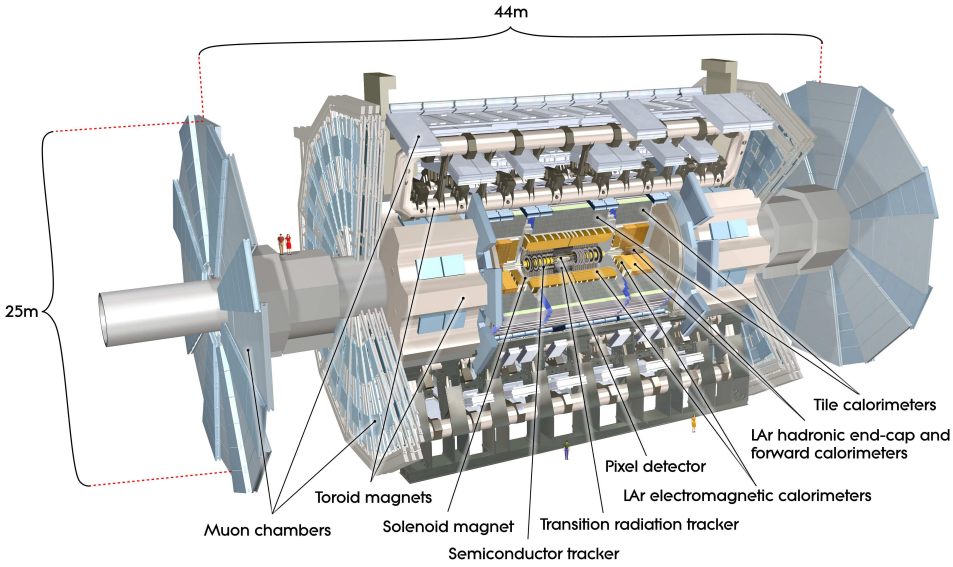

Figure 3.4: Cut-away view of the ATLAS detector [58].

($m_H < 2m_Z$) hadronic Higgs decays are important, but they will be difficult to distinguish from the QCD jet background. Starting with Higgs masses larger than 130 GeV, Higgs decays into dibosons like $H \to WW$ and $H \to ZZ$ become more interesting. These bosons can decay leptonically which requires a good lepton reconstruction and identification. For Higgs masses above 600 GeV a good detection of forward jets is needed because the W and Z bosons in the diboson Higgs decays have mainly jets in their final state.

A good sensitivity for processes with τ leptons is required because τ leptons are often final state particles in supersymmetric scenarios and other extensions of the Standard Model (see Sec. 2.3). Good reconstruction of missing energy is also important, due to the fact that missing energy is often predicted in many new physics scenarios such as in R-parity conserving SUSY, where the lightest neutralino is stable, and thus escapes the detector.

To achieve all these physics aims, one can summarise the requirements on the ATLAS detector as follows:

- fast, radiation-hard electronics and sensor elements, due to extreme experimental conditions at the LHC,
- high detector granularity to handle high particle fluxes and to reduce influence of overlapping events,
- almost full azimuthal angle coverage for a large acceptance in pseudorapidity,
- good charged-particle momentum resolution and reconstruction efficiency in the inner tracker,
- vertex detectors close to the interaction region to observe secondary vertices for reconstruction of τ leptons and b-quark jets,
- very good electromagnetic (EM) calorimeter for electron and photon identification and energy measurements,

Detector component	Required resolution	η coverage	
		Measurement	Trigger
Tracking	$\sigma_{p_T}/p_T = 0.05\% p_T \oplus 1\%$	± 2.5	
EM calorimetry	$\sigma_E/E = 10\%/\sqrt{E} \oplus 0.7\%$	± 3.2	± 2.5
Hadronic calorimetry (jets)			
barrel and end-cap	$\sigma_E/E = 50\%/\sqrt{E} \oplus 3\%$	± 3.2	± 3.2
forward	$\sigma_E/E = 100\%/\sqrt{E} \oplus 10\%$	$3.1 < \lvert\eta\rvert < 4.9$	$3.1 < \lvert\eta\rvert < 4.9$
Muon spectrometer	$\sigma_{p_T}/p_T = 10\% p_T$ at $p_T = 1\,\text{TeV}$	± 2.7	± 2.4

Table 3.2: Performance goals of the ATLAS detector. It is important to know that the muon spectrometer performance is independent of the inner detector system for high-p_T muons. The units for E and p_T are in GeV [58].

- full-coverage hadronic calorimeter for jet and missing transverse momentum measurements,
- good muon identification and momentum resolution over a wide range, and
- efficient trigger system on low transverse momentum objects with a good background rejection.

The performance goals for the ATLAS detector are listed in Tab. 3.2.

An onion-like structure is chosen for the ATLAS detector (see Fig. 3.4). It is constructed cylindrically for full coverage in the three-dimensional domain and it is forward-backward symmetric about the interaction point like many other detectors in particle physics. Around the beam axis and the interaction point, there is the Inner Detector (tracking system) which is surrounded by a thin superconducting solenoid. A second magnetic field with three superconducting toroids (one barrel and two end-caps) is arranged around the calorimeter system which follows. The muon system forms the outer layer of the detector.

In the following sections, the different subdetectors are described in more detail after introducing the ATLAS coordinate system which defines a common set of variables for the overall description of the detector.

3.2.1 Coordinate system

The origin of the coordinate system is the nominal interaction point, while the beam direction defines the z-axis (positive z-axis anti-clockwise). The x-y plane is transverse to the beam direction. Thereby the positive x-axis points from the interaction point to the center of the LHC and the positive y-axis from the interaction point upwards. In addition, the positive z-axis defines side-A of the detector and the negative z-axis side-C. Usually, the ATLAS coordinate system is described by the z-axis, the azimuthal angle ϕ (measured as usual around the beam axis) and the polar angle θ (measured from the beam axis/z-axis).

Due to the fact that the pseudorapidity η is lorentz invariant with the exception of an additive constant (see [13, 76]), the pseudorapidity η is used instead of the polar angle θ to denote the distance from the z-axis:

$$\eta = -\ln\left(\tan\frac{\theta}{2}\right). \tag{3.3}$$

Distances in the pseudorapidity-azimuthal angle space at ATLAS are measured by

$$\Delta R = \sqrt{\Delta\phi^2 + \Delta\eta^2}. \tag{3.4}$$

ATLAS covers a three-dimensional domain up to a pseudorapidy of $|\eta| = 4.9$ which corresponds to an angle up to 1° to the beam axis. In the case of heavy massive objects like jets, the rapidity y is used instead of the pseudorapidity η

$$y = 1/2 \ln \frac{E + p_z}{E - p_z}. \tag{3.5}$$

Finally, the transverse momentum p_{T}, the transverse energy E_{T} and the missing transverse momentum $E_{\mathrm{T}}^{\mathrm{miss}}$ are measured in the x-y plane.

$$p_{\mathrm{T}} = \sqrt{p_{\mathrm{x}}^2 + p_{\mathrm{y}}^2}. \tag{3.6}$$

The formulas for the transverse energy E_{T} and the missing transverse momentum $E_{\mathrm{T}}^{\mathrm{miss}}$ follow accordingly.

3.2.2 Magnet system

The ATLAS magnet system [77] consists of four superconducting magnets, one central solenoid which is aligned to the beam axis, one barrel toroid and two end-cap toroids. The ATLAS magnet system has a total size of 26 m in length and 22 m in diameter. Its stored energy is 1.6 GJ. These four superconducting magnets provide a magnetic field over a volume of 12 000 m^3.[10] Figure 3.5 shows the layout of the magnet system.

Central solenoid

The central solenoid [78] provides a magnetic axial field of 2 T to diffract the charged particles in the Inner Detector. In order to fulfill the desired calorimeter performance the material thickness in front of the calorimeter has to be as low as possible. In total this results in a contribution of approximately 0.66 radiation lengths [79]. The solenoid has an axial length of 5.8 m and an inner and an outer diameter of 2.46 m and 2.56 m and lies completely inside the calorimeter system. The flux of the magnetic field from the solenoid is returned by the hadronic calorimeter. The operation temperature of the solenoid is 4.5 K and can be charged and discharged in round about 30 minutes.

Toroid

The toroid provides a magnetic field to bend the muons in the muon spectrometer. The magnetic field in the barrel toroid [80] is 0.5 T, while the two end-cap toroids [81] provide a magnetic field of 1 T. The barrel toroid consists of eight coils and has a total length of 25.3 m, with inner and outer diameters of 9.4 m and 20.1 m, respectively.

More details about the ATLAS magnet system can be found in [77, 78, 80, 81].

[10] The magnetic field is defined as the region in which the field exceeds 5 mT.

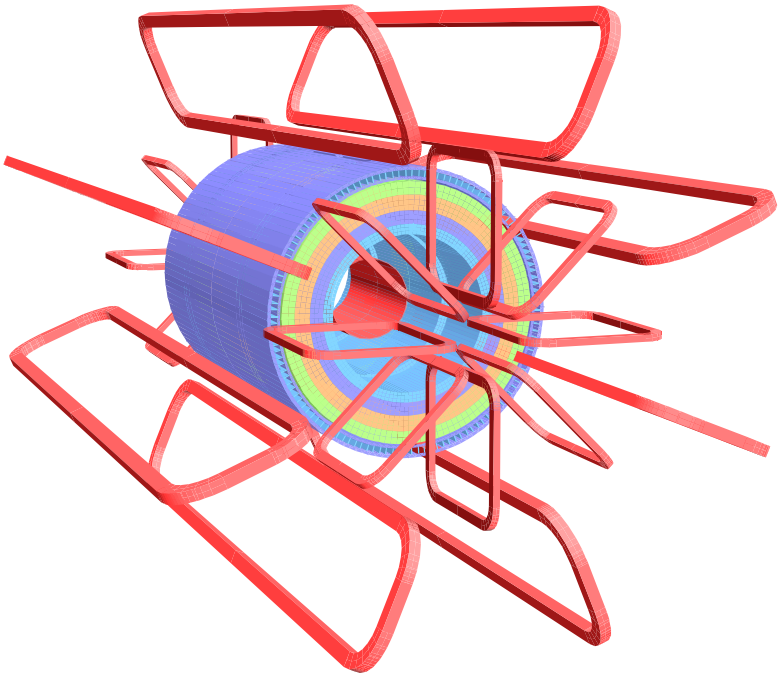

Figure 3.5: Geometry of magnet windings and tile calorimeter steel. The solenoid winding lies inside the calorimeter volume, while the eight barrel toroid coils with the end-cap coils interleaved are visible [58].

3.2.3 Inner detector

The ATLAS Inner Detector (ID) [82] consists of three parts — a Pixel Detector, a Semiconductor Tracker (SCT) and a Transition Radiation Tracker (TRT). The purpose of the Inner Detector is a precise measurement of charged particles (momenta, charge etc.) as well as a good resolution of primary and secondary vertices of charged tracks.

A schematic view of the Inner Detector is given in Fig. 3.6 and a cross section showing the three individual parts in Fig. 3.7. The Inner Detector has a length of 6.2 m, a diameter of 2.1 m and is surrounded by a solenoid, providing a magnetic field of 2 T (see Sec. 3.2.2). The whole Inner Detector covers an area of $|\eta| \leq 2.5$. The Inner Detector allows good measurements of multiple decays, which are important for the identification of τ leptons or heavy quarks. A τ lepton with a momenta of 20 GeV with an average lifetime of $2.91 \cdot 10^{-13}$ s [12] and a mass of 1.777 GeV [12] would cover a short distance of round 980 μm. To measure this τ lepton, all vertices of the decay products has to be resolved and therefore a good vertex reconstruction is definitely needed.

Good track reconstruction performance is also important for the τ lepton reconstruction. A hadronically decaying τ lepton leaves a signature similar to that of a QCD jet; the distinction is that hadronic τ lepton decays are narrower and have a lower track multiplicity (see Sec. 4.4.2). The τ lepton reconstruction algorithms are based on τ leptons decaying hadronically into pions:

$$\tau^{\pm} \rightarrow \pi^{\pm}\nu_{\tau} + n\pi^{0} \text{ and}$$

$$\tau^{\pm} \rightarrow \pi^{\pm}\pi^{\mp}\pi^{\pm}\nu_{\tau} + n\pi^{0} \ .$$

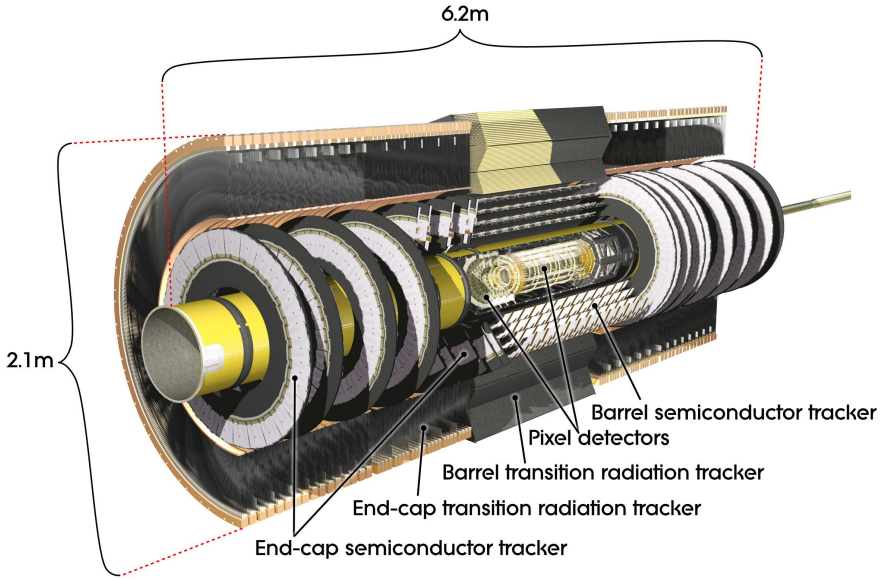

Figure 3.6: Cut-away view of the ATLAS Inner Detector [58].

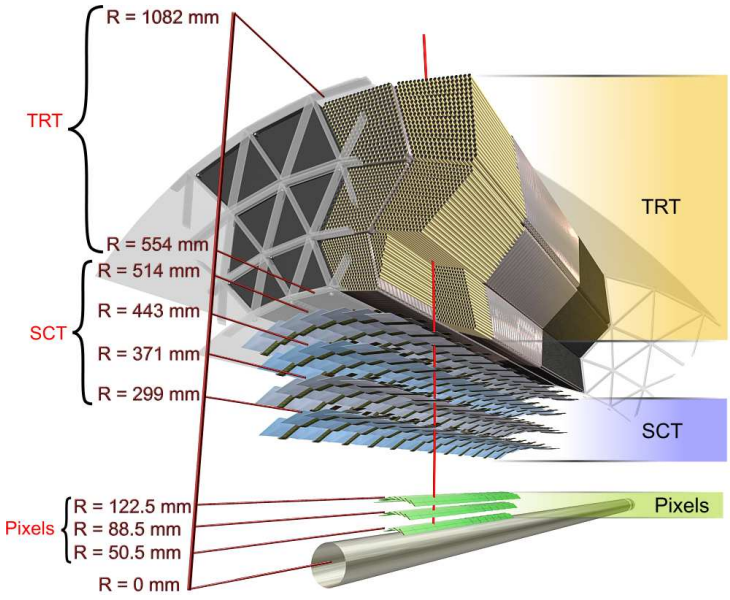

Figure 3.7: Arrangement of the Pixel Detector, the SCT and the TRT in the ATLAS Inner Detector [58].

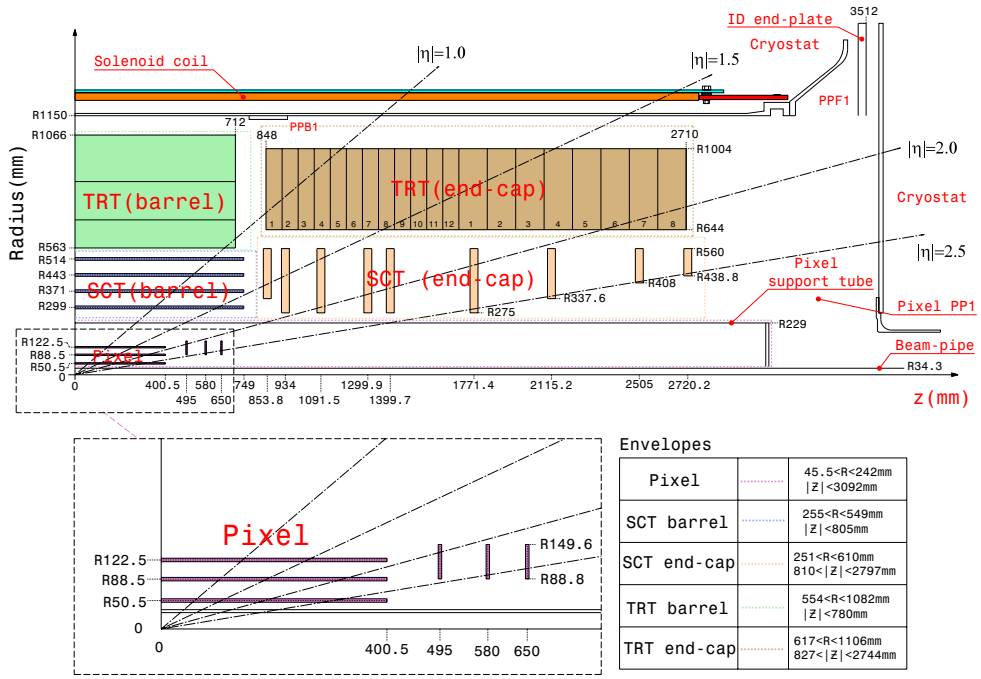

Figure 3.8: Plan view of a quarter section of the ATLAS Inner Detector. The major detector elements are illustrated with its active dimensions and envelopes [58].

The algorithm assigns the tracks from one or three charged pions to a matched calorimeter jet.

Figure 3.8 shows the different subsystems with their active dimensions and envelopes within the Inner Detector. Detailed information about the intrinsic accuracy and the mechanical alignment are given in Tab. 3.3.

Item	**Intrinsic accuracy** (μm)	**Alignment tolerances** (μm)		
		Radial (R)	**Axial (z)**	**Azimuth (R-ϕ)**
Pixel				
Layer-0	10 (R-ϕ) 115 (z)	10	20	7
Layer-1 and -2	10 (R-ϕ) 115 (z)	20	20	7
Disks	10 (R-ϕ) 115 (R)	20	100	7
SCT				
Barrel	17 (R-ϕ) 580 (z)	100	50	12
Disks	17 (R-ϕ) 580 (R)	50	200	12
TRT	130			30

Table 3.3: Intrinsic measurement accuracies and mechanical alignment for the Inner Detector subsystems [58].

Pixel Detector

The Pixel Detector [83] is located close to the interaction point and is the innermost part of the Inner Detector. It was constructed for the resolution of the large number of tracks around the interaction point and for the precise measurement of primary and secondary vertices. It consists of three cylindrical layers in the barrel part, and three discs in the end-caps, and covers a range of $|\eta| \leq 2.5$. It allows a resolution of 10 μm ($R - \phi$) and 115 μm (z) in the barrel and of 10 μm ($R - \phi$) and 115 μm (R) in the discs. In total, the Pixel Detector has 1744 identical, 250 μm thick, pixel sensors. On each sensor, there are 47232 pixels with a size in $R - \phi \times z$ of $50 \times 400 \mu\text{m}^2$ (about 90%) and $50 \times 600 \mu\text{m}^2$.[11] Adding all together, the Pixel detector has approximately 80.4 million readout channels.

Semiconductor Tracker

Right after the Pixel Detector, there is the Semiconductor Tracker (SCT) [84]. It consists of eight strip layers (four space points) which are crossed by each track. The SCT has a resolution of 17 μm ($R - \phi$) and 580 μm (z) in the barrel and of 17 μm ($R - \phi$) and 580 μm (R) in the end-cap region. In the barrel region, small-angle (40 mrad) stereo strips are used to measure both coordinates. One set of strips in each layer is always parallel to the beam direction for the measurement of $R - \phi$. Such a strip consists of two 6.4 cm long daisy-chained sensors. The strip pitch is 80 μm. In the end-cap region, a set of strips are arranged radially and another set of strips at an angle of 40 mrad with an averaged pitch of also 80 μm. In total, the SCT has 6.3 million readout channels.

Transition Radiation Tracker

The outermost part of the ID is the Transition Radiation Tracker (TRT) [85]. 4 mm diameter straw tubes provide a large number of hits per track (typically 36). This drift chamber system in the TRT covers a range up to $\eta \leq 2.0$ and allows an accuracy of 130 μm ($R - \phi$) per straw. The straw tubes act as cathode while the anodes are 31 μm diameter tungsten (99.95%) wires which are plated with 0.5 – 0.7 μm gold. The cathodes have an operation voltage of -1530 V. Inside the straw tubes, there is a gas mixture which contains 70% Xe, 27% CO_2 and 3% O_2. The straws in the barrel region have a length of 144 cm and are parallel to the beam axis, while in the end-cap region, they are 37 cm long and arranged radially. In total, the TRT has 351 000 readout channels.

3.2.4 Calorimeter system

While the inner detector measures primarily the momenta (and the sign of charge) of charged particles, the calorimeter system measures the energy of particles like photons, electrons, jets (incl. τ leptons) and missing energy. In addition, it can reconstruct the direction of the particles. The calorimeter system consists of active material, in which the energy measurement of the particle shower is made, and of passive absorber material in which the particles are stopped. There is a fundamental difference between electromagnetic and hadronic particle showers. Electrons and photons, as an example of an electromagnetic shower, react to the electrical field of the atomic nuclei. This means that the shower is generated by bremsstrahlung and/or pair production. In contrast, hadronic showers originate from the strong interaction with the atomic nuclei.

[11] These are long pixels to cover the gaps between the readout chips.

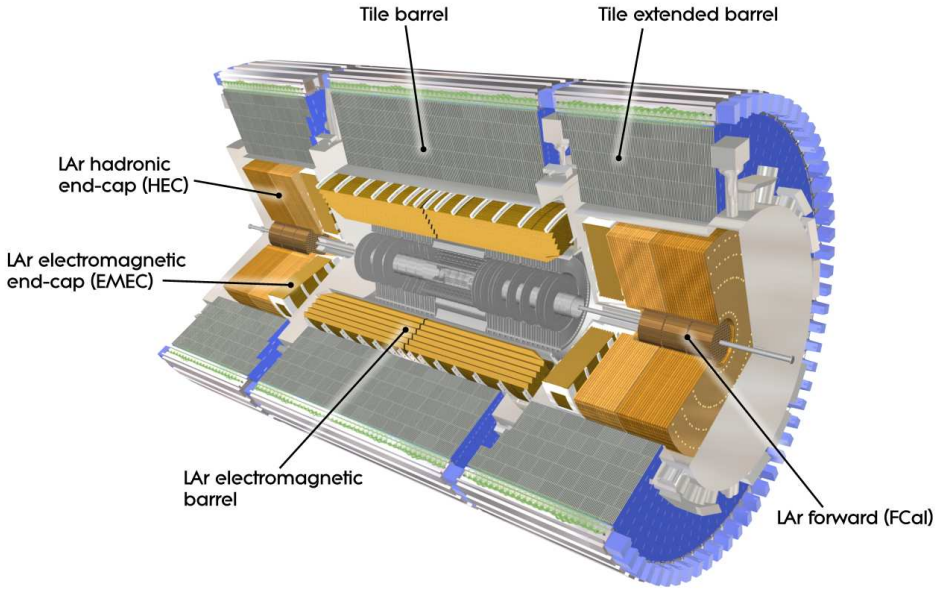

Figure 3.9: Cut-away view of the ATLAS calorimeter system [58].

The difference can be observed in the detector. Hadronic showers are wider, longer and more unbalanced in the shape in comparison to electromagnetic showers. The ATLAS calorimeter system [86, 87] consists of two parts: an electromagnetic and a hadronic calorimeter. Figure 3.9 shows the calorimeter system. The electromagnetic calorimeter covers a range of $|\eta| < 3.2$ and has a thickness of more than 22 radiation lengths (X_0) in the barrel and more than 24 X_0 in the end-caps. For a good resolution of high-energy jets, the active calorimeter has interaction lengths (λ) of $9.7\,\lambda$ in the barrel and $10\,\lambda$ in the end-caps.[12] A detailed list of main parameters of the entire calorimeter system can be found in Tab. 3.4.

Electromagnetic calorimeter

The electromagnetic calorimeter (ECAL) [86] covers an area of $|\eta| \leq 3.2$ in which it is divided into three parts (see Fig. 3.9 and Tab. 3.4): the barrel area ($|\eta| \leq 1.5$) and two end-caps ($1.5 \leq |\eta| \leq 3.2$). It consists of lead plates as passive absorber material which alternate with 4 mm thick areas of liquid argon as active detection material. These materials have proven to be particularly resistant to radiation. The thickness of the lead plates differ from region to region. In the barrel (see Fig. 3.10), they have a thickness of 1.53 mm (1.13 mm) for $\eta < 0.8$ ($\eta > 0.8$) and in the end-caps of 1.7 mm (2.2 mm) for $\eta < 2.5$ ($\eta > 2.5$).

The different layers are designed like an accordion which allows a symmetrical coverage of the detector independent of the angle of incidence of the particle. The calorimeter is built up of three different layers with an averaged granularity of $\Delta\eta \times \Delta\phi = 0.25 \times 0.25$ in the central region $|\eta| \leq 2.5$ (for the individual granularities in the different layers, see Tab. 3.4). With the innermost layer, which has a thickness of $4.3X_0$ and a high granularity of $\Delta\eta \times \Delta\phi = 0.0031 \times 0.098$,

[12] Including $1.3\,\lambda$ from the outer support, the total thickness is $11\,\lambda$ at $\eta = 0$. This seems to be efficient to reduce the punch-through to the muon system as measurements and simulations has shown.

	Barrel		End-cap	
EM calorimeter				
Number of layers and $\|\eta\|$ coverage				
Presampler	1	$\|\eta\| < 1.52$	1	$1.5 < \|\eta\| < 1.8$
Calorimeter	3	$\|\eta\| < 1.35$	2	$1.375 < \|\eta\| < 1.5$
	2	$1.35 < \|\eta\| < 1.475$	3	$1.5 < \|\eta\| < 2.5$
			2	$2.5 < \|\eta\| < 3.2$
Granularity $\Delta\eta \times \Delta\phi$ versus $\|\eta\|$				
Presampler	0.025×0.1	$\|\eta\| < 1.52$	0.025×0.1	$1.5 < \|\eta\| < 1.8$
Calorimeter 1st layer	$0.025/8 \times 0.1$	$\|\eta\| < 1.40$	0.050×0.1	$1.375 < \|\eta\| < 1.425$
	0.025×0.025	$1.40 < \|\eta\| < 1.475$	0.025×0.1	$1.425 < \|\eta\| < 1.5$
			$0.025/8 \times 0.1$	$1.5 < \|\eta\| < 1.8$
			$0.025/6 \times 0.1$	$1.8 < \|\eta\| < 2.0$
			$0.025/4 \times 0.1$	$2.0 < \|\eta\| < 2.4$
			0.025×0.1	$2.4 < \|\eta\| < 2.5$
			0.1×0.1	$2.5 < \|\eta\| < 3.2$
Calorimeter 2nd layer	0.025×0.025	$\|\eta\| < 1.40$	0.050×0.025	$1.375 < \|\eta\| < 1.425$
	0.075×0.025	$1.40 < \|\eta\| < 1.475$	0.025×0.025	$1.425 < \|\eta\| < 2.5$
			0.1×0.1	$2.5 < \|\eta\| < 3.2$
Calorimeter 3rd layer	0.050×0.025	$\|\eta\| < 1.35$	0.050×0.025	$1.5 < \|\eta\| < 2.5$
Number of readout channels				
Presampler	7808		1536 (both sides)	
Calorimeter	101760		62208 (both sides)	
LAr hadronic end-cap				
$\|\eta\|$ coverage			$1.5 < \|\eta\| < 3.2$	
Number of layers			4	
Granularity $\Delta\eta \times \Delta\phi$			0.1×0.1	$1.5 < \|\eta\| < 2.5$
			0.2×0.2	$2.5 < \|\eta\| < 3.2$
Readout channels			5632 (both sides)	
LAr forward calorimeter				
$\|\eta\|$ coverage			$3.1 < \|\eta\| < 4.9$	
Number of layers			3	
Granularity $\Delta x \times \Delta y$ (cm)			FCal1: 3.0×2.6	$3.15 < \|\eta\| < 4.30$
			FCal1: $\sim$ four times finer	$3.10 < \|\eta\| < 3.15$, $4.30 < \|\eta\| < 4.83$
			FCal2: 3.3×4.2	$3.24 < \|\eta\| < 4.50$
			FCal2: $\sim$ four times finer	$3.20 < \|\eta\| < 3.24$, $4.50 < \|\eta\| < 4.81$
			FCal3: 5.4×4.7	$3.32 < \|\eta\| < 4.60$
			FCal3: $\sim$ four times finer	$3.29 < \|\eta\| < 3.32$, $4.60 < \|\eta\| < 4.75$
Readout channels			3524 (both sides)	
Scintillator tile calorimeter				
	Barrel		Extended barrel	
$\|\eta\|$ coverage	$\|\eta\| < 1.0$		$0.8 < \|\eta\| < 1.7$	
Number of layers	3		3	
Granularity $\Delta\eta \times \Delta\phi$	0.1×0.1		0.1×0.1	
Last layer	0.2×0.1		0.2×0.1	
Readout channels	5760		4092 (both sides)	

Table 3.4: Main parameters of the ATLAS calorimeter system [58].

it is possible to differentiate between photons γ and neutral pions π^0 because of the different shower profiles. Electrons can be identified by comparing the shower profile in the electromagnetic calorimeter with tracks in the inner detector. The most energy is in the second layer which has a thickness of $16X_0$ and a granularity of $\Delta\eta \times \Delta\phi = 0.0245 \times 0.0245$. Wide showers of high-energy electromagnetic particles are expected to be in the third layer with a granularity of $\Delta\eta \times \Delta\phi = 0.05 \times 0.0245$ and a thickness of only $2X_0$.

A presampler, consisting of LAr layers, is installed in front of the electromagnetic calorimeter to correct for the energy loss of the particles in the Inner Detector, the solenoid and the cooling system.

Hadronic calorimeter

Following the electromagnetic calorimeter, there is the hadronic calorimeter (HCAL) [87] which measures hadronic showers coming for example from jets or hadronic τ lepton decays. It is also split into three subcalorimeters: the tile calorimeter ($|\eta| < 1.7$), the hadronic end-caps ($1.5 < |\eta| < 3.2$) and the forward calorimeter (FCAL, $3.1 < |\eta| < 4.9$).

The tile calorimeter is a sampling calorimeter and consists of steel plates as absorber and

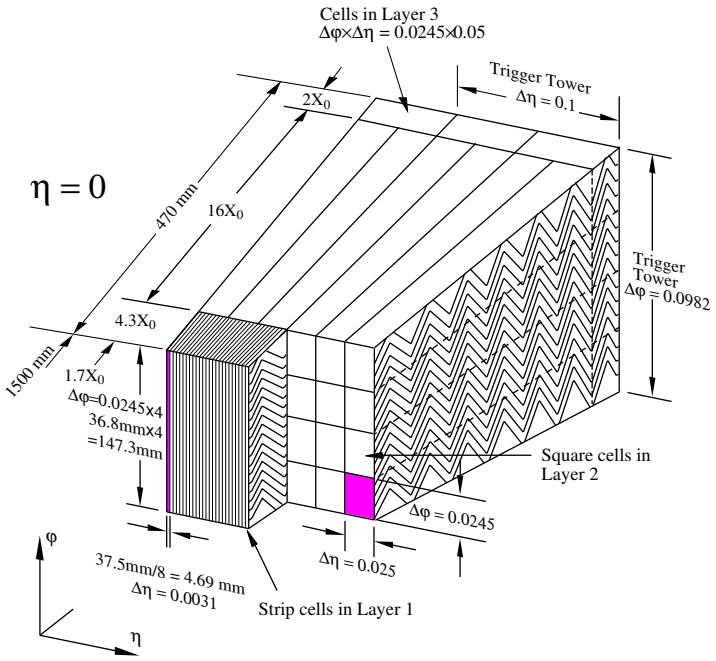

Figure 3.10: Sketch of a barrel module of the electromagnetic calorimeter [58].

scintillating tiles as active material. The barrel part covers a range of $|\eta| < 1.0$ and the extended barrel part $0.8 < |\eta| < 1.7$. Both parts are divided azimuthally into 64 modules. The inner radius is 2.28 m and the outer radius 4.25 m. The total thickness of the detector at $\eta = 0$ is $9.7\,\lambda$. Furthermore, the tile calorimeter is partitioned into three layers with depths of 1.5, 4.1, 1.8 (1.5, 2.6, 3.3) interaction lengths (λ) for the barrel (extended barrel). The readout of the scintillating tiles is done via wavelength shifting fibres into two separate photomultiplier tubes.

Due to the higher radiation level, the LAr hadronic end-cap calorimeter (HEC) consists of copper plates as absorber and liquid argon as active material. It is located directly behind the end-cap electromagnetic calorimeter and consists of two independent wheels per end-cap. It covers a range of $1.5 < |\eta| < 3.2$ and overlaps partly with the forward calorimeter.

The LAr forward calorimeter (FCAL) covers a range of $3.1 < |\eta| < 4.9$. The forward calorimeter is built up of three modules in each end-cap. While the active material is again liquid argon, they have different absorber materials. The first is made of copper and optimised for electromagnetic measurements. The other two use tungsten to measure mainly the energy of hadronic interactions.

To summarise the most important detector components for the reconstruction of τ leptons, one can say, that hadronically decaying τ leptons can be detected with the interaction of the so far described detector components. These τ leptons (τ jets) look like QCD jets in the detector. So they have to be distinguished from QCD jets. In this case, the Inner Detector is needed for the track reconstruction and the measurement of secondary vertices, while the electromagnetic calorimeter can detect the pions from the τ lepton decay (in particular π^0). The hadronic shower is measured with the hadronic calorimeter. The shape of the energy deposition in the hadronic calorimeter of a τ jet is narrower than a 'normal' QCD jet (for more details see Sec. 4.4.2). Due to the neutrino in the τ lepton decay the measurement of missing energy is important too.

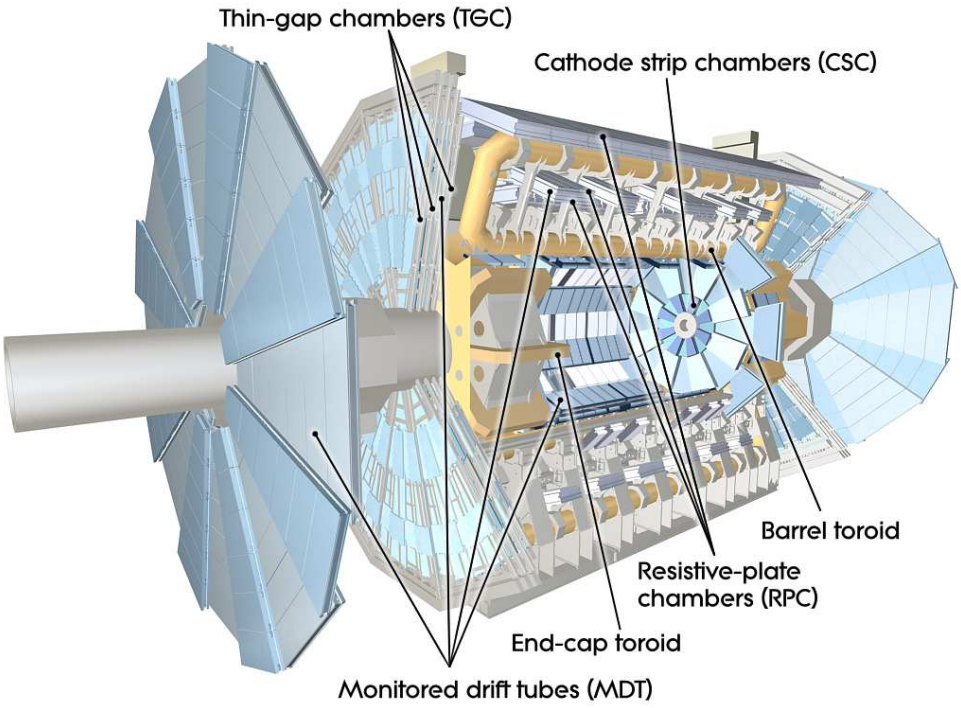

Figure 3.11: Cut-away view of the ATLAS muon system [58].

Certainly, the measurement of missing (transverse) momentum is important for other processes. For example, there is a hope to find the lightest supersymmetric particle (LSP).

3.2.5 Muon spectrometer

The outermost part of the ATLAS detector is the muon spectrometer [88]. Muons are minimal ionising particles, which cross the detector with almost no energy loss. Their properties are measured in the muon chambers. Muons can be identified because they are the only particles to reach the muon system. A schematic view is given in Fig. 3.11. A summary of the main parameters can be found in Tab. 3.5.

The muon spectrometer consists of four parts: the monitored drift tubes and cathode strip chambers for precise tracking and the resistive plate chambers and thin gap chambers as trigger chambers which are part of the Level 1 trigger for the detection of muons.

The monitored drift tubes (MDT) are made of 3 cm thick aluminium tubes as cathode and of 50 μm thick tungsten-rhenium wires as anode. A gas mixture – consisting of 93% argon (Ar) and 7% CO_2 – flows through the aluminium tubes at a pressure of 3 bar. The drift time from the cathode to the anode is 700 ns. One tube achieves a resolution of 80 μm, the whole chamber 35 μm. The MDTs cover the region $|\eta| < 2.7$. The innermost layer only covers a region of $|\eta| < 2.0$. The region $2.0 < |\eta| < 2.7$ is covered by the cathode strip chambers (CSC).

The CSCs are multi-wire propotional chambers. The wires are oriented radially while the cathode planes are perpendicularly segmented. The gas mixture consists of 30% Ar, 50% CO_2, and 20% CD_4. The CSC has a higher resolution than the MDT of 60 μm in the bending plane

Monitored drift tubes	**MDT**
- Coverage	$\lvert\eta\rvert < 2.7$ (innermost layer: $\lvert\eta\rvert < 2.0$)
- Number of chambers	1088 (1150)
- Number of channels	339000 (354000)
- Function	Precision tracking
Cathode strip chambers	**CSC**
- Coverage	$2.0 < \lvert\eta\rvert < 2.7$
- Number of chambers	32
- Number of channels	31000
- Function	Precision tracking
Resisitive plate chambers	**RPC**
- Coverage	$\lvert\eta\rvert < 1.05$
- Number of chambers	544 (606)
- Number of channels	359000 (373000)
- Function	Triggering, second coordinate
Thing gap chambers	**TGC**
- Coverage	$1.05 < \lvert\eta\rvert < 2.7$ (2.4 for triggering)
- Number of chambers	3588
- Number of channels	318000
- Function	Triggering, second coordinate

Table 3.5: Main parameters of the muon spectrometer. Numbers in brackets refer to the final detector configuration of 2009 [58].

(in the non-bending direction the resolution is 5 mm).

In order to achieve the necessary accuracy, the position of each component of the MDTs and CSCs must be known with a precision of 30 μm. This is done by an optical alignment system which controls every deviation from straight lines.

As previously mentioned, the trigger chambers are built up of resistive plate chambers (RPC) and thin gap chambers (TGC) and are part of the level 1 trigger. The RPCs cover the barrel region of $|\eta| < 1.05$ and have a time resolution of 1.5 ns. The RPCs have two parallel plates, made of phenolic-melaminic plastic laminate, as anode at a distance of 2 mm instead of wires. The electrical field is 4.9 kV/mm. Additionally, the gas mixture is different: 94.7% $C_2H_2F_4$, 5% Iso-C_4H_{10} and 0.3% SF_6.

The end-cap region ($1.05 < |\eta| < 2.4$) is covered by the TGCs which have a time resolution of 4 ns. Essentially, the TGCs are built up like the CSCs but with a smaller distance between the parallel plates and a different gas mixture (55% CO_2 and 45% n-pentane).

3.2.6 Trigger and Data Acquisition

To deal with the large amount of data it collects[13], ATLAS needs an efficient data processing system. For this reason, a Trigger and Data Acquisition (TDAQ) composed of three parts was

[13]The LHC was designed for a bunch crossing rate of 40 MHz with 25 interactions per bunch crossing and a luminosity of $10^{34}\,\mathrm{cm}^{-2}\mathrm{s}^{-1}$. This would be 10^9 – 1 billion – interactions per second. With an averaged event size of 1.3 MB, ATLAS would take data in a rate of more than 1 PB/s.

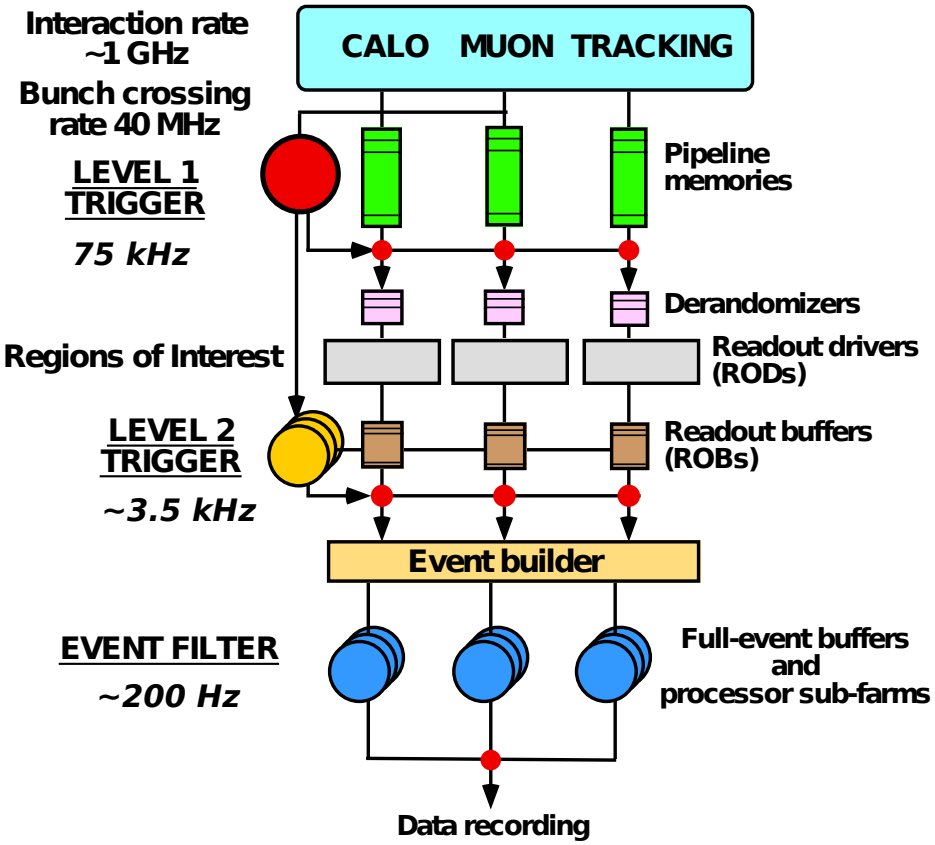

Figure 3.12: Block diagram of the ATLAS Trigger/DAQ system [89].

installed at ATLAS. The Level 1 trigger (L1) is hardware based while the other two parts – the Level 2 trigger (L2) and Event Filter (EF) – are software based and combined to form the High Level Trigger (HLT). The data acquisition system receives the event data from the readout electronics at the L1 trigger accept rate. This is done over 1600 point-to-point readout links (ROL).

Figure 3.12 shows a schematic view of the ATLAS TDAQ system. A reduction of the event rate down to 200 Hz is possible with such a design. This corresponds to a data rate of about 300 MB/s.

Level 1 Trigger (L1)

The hardware-based L1 trigger – shown in Fig. 3.13 – is divided into two parts. It has components in the calorimeter as well as in the muon chambers. The L1 trigger reduces the event rate from 40 MHz to 75 kHz in less than 2.5 μs by using a limited amount of the detector information. It searches for high transverse-momentum muons, electrons, photons, jets, hadronically decaying τ leptons and large missing and total transverse energy.

The L1 calorimeter trigger (L1Calo) looks for all the above mentioned objects except the muons and sends the trigger decision to the Central Trigger Processor (CTP) 1.5 μs after the event occurs. The L1Calo trigger decision is based on 7 000 analogue trigger towers, with a

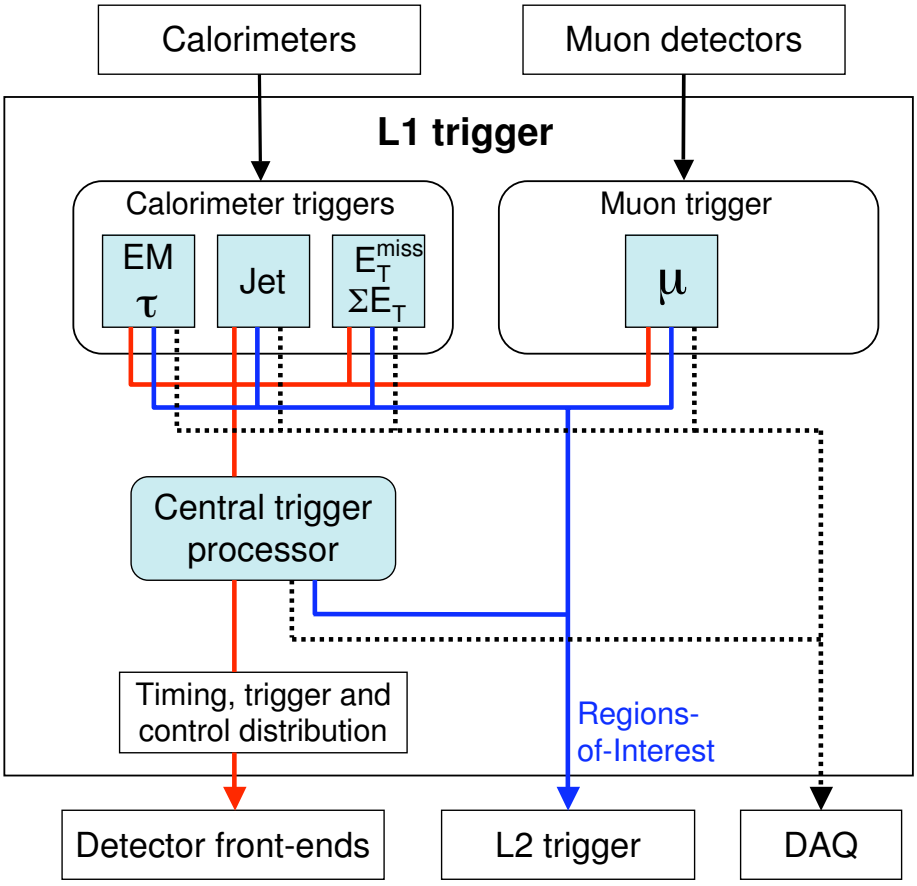

Figure 3.13: Block diagram of the L1 Trigger [58].

granularity of $\Delta\eta \times \Delta\phi = 0.1 \times 0.1$ (larger at high $|\eta|$). As an example, Fig. 3.14 shows the electron/photon and τ lepton trigger algorithms. The L1 τ lepton trigger algorithms combine 2×2 trigger towers to form a core region, surrounded by a 12-tower isolation region. This is repeated for all possible 4×4 windows (known as a Region of Interest or ROI), in order to select narrow hadronic jets.

Afterwards, the stored data from the L1Calo triggers are read out in the data acquisition system if there is an L1 Accept decision from the CTP.

The L1 muon trigger is based on the muon chambers (RPC's in the barrel region and the TGC's in the end-caps) because they have a sufficient timing accuracy to provide a clear identification of the bunch-crossing for the muon candidate. The trigger is based on three stations for the barrel and the end-cap, respectively. The trigger algorithm looks for hits in the different stations and requires coincidences along the path of the muon from the interaction point through the entire detector. Thereby, the p_{T} threshold (e.g. $6-9\,\mathrm{GeV}$ for low p_{T} or $9-35\,\mathrm{GeV}$ for high p_{T}), which is applied, correlates to the width of the path of the muon since lower p_{T} muons will deviate more from a straight line. The signals from the barrel and the muon end-cap trigger are combined and passed to the CTP. Finally, the CTP of the L1 trigger collects information from the L1Calo and L1 muon system and sends it to the Level 2 Trigger (L2), where it is saved

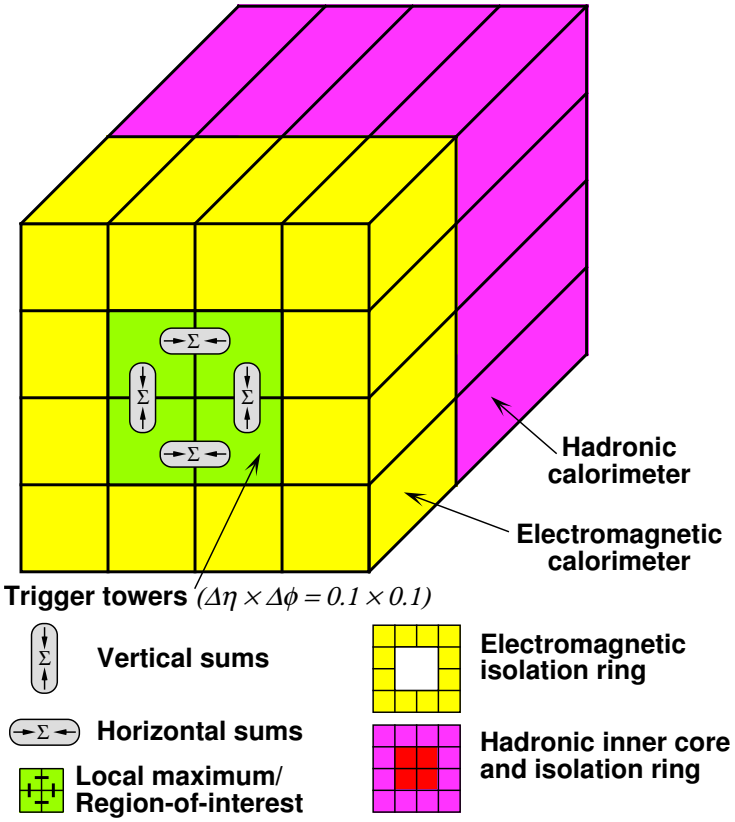

Figure 3.14: Electron/photon and τ lepton trigger algorithms [58].

in so-called Regions of Interest (ROI), and the data acquisition system (DAQ) if the event is accepted. These events in the ROIs are temporarily stored in 1574 Readout Buffers (ROB) until there is a decision by the L2 trigger.

High Level Trigger (HLT) and Data Acquisition system (DAQ)

The software-based High Level Trigger (HLT) is divided into the Level 2 Trigger (L2) and the Event Filter (EF), and uses components from the whole detector from the inner detector to the muon chambers. If the L1 trigger accepts an event, the L2 trigger checks this event in the ROI with fast and 'easy' selection algorithms on criterias like p_{T}, ΔR etc. and decides if the event will be accepted or not. In the case that the event will be rejected, it is directly deleted out of the ROBs. With the L2 trigger, a reduction on the event rate up to 3.5 kHz with an event processing time of about 40 ms is possible.

If an event is accepted by the L2 trigger, the complete event information for the event in the ROB will be forwarded to the event builder, where the event is fully reconstructed, and then analysed by the EF. The EF itself is more or less a computing and processing farm. The event is checked on criterias coming from all components of the detector and finally the EF decides if the event is accepted, and therefore saved in a central data recording facility, or rejected and deleted. At this last step, the event rate is reduced to around 200 Hz.

Tau lepton trigger

The τ lepton trigger [57, 58, 90] has parts in all three subtriggers, L1, L2, and the EF.

As previously mentioned, the L1 τ lepton trigger [91] uses electromagnetic and hadronic calorimeter information from the L1Calo trigger and combines 2×2 trigger towers, each with a granularity of $\Delta\eta \times \Delta\phi = 0.1 \times 0.1$, to define a core region, surrounded by a 12-tower isolation region. This 4×4 window of trigger towers defines the ROI. The center of the ROI defines the τ lepton candidate. Its transverse energy E_{T} is defined by the two most energetic neighbouring towers in the core of the electromagnetic and the full core of the hadronic calorimeter. Different E_{T} thresholds can be defined for the L1 τ lepton triggers. As a generic example, the 'L1_TAUX' trigger requires a τ lepton with $E_{\mathrm{T}} > \mathrm{X\,GeV}$.

The L2 τ trigger is part of the HLT and is software-based. After refining the L1 position using the second sample layer in the electromagnetic calorimeter, its algorithm selects narrow jets by means of a shape variable, the EM radius R_{EM} (see Eq. (4.4)), which is an energy-weighted squared radius in a region of size $\Delta\eta \times \Delta\phi = 0.6 \times 0.6$. The electromagnetic radius R_{EM} together with the total transverse energy, which is calculated from all layers in the electromagnetic and hadronic calorimeters, are the basis of the L2 calorimeter selection. The L2 track reconstruction uses algorithms, with information from the SCT and pixel detectors only, to keep the execution time small, and reconstructs tracks with $p_{\mathrm{T}} > 1.5\,\mathrm{GeV}$ in a rectangular ROI of size $\Delta\eta \times \Delta\phi = 0.6 \times 0.6$ centered on the L2 calorimeter position. Two regions around the identified highest-p_{T} track are defined: the inner cone ($\Delta R < 0.15$) and the isolation ring ($0.15 < \Delta R < 0.3$). These two regions define together with the highest-p_{T} track another base selection variable, the ratio of the scalar sum of the p_{T} of all tracks in the isolation ring and the inner cone.

The EF selection is based on the offline τ lepton reconstruction algorithms [57, 58]. Calorimeter cells within an ROI of 0.8×0.8 around the L2 direction are collected and form topological clusters. All clusters within such an ROI build a jet which is calibrated. Afterwards, the candidate position, the transverse energy, and a number of shower variables are determined. The track reconstruction uses the full offline algorithm to track detector data within the ROI. Typical names of τ lepton triggers at the EF are 'EF_tauX', which require a τ lepton with $E_{\mathrm{T}} > \mathrm{X\,GeV}$.

$E_{\mathrm{T}}^{\mathrm{miss}}$ trigger

The ATLAS trigger system allows to trigger on $E_{\mathrm{T}}^{\mathrm{miss}}$ too. The $E_{\mathrm{T}}^{\mathrm{miss}}$ trigger [92] requires that the magnitude of the vector sum of all transverse energies is larger than some thresholds.

Only calorimeter information from the trigger towers is used at L1. These trigger towers refer to the analogue sum of all calorimeter cells in an (η, ϕ) range of 0.1×0.1. The information is digitised by the preprocessor and noise subtraction to the formed trigger towers is applied. Afterwards, the preprocessor produces jet elements. The calorimeter energy sum along the x-axis (E_x) and y-axis (E_y) are computed by the jet/energy processor by using all jet elements. The transverse energy $E_{\mathrm{T}}^{\mathrm{miss}}$ is not computed from E_x and E_y, but a look-up-table is used to accept or reject the event. The scalar sum of the energy deposited in the calorimeter $\sum E_{\mathrm{T}}$ is determined similarly.

At L2, so-called FEX algorithms (Feature Extraction, software-based algorithms in the HLT which perform the $E_{\mathrm{T}}^{\mathrm{miss}}$ and $\sum E_{\mathrm{T}}$ reconstruction from detector input) refine the L1 result by applying corrections taking into account muons reconstructed at L2.

Contributions from the electromagnetic and hadronic calorimeters as well as from the muon spectrometers are recomputed with the full granularity of the detector at the EF. Only positive energy calorimeter cells above a certain threshold are considered in the $E_{\mathrm{T}}^{\mathrm{miss}}$ and $\sum E_{\mathrm{T}}$ recon-

struction to avoid electronic noise. Triggers on $E_{\mathrm{T}}^{\mathrm{miss}}$ are usually called 'xeY' and 'xeY_noMu', which requires $E_{\mathrm{T}}^{\mathrm{miss}} > \mathrm{Y\,GeV}$ in the event. The term 'noMu' means that $E_{\mathrm{T}}^{\mathrm{miss}}$ is reconstructed using the calorimeter information only (without the muon correction).

Combined triggers

All these individual triggers can be combined to produce triggers dependent on information from several objects. For example, combined τ lepton and $E_{\mathrm{T}}^{\mathrm{miss}}$ triggers are used to identify $W \to \tau\nu_\tau$ events having signatures with τ leptons and missing transverse momentum $E_{\mathrm{T}}^{\mathrm{miss}}$ in the event. The specific triggers used in this thesis are described in Sec. 8.2.3.

3.2.7 Tau lepton and missing transverse momentum $E_{\mathrm{T}}^{\mathrm{miss}}$ performance

The performance of the ATLAS detector has been studied in many ATLAS publications, however, since they are relevant to the $W \to \tau\nu_\tau$ cross section analysis, that was performed as part of this thesis, the ATLAS performance for missing transverse momentum $E_{\mathrm{T}}^{\mathrm{miss}}$ and τ leptons will be briefly described here. Performance studies on τ leptons are done in [93] and [94] as well as for $E_{\mathrm{T}}^{\mathrm{miss}}$ in [95] and [96]. General detector performance, which will not be described here, can be found in [97].

Tau lepton performance

The τ lepton reconstruction and identification performance described in [93] was performed using ATLAS data at a center-of-mass energy of $\sqrt{s} = 7\,\mathrm{TeV}$ and corresponds to an integrated luminosity of $244\,\mathrm{nb}^{-1}$. Although this dataset only has a small number of real τ leptons, background jets reconstructed as τ lepton candidates are used for the performance studies. QCD jet processes are one of the most important backgrounds for signatures such as $Z \to \tau\tau$ and $W \to \tau\nu_\tau$. In [93], MC QCD jet samples (for the settings of the MC sample, see [93]) were used for comparison to data. A MC $Z \to \tau\tau$ sample is used for an MC sample with true τ leptons.

Tau lepton reconstruction is either based on calorimeter seeds or on track seeds [57, 58]. The reconstruction of τ lepton candidates provides little background rejection; the rejection is normally obtained in the following identification step which is based on several discriminating variables like the cluster mass, track mass, track radius, leading track momentum fraction, electromagnetic radius, core energy fraction and the electromagnetic fraction. Figure 3.15 shows some of these variables. The reconstruction and identification of τ leptons are described in Sec. 4.4.2. There is a good agreement between data and MC QCD jets.[14]

For the performance studies, three different identification algorithms – simple cuts, boosted decision trees (BDT) and projective likelihood (LL) – were used. Two important quantities are the signal and background efficiencies:

$$\epsilon_{\mathrm{sig}} = \frac{N^{\tau}_{\mathrm{pass,match}}}{N^{\tau}_{\mathrm{match}}} \tag{3.7}$$

and

$$\epsilon_{\mathrm{bkgd}} = \frac{N^{\mathrm{bkgd}}_{\mathrm{pass}}}{N^{\mathrm{bkgd}}_{\mathrm{total}}} \tag{3.8}$$

[14] There is a difference between data and MC of $Z \to \tau\tau$ because QCD jets were used for the performance studies.

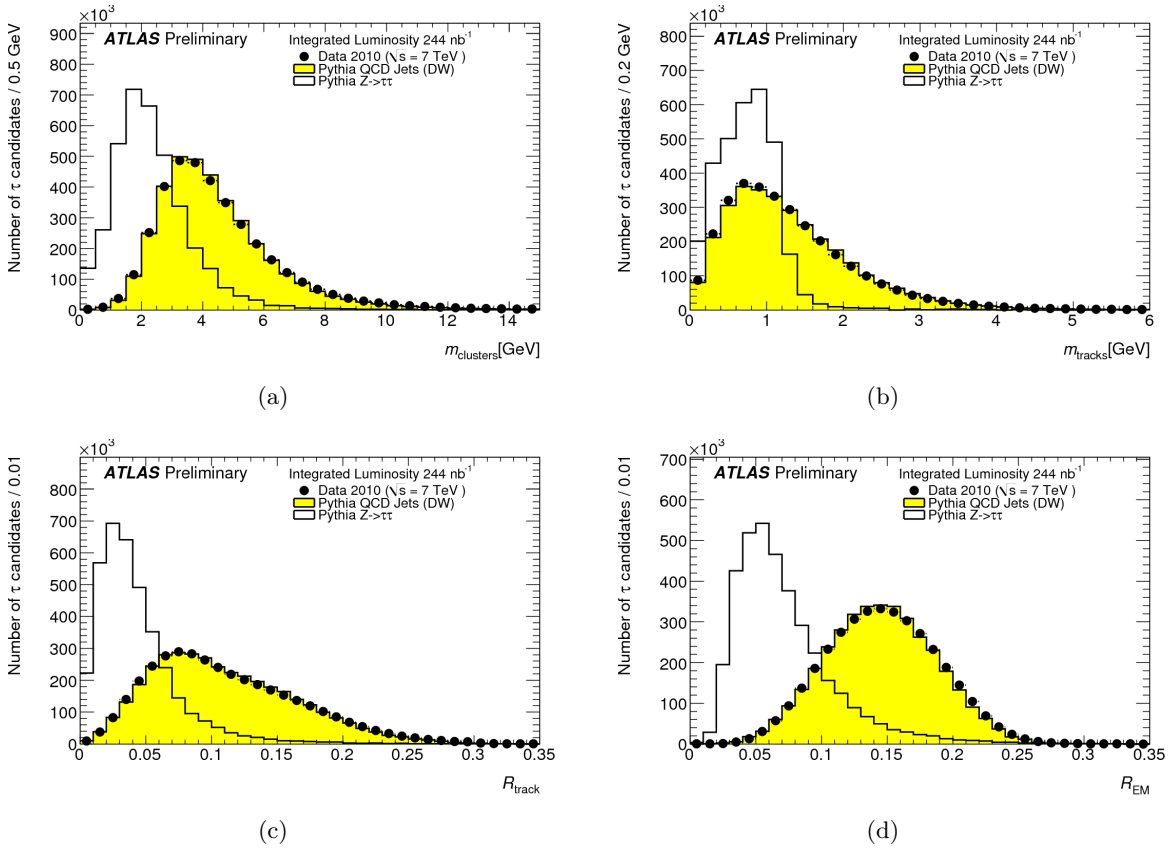

Figure 3.15: (a) Cluster mass, (b) track mass (c) track radius, and (d) EM radius of τ lepton candidates [93].

with N^{τ}_{match} as the number of reconstructed τ lepton candidates that are matched within $\Delta R < 0.2$ of a true, hadronically decaying τ lepton with visible transverse momentum $p_{\text{T}}^{\text{vis}} > 15\,\text{GeV}$ and visible pseudorapidity $\left|\eta^{\text{vis}}\right| < 2.5$, reconstructed with the correct number of associated tracks. $N^{\tau}_{\text{pass,match}}$ passes the identification criteria in addition. $N^{\text{bkgd}}_{\text{pass}}$ is the number of τ lepton candidates that pass the identification criteria and $N^{\text{bkgd}}_{\text{total}}$ the number of all τ lepton candidates, determined from MC background samples (QCD jets).

As a summary, Fig. 3.16 shows the signal and background efficiencies as function of the reconstructed p_{T} for the three different methods. There is again a good agreement between data and MC.

The performance studies in [94] used a smaller dataset and some slightly changes in the analysis procedure and came to the same result. In addition, the performance for $\tau + E_{\text{T}}^{\text{miss}}$ events were added, and the event selection was adapted to such events.[15] Figure 3.17 shows the $\Delta\phi$ between $E_{\text{T}}^{\text{miss}}$ and the τ lepton candidate as well as the transverse mass m_{T} of the τ lepton candidate and the $E_{\text{T}}^{\text{miss}}$ system. The MC describes the data quite well.

[15] Instead of looking for two τ lepton candidates, only one τ lepton candidate and $E_{\text{T}}^{\text{miss}}$ is required.

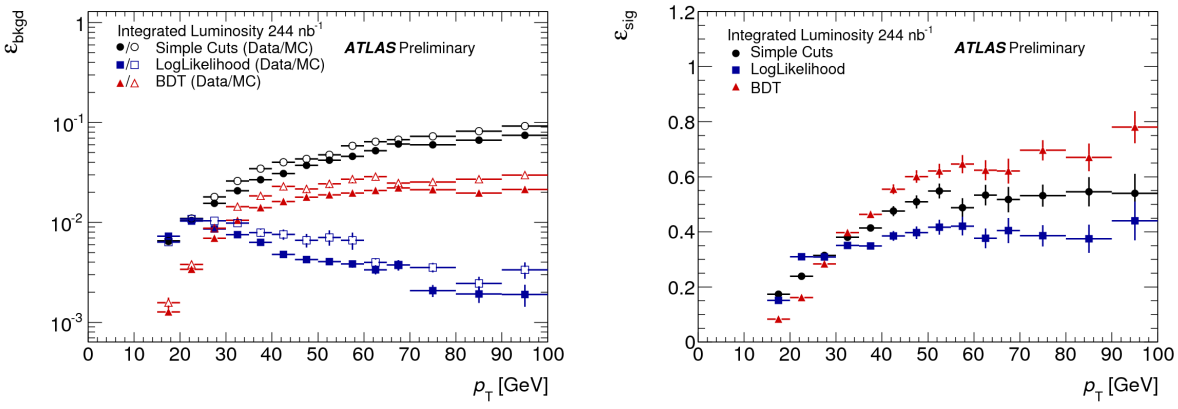

(a) (b)

Figure 3.16: (a) Background efficiencies in data and MC and (b) signal efficiencies from MC as a function of p_{T}^{τ} with the tight selection for cut-based, BDT and LL identification methods [93].

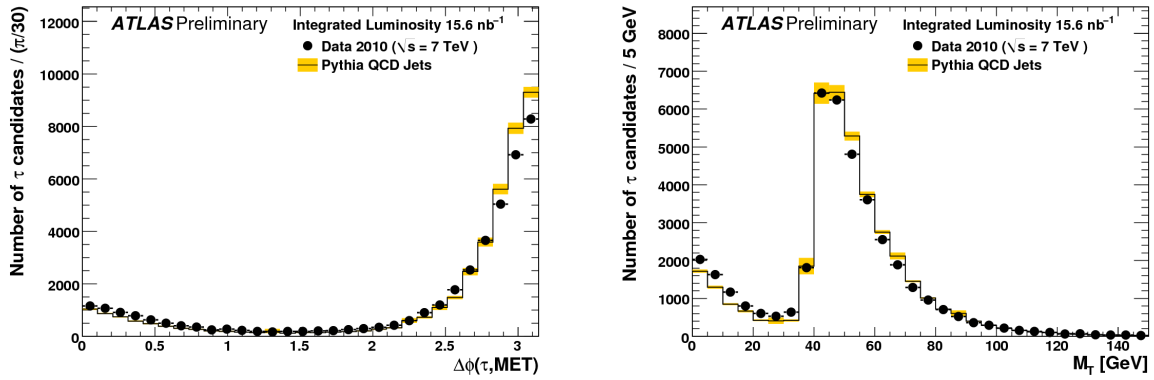

(a) (b)

Figure 3.17: (a) $\Delta\phi$ between $E_{\mathrm{T}}^{\mathrm{miss}}$ and the τ lepton candidate and (b) transverse mass of the τ lepton candidate and $E_{\mathrm{T}}^{\mathrm{miss}}$ system for events passing the $\tau + E_{\mathrm{T}}^{\mathrm{miss}}$ selection. The edge at 40 GeV is due to selection criteria. The yellow band around the MC expectation demonstrates the statistical uncertainty on the simulated samples [94].

$E_{\mathrm{T}}^{\mathrm{miss}}$ performance

The comparisons and results in [95] show that the $E_{\mathrm{T}}^{\mathrm{miss}}$ reconstruction and calibration are well under control and reach the expected performance. Data from proton-proton collisions at ATLAS with 7 TeV center-of-mass energy recorded in April and May 2010 was used for this study. For the comparison with MC, a sample with minimum bias events and another with QCD jet events were used. In priniciple, the $E_{\mathrm{T}}^{\mathrm{miss}}$ reconstruction at ATLAS is done with the following formula

$$E_{\mathrm{x(y)}}^{\mathrm{miss}} = E_{\mathrm{x(y)}}^{\mathrm{miss,calo}} + E_{\mathrm{x(y)}}^{\mathrm{miss,cryo}} + E_{\mathrm{x(y)}}^{\mathrm{miss,muon}} \tag{3.9}$$

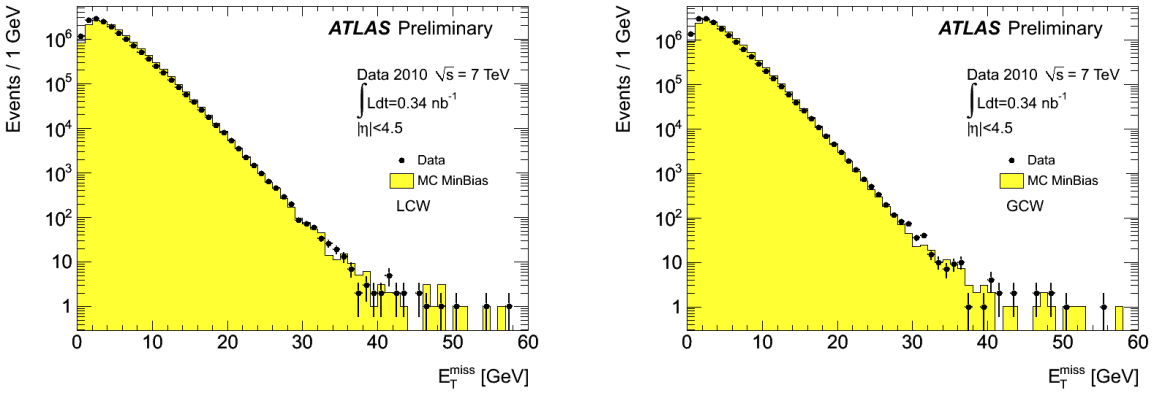

(a) (b)

Figure 3.18: $E_{\mathrm{T}}^{\mathrm{miss}}$ distribitutions in a data sample of 15.2 million selected minimum bias events at 7 TeV center-of-mass energy, recorded in April 2010. Only topoclusters are used in the calculation, with energies that are calibrated with the LCW (a) and the GCW (b) methods [95].

and contains information from the calorimeter, corrections for energy loss in the cryostat and measured muons. A more detailed description of the recontruction of missing transverse momentum can be found in Sec. 4.4.3.

In [95], a more refined reconstruction of $E_{\mathrm{T}}^{\mathrm{miss}}$[16] is compared with different methods of calorimeter cell calibration and the influence from muons in the event is studied. The $E_{\mathrm{T}}^{\mathrm{miss}}$ distributions for two different methods (global cell energy-density weighting (GCW) and local cluster weighting (LCW))[17] for topoclusters only are illustrated in Fig. 3.18 and show a good agreement to MC.

Reference [96] is based on [95] but with more data, and so corresponds to an integrated luminosity of $36\,\mathrm{pb}^{-1}$. Furthermore, this data sample allows an estimation of the $E_{\mathrm{T}}^{\mathrm{miss}}$ performance in the presence of Z and W bosons which decay into electrons and/or muons. The $E_{\mathrm{T}}^{\mathrm{miss}}$ distributions for $W \to e\nu_e$ and $W \to \mu\nu_\mu$ events are shown in Fig. 3.19, again with a good agreement between MC and data.

To summarise, there is a very good agreement between data and MC and all the different detector components necessary for τ lepton reconstruction and $E_{\mathrm{T}}^{\mathrm{miss}}$ measurements work well.

[16] The calorimeter energy is corrected for energy losses in dead material and for the non-compensating calorimeter design.

[17] These methods are described in Sec. 4.4.3.

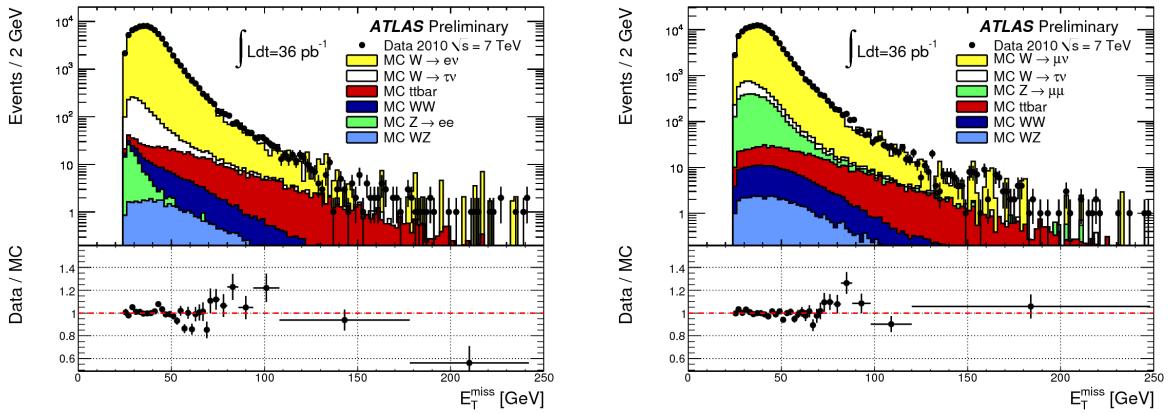

(a) (b)

Figure 3.19: $E_{\mathrm{T}}^{\mathrm{miss}}$ distribitutions in a data sample of $W \to e\nu_e$ (a) and $W \to \mu\nu_\mu$ (b) events [96].

4 Data taking, ATLAS software framework Athena and object reconstruction

High-energy experiments need a well working technique and optimised software. The ATLAS software framework Athena [98] performs Monte Carlo (MC) event generation, detector simulation and object reconstruction.

This chapter describes the ATLAS data taking and the ATLAS software framework Athena. The whole simulation chain from MC event generation to object reconstruction is illustrated.

4.1 Data taking at ATLAS

ATLAS data taking started November 23rd 2009 with the SPS injection energy of 450 GeV. From March 30th 2010 until the end of 2011 ATLAS collected data at a center-of-mass energy of 7 TeV (see Sec. 3.1). So far, ATLAS recorded data with an integrated luminosity of $5.25\,\mathrm{fb}^{-1}$, while a luminosity of $5.61\,\mathrm{fb}^{-1}$ have been delivered during stable beams in proton-proton collisions [99]. The total integrated and the instananeous luminosity for 2011 and 2010 are shown in Figs. 4.1 and 4.2, respectively. In 2010, an integrated luminosity of $45.0\,\mathrm{pb}^{-1}$ has been recorded, while $48.1\,\mathrm{pb}^{-1}$ has been delivered [100, 101]. The data of 2010, which is analysed in this thesis (see Chap. 8), is important for SM measurements because the pile-up effect is still small and the statistic is high enough. The luminosity $\mathcal{L}$ is calculated by

$$\mathcal{L} = \frac{\mu n_\mathrm{b} f_\mathrm{r}}{\sigma_\mathrm{inel}} = \frac{\mu^\mathrm{meas} n_\mathrm{b} f_\mathrm{r}}{\varepsilon \sigma_\mathrm{inel}} = \frac{\mu^\mathrm{meas} n_\mathrm{b} f_\mathrm{r}}{\sigma_\mathrm{vis}}, \tag{4.1}$$

where μ is the average number of interactions per bunch crossing, n_b the number of bunches colliding at the interaction point, f_r the machine revolution frequency, σ_inel the inelastic cross section, ε the efficiency of the luminosity algorithm (including the acceptance) for a certain detector, $\mu^\mathrm{meas} = \varepsilon\mu$ the average number of interactions per bunch crossing that pass the selection requirements of the algorithm, and σ_vis the 'visible' cross section (the detector calibration constant).[1]

The ATLAS data taking is divided into periods, while each period corresponds to different detector configuration and trigger settings. These periods are divided into runs, whereby one run corresponds to one LHC run. Each run is divided into Luminosity Blocks (LBs) in which the luminosity (as well as data quality information) is stored. The length of a LB is approximately 2 minutes in which the instantaneous luminosity is constant.[2] The start and end times are set by the ATLAS data acquisition system (DAQ) [100]. Luminosity blocks with good data quality are centrally provided in so-called Good Run Lists (GRLs) which can vary depending on the needed settings for each analysis.

A summary of the individual 2010 data periods is given in Tab. 4.1.

[1] This equation is only valid in case of linear detector response with respect to μ. If this is not the case, corrections are needed for the non-linearity of the detector response.

[2] The exact length is dependent on stable beam and detector conditions.

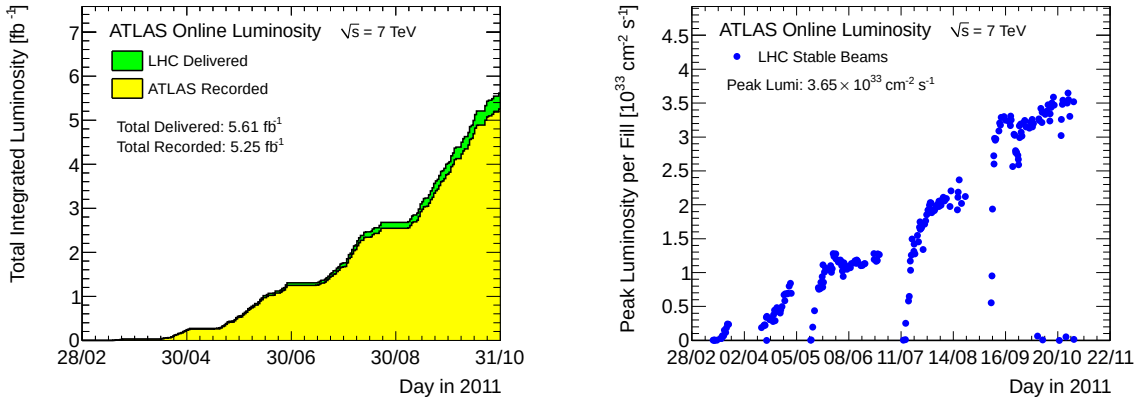

(a) (b)

Figure 4.1: Total integrated luminosity in 2011. (a) shows the cumulative integrated luminosity versus day during stable beams and for proton-proton collisions at $\sqrt{s} = 7\,\text{TeV}$ recorded by ATLAS (yellow) and delivered by the LHC (green). (b) shows the maximum instantaneous luminosity per fill versus day delivered to ATLAS [99].

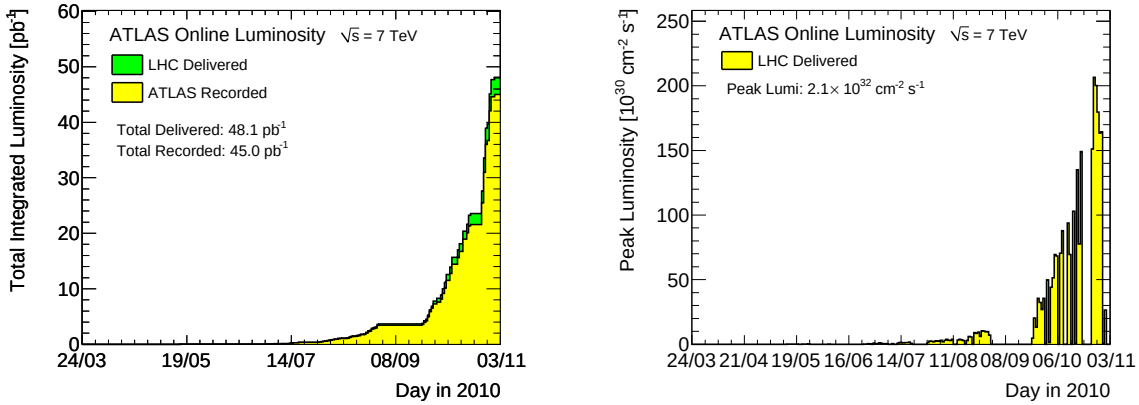

(a) (b)

Figure 4.2: Total integrated luminosity in 2010. (a) shows the cumulative integrated luminosity versus day during stable beams and for proton-proton collisions at $\sqrt{s} = 7\,\text{TeV}$ recorded by ATLAS (yellow) and delivered by the LHC (green). (b) shows the maximum instantaneous luminosity per fill versus day delivered to ATLAS [99].

Period	Run Range	Luminosity (nb^{-1})
A	152166–153200	0.4
B	153565–155160	9
C	155228–156682	9.5
D	158045–159224	320
E	160387–161948	144
F	162347–162882	580
G	165591–166383	780
H	166466–166964	6500
I	167575–167844	14500

Table 4.1: Data periods of 2010 data. The informations and details (detector and trigger settings etc.) of each period can be found in [102–104].

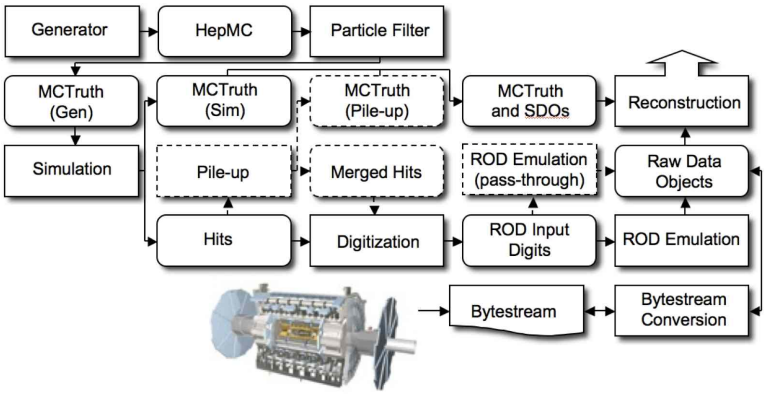

Figure 4.3: ATLAS simulation chain in Athena. Algorithms are in square-cornered boxes and persistent data objects in rounded boxes [108]. The optional pile-up portion of the chain is in dashed boxes. These are only used when events are overlaid.

4.2 ATLAS software framework Athena

The ATLAS software framework Athena [98] is based on the high-energy software framework Gaudi [105, 106] which was originally developed for LHCb [107]. It is organised in different modules so that different packages can be executed. The settings of an individual job depending on these packages is done via configuration files, so-called job option files, in Athena. The entire physics analysis for MC and data can be performed with Athena.

The MC simulation chain is divided into different steps: MC event generation, detector simulation, digitisation and (object) reconstruction (see Fig. 4.3). Real data are directly called on the (object) reconstruction, the first three steps are dropped. The generated events of a MC generator are stored in the standard HepMC event record [109, 110][3] and can be filtered at generation time. Only particles with certain properties (e.g. leptonic decays or particles with energies above a threshold) are kept. Although a generator is sensitive on prompt decays, only 'stable' particles[4] are saved. Afterwards, the events are read into the detector simulation and

[3]The HepMC event record is described in Sec. 6.1.

[4]Stable particle means in this context a particle that covers a certain distance in the detector.

Figure 4.4: Different ATLAS data formats for the physics analysis [113]. From raw data format to physics analysis data format (lef to right).

every generated particle of each event has to be simulated through the full ATLAS detector by the detector simulation GEANT4 [111, 112] used at ATLAS [108]. Two different formats are the output of the detector simulation. In one of these formats – MCTruth – so called 'truth' information of each particle in the event (e.g. tracks, mother particle etc.) is saved and further processed in the reconstruction step. If needed, it can be used during the analysis of simulated data accordingly. The simulated events are also stored in (G4) hits which go to the next step. During the digitisation, the detector response (e.g. electronic noise) is simulated and added to the hits. After the full step (read out drivers (ROD) input digits, ROD emulation), the events are saved in Raw Data Objects (RDO). In addition, simulated data objects (SDO) are created from the MCTruth during the digitisation. As an optional function, the overlay of events (pile-up events) is possible during the digitisation step to save CPU time required by the simulation. Finally, all these three formats (RDO, MCTruth and SDO) pass to the reconstruction step. Real data in the form of byte streams is directly saved in the RDO and RAW format[5], respectively and pass directly to the reconstruction step.

The reconstructed events are also stored in different formats as seen in Fig. 4.4 [113]. The RAW/RDO format contains only events coming from the last trigger level, the Event Filter. The reconstruction step is applied on these events, which are stored as Event Summary Data (ESD). Although the ESD has already an object-oriented representation, the event size of approximately 1 MB (target size 500 kB) is too large. So the Analysis Object Data (AOD) is a reduced ESD with a size of approximately 100 kB per event and can already be used for an analysis. The Tag Data (TAG) coming from the AOD are event-level metadata with a size of 1 kB per event. But coming from the AOD, there is also the Derived Physics Data (DPD) for physics analysis.

The DPDs are distributed in three different levels [114]. The primary DPDs (D1PDs) are separated into a performance and a physics part. Out of these D1PDs, DPDs from a higher level are produced, which have a smaller size than the D1PDs. Although secondary DPDs (D2PDs) are smaller than D1PDs, they can store additional information which can be computed during the production. D2PDs have the same data format as ESDs, AODs and D1PDs, the POOL data format [115]. The tertiary DPDs (D3PDs) in ROOT format [116] are defined by the user. The user can store the information which is needed for the individual analysis. Furthermore, it is possible to produce D2PDs and D3PDs directly out of ESDs and AODs. D3PDs are used in this thesis (see Sec. 8.1).

Due to the fact that all these different steps need a lot of CPU time, data samples are usually

[5]Usually, RDO applies to MC events and RAW to real data.

centrally produced. For this, the LHC Computing Grid (WLCG, Grid) [117] is used. A single task is parallelised into many jobs dependent on the task content. The output of each job is registered with the ATLAS Distributed Data Mangement system (DDM) [118] and can be used via DQ2 [118] amongst other things for bookkeeping and analyses.

4.3 Event generation, simulation and reconstruction at ATLAS

As already mentioned, it is possible with Athena to run the full chain from MC event generation over detector simulation and digitisation up to object reconstruction. If it is desired, the physics analysis can also be done within Athena. In the following, the different steps are described.

4.3.1 Event generation

Simulations are needed for the description and understanding of real data. The starting point of the MC simulation is the event generation, which is based on probability based algorithms. They calculate the physics process according to the structure functions and cross sections and are independent of the detector. These MC simulations are calculated in MC generators. A more detailed description of MC simulations and MC generators is given in Chap. 5. For completeness, the fundamental principle of the event generation is described here. Proton-proton collisions, which take place at ATLAS, pass through the following different steps [119, 120]:

1. hard scattering process: interaction between two partons (quarks or gluons) of the proton,
2. parton shower,
3. underlying/minimum bias events: interaction and production of particles that are not involved in the hard process,
4. hadronisation of particles created during parton shower, and
5. decay of (probably) produced short-lived resonances into observable particles (leptons, hadrons)

The event generation at ATLAS is done within the ATLAS software framework Athena.[6]

4.3.2 Detector simulation and digitisation

As a second step, the generated events have to pass through the ATLAS detector simulation which is based on GEANT4 [111, 112]. So far, the generated events demonstrate the knowledge about physics processes themselves. In order to measure these processes, the material of the detector, noise, energy loss etc. have to be considered in the description of generated physics events. Each particle of the event passes through every subsystem of the entire detector. At every detector position, the interaction of the particle with the detector material is calculated and stored as energy depositions (hits). For this, the exact knowledge of the detector geometry and every individual subdetector as well as the magnetic field etc. is needed. Each event has a size of about 2 MB after the detector simulation [108].

[6] It is technically implemented that Athena provides mostly interface packages and links to an external installation of the MC generator in Genser (Generator Services Project) [121] and uses the libraries of the individual generators installed there.

Afterwards, all the stored energy depositions in form of hits are transferred to electronic signal in form of digits during the digitisation step. These digits are finally written out as RDOs, the input of the reconstruction, and have a size of approximately 2.5 MB [108]. As mentioned above, it is also possible during the digitisation step to overlay events and create pile-up events. These pile-up events describe real events in a better way because there are usually more than one collision of two particles in the event. The output after the digitisation corresponds to the output of real detector raw data, coming from particle collisions.

4.3.3 Event reconstruction

Finally, the events are reconstructed. Different objects in the event are defined. These objects are reconstructed with different algorithms both for MC and real data, which is illustrated in Sec. 4.4.

4.4 Object reconstruction

In the following, the reconstruction of different objects like jets, hadronically decaying τ leptons and missing transverse momentum $E_{\mathrm{T}}^{\mathrm{miss}}$, needed for the selection of $W \rightarrow \tau\nu_{\tau}$ events, are described. For completeness, the reconstruction of electrons, photons and muons is briefly discussed as well.

4.4.1 Jet reconstruction

Partons (quarks and gluons) are produced in proton-proton collisions at the LHC, either in intermediate steps of the collision or from the proton remnants. These partons fragment and hadronise into charged particles which form tracks and clusters in the detector. The finally resulting electrons, photons, and hadrons leave energy depositions in the calorimeter. A jet is a combination of all these elements. Figure 4.5(a) illustrates different jet types. There are parton jets coming from the energy of the initial parton, particle jets which are reconstructed by applying jet algorithms on stable particles, and calorimeter jets which are based on the energy depositions in the calorimeters.

In experiments, jets can be reconstructed either from the track information or the cluster information in the detector or mostly from a combination of both.

Originally, several jet algorithms like cone algorithms and/or k_{t}-algorithms have been developed and used at ATLAS, but since spring 2009 the anti-k_{t}-algorithm is the default ATLAS jet algorithm [123, 124]. The different steps of the ATLAS jet reconstruction are shown in Fig. 4.5(b). From the calorimeter cells, either clusters or towers are built, which are the input of jet finding algorithms.

Calorimeter towers (see Fig. 4.6(a)) are built from calorimeter cells within a fixed width with a size of $\Delta\eta \times \Delta\phi = 0.1 \times 0.1$ [58]. These towers usually have a fixed radius. All the signals of the individual cells are added together, while in the overlap area only a fraction of the signal corresponding to the overlap area fraction between the tower bin and the cell in $\Delta\eta$ and $\Delta\phi$ is added to the calorimeter tower. All cells with a negative energy are suppressed to avoid noise.

Topological clustering (see Fig. 4.6(b)) combines three-dimensional energy depositions in the calorimeter [58]. Topological cell clusters include a better noise suppression compared to calorimeter towers. To start the cell clustering, seed cells with a significant absolute signal over a certain threshold of $|E| > 4\sigma_{\mathrm{cell}}$ of the total noise (electronics and pile-up) are chosen. Around these primary seeds, all immediate neighbour cells (secondary seeds) with

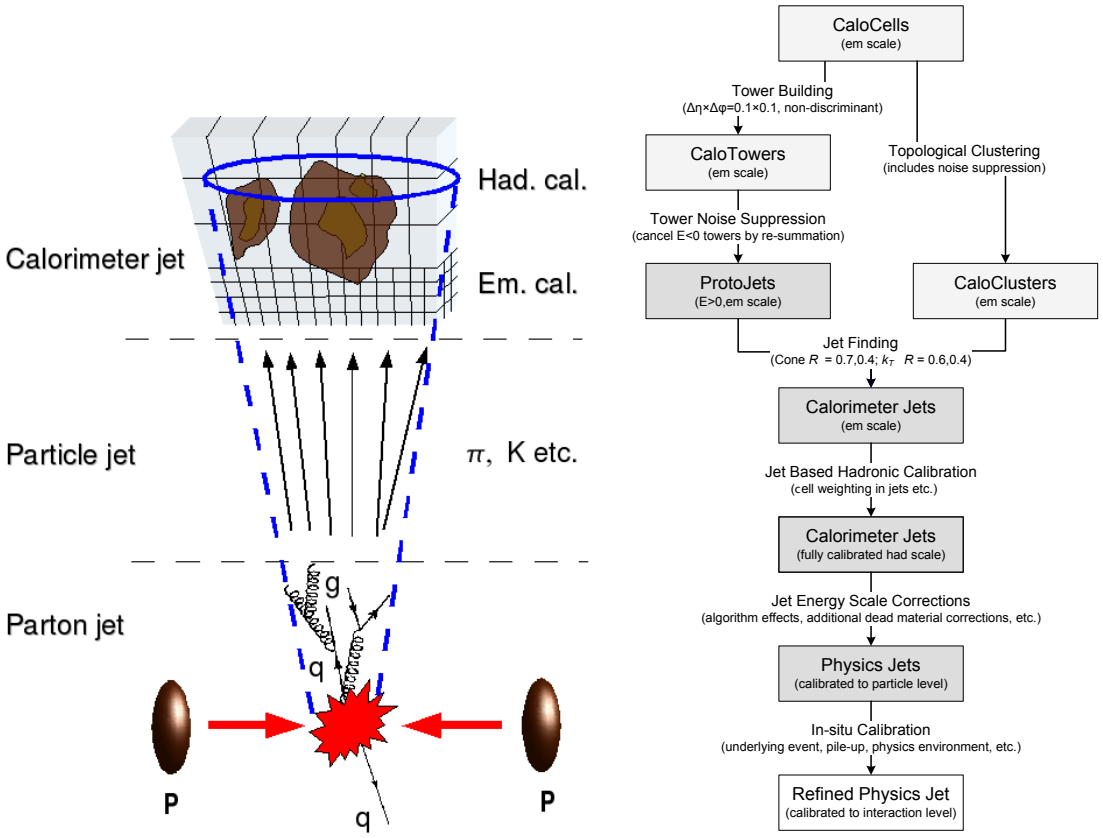

(a) (b)

Figure 4.5: (a) Different types of a jet [122], (b) Jet reconstruction flow based on calorimeter towers or clusters [58].

an energy of $|E| > 2\sigma_{\text{cell}}$ are added to the jets. Next, all surrounding cells with a basic threshold of $|E| > 0\sigma_{\text{cell}}$ are added to the jet. Finally, the resulting cluster is checked for local signal maxima. If there are more then one maximum, the cluster is split into smaller clusters.

In the following, two different jet clustering algorithms, based on tower and topological clusters, are described.

Many jet algorithms use the cone algorithm [58, 125]. Its goal is to maximise the energy (or p_{T}) in a geometric cone. The seeded cone algorithm at ATLAS uses two parameters: the transverse energy threshold for a seed $E_{\text{T}} = 1\,\text{GeV}$ for all cone jets and the cone size $\Delta R = \sqrt{\Delta\eta^2 + \Delta\phi^2}$. For narrow jets, $\Delta R = 0.4$ is chosen, for wide jets $\Delta R = 0.7$. The jet algorithm starts with input objects – the jet candidates – coming from a topological cluster and a tower jet. All these input objects are sorted by their transverse energy E_{T}. If the highest E_{T} object is above the threshold of 1 GeV, a cone around this object is created with the previously mentioned cone size ΔR of 0.4 or 0.7. A graphical visualisation is given in Fig. 4.7(a). The centroid of this cone is calculated which defines the new center of the object (recombination). Afterwards, a new cone is drawn and all objects inside this cone are calculated and again recombined, until there is no change for the centroid and a stable cone is found. If the cones of

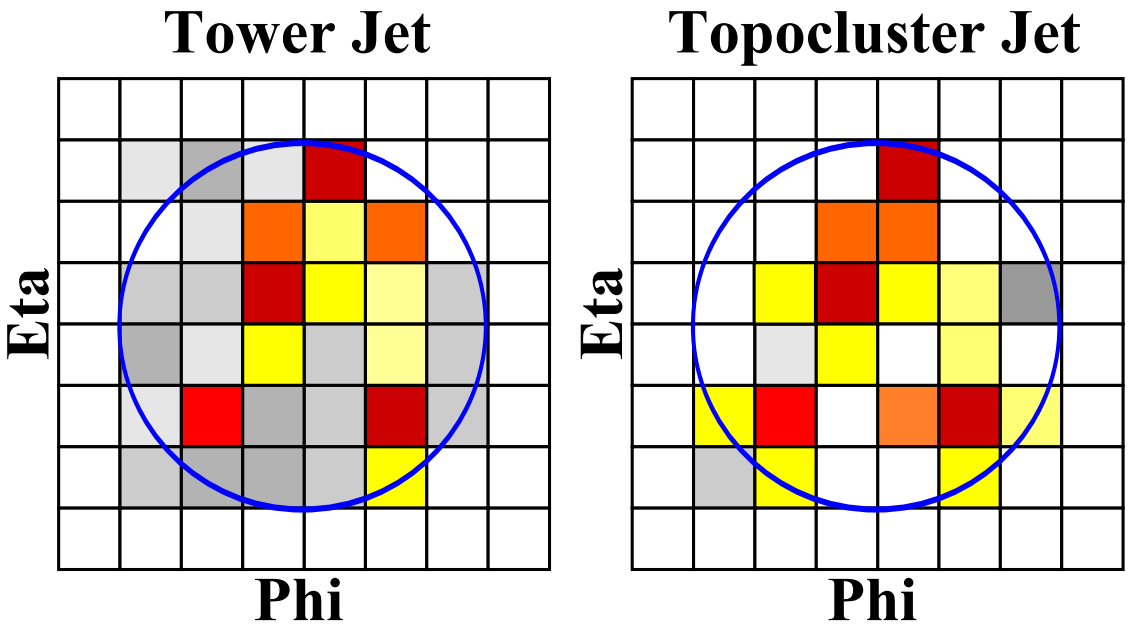

(a) (b)

Figure 4.6: Two different jet definitions: (a) tower jets and (b) topocluster jets. The different shapes of the cell clusters, used in the jet definitions, is visualised.

two jets overlap, they are split or merged. The overlap fraction is usually 50% for the decision of splitting or merging. If the overlap region has to be split, the splitting is calcuated percentaged to both of the cones, respectively.

The described cone algorithm is affected by so-called dark towers, which are energetic clusters outside of any jet in the event (see Fig. 4.7(b)). A solution of this problem is the clustering ansatz [125, 127–129]. This method is based on pair-wise clustering of the input objects and a distance measurement between the two objects of a pair. All input objects are listed in a list of protojets. The distance between all possible pairs of two protojets i and j of this list is measured as follows [127]:

$$d_{ij} = \min\left(k_{ti}^{2p}, k_{tj}^{2p}\right)\frac{\Delta R_{ij}^2}{R^2} \tag{4.2}$$

$$d_{iB} = k_{ti}^{2p} \tag{4.3}$$

with $\Delta R_{ij}^2 = (y_i - y_j)^2 + (\phi_i - \phi_j)^2$ as the relative distance between object i and j and $k_{ti(j)}$, $y_{ti(j)}$ and $\phi_{ti(j)}$ as the transverse momentum, rapidity and the azimuth angle of object i (j). d_{iB} is the distance between object i and the beam. In ATLAS, $\Delta R = 0.4$ and $\Delta R = 0.6$ are used for narrow and wide jets, respectively.
The values d_{ij} and d_{iB} are calculated for all possible combinations and the minimal value d_{min} has to be found. If the minimal value d_{min} is from the d_{ij} measurement the two protojets i and j are merged together into a new protojet k. The two protojets i and j are removed from the list of protojets and replaced by the new protojet k. The distance measurement is repeated with the new protojet k.

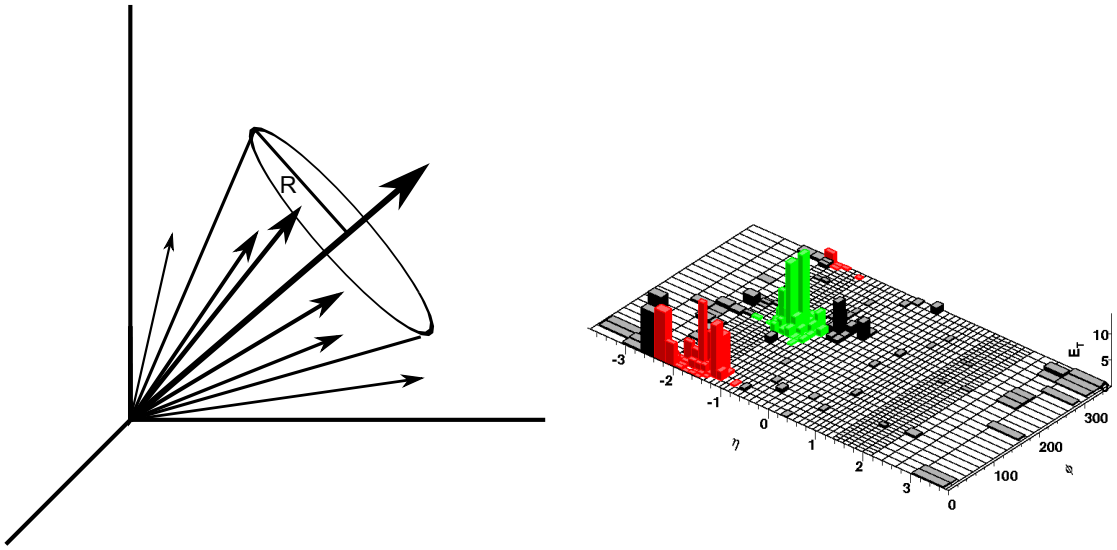

(a) (b)

Figure 4.7: (a) Visualisation of a cone algorithm for jet finding, (b) Dark towers, energetic clusters outside of any jet in the event as a problem of the cone algorithm [126].

If the minimum d_{min} is from d_{iB}, the protojet is not mergeable anymore. The protojet is classified as a jet and removed from the list of protojets. This procedure is repeated until the list of protojets is empty.

The value p (see Eqs. (4.2) and (4.3)) takes different values, which correspond to the accordant jet algorithm. A p-value of 1 is the so-called k_t-algorithm and of 0 the Cambridge/Aachen-algorithm [127, 128].
At ATLAS the anti-k_t algorithm is used which corresponds to a p-value of -1 [127]. Figure 4.8 shows an example of all four different jet algorithms. One can see that the k_t- and the Cambridge/Aachen-algorithms are useful in its response to soft particles resulting in a complex jet shape (see Figs. 4.8(a) and 4.8(b)). Many 'ghosts'[7] are included in these jets, so it should not be used for hard jets. Composite jets have more varied shapes in the cone algorithm (see Fig. 4.8(c)), which results in irregular cones. The shape is regular for single-particle jets. The hard jets are circular and only the softer ones have a more complex shape. However, the most circular jet cones are given for the anti-k_t algorithm (see Fig. 4.8(d)).

Before the jet can be used, the calorimeter cells are calibrated at the EM scale, which correctly gives the energy deposition in the calorimeter of electromagnetic showers. According to this, the aim of the jet energy scale calibration is the correction of the energy and the momentum of jets which are measured in the calorimeter to those at the hadronic scale. Several effects are corrected: partial measurement of the energy depositions of hadrons, energy losses in dead detector material, energy depositions from particles outside the calorimeter and signal losses during the clustering and the jet reconstruction in the calorimeter.

ATLAS uses a calibration scheme called jet energy scale (JES) calibration. These are jet-by-jet corrections as a function of the jet energy and pseudorapidity at the electromagnetic scale. The JES calibration is done in three steps. As a starting point, the averaged additional energy due to

[7] A 'ghost' is a single infinitely soft particle.

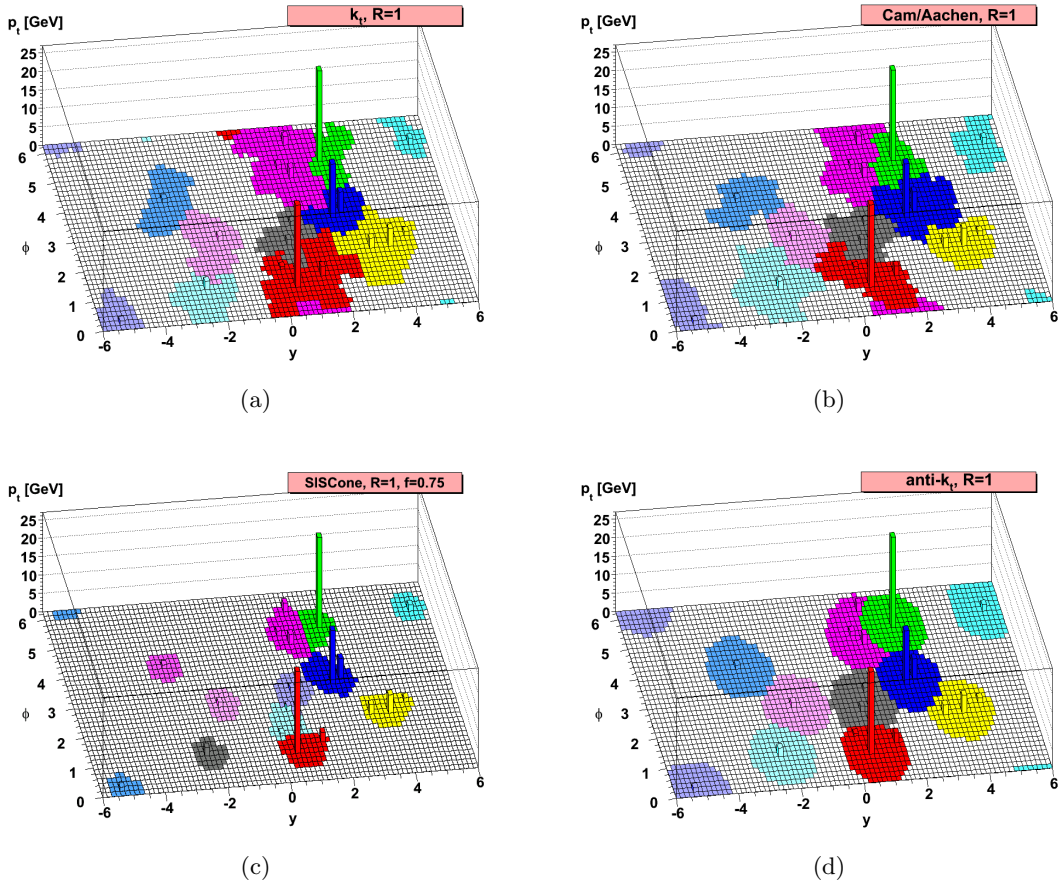

Figure 4.8: A parton-level event (together with many random soft 'ghosts') for the four different jet algorithms: (a) k_t-algorithm, (b) Cambridge/Aachen-algorithm, (c) Cone algorithm, and (d) anti-k_t-algorithm [127].

pile-up effects is subtracted from the energy in the calorimeter still at the electromagnetic scale. This correction is assigned by using minimum bias data as a function of number of reconstructed primary vertices and jet pseudorapidity. As a second step, the position of the jet is corrected. Instead of pointing to the geometrical center of the ATLAS detector, the jet direction points to the primary vertex of the interaction. Finally, the jet energy reconstructed in the detector and the position are corrected by using correction factors coming from the comparison of the reconstructed and the corresponding MC truth jet. Further details as well as jet energy scale systematic uncertainties can be found in [58] and [130].

4.4.2 Tau lepton reconstruction

The most difficult lepton to reconstruct and identify is the τ lepton. Due to their similar signature in the detector, it is difficult to distinguish between leptons from a leptonically decaying τ lepton and prompt leptons, hence, only hadronically decaying τ leptons are reconstructed.

In principle hadronically decaying τ leptons, which are analysed in this thesis, leaves a signature in the detector which is similar to the one of a QCD jet coming from gluons and/or quarks

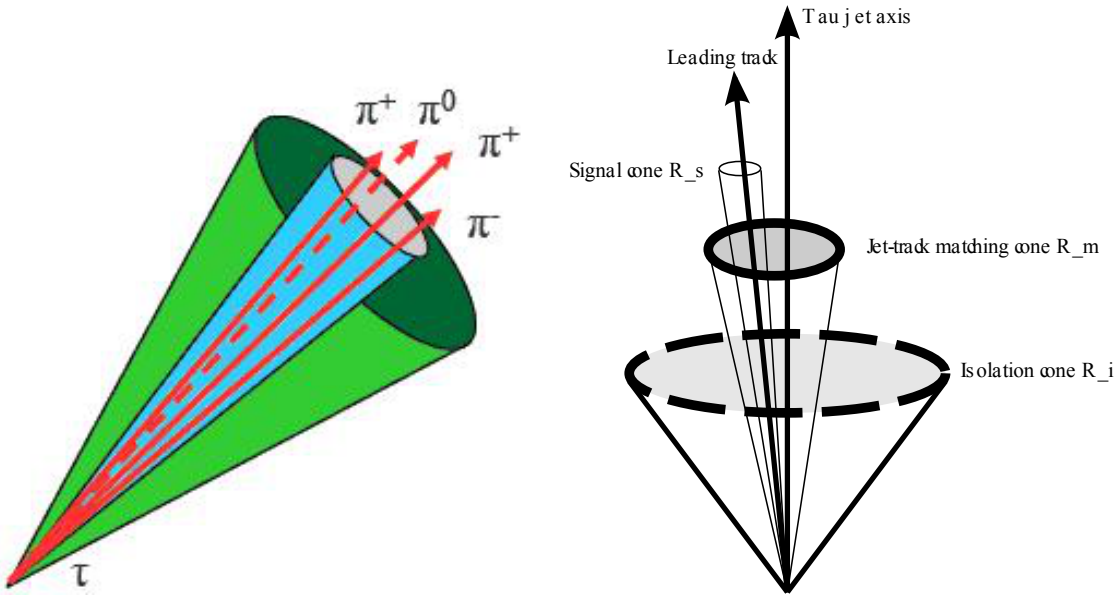

(a) (b)

Figure 4.9: (a) Typical τ lepton decay; modified from [131], (b) track isolation cone for a hadronically decaying τ lepton.

in the detector. As mentioned in Sec. 2.1.5, τ leptons decay hadronically in 64.79% of the cases. In these decays, there are usually one (1-prong, single-prong) or three (3-prong, multi-prong[8]) charged mesons (mostly pions, but there is also a small fraction of Kaons) in the final state.[9] This decay has to be distinguished from other jets. A hadronic τ lepton decay into n charged particles is commonly termed as n-prong decay.

A typical 3-prong decay is illustrated in Fig. 4.9(a). One can see that a high-p_{T} (compared to its mass) τ lepton produces a very collimated jet, which leaves significant energy depositions in the calorimeter, and whose decay has a small track multiplicity with bundled tracks. To summarise, the shape of a τ lepton or a τ jet (both terms are used equivalent) is similar to the one of a narrow QCD jet (see Fig 4.9 and Sec. 2.1.5).

The track isolation for the τ lepton reconstruction is illustrated in Fig. 4.9(b). The τ jet axis from the calorimeter jet defines the direction of the τ lepton. All tracks with a transverse momentum p_{T} above a certain threshold and in a matching cone with radius R_{m} are taken into account for the search of signal tracks. The track with the highest p_{T} inside this cone is the leading track; the second leading accordingly. If there is any other track in a signal cone of the leading track with smaller radius R_{s} and with a z-impact parameter close by the one of the leading track, it is assumed that this track comes from the τ lepton decay. These tracks inside the R_{s} cone smaller than a given cut-off and with transverse momentum above a certain threshold are reconstructed inside a larger cone with radius R_{i}. If there are no other tracks inside the cone with radius R_{i} except the one which is already in the cone with radius R_{s}, the isolation criteria is fulfilled. The leading track is then a track coming from the τ lepton (decay)

[8] In this context multi-prong means more than 1-prong.
[9] There is also negligible amount of events with 5 charged particles, which are more difficult to distinguish from QCD jets.

and all the tracks together build a τ lepton candidate [58, 93, 94]. For the second leading track etc., the procedure is applied accordingly.

Reconstruction of τ lepton candidates

There are two τ lepton reconstruction algorithms, one being calorimeter- and one track-based. The track-based τ lepton reconstruction algorithm requires a leading track with a transverse momentum larger than 9 GeV and has to fulfill certain criteria [58, 93, 94].
The hadronic τ lepton reconstruction, which is used in this thesis, starts from calorimeter jets reconstructed with the anti-k_t jet reconstruction algorithm from topological clusters of calorimeter cells and has a distance parameter of $R = 0.4$ (corresponds to the above R_m). These jets are seeds for the τ lepton reconstruction algorithm. The τ lepton reconstruction algorithm runs on all seed jets in $|\eta| < 2.5$, associates tracks to every seed jet and calculates variables from tracking and calorimeter information. Tracks, which are associated to a τ lepton candidate, have to be in a core cone of $\Delta R < 0.2$ (corresponds to the above R_s) and have to fulfill the following quality criteria:

- $p_T > 1\,\text{GeV}$,
- number of B-layer hits $N_{\text{hit}}^{\text{B-layer}} \geq 1$,
- number of pixel hits $N_{\text{hit}}^{\text{pixel}} \geq 2$,
- number of pixel and SCT hits $N_{\text{hit}}^{\text{pixel}} + N_{\text{hit}}^{\text{SCT}} \geq 7$,
- distance of closest approach of the track to the reconstructed primary vertex in the transverse plane $|d_0| < 1.0\,\text{mm}$, and
- $|z_0 \sin\theta| < 1.5\,\text{mm}$ with z_0 as the longitudinal distance of the closest approach $d = 0$.

As already mentioned, τ lepton candidates are categorised as single-prong or multi-prong candidates depending on the number of tracks in the core cone of the τ lepton candidate. The charge of this candidate is calculated as the sum of all reconstructed tracks. The charge misidentification for the leading track is approximately 0.2% [58] but the overall charge misidentification is higher due to combinatorial effects[10] and around 0.3% [58, 132].

In order to suppress leptonically decaying τ leptons, electron and muon vetoes are applied [58].

The energy of hadronic τ lepton candidates is also calibrated as for the jets by applying a correction to the reconstructed energy at the electromagnetic energy scale[11] [132].

Identification of hadronic τ lepton candidates

The reconstruction described above is more related to the general kinematic of the object, whereas the identification has a tighter list of criteria, which is described in the following. There are three different methods for the identification (ID) of τ lepton candidates: a cut based ID (mainly for first data), a projective likelihood ID (LL) and a boosted decision tree ID (BDT) [132]. All these methods are based on several variables that are described here [132]:

[10] Single-prong decays could be reconstructed as a 3-prong τ lepton due to photon conversions or the presence of additional tracks from the underlying event. Furthermore, a 3-prong candidate could be reconstructed as a 1-prong due to inefficiencies of the track reconstruction and selection.

[11] In this case, the electromagnetic energy scale is a sum over the energies of cells which form the topological clusters of the jet seed as explained above.

Electromagnetic radius: Transverse energy weighted shower width in the electromagnetic (EM) calorimeter:

$$R_{\mathrm{EM}} = \frac{\sum_{i\in\{\mathrm{EM\ 0-2}\}}^{\Delta R_i<0.4} E_{\mathrm{T},i}^{\mathrm{EM}}\,\Delta R_i}{\sum_{i\in\{\mathrm{EM\ 0-2}\}}^{\Delta R_i<0.4} E_{\mathrm{T},i}^{\mathrm{EM}}}, \tag{4.4}$$

i runs over cells associated to the τ lepton candidate. ΔR_i is the distance between a calorimeter cell and the seed axis of the τ jet as well as $E_{\mathrm{T},i}^{\mathrm{EM}}$ the cell transverse energy, calibrated at the EM scale.

Track radius: p_{T} weighted track width:

$$R_{\mathrm{track}} = \frac{\sum_{i}^{\Delta R_i<0.4} p_{\mathrm{T},i}\,\Delta R_i}{\sum_{i}^{\Delta R_i<0.4} p_{\mathrm{T},i}}, \tag{4.5}$$

i runs over all core and isolation tracks of the τ lepton candidate within $\Delta R_i < 0.4$. ΔR_i is defined relative to the τ jet seed axis and $p_{\mathrm{T},i}$ transverse momentum of the track.

Leading track momentum fraction:

$$f_{\mathrm{track}} = \frac{p_{\mathrm{T},1}^{\mathrm{track}}}{p_{\mathrm{T}}^{\tau}}, \tag{4.6}$$

$p_{\mathrm{T},1}^{\mathrm{track}}$ is the transverse momentum of the leading core track of the τ lepton candidate and p_{T}^{τ} the transverse momentum of the τ lepton candidate, both calibrated at the EM energy scale.

Core energy fraction: Fraction of transverse energy in the core ($\Delta R < 0.1$) of the τ lepton candidate:

$$f_{\mathrm{core}} = \frac{\sum_{i\in\{\mathrm{all}\}}^{\Delta R_i<0.1} E_{\mathrm{T},i}^{\mathrm{EM}}}{\sum_{i\in\{\mathrm{all}\}}^{\Delta R_i<0.4} E_{\mathrm{T},i}^{\mathrm{EM}}}, \tag{4.7}$$

i runs over all cells calibrated at the EM scale which are associated to the τ lepton candidate within $\Delta R < 0.1(0.4)$ of the τ jet seed axis.

Electromagnetic fraction: Fraction of transverse energy in cell i and j of the τ lepton candidate deposited in the EM calorimeter:

$$f_{\mathrm{EM}} = \frac{\sum_{i\in\{\mathrm{EM\ 0-2}\}}^{\Delta R_i<0.4} E_{\mathrm{T},i}^{\mathrm{EM}}}{\sum_{j\in\{\mathrm{all}\}}^{\Delta R_j<0.4} E_{\mathrm{T},j}^{\mathrm{EM}}}, \tag{4.8}$$

$E_{\mathrm{T},i}$ ($E_{\mathrm{T},j}$) is the transverse energy which is calibrated at the EM energy scale and deposited in cell i (j). i runs over the cells in the first three layers of the electromagnetic calorimeter and j over the cells in all layers of the calorimeter.

Cluster mass: Invariant mass of the constituent clusters of the seed jet at the EM energy scale:

$$m_{\mathrm{clusters}} = \sqrt{\left(\sum_{\mathrm{clusters}} E\right)^2 - \left(\sum_{\mathrm{clusters}} \mathbf{p}\right)^2}. \tag{4.9}$$

	R_{EM}	R_{track}	f_{track}	f_{core}	f_{EM}	m_{clusters}	m_{tracks}	$S_{\mathrm{T}}^{\mathrm{flight}}$	f_{HT}
Cuts	•	•	•						
Likelihood single-prong	•	•				•			
Likelihood multi-prong	•		•		•		•	•	
Jet BDT single-prong	•	•	•	•	•	•			
Jet BDT multi-prong	•	•	•	•	•	•	•	•	
Electron BDT single-prong	•	•	•	•	•	•			•
Electron BDT multi-prong	•	•	•	•	•	•	•	•	•

Table 4.2: Comparison of variables used by each τ lepton identification method [132].

Track mass: Invariant mass of the track system. The tracks used for the invariant mass calculation use core and isolation tracks:

$$m_{\mathrm{tracks}} = \sqrt{\left(\sum_{\mathrm{tracks}} E\right)^2 - \left(\sum_{\mathrm{tracks}} \mathbf{p}\right)^2}. \tag{4.10}$$

Transverse flight path significance: Decay length significance of the secondary vertex for multi-track τ lepton candidates in the transverse plane:

$$S_{\mathrm{T}}^{\mathrm{flight}} = \frac{L_{\mathrm{T}}^{\mathrm{flight}}}{\delta L_{\mathrm{T}}^{\mathrm{flight}}}. \tag{4.11}$$

$L_{\mathrm{T}}^{\mathrm{flight}}$ is the reconstructed decay length and $\delta L_{\mathrm{T}}^{\mathrm{flight}}$ its estimated uncertainty.

TRT HT fraction: Number of high threshold hits over number of low threshold hits (including outlier hits) in the Transition Radiation Tracker (TRT) of the highest p_{T} core track associated to the τ lepton candidate for discriminating hadronically decaying 1-prong τ lepton candidates from electrons:

$$f_{\mathrm{HT}} = \frac{N_{\mathrm{hit}}^{HT}}{N_{\mathrm{hit}}^{LT}}. \tag{4.12}$$

Some of these variables are visualised in Fig. 4.10 and 4.11. A good separation of these variables can be used to reject QCD jet background (blue) from the signal (red; in this case $W \to \tau\nu_\tau + Z \to \tau\tau$).

Furthermore, the used variables for the three different methods – cut based, LL and BDT – are summarised in Tab. 4.2. These three methods are optimised for three different signal efficiencies of 70% (loose), 50% (medium), and 30% (tight) with the following signal and background efficiencies [132, 133]:

$$\epsilon_{\mathrm{sig}}^{1/3-\mathrm{prong}} = \frac{\#\text{ of truth matched } 1/3-\text{prong } \tau \text{ candidates passing ID cuts}}{\#\text{ of true hadronically decaying } 1/3-\text{prong } \tau \text{ candidates}} \tag{4.13}$$

and

$$\epsilon_{\mathrm{bkg}}^{1/3-\mathrm{prong}} = \frac{\#\text{ of } 1/3-\text{prong } \tau \text{ candidates passing ID cuts}}{\#\text{ of all reconstructed } 1/3-\text{prong } \tau \text{ candidates}} \tag{4.14}$$

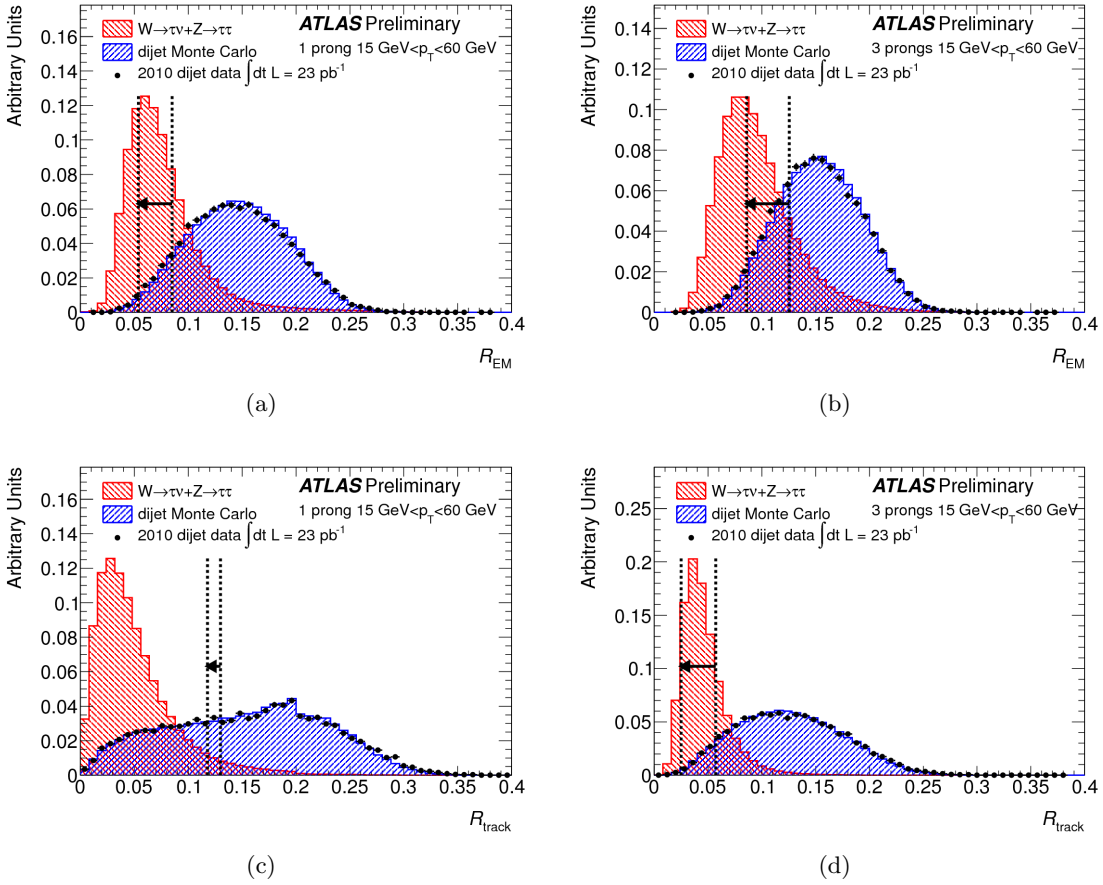

Figure 4.10: Distributions of (a) and (b) R_{EM} and (c) and (d) R_{track} for 1-prong (left) and 3-prong (right) τ lepton candidates [132].

with the background rejection[12]

$$r = \frac{1}{\epsilon_{\mathrm{bkg}}} - 1. \tag{4.15}$$

In the following the three methods are shortly introduced.

Cut-based identification The cut-based ID [132, 133] has been developed for early data to have a fast, simple, and easy comprehensible identification of τ leptons. The cut-based ID relies on three variables: R_{EM}, R_{track} and f_{track} (see Tab. 4.2). Important is, that two of these three variables, R_{EM} and R_{track}, are parametrised by the transverse momentum of the τ lepton candidate. The optimised cuts for these two parameters are very dependent on the transverse momentum due to the Lorentz collimation of the decay products in hadronic τ lepton decays. Tau leptons are not produced at rest at ATLAS. While the decay products can point in any direction in the τ lepton rest frame, they are highly collimated along the momentum of the τ lepton in the laboratory frame. The consequence is that width-like variables R should collimate

[12]The background rejection gives the ratio of rejected to accepted candidates.

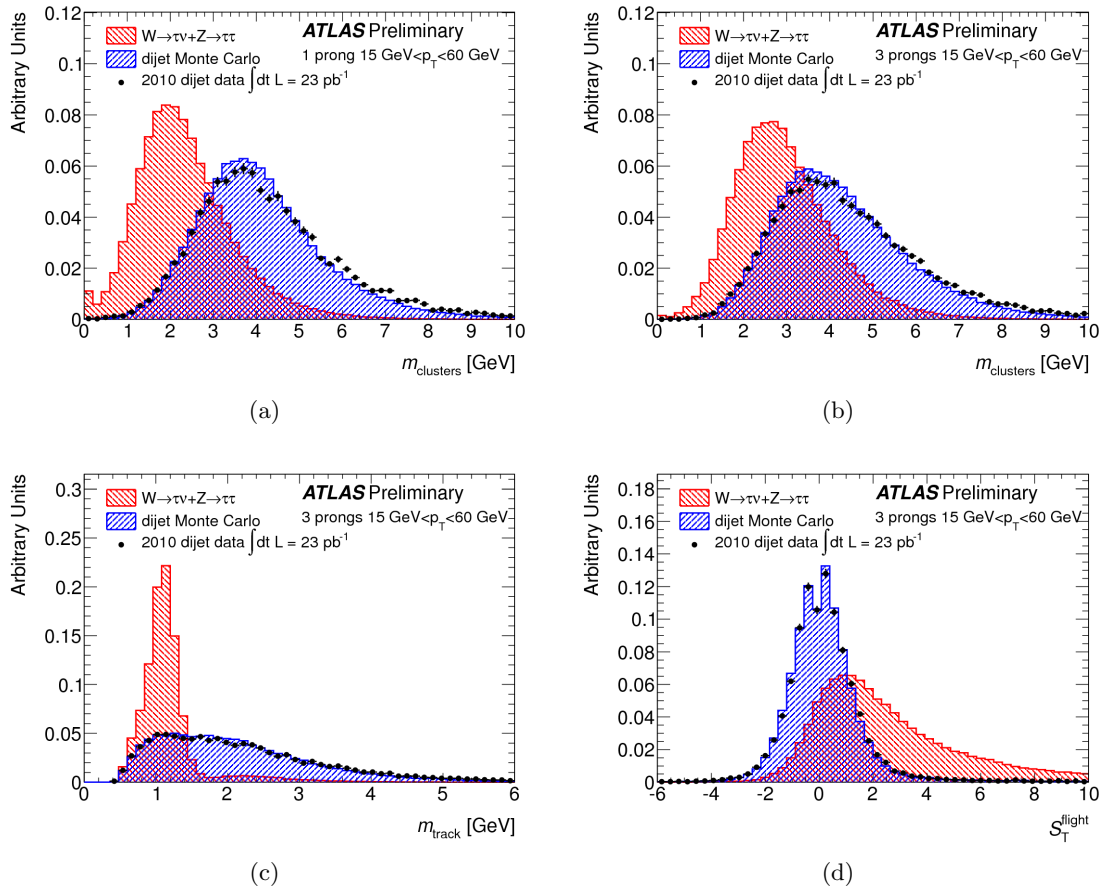

Figure 4.11: Distributions of (a) and (b) m_{clusters} for 1-prong (top left) and 3-prong (top right) τ lepton candidates, (c) m_{tracks} for 3-prong τ lepton candidates, and (d) $S_{\text{T}}^{\text{flight}}$ for 3-prong τ lepton candidates [132].

as:

$$R\left(p_{\text{T}}\right) \propto 1/p_{\text{T}} \tag{4.16}$$

The p_{T}-dependence is leveled by multiplying Eq. (4.16) by p_{T}. Fitting the remaining p_{T}-dependence by a second-order polynomial to the means of $R \times p_{\text{T}}$ for signal and background distributions gives the parameterisation of the distributions:

$$g(p_{\text{T}}) = a_0 + a_1 p_{\text{T}} + a_2 p_{\text{T}}^2 \tag{4.17}$$

Finally, possible cut curves for different values x between signal and background distributions can be calculated with

$$R^{\text{cut}}(p_{\text{T}}; x) p_{\text{T}} = (1 - x) g_{\text{sig}}(p_{\text{T}}) + x g_{\text{bkg}}(p_{\text{T}}) \tag{4.18}$$

There are two edge cases, $x = 1$ gives the mean of the signal distribution and $x = 0$ the one for the background.
The dashed lines in Fig. 4.10 demonstrate the best cut value range for tight τ leptons p_{T} of

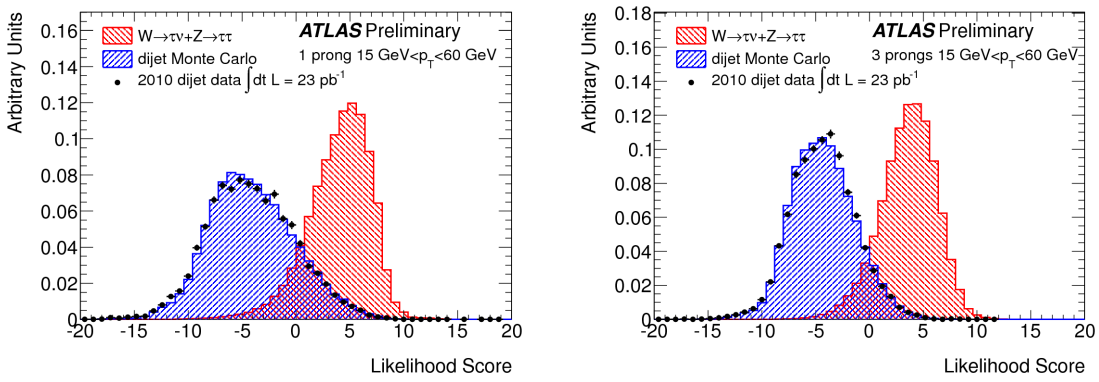

(a) (b)

Figure 4.12: Log-likelihood-ratio for (a) 1-prong and (b) 3-prong τ lepton candidates [132].

20 GeV and 60 GeV.[13]

Projective likelihood identification As mentioned before, the cut-based ID was used only for early data. With more data, it is replaced by the multivariate techniques projective likelihood identification and boosted decision tree identification [132].

The likelihood (LL) function $L_{S(B)}$ for signal (background) is defined as

$$L_{S(B)} = \prod_{i=1}^{N} p_i^{S(B)}(x_i) \tag{4.19}$$

with $p_i^{S(B)}(x_i)$ being the probability density function for signal (background) of the identification variable x_i of N variables. The identification variables are listed in Tab. 4.2. The discriminant of the likelihood method is given by the log-likelihood-ratio d between signal and background

$$d = \ln\left(\frac{L_S}{L_B}\right) = \sum_{i=1}^{N} \ln\left(\frac{p_i^{S(x_i)}}{p_i^{B(x_i)}}\right). \tag{4.20}$$

The likelihood ID has been optimised and developed in different and separate categories like the transverse momentum of the τ lepton candidate, the track multiplicity, track quality criteria, and the pile-up activity in the event.

The distributions of the log-likelihood-ratio d in Fig. 4.12 illustrates the good separation between signal and QCD jet background.

Boosted decision tree For the cross section measurement done in this thesis (see Chap. 8), boosted decision trees (BDTs) [132] are used for the τ lepton identification. A decision tree [134] performs a series of cuts on a set of identification variables. In principle, it is based on a simple cut-based approach, but this technique is much more powerful and usually runs in a multivariate environment. Another significant difference is that decision trees produce a

[13] The arrow points from the τ lepton candidate with 20 GeV to the one with 60 GeV.

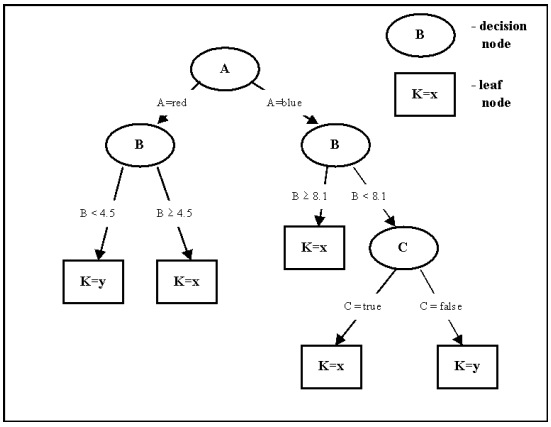

Figure 4.13: An example of a decision tree as described in the text [135].

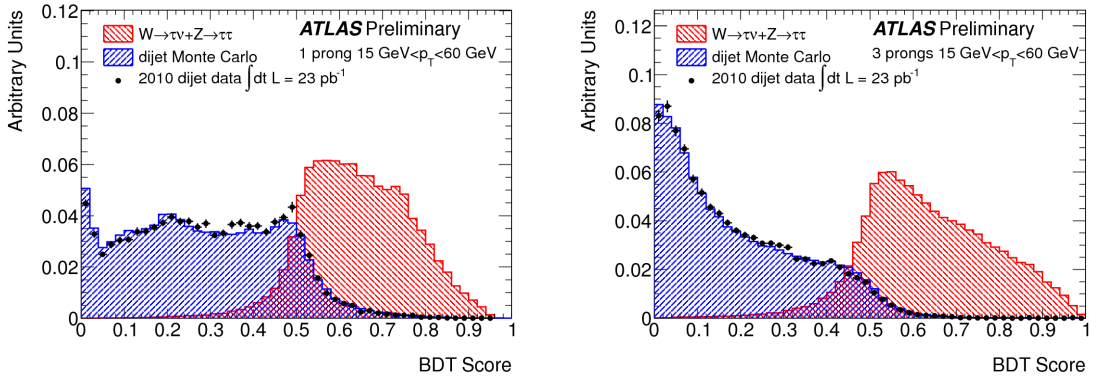

(a) (b)

Figure 4.14: Jet BDT score for (a) 1-prong and (b) 3-prong τ lepton candidates [132].

continuous score between 0 (background) and 1 (signal).

The optimal cut value is determined separately for each identification variable, whereby the decision tree algorithm starts with the entire sample at the root node. The best of these different cuts is chosen, builds the 'border' of two child nodes (left and right or -1 and +1). Then, the objects are sorted in a way that all objects below this cut are passed to the left and all objects above to the right node. In the following step the same algorithm is applied recursively on each child node on the remaining variables. The best cut is chosen again, on each child node two new nodes are constructed, the objects are sorted and the algorithm runs again. The result is a binary tree structure visualised in Fig. 4.13. The algorithm works until the leaf node is reached and a stop condition is confirmed (like e.g. the number on τ lepton candidates).

The advantage of a boosted decision tree (BDT) [136] is that it uses multiple decision trees with a normalised weighted sum of their outputs. Correlations between variables are taken into account and each decision tree is focused on correctly classifying objects for the case that these are misclassified in the previous decision tree.

There are BDTs for jet rejection (in the following: jet BDT) as well as for electron rejection

on candidates with one and three tracks, respectively.[14] The individual identification variables for each of the BDTs can be found in Tab. 4.2. The jet BDT score is shown in Fig. 4.14. A good separation can be recognised between signal and background. In this thesis, jet BDT scores are used for the cross section measurement of $pp \to W \to \tau\nu_\tau$ events (see Sec. 8.2.2).

4.4.3 Reconstruction of missing transverse momentum

A good knowledge of the missing transverse momentum $E_{\mathrm{T}}^{\mathrm{miss}}$ is very important for the study of many different physics channels in ATLAS, such as the search for signals from new physics like supersymmetry or extra dimensions, but also for the reconstruction of top quarks and τ leptons. Furthermore, it is important for the reconstruction of the neutrino of $pp \to W + \mathrm{X} \to \tau\nu_\tau + \mathrm{X}$ events, which cannot be detected directly, but is reconstructed as missing transverse momentum in the detector.

The current $E_{\mathrm{T}}^{\mathrm{miss}}$ reconstruction algorithm [95, 96] in ATLAS is based on transverse energy depositions in the calorimeters and on corrections for energy loss in the cryostat and measured muons

$$E_{x(y)}^{\mathrm{miss}} = E_{x(y)}^{\mathrm{miss,calo}} + E_{x(y)}^{\mathrm{miss,cryo}} + E_{x(y)}^{\mathrm{miss,muon}} \tag{4.21}$$

with the transverse missing energy $E_{\mathrm{T}}^{\mathrm{miss}}$

$$E_{\mathrm{T}}^{\mathrm{miss}} = \sqrt{\left(E_x^{\mathrm{miss}}\right)^2 + \left(E_y^{\mathrm{miss}}\right)^2} \tag{4.22}$$

and its azimuthal position ϕ^{miss}

$$\phi^{\mathrm{miss}} = \arctan\left(E_y^{\mathrm{miss}}/E_x^{\mathrm{miss}}\right). \tag{4.23}$$

The calorimeter term in these formulas is defined as

$$E_{\mathrm{x}}^{\mathrm{miss,calo}} = -\sum_{i=1}^{N_{\mathrm{cell}}} E_i \sin\theta_i \cos\phi_i, \tag{4.24}$$

$$E_{\mathrm{y}}^{\mathrm{miss,calo}} = -\sum_{i=1}^{N_{\mathrm{cell}}} E_i \sin\theta_i \sin\phi_i, \tag{4.25}$$

and

$$E_{\mathrm{T}}^{\mathrm{miss,calo}} = \sqrt{\left(E_x^{\mathrm{miss,calo}}\right)^2 + \left(E_y^{\mathrm{miss,calo}}\right)^2}, \tag{4.26}$$

where E_i is the cell energy, θ_i the polar angle and ϕ_i the azimuthal angle in a pseurorapidity range of $|\eta| < 4.5$. A noise supression is essential due to the high granularity of the calorimeter. Only cells belonging to a topological cluster (topocluster) are considered for the calculation of the missing transverse momentum.[15]

As for the jets, the missing transverse momentum also needs to be calibrated since cell energies

[14] The jet BDT for 3-prong candidates is used for classifying any candidate with two or more tracks. The jet BDTs are trained in unconnected categories which are defined by the number of reconstructed vertices of 1–2 and more than 2.

[15] The seed cells of these topoclusters are cells with a deposited energy of $|E_i| > 4\sigma_{\mathrm{noise}}$ with σ_{noise} as the Gaussian width of the cell energy distribution. The topoclusters are constructed by adding all neighbour cells with $|E_i| > 2\sigma_{\mathrm{noise}}$ and then by all surrounded cells with a cell energy $|E_i| > 0\sigma_{\mathrm{noise}}$ (see Sec. 4.4.1).

on the EM scale in the calorimeters are used so far. There are different approaches for the $E_{\mathrm{T}}^{\mathrm{miss}}$ calibration: a global cell energy-density weighting calibration scheme (global calibration or GCW), a local cluster weighting calibration scheme (local hadronic calibration or LCW) and a more refined one. While in the GCW cell-level signal weights are applied to compensate the different calorimeter reponse between electromagnetic and hadronic energy depositions, the LCW uses properties of topological clusters to calibrate them individually. The LCW categorises the calorimeter topoclusters as electromagnetic or hadronic and weights all the cell signals corresponding to the topocluster energy and cell energy density. Additional corrections are also applied for dead calorimeter material and energy loss.
As a more refined cell calibration for more data, the cells are sorted into categories of physical objects which are individually calibrated. The calibrated missing energy is given by the negative sum of all objects

$$E_{x,y}^{\mathrm{miss,calo,calib}} = -E_{x(y)}^{\mathrm{miss},e} - E_{x(y)}^{\mathrm{miss},\gamma} - E_{x(y)}^{\mathrm{miss},\tau} - E_{x(y)}^{\mathrm{miss,jets}} - E_{x(y)}^{\mathrm{miss,calo},\mu} - E_{x(y)}^{\mathrm{miss,CellOut}}, \quad (4.27)$$

where $E_{x(y)}^{\mathrm{miss,calo},\mu}$ is the contribution from the energy lost by muons in the calorimeter and $E_{x(y)}^{\mathrm{miss,CellOut}}$ the sum from cells in the topocluster which do not belong to any reconstructed object [95, 96].

In addition to the calorimeter term in Eq. (4.21), there are also the muon and the cryostat terms. The $E_{\mathrm{T}}^{\mathrm{miss}}$ muon term is given by the momenta of the muon tracks in $|\eta| < 2.7$

$$E_{\mathrm{x(y)}}^{\mathrm{miss},\mu} = -\sum_{\text{selected muons}} p_{x(y)}^{\mu}. \quad (4.28)$$

This term has to be considered for high-p_{T} muons due to the limited coverage of the muon spectrometer. Muons are lost outside the acceptance of the muon spectrometer ($|\eta| > 2.7$) and also in smaller regions around $|\eta| = 0$ and $|\eta| \approx 1.2$. Finally, the cryostat term corrects for the energy loss from hadronic showers between the LAr barrel electromagnetic calorimeter and the TileCal barrel hadronic calorimeter.

For the cross section measurement of $pp \to W \to \tau\nu_\tau$ events (see Chap. 8), a missing transverse momentum reconstruction method called MET_LocHadTopo is used, which is based on the reconstruction of $E_{\mathrm{T}}^{\mathrm{miss}}$ explained in the beginning of this subsection with the LCW calibration method [137–139].

4.4.4 Reconstruction of electrons, photons and muons

For completeness, the reconstruction of electrons, photons and muons is shortly given because they can fake hadronically decaying τ leptons.

Electrons and photons are reconstructed by using information from the Inner Detector and the electromagnetic calorimeter. The reconstruction is performed by looking for an energy deposition in the electromagnetic calorimeter with certain criteria (like e.g. energy, ratio of transverse energy to transverse momentum) and matching this deposition to a track in the Inner Detector. If there is a track, an electron is reconstructed, otherwise it is reconstructed as a photon. Both photon and electron reconstruction is performed by maximising the energy in a cluster of fixed size using a sliding-window algorithm with a window size of 5×5 cells. Following, the mentioned matching on a possible track is conducted. One has to pay attention on hadrons, which also create energy depositions in the

electromagnetic calorimeter that have similar shapes like electrons or photons. These so called fakes can be diagnosed by comparing the electromagnetic cluster with clusters in the hadronic calorimeter, and by checking if the origin of these clusters are hadrons. For more details see [58].

The reconstruction of muons is performed with the Inner Detector and the muon system. Muons pass through the whole detector and leave signals in all subsystems, so the muon reconstruction algorithms combine all the information of the individual subsystems. There are two main algorithms to find muons in the detector: algorithms for standalone muons and combined muons, respectively. In principle, both start with a track in the muon chambers and are considered if this track points to the interaction point. Muons, which are identified only by the muon system, are called standalone muons. Combined muons use additional information of the Inner Detector. This algorithm checks supplementary, if the track in the muon chamber has a corresponding track in the Inner Detector, and combines the information of the muon system and the Inner Detector. More information about the muon reconstruction can be found in [58].

5 Monte Carlo event generation and Monte Carlo generators

Event generation plays an important role in many aspects of high-energy physics (HEP). It is usually based on Monte Carlo (MC) techniques which are useful if analytical calculations are impossible or for simulation systems with many degrees of freedom. These MC simulations are probability-based simulations which calculate the physics process according to the structure functions and cross sections and are independent from the experiment. There are two mainly used HEP MC generators, PYTHIA [140] and HERWIG [141, 142]. The methods used in these generators are described below.

In this chapter the MC event generation in HEP is shortly illustrated and the main MC generators are briefly introduced, both based on LHC physics, namely proton-proton collisions. In order to describe the reality, one cannot use MC simulations only, the MC generators have to be tuned to agree with real data. A nice and more detailed overview of MC event generation and MC generators is given in [119] and [120] as well as in the manuals of different MC generators e.g. PYTHIA [140, 143] and HERWIG [141, 142, 144].

5.1 Monte Carlo event generation

The starting step of each event generation is the calculation of the hard scattering process, mainly the calculation of the matrix element of the partonic cross section, at a fixed order of the strong coupling including the randomly chosen momenta of the ingoing partons, which are based on the parton distribution functions (PDFs). Higher order QCD effects are added by using different generator dependent parton evolution equations during the following parton shower. As a next step, there is the hadronisation of the partons done with different hadronisation models. Here, the underlying event/multi parton interaction (UE/MPI) is also taken into account because they depend on the description of the hadronisation. Finally, unstable hadrons like short-lived resonances decay to stable particles. The fundamental principle of the above described MC event generation for a proton-proton collision is illustrated in Fig. 5.1, while the complexity and the overlap of all the different steps of such an event is given in Fig. 2.3. In the following the indiviual steps of an event generation are described in more detail.

5.1.1 Matrix element

The first step in the event generation is the calculation of the matrix element at a fixed order of the strong coupling (LO, NLO, NNLO, ...) in the hard process. Out of this matrix element, which symbolises the amplitude of the interaction, the partonic cross section can be determined by integrating the squared matrix element over the whole phase space of the interaction. These calculations are often done numerically. Because of the possibility to exclude particular regions of the phase space, divergencies can be avoided.

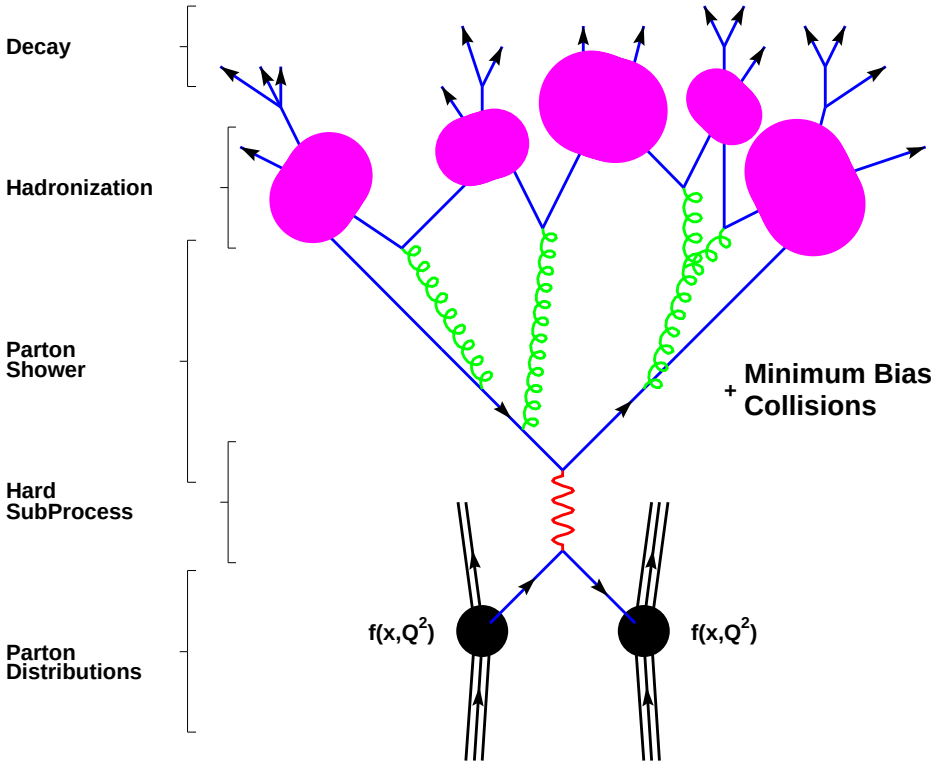

Figure 5.1: Scheme of the basic structure of a showering and hadronisation generator event [120].

5.1.2 Parton shower

As it can be seen in Fig. 5.1, the interaction between two protons occurs through their partons. Due to gluon radiation ($q \to qg$, $\overline{q} \to \overline{q}g$) and pair production ($g \to q\overline{q}$) new particles arise which cause a parton shower. So, parton showers play an important role in event generation. They simulate the initial (ISR) and final state radiation (FSR), gluon radiation before (ISR) and after (FSR) the hard process, in a collision. The general approach of simulating ISR and FSR is based on the same method, although the execution is different due to the fact that the cascades of ISR are space-like and of FSR time-like. Nonetheless, the calculations are done via DGLAP equations which describe the development, kinematics, and flavours of the emitted partons.[1] The two main generators PYTHIA and HERWIG have two different methods for the evolution in the DGLAP equations. In PYTHIA, the evolution variable is either the virtuality of the parent parton, Q^2, or the squared transverse momentum of the two emitted partons k_T^2. In HERWIG, the parton shower is angular-ordered and the evolution variable $E^2\,(1-\cos\theta)$ is a bit more complex. It depends on the energy E of the parent parton and the angle θ between the two emitted showered partons. Both approaches cancel out infrared singularities. The parton shower finishes when the virtuality of the partons Q^2 reaches a minimum value of e.g. $Q_0^2 = 1\mathrm{GeV}^2$.

[1] Partons from the hard process are assigned to partons at the Λ_{QCD} scale.

5.1.3 Hadronisation

In the following hadronisation, all coloured particles compose colourless hadrons. Several iterative models have been developed for the hadronisation. The two predominantly models used are the Lund string model [145–147] and the cluster fragmentation model [148–150].

In the cluster fragmentation model, final state gluons split into $q\overline{q}$ pairs. Pairs of quarks and anti-quarks group together so that they build colour neutral clusters which usually decay into smaller clusters until hadrons are formed. If a cluster is too light to fragment into a hadron, a light hadron replaces the cluster directly.

In the Lund string model, there are colour flux tubes or strings between strongly interacting particles which stands for the potential energy between them. These strings are uniform in length, have insignificant transverse momenta and have a diameter of a meson (1 fm). The principles of the confinement are valid for the strings. The larger the distance between the partons, the higher the energy is between them. Therefore, the energy increases linearly with the distance $E(d) \propto \kappa d$. At one point, the distance and therefore the energy of a $q\overline{q}$ pair is so large that it is more energetic to fragment and create a new $q\overline{q}$ pair. During this process a virtual $q\overline{q}$ pair fluctuates out of the vacuum on the string with the same colour as the quarks at the endpoints, the colour field is compensated, the string breaks into two pieces, and two $q\overline{q}$ pairs are arisen. This procedure is repeated until no further fragmentation, respectively string breaking, is possible. For both methods, baryons are produced by creating diquark pairs instead of quark pairs.

Multi parton interactions, which are covered in section 5.1.4, are also taken into account during the hadronisation. After the full hadronisation, unstable particles decay according to their branching ratios.

5.1.4 Multi parton interaction and underlying event

Due to the fact that the proton is not pointlike but exists of quarks and gluons, there are also multi parton interactions (MPIs) next to the hard process and gluon radiation (ISR, FSR) in the event (see Fig. 2.3). In the collision of two composite particles like protons, there is always the possibility that more than one pair of partons interact. All these secondary collisions are called MPIs and are especially important in the regions of small momentum fraction x of the proton. In general MPIs are usually soft (low transverse momentum) but they can also be hard with enough transverse momentum to build jets. There are different models to simulate MPIs. One important parameter of these models is a low transverse momentum cut-off $p_{T,\mathrm{min}}$. The cross section of the hard scattering process above $p_{T,\mathrm{min}}$ can be calculated as [151]

$$\sigma_{\mathrm{hard}}\left(p_{T,\mathrm{min}}\right) = \int_{p_{T,\mathrm{min}}}^{\sqrt{s}/2} \frac{d\sigma}{dp_{\mathrm{T}}} dp_{\mathrm{T}} \propto \frac{1}{p_{T,\mathrm{min}}^2}. \tag{5.1}$$

A $p_{T,\mathrm{min}}$ cut-off has to be introduced because otherwise the calculated differential cross section would diverge like $1/p_{\mathrm{T}}^4$. For an infinitely small $p_{T,\mathrm{min}}$, the total integrated cross section still diverges and reaches a value larger than the total pp cross section, which is why this lower limit on the minimum transverse momentum of the interaction is introduced to suppress all scatters below $p_{T,\mathrm{min}}$. This cut-off $p_{T,\mathrm{min}}$ is chosen to be reasonable small to have unbiased events with a realistic amount of soft activity in the event. The event generator PYTHIA uses an adjustable variable for this cut-off while HERWIG has an abrupt $p_{T,\mathrm{min}}$ cut-off.

The hard cross section σ_{hard} contributes only once to the total cross section σ_{tot} so that the

number of averaged parton-parton interactions $\langle n \rangle$ above $p_{T,\min}$ in an event is given by

$$\langle n \rangle = \frac{\sigma_{\text{hard}}}{\sigma_{\text{tot}}}. \tag{5.2}$$

MPI and UE are often used in the same context, although there is a difference between both terms. The UE is more generic than MPI and consists usually of MPIs, beam-beam remnants (BBR)[2], ISR and FSR. This gives a definition of the UE: all the activity which is not associated to the primary hard process. At high energies, MPIs are a predominant source of UE activities in the event, which is why MPI and UE are often used equivalently.

5.2 Monte Carlo generators

Monte Carlo generators cover all the discussed properties of MC event generation and simulate events in high-energy physics by factorising the whole event into these different steps (see Sec. 5.1). Many MC event generators are available: PYTHIA [140, 143], HERWIG [141, 142, 144], ALPGEN [152], SHERPA [153, 154], CASCADE [155], TAUOLA [156], ... These are partly multipurpose but also specialised generators that concentrate on particular event topologies and physics channels or on the treatment of properties not covered by multipurpose generators (e.g. spin correlation of particles). The two main multipurpose generators currently used in HEP are PYTHIA and HERWIG and are briefly discussed in this section. In parts of this thesis (e.g. analysis and tests with the HepMCAnalysis Tool, see Chap. 6), other generators are also used which will be therefore shortly mentioned in Sec. 5.2.3.

5.2.1 PYTHIA

PYTHIA is one of the most common used multipurpose generators for hadronic events in pp, e^+e^-, and ep colliders. It is available in two versions, PYTHIA6 [140] and PYTHIA8 [143]. PYTHIA8 is basically the C++ rewritten version of (Fortran) PYTHIA6, but not yet in the same state as PYTHIA6 with its functionalities and processes. PYTHIA6 covers the whole area of event generation and contains a large range of physics processes, initial and final state parton showers (ISR and FSR), underlying event, hadronisation, and particle decays.

A large physics area from QCD over Standard Model processes to SUSY and Exotics is covered with its several hundred implemented different $2 \to$ n subprocesses, most of them $2 \to 2$, but also some $2 \to 1$ and $2 \to 3$. A detailed list of the physics processes is given in the manual [140] and is summarised in [120]:

- QCD: $2 \to 2$ partonic scattering, heavy flavour, elastic and diffractive processes,
- Standard Model: $\gamma/\gamma^*/Z^0/W^\pm$ single or in pairs, or with a quark or gluon, Higgs,
- SUSY: two Higgs doublets, sfermion and gauginos pairs, R-parity-violating decays, and
- Exotics: Technicolor, new gauge boson, compositeness, leptoquarks, double charged Higgs bosons, extra dimensions.

The parton showers (ISR and FSR) are calculated space-like and time-like. ISR is based on backwards evolution in terms of a decreasing space-like virtuality Q^2 and also includes coherence

[2] Beam-beam remnants result from the hadronisation of the partonic constituents which did not participate in any scattering.

effects. For the calculation, the hard scattering process is chosen as the starting point from which one moves backwards in time to the shower initiators. Partons from ISR can cause FSR.

Final state radiaton is based on forward evolution in terms of a decreasing time-like virtuality m^2. Final state radiation is usually angular-ordered. The calculations are done in LO but also include NLO aspects, e.g. energy-momentum conservation, $\alpha_s\left(p_T^2\right)$, and coherence. Many other features like gluon polarisation effects and photon emission are also included.

Although ISR and FSR are calculated independently, they are finally matched to each other by maximum emission cones.

The UE in PYTHIA6 is described by perturbation theory including all constituents of the UE. The calculations are approximated by a set of separate $2 \to 2$ scatterings which are (colour-) connected with each other. The $p_{T,\min}$ cut-off is 2 GeV so that below this value, no interaction is allowed.

The hadronisation is simulated with the Lund string model which creates stable and unstable hadrons in the event generation. Finally, unstable hadrons decay corresponding to their branching ratios. If better decay models are available for certain particle decays, these decays can be assigned to specialised generators (e.g. TAUOLA [156] for τ lepton decays including spin information).

PYTHIA6 contains a lot of free parameters which have to be combined to describe the reality. Combinations of these parameters are summarised in so-called tunes which are introduced in Sec. 5.3.

5.2.2 HERWIG

HERWIG is another multipurpose generator and exists in two versions too, a Fortran and a C++ one, which is called HERWIG++. HERWIG++ is mainly the C++ rewritten version of Fortran HERWIG and will replace it. Except for bug fixes, there is no further support or development of Fortran HERWIG (in the following, HERWIG only).

HERWIG [141, 142] is a multipurpose generator for the simulation of hadron-hadron, lepton-hadron and lepton-lepton collisions including many hard scattering processes, angular-ordered parton shower, underlying event simulation, hadronisation, and hadron decays. As in PYTHIA, HERWIG contains a large library of hard $2 \to n$ scattering Standard Model and supersymmetric processes. It is partly specialised on the decay of unstable resonances. HERWIG covers this summarised list of physics process [120]:

- QCD: $2 \to 2$ scattering processes including heavy flavour production,
- Electroweak: $\gamma/\gamma^*/Z^0/W^\pm/H^0$ single or pair production; often with additional hard jets,
- SUSY: large range of MSSM production processes in hadron-hadron and lepton-lepton collisions including Higgs production; the option of R-parity violating decays and hard production processes, and
- Exotics: new gauge boson and resonant graviton production.

HERWIG is also interfaced to TAUOLA to handle the correct polarisation in the τ lepton decay. Furthermore, additional processes can be added by using the Les Houches Accord (LHA) event record [157].

HERWIG uses an angular-ordered shower for both ISR and FSR which is related on a coherent branching algorithm. Leading soft and collinear singularities are considered as well as azimuthal

corrections due to spin effects in the parton shower and the dead-cone effect for radiation from massive quarks.

The UE in HERWIG is based on the minimum bias $p\overline{p}$ generator of the UA5 Collaboration [158] which is modified for using the cluster fragmentation algorithm. HERWIG is also interfaced to JIMMY [159, 160] for a better simulation of multiple scattering in the UE.

HERWIG uses the cluster fragmentation model based on colour preconfinement properties of the angular-ordered shower as hadronisation (see Sec. 5.1.3). High mass clusters split into lower mass clusters with a string-like mechanism which decay into observed hadrons. The unstable hadrons decay into stable particles according to their branching ratios and phase space.

HERWIG++ [144] is a multipurpose generator based on the experience of Fortran HERWIG rewritten completely in C++. HERWIG++ depends on the Toolkit for High Energy Physics Event Generation (ThePEG) [161] and the Class Library for High Energy Physics (CLHEP) [162]. Its goal is that it has a greater flexibility, generality, and ease of maintenance in their improved capabilities like the angular-ordered parton shower and the cluster fragmentation model as well as correlation features (e.g. polarisation) than HERWIG. But in principle its main functionality is the same as in HERWIG. The processes are mainly LO, but there are also some NLO processes in HERWIG++. The main difference in the parton shower is the use of new evolution variables to describe radiation from heavy quarks as well as from light partons. The improvement for the hadronisation amounts to a new cluster fragmentation model developed for HERWIG++. The flavour selection in cluster decays changed. The probability of choosing a given light hadron is not lowered anymore if heavier states are added to the particle tables. Additionally, the meson and baryon sectors are dealt with independently [144]. Models of hadron and τ lepton decays are included so that there is no need to use external packages. These decays are simulated by using matrix elements including momentas of decay products, spin correlations etc. . Finally, HERWIG++ also contains UE models which rely only on a small number of parameters to simulate the MPI.

5.2.3 Other MC generators

There is a multiplicity of other MC generators, multipurpose but also a lot of specialised generators which are in use with one of the multipurpose generators. Some of them used in parts of this thesis are briefly mentioned here and described in detail in the references.

AcerMC

The AcerMC MC generator [163, 164] is a special MC generator for the generation of Standard Model background processes in proton-proton collisions at the LHC. It contains mainly W and Z/γ^* as well as top and bottom quark production and their combinations. AcerMC provides a library of the massive matrix elements and phase space modules for the generation of the implemented processes. After the calculation of the hard process, AcerMC has to be interfaced to another generator, e.g. PYTHIA or HERWIG, for the simulation of the parton shower, the hadronisation and the decay of particles. It is also possible to interface AcerMC to other specialised generators like TAUOLA or PHOTOS for the simulation of complex particle decays.

ALPGEN

ALPGEN [152] is designed for Standard Model processes in hadronic collisions. The focus of the generated events lies on final states with high jet multiplicities. Partonic matrix elements are

calculated in an exact leading order evaluation. There is the possibility to generate events in a weighted and an unweighted mode, and to define user analysis cuts and distributions. Running ALPGEN in the weighted mode is for instance useful for high-statistics parton-level studies, while events in the unweighted mode can be passed to other generators to process the parton shower and hadronisation. For this, default interfaces for PYTHIA and HERWIG are provided. ALPGEN, like almost all other generators, allows the use of LHAPDF [165] for different parton distribution functions.

CASCADE

CASCADE [155] is a full hadron level MC generator for small x processes in ep, γp, $p\overline{p}$ and pp collisions. It uses the CCFM evolution equations for the initial state radiation in a backward evolution approach for the hard scattering process. The angular-ordered initial state parton shower consists so far only of gluons. The final state parton shower uses the parton shower routine of PYTHIA, while the hadronisation can be done by any MC generator (e.g. HERWIG, PYTHIA) using the LHA event record.

CompHEP

CompHEP [166], a package written in C for evaluating Feynman diagrams, generates unweighted events including colour flow information. This package generates events with a high level of automation and integrates over multi-particle phase space. CompHEP does basically event calculations at leading order, but it allows partly NLO corrections like NLO tree level $2 \to N+1$ real emission corrections to $2 \to N$ processes, NLO structure functions, ... The generated events are provided in the LHA event record, so CompHEP is interfaced to PYTHIA and HERWIG and can easily be interfaced to other generators for the parton shower and hadronisation processes.

JIMMY

JIMMY [159, 160] is a package for HERWIG and HERWIG based generators. It should be linked to HERWIG (based) generators for a better description of multi parton scattered events, the design goal of JIMMY. It is possible to generate multi parton scattered events in hadron-hadron, hadron-photon and photon-photon events. The hard process taking place before has to be calculated with another generator like HERWIG, MC@NLO or others.

MC@NLO

MC@NLO [167] is a specialised MC generator which calculates the hard scattering process including the full next-to-leading order QCD corrections. Mass effects as well as spin correlations for the decay products are included in most of the processes. MC@NLO also gives a sensible description of multiple soft and collinear emissions. It is a standalone package writing an event file in the LHA event record for reading by general purpose showering and hadronisation code. MC@NLO has to be interfaced to a multipurpose generator, usually HERWIG, for simulating the parton shower and the hadronisation.

PHOTOS

PHOTOS [168, 169] is a package for the simulation of QED bremsstrahlung corrections. As with many other specialised generators, it is linked to multipurpose generators during event generation.

POWHEG

POWHEG [170–172] is an alternative to the MC@NLO generator. POWHEG calculates the hard process in NLO calculations and can be interfaced to various other parton shower generators by using the LHA event record. Leading order accuracy of the parton shower and NLO accuracy for the hard process are both supported.

SHERPA

SHERPA [153, 154] is a multipurpose event generator for hadron-hadron, lepton-hadron, lepton-lepton as well as lepton-photon and photon-photon collisions with focus on matrix element and parton shower merging with the CKKW method [173]. It is independently developed from PYTHIA and HERWIG and has all the necessary functionalities of a multipurpose generator. Interfaces to common event records like HepMC (see Sec. 6.1) are included.

TAUOLA

TAUOLA [156] is a dedicated package for the generation of τ lepton decays including spin polarisation and can be interfaced in several generators. For each decay mode, there is an individual phase space generator, a part describing the weak current (including first order QED corrections for leptonic decays, tau neutrino mass, ...), a part describing the hadronic current, and a part which is responsible for the choice of the τ lepton decay mode and the overall administration. It is recommended that it should be used in combination with PHOTOS.

5.3 Tuning of Monte Carlo generators

Monte Carlo generators (respectively MC simulations) are based on perturbative calculations as well as on phenomenological models and depend on a large number of different models (see Sec. 5.1 and 5.2). Therefore, they have a number of free parameters for the settings to be changed. While the perturbative part (e.g. the hard process) is calculated quite similarly, there could be larger differences in the non-perturbative parts. The latter part can be adjusted with a large number of free tunable parameters to agree with experimental data. A set of such tunable parameters is called a tune and differs often in its choice of flavour, fragmentation and UE properties. Underlying event tunes, for example, often include specifications on the $\sqrt{s}$-energy and the $p_{T,\min}$ cut-off, possible momentum correlations, parton showering, MPI model, and choice of PDFs. But it is also possible to tune other parameters like the scaling of α_s. A choice has to be made between a model with many free tunable parameters and a model with only a few but more physically affected parameters. Models with many parameters are sometimes difficult to handle due to the multiplicity of parameter settings. Non-physical parameters are also often included in these descriptions, for which reason models with only a few free tunable parameters have a deeper physical specification but less flexibility. In the following, two examples

parameter	PYTHIA6 setting	range used
scaling of α_s	PARP(64)	$0.5 - 2.0$
$p_{T,\text{min}}$ cut-off	PARP(62)	$0.5 - 2.5\,\text{GeV}$
intrinsic momentum	PARP(91)	$0.5 - 4.0\,\text{GeV}$
intrinsic momentum maximum cut-off	PARP(93)	$5.0 - 20.0\,\text{GeV}$

Table 5.1: Settings used for parameter variations [174].

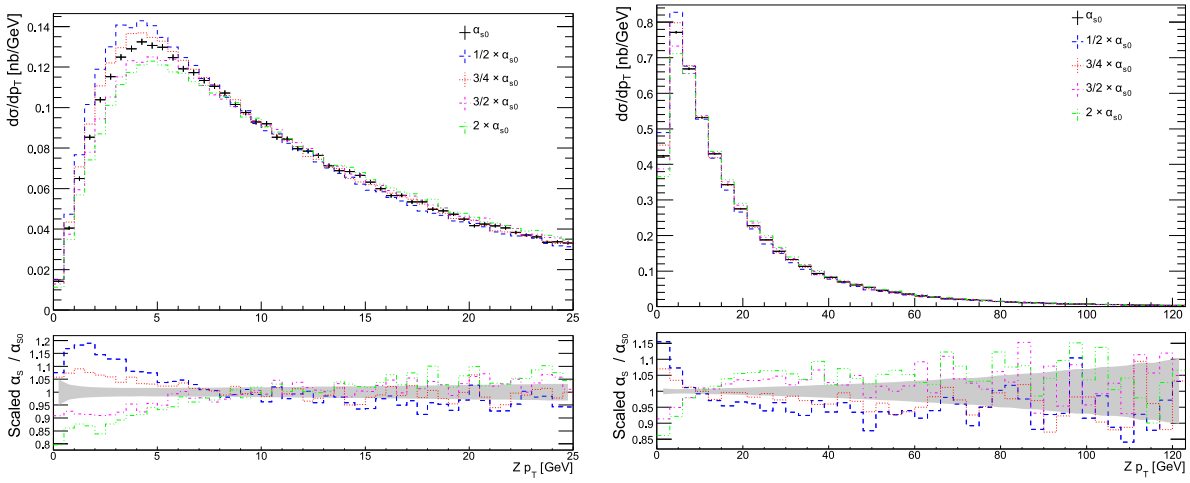

(a) (b)

Figure 5.2: Z boson p_T distribution normalised to the differential cross section for the scaling of α_s for (a) below 25 GeV and (b) up to 120 GeV [174].

of tunable parameters are given [174].[3] In this study, 300 000 single Z boson events are generated with PYTHIA6.4 and CTEQ6L1 [175] as PDF set. The parameters, which are varied, are given in Tab. 5.1. Two of them, the scaling of α_s and the $p_{T,\text{min}}$ cut-off, are chosen here for demonstration.

The variation of the strong coupling constant α_s results in a change of the transverse momentum of the Z boson for low and high transverse momenta as shown in Fig. 5.2. The changes are quite significant and add up to an overall effect of around $\pm 5\%$ mainly for high, and up to $\pm 20\%$ for low transverse momenta.

Varying the $p_{T,\text{min}}$ cut-off has an effect on the overall cross section of the event. Table 5.2 illustrates that for an increase of $p_{T,\text{min}}$ the cross sections decreases, resulting in a reduction of the number of events. Although the cross sections differ slightly, the distributions of the Z boson transverse momentum does not show significant effects (see Fig. 5.3). The shapes look similar in the weighted distributions and overall reduction of the events is adumbrated.

There are several tunes, for example the AMBT1 [176], DW [177], Perugia2010 [178], and AUET1 [179] tunes. The AMBT1 and AUET1 tunes are new tunes created with ATLAS data

[3] This study was performed in collaboration with Adam Bailey who worked as a summer student at the DESY ATLAS group in summer 2011.

PARP(62)	σ [nb]
0.5	5.041
1.0	5.026
1.5	5.031
2.0	4.950
2.5	4.872

Table 5.2: Cross sections for ISR $p_{T,\mathrm{min}}$ cut-off [174].

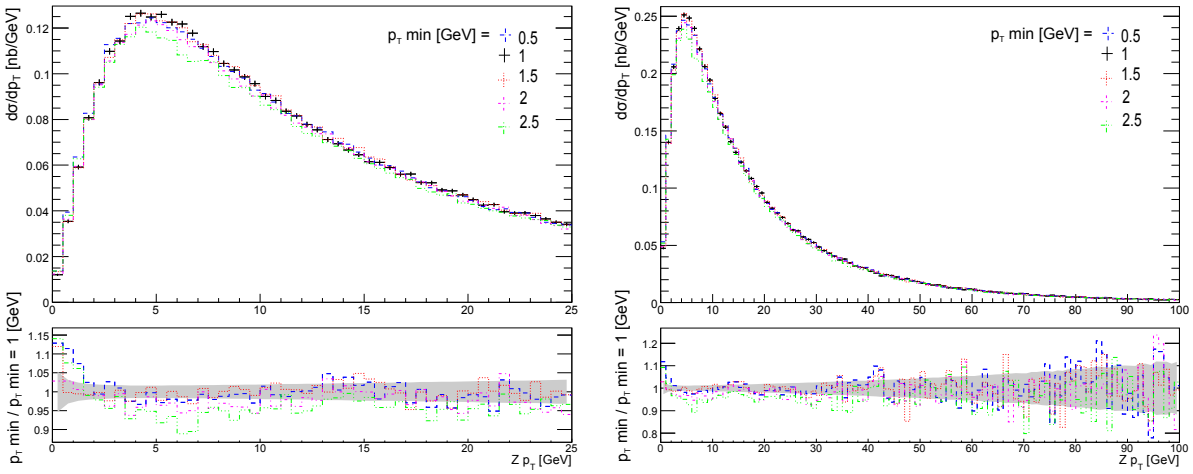

(a) (b)

Figure 5.3: Z boson p_T distribution normalised to the differential cross section for different ISR $p_{T,\mathrm{min}}$ cut-off values for (a) below 25 GeV and (b) up to 120 GeV [174].

only, while in DW and Perugia2010, Tevatron data is implemented. The DW tune is a Q^2-ordered tune with more MPIs and a wider shower than only p_T-ordered tunes and shows better agreement with data. The Perugia2010 tune is a further development of the Perugia0 tune [178] with the amount of final state radiation outside resonance decays increased to agree with the level inside them. Additionally, it should improve the jet shapes description. AMBT1 and AUET1 are p_T-ordered shower tunes and used in different generators, AMBT1 for PYTHIA and AUET1 for all HERWIG/JIMMY based generators. The major benefit of these tunes is a better description of the MPI up to very low transverse momenta.

At ATLAS, the PROFESSOR tool [180], which is based on an interpolation of the generator response in each bin of the distributions considered for tuning is often used for the development of new tools. Figure 5.4 shows the η distribution of charged particles of the AMBT1 tune evaluated with PROFESSOR. The RIVET package [181] is used for data MC comparisons in these distributions.

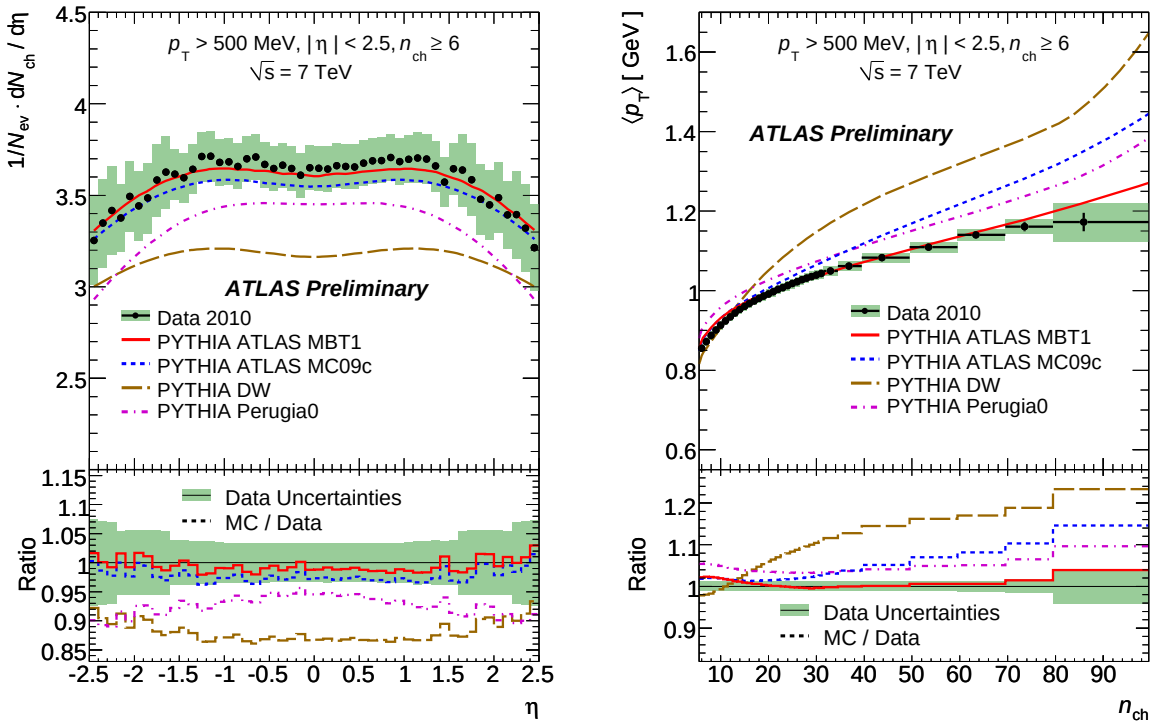

(a) (b)

Figure 5.4: ATLAS minimum bias distributions: (a) η of charged particles and (b) number of charged particles n_{ch} at 7 TeV with $n_{ch} \geq 6$ compared to the new tune AMBT1 (red solid line), the MC09c tune (blue dashed line), Perugia0 tune (magenta dash-dotted line) and DW tune (brown long dashed line) [176].

6 The HepMCAnalysis Tool

Monte Carlo (MC) generators use their own internal event record and convert it to a standard format at the end. Newer generators for high-energy physics (HEP) use the HepMC event record.[1] A framework to analyse the output of all the different MC generators generator independently is given by the HepMCAnalysis Tool.

After a short introduction of the HepMC event record, the HepMCAnalysis Tool and its wide range of applications is described.

6.1 HepMC event record

With the introduction of object oriented (OO) computing and programming in the high-energy physics (HEP) community, an object oriented event record was needed. So, the HepMC event record [109, 110] has been developed to replace (and also extend) HEPEVT [182] which is the HEP standard for HEP software and MC generators written in Fortran.

This object oriented HepMC format, written in C++, can be used for all HEP Monte Carlo generators independently of the generator. It gives a simple and easy access to the event information. In this event record, the whole physics event (from the hard scattering process over showering, hadronisation etc. to particle decay, see Sec. 5.1) is stored in container classes.

Figure 6.1 visualises the graph structure of the HepMC event record. On the left side, a physics event is shown including the parton distribution functions, the hard subprocess, parton cascades, hadronisation and decay of originated particles. The right side shows the same event in the HepMC event record where the points represent vertices implemented in a Vertex class and the arrows represent the particles implemented in a particle class. The connection between particles and vertices shown in the picture as connected lines are implemented as pointers in the corresponding classes.

So, the HepMC event record structures the event into containers, particles, and vertices. The fundamental unit is a HepMC event container class with particles and vertices. The particle class stores information on its Lorentz vector (thus the four momentum), flow and polarisation information, particle identification (ID)[2] and status information, as well as the above mentioned pointers to its production and end vertex. It is common standard to fill at least all final state particles of the event into the event record by using the particles status information (status code). It is differed in status codes of 1 and 2 for (stable) final state particles and decaying particles like the τ lepton, and status codes of 3 and larger for internal use of the generator. The last are so-called 'documentary' particles and usually exist as intermediate states during the event generation. Each particle belongs at least to one vertex. The pointers provide an access to the different particles and their relations whereby the pointers can only be set from the vertex. A vertex is a node between two particles in this graph structure (see Fig. 6.1), which comprehends with a list of the incoming and outgoing particles, its position (in terms of a

[1] There was already the HEPEVT [182], a standard for HEP software written in Fortran during the Fortran time.

[2] The conventions of the Particle Data Group (PDG) [12, 183] is used for particle identification in the HepMC event record.

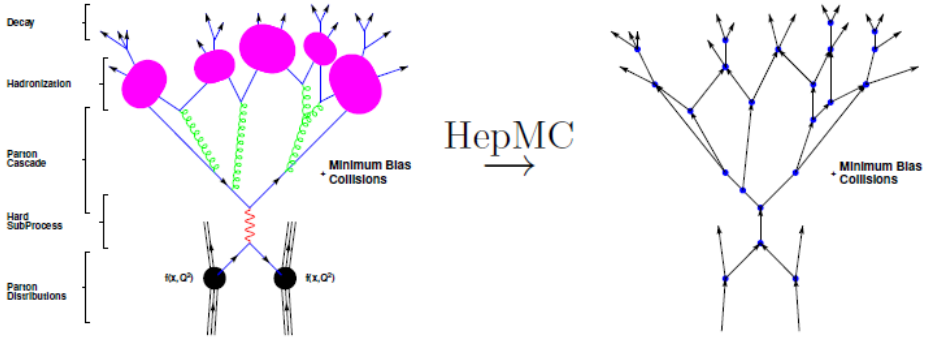

Figure 6.1: Visualisation of the collision of a physics event (left) and the concerning graph structure with edges and nodes in the HepMC event record (right) [110].

Lorentz vector), as well as a vertex identifier. In addition, there is a container of weights for each vertex with additional information belonging to the vertex like colour flow and/or helicity (spin density matrices). All vertices of an event are stored in a container of (all) vertices (belonging to this event). As an additional option, a pointer to the primary vertex can be saved in this container. And furthermore, there is the possibility to store a process ID, if many processes are generated in the same job, and to extend it with features like event weights and states of random number generators. Iterators are provided to access the vertices and particles in the event record.

6.2 HepMCAnalysis Tool - structure and design

The HepMCAnalysis Tool is a framework, which uses the HepMC event record, to validate MC generators and perform MC generator studies. The HepMCAnalysis Tool is published in [184] and has been presented in several talks. Further information can also be found on the tool's webpage at [185].

The idea of the development of the HepMCAnalysis Tool is to have a framework with minimal dependencies on other packages which allows an easy acces to generator level information in the HepMC event record in a generator independent way. This already defines the design goals of the HepMCAnalysis Tool

- robustness: minimal dependencies on other software packages and a minimal framework,
- simplicity: easy understandable code, written in C++, and
- scalability: easy extendable for user analysis or other applications.

Thereby, analysing events with the HepMCAnalysis Tool covers the various aspects of event generation like hard process, parton shower, multi parton interaction/underlying event and hadronisation and furthermore different physics procceses like $pp \to t\bar{t}$, $pp \to Z \to \tau\tau$, $pp \to$ Jets, $pp \to W/Z$ (+Jets) and many other. It is available on [185] but also pre-installed in Genser (Generator Services Project) [121][3].

[3]Genser is a part of the already mentioned LHC Computing Grid Project [117] and provides a large number

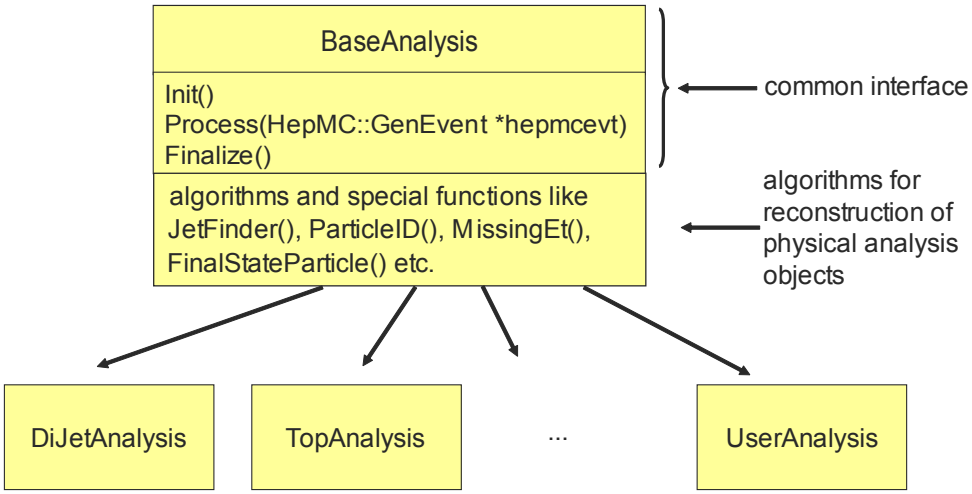

Figure 6.2: Class library structure of the HepMCAnalysis Tool.

The framework provide all the different parts which are needed for an analysis of MC generator predictions

- the HepMCAnalysis class library, which only depends on ROOT [116], the HepMC event record, and FastJet [186], with different physics analyses,
- a software environment to run and analyse MC generators with setup scripts, Makefiles, links to the MC generator software with parton distribution functions (PDFs), the HepMC event record, and ROOT, in an executable main program,
- steering files for different generators and their settings, and
- scripts for a web display and for comparisons of the output.

The technical implementation of the tool is summarised in Fig. 6.2 for the class structure of the physics libraries and in Fig. 6.3 for the workflow of the tool.

6.2.1 The class library

The class library with the different physics analysis classes is shown in Fig. 6.2. A baseAnalysis class is given which defines a common interface with functions like Init() for the initialisation of histograms and other values, a Process() function, in which the physics event is analysed and the results are filled into histograms, and a Finalize() function for final calculations and the write-out of histograms into ROOT files. Furthermore, there are some special algorithms for jet finding (FastJet is interfaced for this), particle identification, missing energy calculations, algorithms for identifying of final state particles and many others. All the different physics classes inherit all the functions of the baseAnalysis class which can be modified for the individual physics analysis. Also other functions can be added in these classes. Currently these physics classes are implemented:

of centrally installed MC generators as libraries and source code in the afs file system. Furthermore, Genser provides libraries for HepMC and FastJet too. Also libraries of the HepMCAnalysis Tool are installed at Genser. Before the installation of the libraries, they are adequate tested by Genser. The Genser installations are used by the LHC experiments but also by theorists.

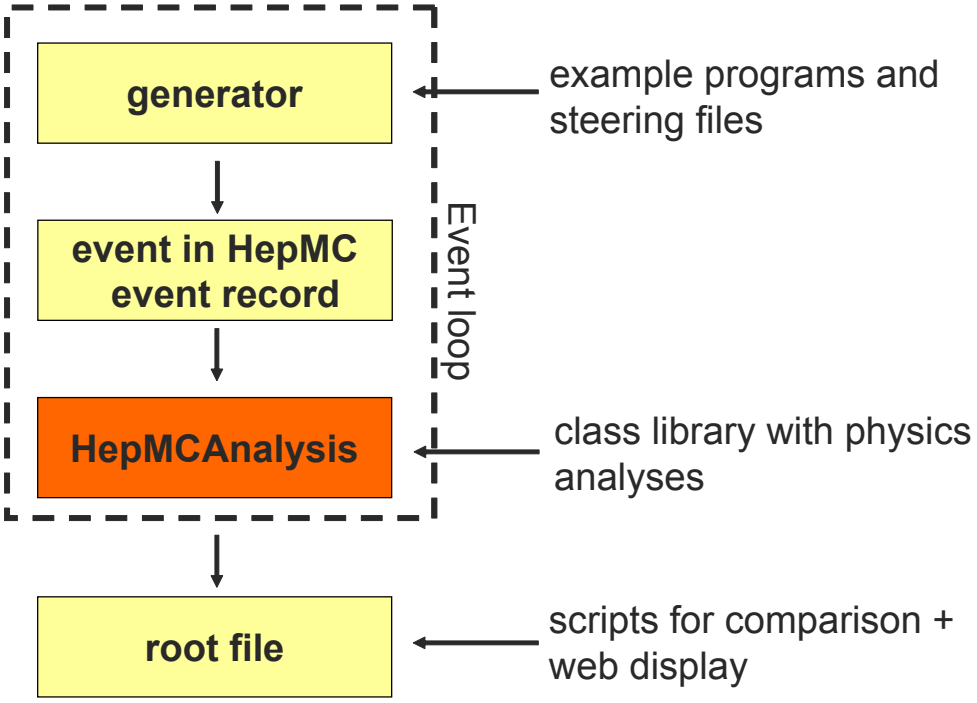

Figure 6.3: Workflow of the HepMCAnalysis Tool, events are generated with provided example programs and steering files, temporary stored in HepMC event record, and analysed with the HepMCAnalysis class library. After analysing all events, the results in form of histograms are written out to ROOT files which can be analysed and displayed with provided scripts for comparison and a web display.

- bbbarAnalysis for the analysis of $b\bar{b}$ events
- ElasScatAnalysis for the analysis of elastic scattered protons
- EtMissAnalysis for the analysis of missing energy
- JetAnalysis for the analysis of jet events
- ttbarAnalysis for $t\bar{t}$ events
- UEAnalysis for the analysis of the underlying event
- WplusJetAnalysis for the analysis of W + Jets events
- WtaunuAnalysis for $W \rightarrow \tau\nu_\tau$ events
- ZAnalysis for Z events
- ZtautauAnalysis for $Z \rightarrow \tau\tau$ events
- UserAnalysis for the individual analysis

As it can be seen, there is also a UserAnalysis in which the own analysis can easily be implemented. All the different physics analysis classes can be used modularly independently

from the physics process.

6.2.2 Event generation of MC events

Example programs (including steering files for the settings of the physics events and MC generator specific functions for configuration, initialisation and event generation) for the event generation are provided for different MC generators (so far PYTHIA6 [140], PYTHIA8 [143], HERWIG [141, 142], HERWIG++ [144], CASCADE [155] and ALPGEN [152]). Furthermore there is one example program to read in HepMC files. Following the design goals, the tool uses per default centrally installed MC generators from Genser. However, it is also possible to use locally installed generators by changing the setup scripts.

The HepMCAnalysis Tool provides homogenous configuration mechanisms and steerings for all supported generators. A so called 'Configuration' class reads a global configuration file (e.g. Process.config), which is illustrated in Fig. 6.4, and includes the following information:

- configuration file for the generator with information of the physics process, PDF sets, center-of-mass energy etc.
- switches on/off for the analysis classes and the analysis class parameter settings
- global settings as number of events to be generated, ROOT output filename, jet parameters etc.

The individual generator parameters are written in separate configuration files[4] which are loaded in an other configuration file. It is also possible to specify a list of generator configuration files, which are read in one after the other. The whole configuration (the global as well as the generator settings) is interpreted line by line.

Figure 6.3 illustrates the workflow of the HepMCAnalysis Tool. The generated event (of the example program) is stored in memory in the HepMC event record for further analysis. Afterwards the HepMCAnalysis library is called to analyse the event and to write the output into histograms provided by ROOT. These steps are done event by event. The event is generated, temporary stored in HepMC event record and analysed with the HepMCAnalysis class library. The advantage of this procedure is that there is no need to save the event in HepMC format on disc. In this way one can save a lot of disc space. The file size of events saved in the HepMC event record is quite large to store all the different information (60.5 Mbytes for 1 000 $pp \to W\gamma$ events generated with PYTHIA6 [110]). But optionally, there is the possibility to store the events on disc. After running over all events when the event loop is finished, the results in form of histograms are ordered in different folders, which follow the different physics analyses that have been running, and are saved in ROOT files.

6.2.3 Check and display of the output

In order to have a fast access to the results, there are scripts for comparison and a web display inside the provided software of the HepMCAnalysis Tool. With these scripts, which are simple ROOT macros, the resulting ROOT files can be opened and histograms can be extracted. The

[4] The generator settings are different from generator to generator but can be interpreted in the HepMCAnalysis Tool with the style used in these separate configuration files. In the tool, there are examples for the steering and configuration of many physics processes for each supported generator.

```
# Nr of Events to be generated
nevents       100
# randomseed ...
# if no randomseed is specified time in seconds will be set
rseed         1234567

# The histograms will be saved into File
OutputFileName      Pythia6_test.root

# use the following Configuration files for the generator
# several may be specified
ConfigFileNames     configfiles/Pythia6_Common.config
ConfigFileNames     configfiles/Pythia6_PDF.config
ConfigFileNames     configfiles/Pythia6_ttbar.config

# enable Analysis to be performed
jet_analysis            true
z_analysis              false
wplusjet_analysis       false
ztautau_analysis        false
wtaunu_analysis         false
bbbar_analysis          true
ttbar_analysis          true
ue_analysis             false
etmiss_analysis         false
elasScat_analysis       false
user_analysis           true

# master switches for FSR, ISR and MI
# these switches are set in Pythia6_Common.config

# set Jet parameter
jet_coneRadius          0.4
jet_overlapThreshold    0.75
jet_ptmin               15.0
lepton_ptmin            15.0
DeltaR_lepton_track     0.4
max_eta                 2.5 # cut on tracks for jet finder
min_pt                  0.5 # cut on tracks for jet finder
```

Figure 6.4: Example of a configuration file of the HepMCAnalysis Tool for the generator PYTHIA6. This skeletal structure is the same for all supported generators.

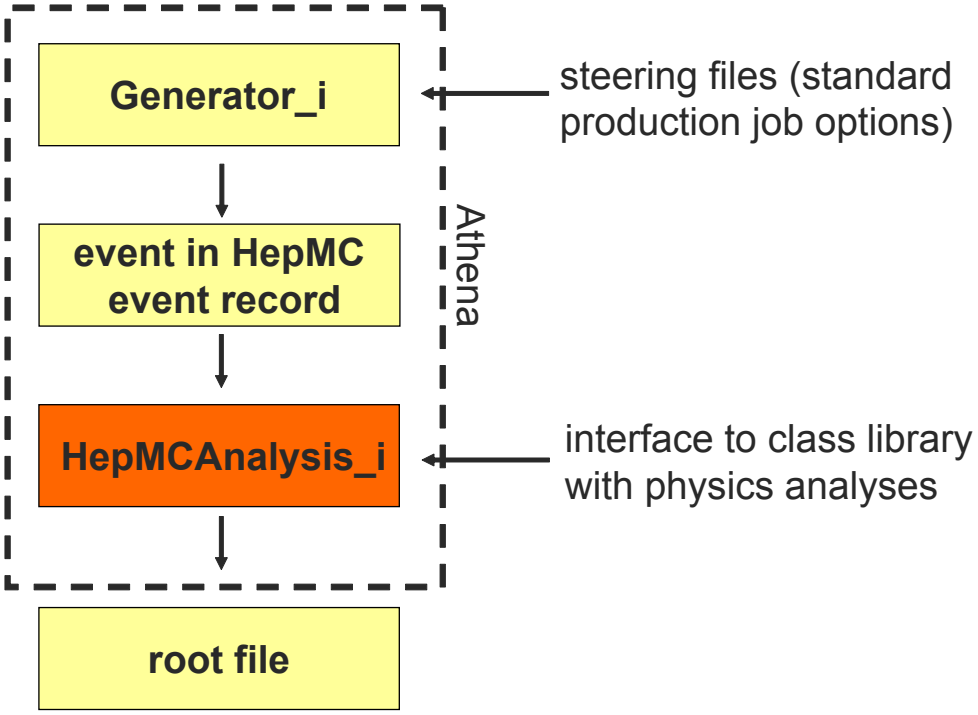

Figure 6.5: Athena interface of the HepMCAnalysis Tool.

same histograms from different input ROOT files can be extracted and displayed in one canvas, whereby the distribution are compared and performed with tests like Kolmogorov-Smirnoff- and χ^2-tests. Finally, image files with the results and statistics are created which can be summarised in automatically created webpages.

6.2.4 Interface to the ATLAS software framework Athena

The HepMCAnalysis Tool is also used by the ATLAS collaboration. The HepMCAnalysisInterface provides a skeleton for the analysis of existing evgen/EVNT files[5] or the generation of events within the ATLAS software framework Athena (see Sec. 4.2), the analysis of generator information with predefined analysis classes or a developped user analysis. It is implemented via a so called glue package[6], which links the interface to the installation of the HepMCAnalysis Tool in Genser, and an interface package[7], that defines the skeleton for the analysis, in Athena.

The principal functionality, visualised in Fig. 6.5, is the same as for the standalone HepMCAnalysis Tool. A detailed description for the interface can be found at [187]. Inside Athena, the interface of a MC generator generates events which are stored transiently as HepMC event record in memory. Alternatively, it is also possible to read in a HepMC event from file in evgen/EVNT format instead of running a generator. The stored event is analysed and the results filled in histograms via the HepMCAnalysis_i, the interface to the class library with the different physics analyses. Thereby, it is also possible to modify or create an own user analysis

[5]Generated events can be stored in these files in the HepMC event record.
[6]This external package can be found in External/AtlasHepMCAnalysis of the ATLAS software.
[7]This package can be found in Generators/HepMCAnalysis_i inside Athena.

inside Athena.[8] The event loop is done within Athena. After it, the histograms are written out inside Athena using the Athena histogram service THistSvc [188] to a ROOT file which can be used externally.

The settings and configurations for such a job are done within ATLAS configuration files, so-called job option files, (corresponding to the configuration files of the standalone HepMCAnalysis Tool) as it is usually done in Athena.

6.3 Application of the HepMCAnalysis Tool

The HepMCAnalysis Tool is in a wide range of use. Next to Monte Carlo schools [189, 190] of the Helmholtz Alliance 'Physics at the Terascale' [191] at DESY (Deutsches Elektronen-Synchrotron) [192], other workshops and validation tests on the HepMCAnalysis Tool webpage [185], it is also utilised for MC generator validation and regression tests in Genser and ATLAS as well as in generator level studies and preparations of analyses, and other applications. Hence it uses the above discussed generator independent HepMC event record, it is also possible to discriminate between bugs of MC generators due to the same analysis code which is used. A short extract of some applications is given here. In the following, $pp \to \mathrm{A} + \mathrm{X} \to l\nu_l\,(qq') + \mathrm{X}$ events are denoted as $pp \to \mathrm{A} \to l\nu_l\,(qq')$.

6.3.1 Histogram based validation in Genser

One of the applications of the HepMCAnalysis Tool is histogram based validation of MC generators in Genser [121]. Regression tests of several of the supported generators by Genser are done with the HepMCAnalysis Tool for a histogram based validation. Figure 6.6 shows a screenshot [193] of a part of the histogram based validation in Genser with the HepMCAnalysis Tool. The layout of this webpage is a modified version of the scripts of the HepMCAnalysis Tool. It gives an overview of the whole analysis and it is possible to follow the whole analysis. There are links to the generator settings and the source code of the analysis.

Furthermore, it was discovered by this histogram based validation in Genser that there was a change in the event record for Z bosons of HERWIG++ 2.5.0 with respect to version 2.4.2 [194].

In addition, it is also planned that the HepMCAnalysis Tool runs in nightly tests for regression tests in Genser [195].

6.3.2 Regression tests in ATLAS

Another application for regression tests and tests on generator code changes and/or bugs is the use of the HepMCAnalysis Tool in nightly tests of ATLAS [196]. For this purpose test jobs of the ATLAS interface of the HepMCAnalysis Tool run in the RunTimeTester (RTT) [197], a framework used to test the ATLAS software, next to other test jobs of other packages. The test jobs of the HepMCAnalysis Tool are mainly Standard Model tests, which demonstrate the principal functionality of the software and the generator if the results are reasonable. Results can be found at the RTT homepage [198] or in the Figures 6.7, 6.8, 6.9, and 6.10 which show parts of

[8] To do so, one has to modify the files HepMCAnalysis_i/src/UserAnalysis.cxx and HepMCAnalysis_i/HepMCAnalysis_i/UserAnalysis.h and recompile.

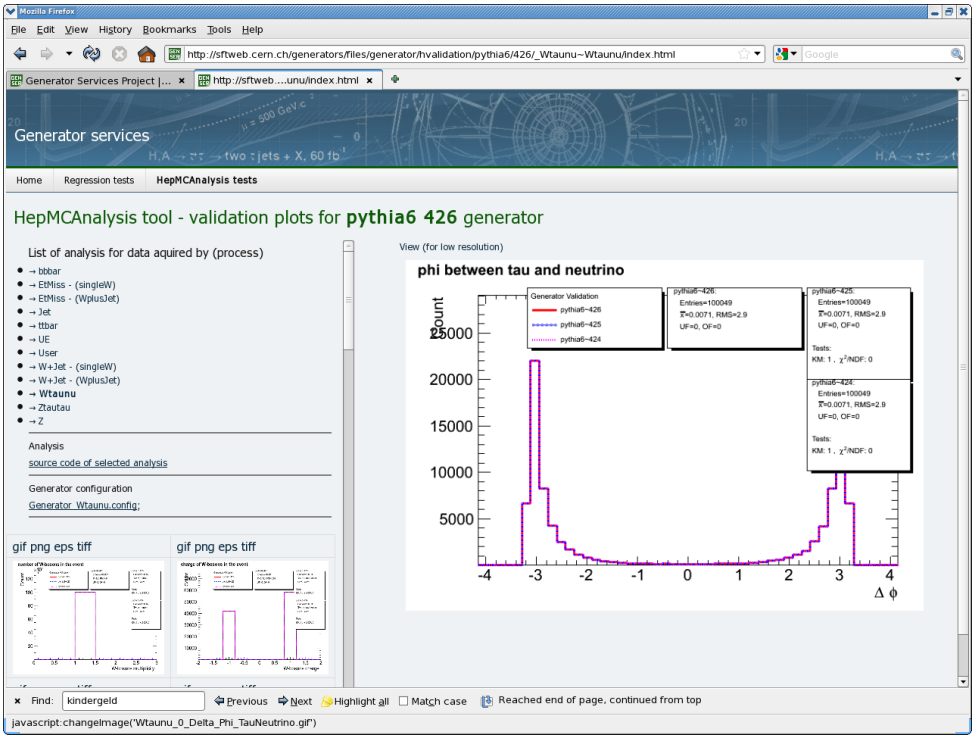

Figure 6.6: Screenshot of a part of the Genser webpage in which the histgram based validation with the HepMCAnalysis Tool is demonstrated [193]. The angle ϕ between a τ lepton and the corresponding ν_τ of $pp \to W \to \tau\nu_\tau$ events for the MC generator PYTHIA 6.4.26 is mapped in this histogram and shows a good agreement to previous generator versions. Furthermore, links to the generator configurations as well as the source code are available on this webpage.

the RTT homepage for test jobs of the Athena interface HepMCAnalysis_i of the HepMCAnalysis Tool.

To get to these results, one has to search for 'HepMCAnalysis_i' from the RTT start page [198]. Some of the running test jobs of the HepMCAnalysis interface are listed in Fig. 6.7 while in Fig. 6.8 one of these test jobs, $pp \to W \to \tau\nu_\tau$ events of the MC generator PYTHIA6, is chosen with many information like logfiles, job settings and output files. The graphical visualisation of the histograms in the resulting ROOT files is done via the DCube Service [199, 200]. Figure 6.9 illustrates the principal layout of this service of the above job already with a lot of information of folders and histograms in the ROOT files as well as tests which are done between the resulting ROOT file and a reference file. Finally, Fig. 6.10 demonstrates the plot view between the resulting and the reference file. It can be seen that there are no large differences between the two files which means that there have not been large changes (or bugs) in the ATLAS software from the version of 'today' and the version created by the reference ROOT file.

A major revision of the RTT is ongoing at the moment, which will change parts of the description.

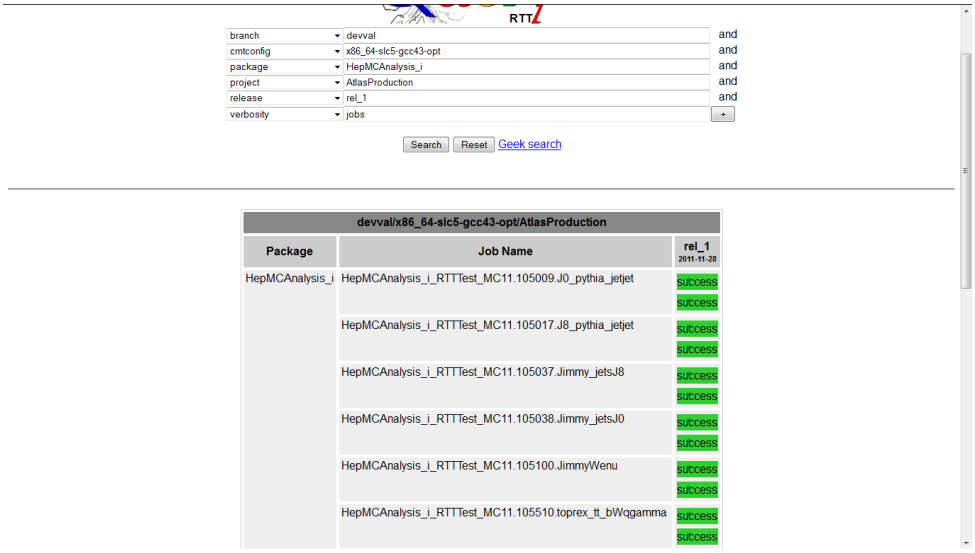

Figure 6.7: Screenshot of a part of the RTT homepage [198]. A list of test jobs for the HepMCAnalysis interface is illustrated.

Figure 6.8: Screenshot of a part of the RTT homepage [198]. Results of one of these test jobs for $pp \to W \to \tau\nu_\tau$ events of the MC generator PYTHIA6. A list of many files is shown. A graphical visualisation of this test job is done via the DCube Service [199, 200].

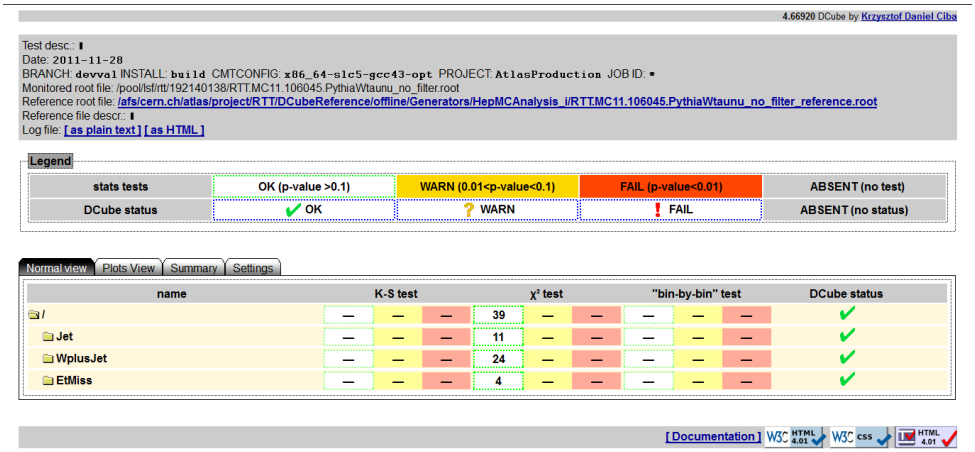

Figure 6.9: Screenshot of a part of the RTT homepage [198]. This part demonstrates an overview of the used DCube Service [199, 200] for illustrating the histograms of the ROOT files in comparison with reference files.

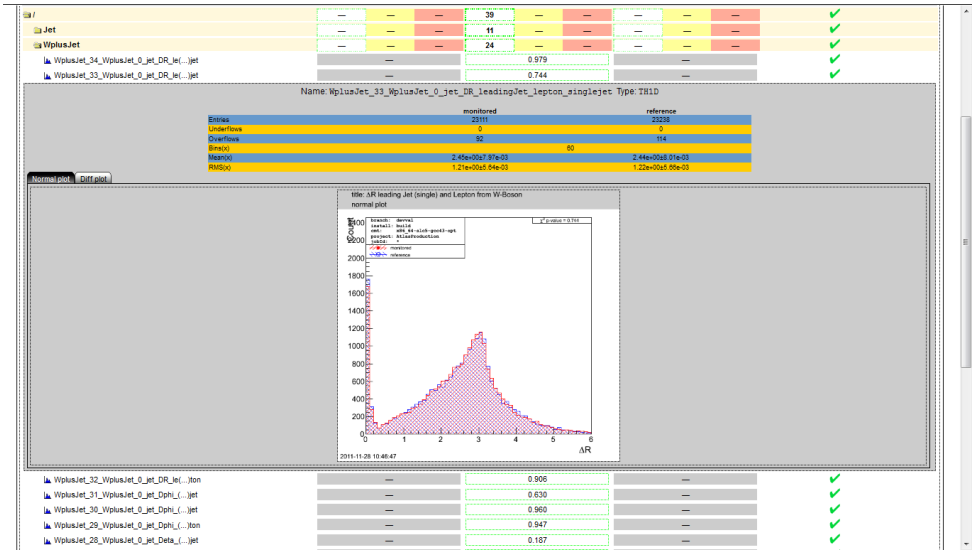

Figure 6.10: Screenshot of a part of the RTT homepage [198]. One of the resulting histograms are plotted in comparison with a reference file using the DCube Service [199, 200]. Different tests can be run like a Kolmogorov-Smirnoff-, a χ^2-, and/or a bin-by-bin-test. In this job, all tests are successful and there are no larger differences between the resulting ROOT file of the test job and the reference ROOT file. This means that there are no larger changes in the source code of the MC generator PYTHIA6 (concerning $pp \to W \to \tau\nu_\tau$ events).

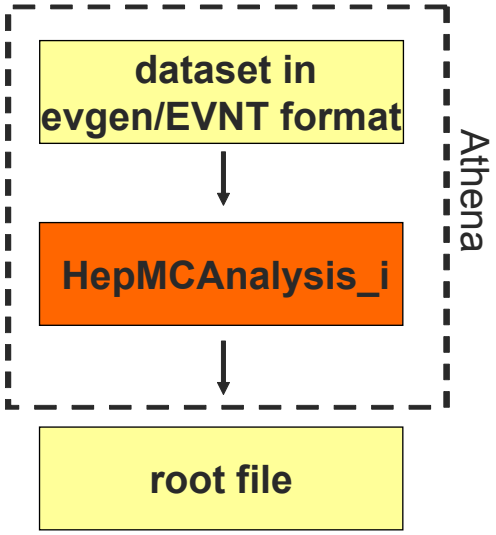

Figure 6.11: Read in of a dataset in evgen/EVNT format in the Athena interface of the HepMCAnalysis Tool for a so-called sample B validation of ATLAS.

6.3.3 Validation for ATLAS MC production

A validation has been done with the Athena interface of the HepMCAnalysis Tool. This so-called sample B validation was a test (in addition to expert checks) of the validity of MC generators and their production scripts of different MC samples for a central production for 2009 in ATLAS in comparison with the central production of 2008. The datasets which has been validated are summarised in Tab. 6.1. To analyse these datasets in evgen/EVNT format[9], the HepMCAnalysis interface has to read in dataset files in HepMC event record instead of running a generator (interface), see Fig. 6.11. The rest of the functionality is as described previously.

The results of the validation have been mainly presented online using the automatic web interface scripts[10], but parts of the validation are summarised in Figs. 6.12 and 6.13.

While there is a good agreement in the transverse momentum of the top and antitop quark in $pp \to t\bar{t}$ events for PYTHIA6 (Fig. 6.12(a)), differences can be observed in the ϕ distribution of stable particles (excluding neutrinos) (Fig. 6.12(b)) in these events. The underlying event has been improved from the 2008 (MC08) to the 2009 (MC09) MC central production. The distributions (ϕ of W boson, η of W boson, $\Delta\phi$ between top and antitop, number of jets) for $pp \to t\bar{t}$ events but with different generators in Figs. 6.12(c), 6.12(d), 6.12(e), and 6.12(f) show a good agreement and illustrate that there has not been larger changes in these issues, respectively bugs between the two central productions. For further processes and generators, the mass of the Z boson and the pseudorapidity η of the Z boson for $pp \to Z \to \mu\mu$ events of ALPGEN+JIMMY+HERWIG are given in Figs. 6.13(a) and 6.13(b). The transverse mass in $pp \to W \to e\nu_e$ events of JIMMY+HERWIG is given in Fig. 6.13(c). The pdg ID (particle data group identification number) of the lepton coming from the W boson decay in Fig. 6.13(d) illustrates nicely the asymmetry of W^+ and W^- boson production in proton-proton collisions due to the parton distribution functions and the valence quarks in the proton.

[9]This ATLAS term corresponds to the HepMC event record.
[10]The website is offline in the meantime.

Process	Generator	Dataset ID	Dataset Name (starting with mc08_valid./mc09_valid.)
$t\bar{t}$	PYTHIA6	108870	108870.f_pythia_val_ttbar.evgen.EVNT.e430_tid075883
$t\bar{t}$	MC@NLO+JIMMY+HERWIG	105200	105200.T1_McAtNlo_Jimmy.evgen.EVNT.e430_tid075877
$t\bar{t}$	POWHEG+JIMMY+HERWIG	105860	105860.TTbar_PowHeg_Jimmy.evgen.EVNT.e430_tid075876
$t\bar{t}$	AcerMC+PYTHIA6	105205	105205.AcerMCttbar.evgen.EVNT.e430_tid076765
$W \rightarrow e\nu_e$	JIMMY+HERWIG	105100	105100.JimmyWenu.evgen.EVNT.e430_tid075879
$W + 3$ Jets $\rightarrow \tau\nu_\tau + \mathrm{X}$	SHERPA	108859	108859.SherpaW3jetstotaunuQCD.evgen.EVNT.e430_tid076401
$Z \rightarrow \mu\mu$	ALPGEN+JIMMY+HERWIG	107663	107663.AlpgenJimmyZmumuNp3_pt20.evgen.EVNT.e430_tid075884

Table 6.1: List of datasets tested for the sample B validation in ATLAS in proton-proton collisions.

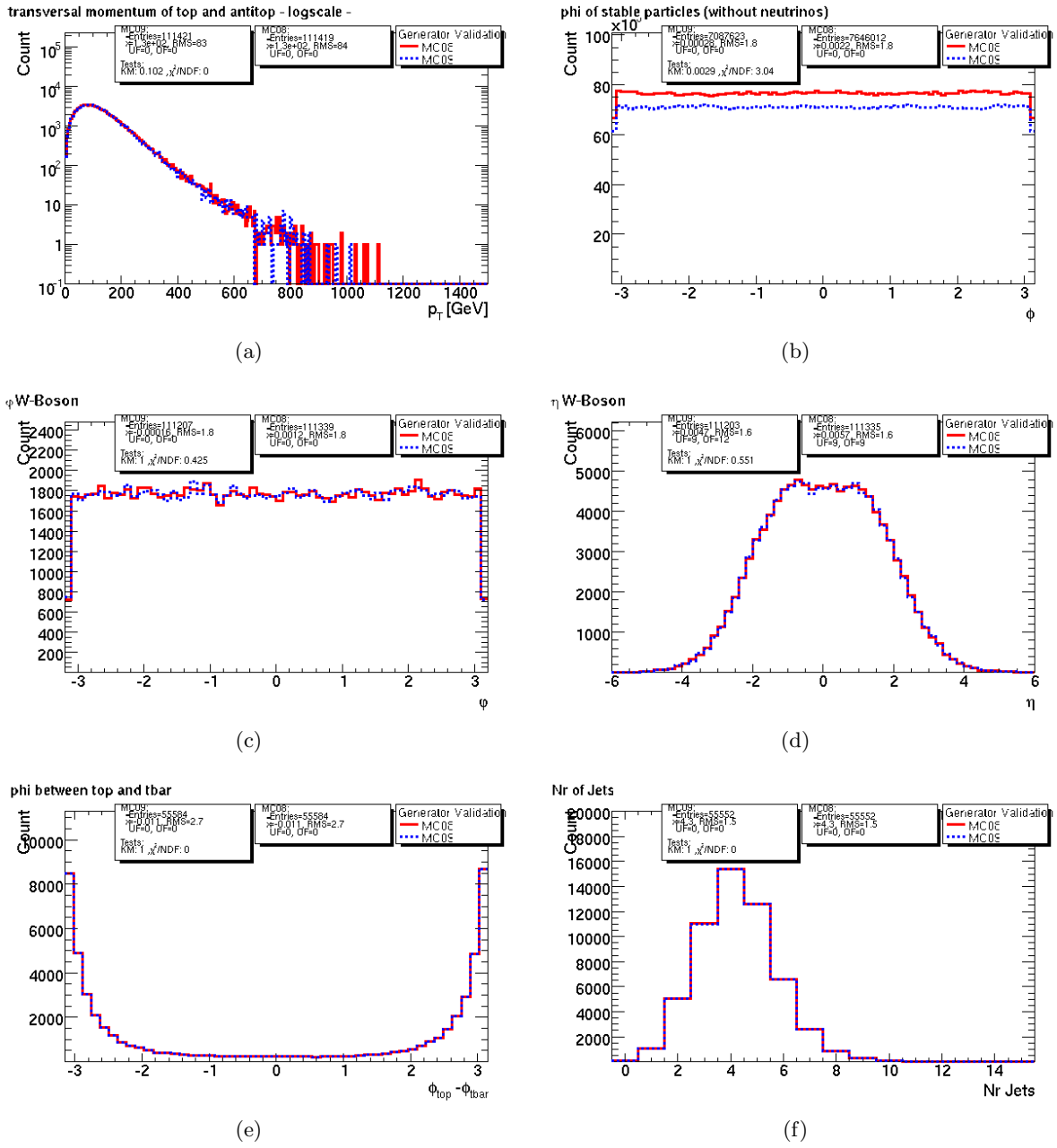

Figure 6.12: (a) Transverse momentum of the top and antitop quark in $pp \rightarrow t\bar{t}$ events of PYTHIA6, (b) angle ϕ of stable particles (excluding neutrinos) in $pp \rightarrow t\bar{t}$ events of PYTHIA6, (c) angle ϕ of the W boson coming from the top decay in $pp \rightarrow t\bar{t}$ events of POWHEG+JIMMY+HERWIG, (d) pseudorapidity η of the W boson coming from the top decay in $pp \rightarrow t\bar{t}$ events of POWHEG+JIMMY+HERWIG, (e) angle $\Delta\phi$ between the top and antitop quark in $pp \rightarrow t\bar{t}$ events of MC@NLO+JIMMY+HERWIG, and (f) number of jets coming from initial and final state radiation as well as from multi parton interaction in $pp \rightarrow t\bar{t}$ events of MC@NLO+JIMMY+HERWIG.

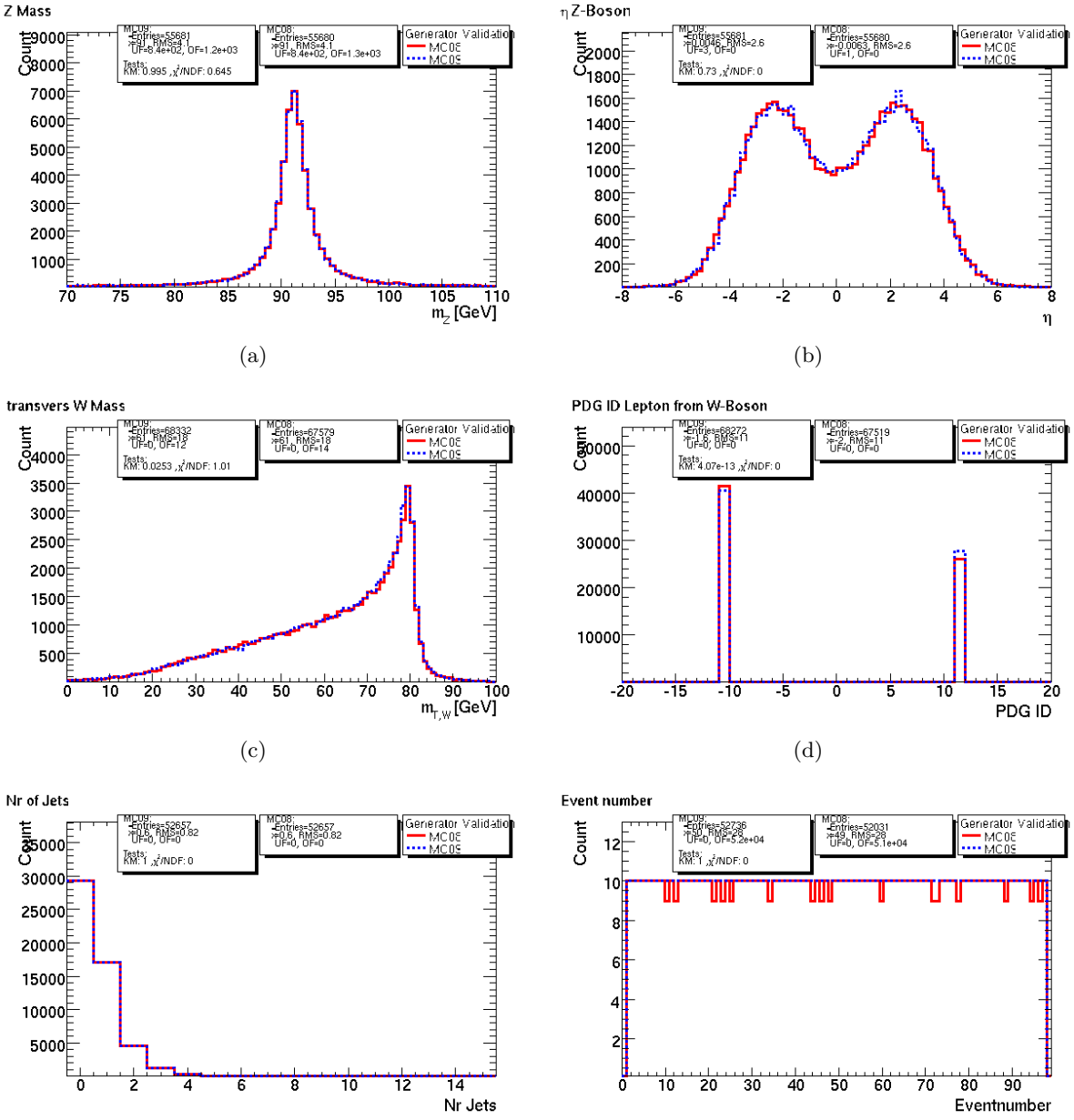

Figure 6.13: (a) Mass of the Z boson in $pp \to Z \to \mu\mu$ events of ALPGEN+JIMMY+HERWIG, (b) pseudorapidity η of the Z boson in $pp \to Z \to \mu\mu$ events of ALPGEN+JIMMY+HERWIG, (c) transverse mass of the W boson in $pp \to W \to e\nu_e$ events of JIMMY+HERWIG, (d) pdg ID of the lepton coming from the W boson decay in $pp \to W \to e\nu_e$ events of JIMMY+HERWIG, (e) number of jets in $pp \to W + 3$ jets $\to \tau\nu_\tau +$ X events of SHERPA, and (f) event number $pp \to t\bar{t}$ events of AcerMC+PYTHIA6.

Although good agreements are demonstrated so far for the sample B validation, the sense of it is to test the general functionality and validity of MC generator and production scripts for a central MC production. While the number of jets in $pp \to W + 3\text{jets} \to \tau\nu_\tau + \text{X}$ events of SHERPA in Fig. 6.13(e) still show a good agreement, discrepancies in the number of events in $pp \to t\bar{t}$ events of AcerMC+PYTHIA6 can be observed in Fig. 6.13(f). During the validation it could be figured out in time that there were empty events in the dataset which were skipped during the generation. These 'broken' datasets could be corrected before the central production started.

6.3.4 Further studies

Next to regression and validation tests, the HepMCAnalysis Tool is also a good framework for fast checks and tests as well as for physics studies. For instance, it is often used as a first check for a version change of generator or other packages like LHAPDF [165] if obvious differences can be expected or not.
There are also a few more studies which have been done with the HepMCAnalysis Tool. It is also possible to use it for fast analysis checks. For closing this chapter, three of them are presented here.

PDF study

A PDF study introduced here was done in reference to [201] for a better understanding of so-called modified leading order parton distribution functions (modLO PDFs). Modified LO PDFs are special developed PDFs for LO MC generators to reach as close as possible the NLO (next-to-leading order) distributions. These new PDFs are achieved by relaxing the momentum conservation and allowing NLO couplings in the fit which results in an increased gluon density at low x and a total momentum carried by the input partons of round 113% [201]. For this study 100 000 $pp \to W \to \mu\nu_\mu$ events have been generated with PYTHIA6 and CTEQ6L1 [175] and mLOMRST/MRST2007lomod [201] as PDF sets. In the reference [201] HERWIG/CompHEP [166] with the PDF sets MRST2001LO [202] and MRSTLO*/MRST2007lomod have been used. The corresponding cross sections are 17.25 nb for CTEQ6L1 (17.5 nb in [201]) and 19.37 nb for MRST2007lomod (20.6 nb in [201]).

The idea of the modified leading order PDFs studied in [201] could be confirmed in this analysis. As an example, Fig. 6.14 shows the rapidity distribution normalised to the cross section of the W boson in $pp \to W \to \mu\nu_\mu$ events. The distributions for the LO PDF (CTEQ6L1) as well as for the modLO PDF (MRST2007lomod) agree quite well with the corresponding ones in [201].

In addition to [201], jets coming from the parton shower could be ovserved (Fig. 6.15) which are produced due to initial state radiation (ISR) and multi parton interaction (MPI) (see below).

Furthermore, this study with the above PDFs has been done also for other generation processes which could also confirm the results found in [201] and the idea of modLO PDFs. Control histograms and further histograms can be found in Chap. A.

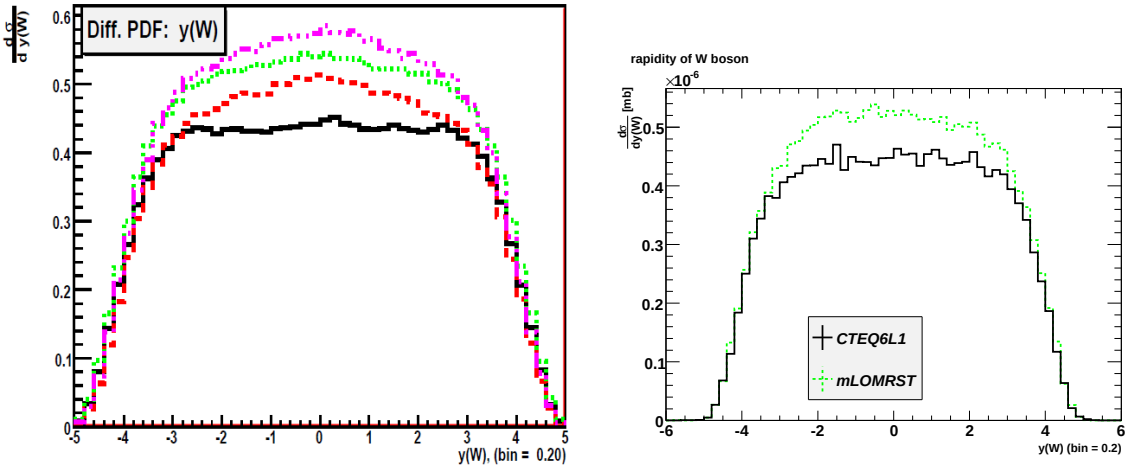

(a) (b)

Figure 6.14: Rapidity of the W boson in $pp \to W \to \mu\nu_\mu$ events in (a) [201] and (b) this thesis normalised to the cross section. The LO distribution is in black, modLO in green, and NLO in violett in [201]. The rapidity distribution could be confirmed.

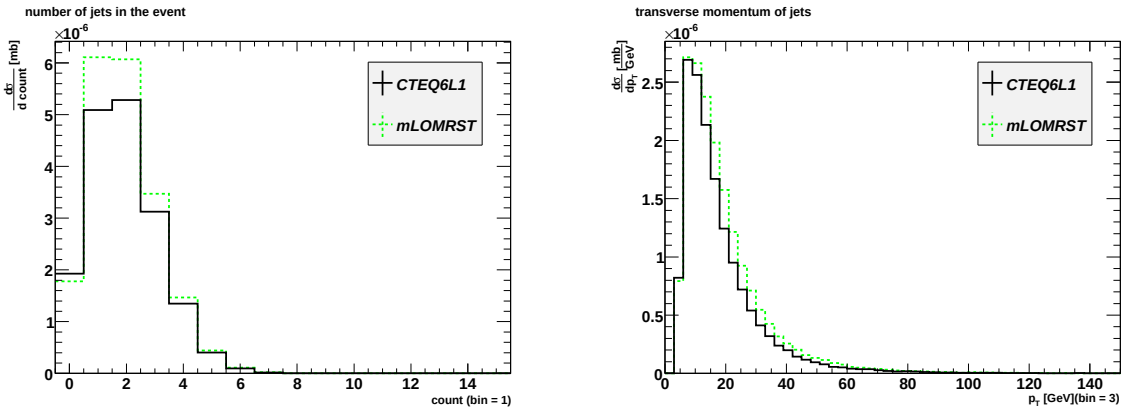

(a) (b)

Figure 6.15: (a) Number of jets and (b) the transverse momentum of jets in $pp \to W \to \mu\nu_\mu$ events normalised to the cross section; more jets with higher p_T are produced for modLO PDF generated events.

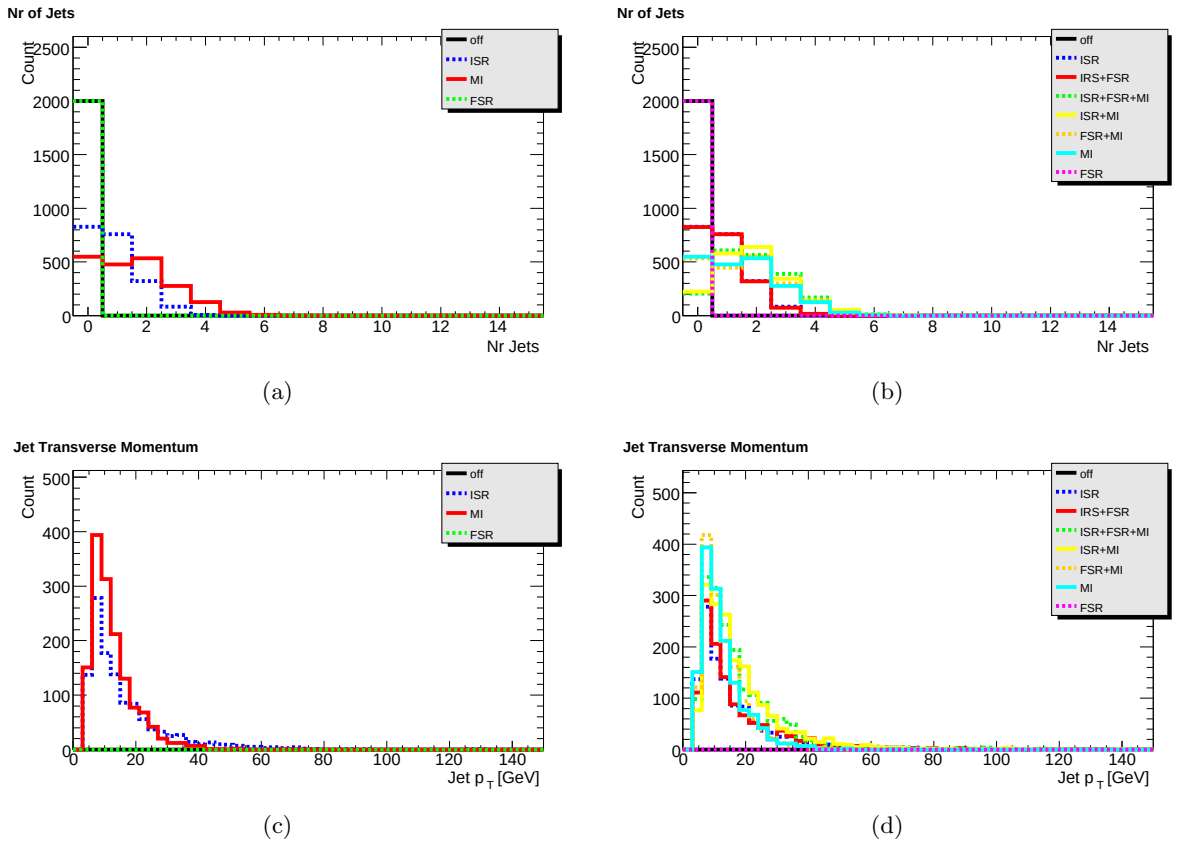

Figure 6.16: (a) and (b) Number of jets and (c) and (d) the transverse momentum of jets for ISR, FSR, MPI, and without ISR/FSR/MPI each on the left side and for all combinations on the right side.

ISR, FSR and MPI

The aim of this study was to figure out, where jets in $pp \to W \to l\nu_l$ events come from. This question came up during the above PDF study. It was assumed that they come from initial (ISR) and final (FSR) state radiation as well as from multi parton interaction (MPI). 2 000 PYTHIA6 $pp \to W \to l\nu_l$ events with the same setup as in the above PDF study but only for CTEQ6L1 as PDF set have been generated for this purpose. Initial and final state radiation as well as multi parton interaction have been simulated by switching ISR, FSR, and MPI in the settings of PYTHIA6 on and off.

A summary can be seen in Fig. 6.16. The number of jets as well as the transverse momentum of the jets are shown for ISR, FSR, MI, and without ISR/FSR/MI as well as for all combinations of ISR, FSR, and MPI. It can be seen that the jets are not coming from FSR but only from ISR and MPI in $pp \to W \to l\nu_l$ events. Thereby, MPI produces more but lower-energetic jets than the ISR.

Process	Generator	Dataset ID	Production job option file
$Z \rightarrow ee$	HERWIG++	108294	MC9.108294.HerwigppZee
$Z \rightarrow \mu\mu$	HERWIG++	108295	MC9.108295.HerwigppZmumu
$Z \rightarrow \tau\tau$	HERWIG++	108296	MC9.108296.HerwigppZtautau
$W \rightarrow e\nu_e$	HERWIG++	108291	MC9.108291.HerwigppWenu
$W \rightarrow \mu\nu_\mu$	HERWIG++	108292	MC9.108292.HerwigppWmunu
$W \rightarrow \tau\nu_\tau$	HERWIG++	108293	MC9.108293.HerwigppWtaunu
reference datasamples			
$Z \rightarrow ee$	JIMMY+HERWIG	106057	MC9.106057.JimmyZee_no_filter
$Z \rightarrow \mu\mu$	JIMMY+HERWIG	106058	MC9.106057.JimmyZmumu_no_filter
$Z \rightarrow \tau\tau$	JIMMY+HERWIG	-	MC9.myJimmyZmumu_no_filter
$W \rightarrow e\nu_e$	JIMMY+HERWIG	105100	MC9.105100.JimmyWenu
$W \rightarrow \mu\nu_\mu$	JIMMY+HERWIG	106056	MC9.106056.JimmyWmunu_no_filter
$W \rightarrow \tau\nu_\tau$	JIMMY+HERWIG	106045	MC9.106045.JimmyWtaunu_no_filter

Table 6.2: List of datasets which were prevalidated before the sample B validation in ATLAS.

HERWIG++ validation

Concerning the sample B validation (see Sec. 6.3.3), the ATLAS interface of the HepMCAnalysis Tool has been used for a prevalidation of different HERWIG++ datasets based on preliminary production job option files listed in Tab. 6.2. These datasets were not official at this time and produced privately for these first tests. The reference datasets created with Fortran HERWIG are also listed in Tab. 6.2.[11]

Figures 6.17, 6.18, and 6.19 show some of the results for the Z data samples. While there are small differences in the number of Z bosons (Fig. 6.17(a)) of $pp \rightarrow Z \rightarrow ee$ events, the mass of Z bosons (Fig. 6.17(b)) shows quite a good agreement between both generators. Some discrepancies have been found in the transverse momentum p_{T} of Z bosons and the pseudorapidity η of Z bosons in $pp \rightarrow Z \rightarrow \mu\mu$ events (Fig. 6.18). The number of tracks in the τ lepton decay of $pp \rightarrow Z \rightarrow \tau\tau$ events in Fig. 6.19 agree quite well. The differences in the number of tracks (Fig. 6.19(a)) are explained by the fact that HERWIG++ has an own τ lepton decay package while Fortran HERWIG uses Tauola [156] to simulate the τ lepton decay. Better agreement exists in the transverse momentum p_{T} of the highest p_{T} track from the τ lepton decay of these events.

6.4 Summary

The HepMCAnalysis Tool is a package for MC generator validation and comparisons. It is a stable, easy-to-use, and extendable framework allowing easy access to generator level analysis, using the generator independent HepMC event record. It contains a class library with benchmark physics processes and a user analysis, in which the own analysis can easily be implemented, to analyse events at generator level and to fill results into ROOT histograms. The HepMCAnalysis

[11] As a technical note: The validation was done with Athena version 15.5.1 and the Athena interface of HepMCAnalysis Tool 3.1. The samples have been requested by the Standard Model group in ATLAS and are provided in evgen/EVNT format.

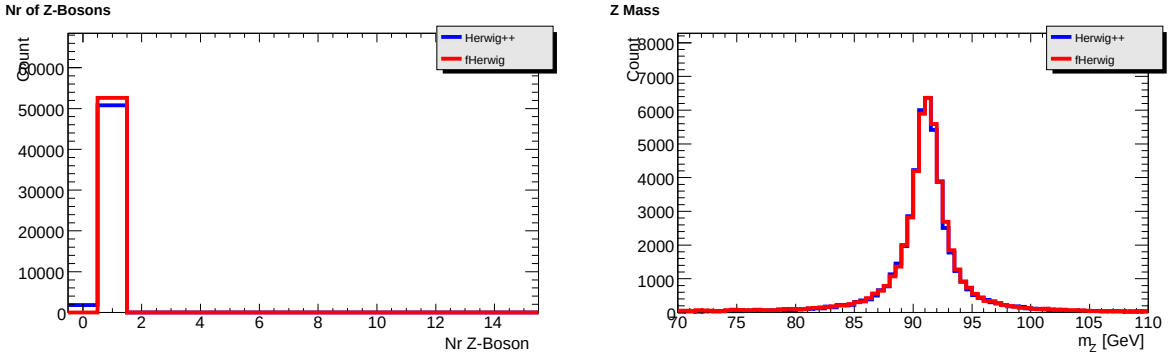

(a) (b)

Figure 6.17: (a) Number of Z bosons and (b) mass of Z bosons in $pp \to Z \to ee$ events.

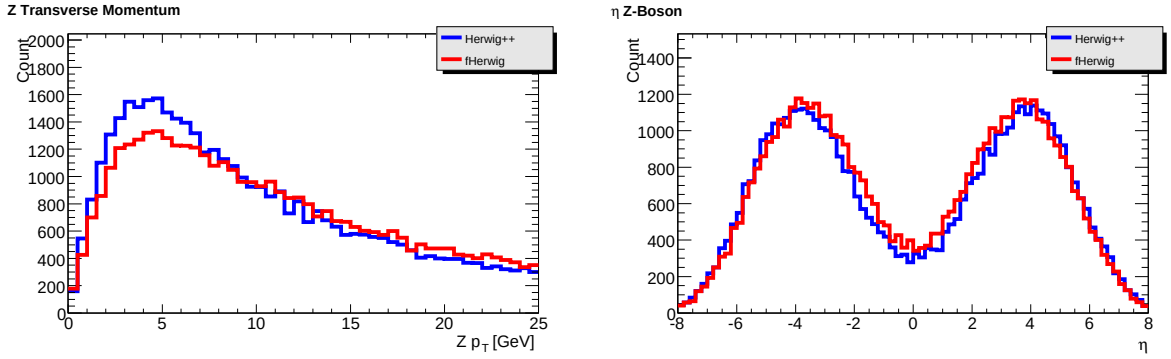

(a) (b)

Figure 6.18: (a) Transverse momentum p_{T} of Z bosons and (b) η of Z bosons in $pp \to Z \to \mu\mu$ events.

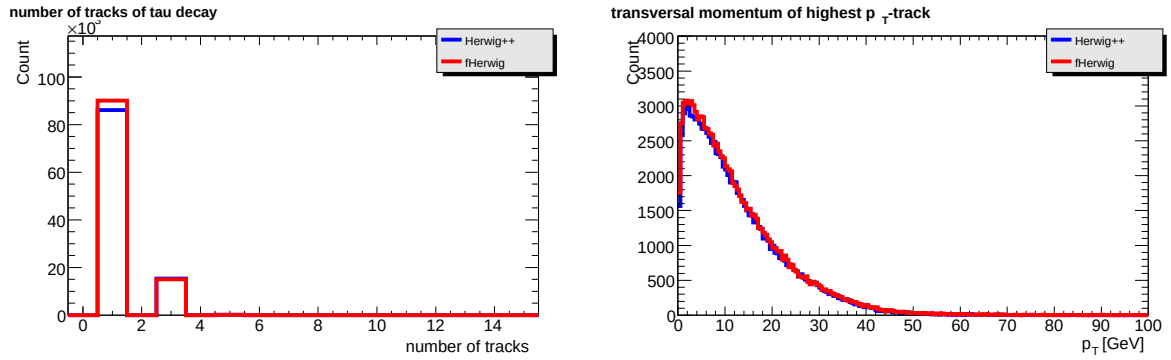

(a) (b)

Figure 6.19: (a) Number of tracks in the τ lepton decay and (b) transverse momentum p_{T} of the highest p_{T} track from the τ lepton decay in $pp \to Z \to \tau\tau$ events.

Tool includes steerable example programs for MC event generation. Scripts for a web display and comparisons of the ROOT histograms are provided, including Kolmogorov-Smirnoff- and χ^2-tests. The HepMCAnalysis Tool is available on its webpage [185] and in Genser (Generator Services Project).

The tool is in use for a variety of applications. An interface to the ATLAS software framework Athena is available, where it runs for validation and (nightly) regression tests of MC production scripts as well as for generator level studies and preparations for private analyses. Several (pre-)validations for large production of ATLAS MC datasets were performed and bugs could be discovered early enough in the MC datasets. Other applications are histogram based validation in Genser, as framework in MC schools, in generator level studies, and in preparations for user analyses, like the PDF study presented here. The running of nightly tests in Genser is also planned.

7 General aspects of $W \rightarrow \tau\nu_\tau$ events in proton-proton collisions

This chapter describes general aspects of the process $pp \rightarrow W + \mathrm{X} \rightarrow \tau\nu_\tau + \mathrm{X}$ at ATLAS. In the following, the process $pp \rightarrow W + \mathrm{X} \rightarrow \tau\nu_\tau + \mathrm{X}$ is denoted as $W \rightarrow \tau\nu_\tau$ for simplification. The W boson and the τ lepton were already introduced in Sec. 2.1.5 with their major properties. In this chapter, the τ lepton and W boson are summarised in context of LHC physics. The W boson production at a proton-proton collider is illustrated as well as expectations of $W \rightarrow \tau\nu_\tau$ events.

7.1 Physics of the W boson

Since general aspects of the W boson, like mass, were already covered in Sec. 2.1.5, the focus is put on physics of the W boson at the LHC in this section.

Single massive vector bosons are mainly produced via quark-quark scattering from the incoming hadrons in a hadron collider like the LHC (see Fig. 7.1). The rest of the hadrons, the spectator partons, build up a part of the underlying event. The specific Feynman diagrams up to NLO calculations for the production of a W boson decaying into a τ lepton and a τ neutrino are given in Fig. 7.2.

The hard process cross section for each individual generating process can be calculated with the factorisation theorem (see Sec. 2.1.4 and Eq. (2.19)). Due to the fact that the cross section is also an observable, it can be directly measured in experiments

$$\sigma_W = \frac{N_{\mathrm{obs}} - N_{\mathrm{bkg}}}{A_W C_W \mathcal{L}} \tag{7.1}$$

with N_{obs} as number of events passing the final selection, N_{bkg} as number of background events, A_W as acceptance, C_W as correction factor and $\mathcal{L}$ as integrated luminosity (see Sec. 8.5 for details). The total W boson production cross section is given in Fig. 3.3, that shows that the W boson production cross section is approximately ten times larger than that of Z bosons. The W boson decays into a quark pair or into a charged lepton and a corresponding neutrino. The ATLAS physics program for W bosons in early data comprehends several topics to have a good understanding of SM processes and for the search of new physics:

- measurement of the inclusive W boson production cross section,
- W boson charge asymmetry,
- measurement of differential cross section in the W boson production, and
- precision measurements of the W boson mass and decay width.

The cross sections of $W \rightarrow e\nu_e$ and $W \rightarrow \mu\nu_\mu$ processes have been already measured in 7 TeV ATLAS data and was found to be in agreement with the value from the NNLO calculation of

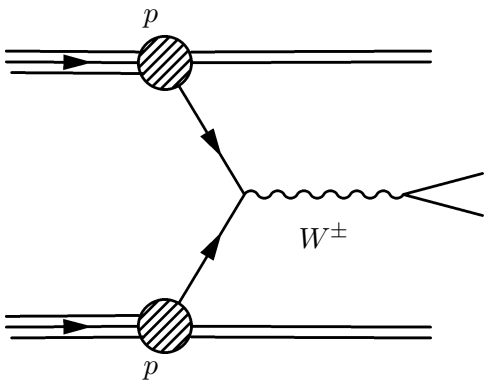

Figure 7.1: Scheme for $W^\pm$ boson production at a proton-proton collider.

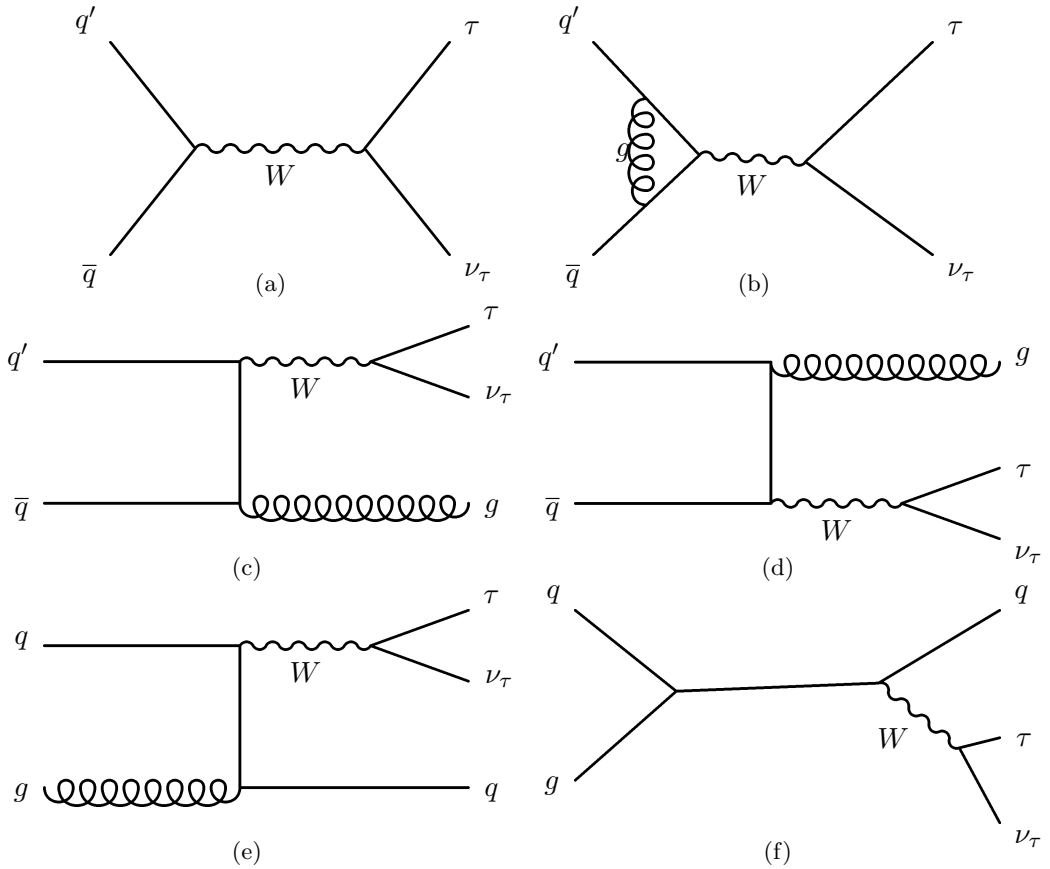

Figure 7.2: Feynman diagrams for single W boson production decaying into a τ lepton and a corresponding τ neutrino.

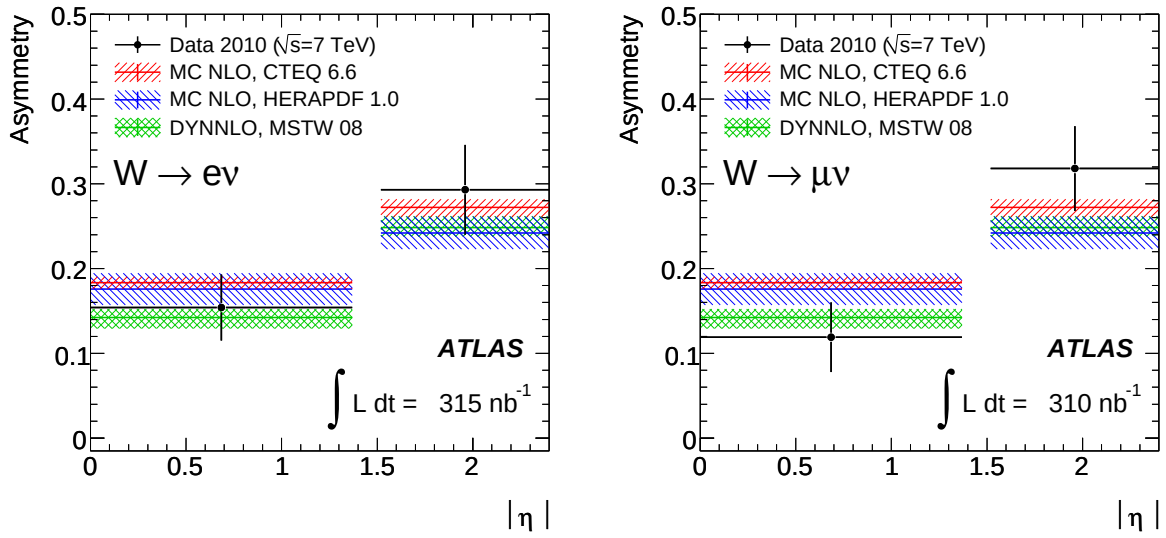

(a) (b)

Figure 7.3: Lepton charged asymmetries for the (a) electron and (b) muon channels including the superimposition of several theoretical predictions [203].

10.46 nb [203]. The cross section for $W \to \tau\nu_\tau$ processes in first ATLAS data was published in [137, 138] and will be described in Chap. 8.

The measurement of the W boson charge asymmetry provides information about parton distribution functions (PDFs). Inclusive measurements have been performed at the TEVATRON [204–207] whose data has been included in global fits of PDFs [22, 175]. The asymmetry of the W boson decay can be obtained by comparing the positively and negatively charged decay cross sections. Formally, the lepton charge asymmetry A_l is defined as

$$A_l = \frac{\sigma^{l+}_{W+} - \sigma^{l-}_{W-}}{\sigma^{l+}_{W+} + \sigma^{l-}_{W-}}, \tag{7.2}$$

where σ^{l+}_{W+} and σ^{l-}_{W-} are respectively the positively and negatively charged W boson fiducial cross sections.

The charge asymmetry is different from zero due to the different numbers of u and d valence quarks in the proton and it differs from the charge asymmetry in proton-antiproton collisions. The charge asymmetry of W bosons has been already measured in $W \to e\nu_e$ and $W \to \mu\nu_\mu$ events by ATLAS with 7 TeV data and is in agreement with the predictions (see Fig. 7.3) [203].

7.2 Physics of the τ lepton

The τ lepton was already introduced in Sec. 2.1.5. Its main physics aspects are summarised here.

The τ lepton belongs to the third generation of leptons. It is the heaviest with a mass of 1.777 GeV and it has a rather short lifetime of 2.9×10^{-13} s. It decays in 64.79% of the cases hadronically and 35.21% leptonically [12]. Its decay is given in Fig. 2.5. Due to their similar signature in the detector, leptonically decaying τ leptons are difficult to distinguish from primary

electrons or muons. The additional neutrino in the leptonic τ lepton decay like $\tau \to \mu\nu_\mu\nu_\tau$ results in a visible energy of the τ lepton less than in the hadronic decay. This high missing transverse momentum in the leptonic τ lepton decay is a big challenge for the leptonic τ lepton reconstruction. So, the τ lepton reconstruction algorithms at ATLAS focusses on hadronically decaying τ leptons only (in the following τ_h leptons, see Sec. 4.4.2). These are characterised by an odd number of charged mesons, mainly one or three pions, in the decay. There are also neutral particles, mainly neutral pions π^0, in the 1- and 3-prong decays that can be registered as electromagnetic energy depositions (e.g. $\pi^0 \to \gamma\gamma$).

A central aspect in the physics of the τ lepton is its polarisation, which has been thoroughly analysed at the Large Electron Positron (LEP) collider in $e^+e^- \to Z \to \tau^+\tau^-$ processes, and gives a hint on parity violating processes [208]. The τ lepton polarisation can be calculated by

$$P_\tau = -2\frac{g_{V,\tau}/g_{A,\tau}}{1+\left(g_{V\tau}/g_{A\tau}\right)^2} \approx -2\frac{g_{V,\tau}}{g_{A,\tau}} = -2\left(1-4\sin^2\theta_W\right), \tag{7.3}$$

where $g_{V,\tau}/g_{A,\tau}$ is the ratio of the vector and axial vector coupling constants of the τ lepton to the Z boson. The polarisation of the τ lepton has been measured to be $P_\tau = -0.152 \pm 0.045$, which provides a mixing angle of $\sin^2\theta_W\left(M_Z^2\right) = 0.2302 \pm 0.0058$ [208]. The aspect of the τ lepton polarisation is quite important as a probe of new physics. New heavy particles can be identified via their decay into τ leptons, such as the charged Higgs boson, which can decay in a right-handed τ lepton and a corresponding neutrino [209].

Furthermore, τ leptons play an important role in many physics processes, in SM physics as well as in physics beyond the SM (see Sec. 2.3). For light Higgs boson masses, the τ lepton can be often found in the Higgs boson decay, both in the neutral and in the charged Higgs boson decay. The τ lepton is also an important final state particle in many supersymmetric scenarios. Thus, the τ lepton is important on the one hand for understanding SM background in the search for new physics, and on the other hand for precision measurements in the SM. Significant SM events with τ leptons are $W \to \tau\nu_\tau$ and $Z \to \tau\tau$ events, which can be used for calibration and validation of the τ lepton reconstruction and identification in first data. In addition, $t\bar{t}$ events are crucial events with τ leptons for the measurement of the top quark mass in the decay channels $t\bar{t} \to W\left(\to q\bar{q}\right)W\left(\to \tau\nu_\tau\right)b\bar{b}$ and $t\bar{t} \to W\left(\to e\nu_e/\mu\nu_\mu\right)W\left(\to \tau\nu_\tau\right)b\bar{b}$, too.

7.3 Expectation from $W \to \tau\nu_\tau$ events

The process $W \to \tau\nu_\tau$ plays an important role for physics with τ leptons in first ATLAS data. It is used for validation of the reconstruction and identification techniques for τ leptons and of the measurement of the missing transverse momentum. Furthermore, the process $W \to \tau\nu_\tau$ can also be used in the search for physics beyond the SM (like charged Higgs bosons). Although other channels like $Z \to \tau\tau$ are easier to select, the $W \to \tau\nu_\tau$ process has a ten times higher cross section of $\sigma \times \mathrm{BR} = 10.46 \cdot 10^3\,\mathrm{pb}$ (NNLO) at $\sqrt{s} = 7\,\mathrm{TeV}$ [203] ($\sigma \times \mathrm{BR} = 1.7 \cdot 10^4\,\mathrm{pb}$ (LO) at $\sqrt{s} = 14\,\mathrm{TeV}$ [57, 58]). Its branching ratio is $(11.25 \pm 0.20)\,\%$ [12]. The main production processes of $W \to \tau\nu_\tau$ events are summarised in Fig. 7.2.

The process $W \to \tau_\mathrm{h}\nu_\tau$ is dominated by events with low transverse momentum of the W boson which result in soft τ leptons with low missing transverse momentum as illustrated in Fig. 7.4. The neutrino in the decay carries a large fraction of the W boson energy away, which results in visible measurable low reconstructed momenta.

Measurements concerning the $W \to \tau_\mathrm{h}\nu_\tau$ channel have been already performed at hadron

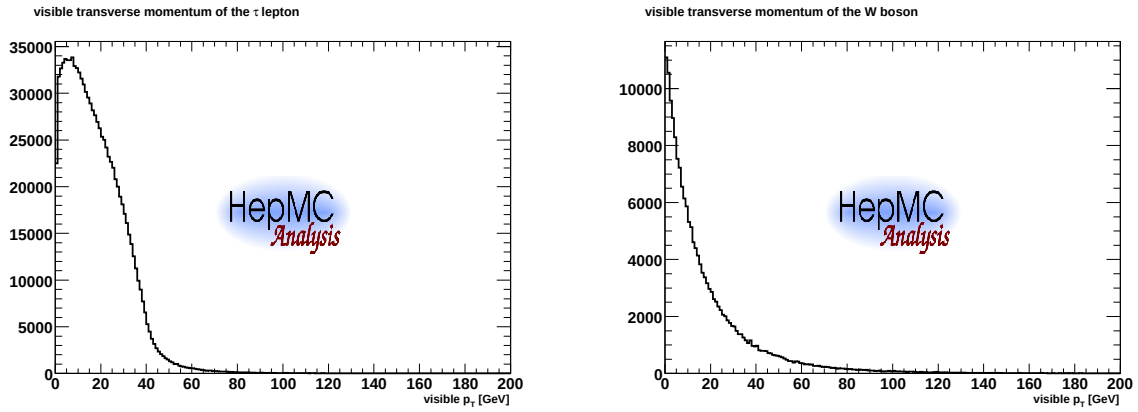

(a) (b)

Figure 7.4: Visible momenta of the (a) τ lepton and (b) W boson in $W \to \tau_{\mathrm{h}}\nu_\tau$ events at generator level generated with PYTHIA6. Visible momentum means that only decay products are implemented in the momentum which can be detected in a detector.

colliders by the TEVATRON experiments to test for example the lepton universality.

The CDF Collaboration measured the cross section $\sigma(p\overline{p} \to W) \times BR(W \to \tau\nu_\tau)$ and the ratio $BR(W \to \tau\nu_\tau)/BR(W \to e\nu_e)$ in $p\overline{p}$ collisions at $\sqrt{s} = 1.8\,\mathrm{TeV}$ on data with an integrated luminosity of $4.05\,\mathrm{pb}^{-1}$ [210]. They obtained a value for the cross section of $\sigma(p\overline{p} \to W) \times BR(W \to \tau\nu_\tau) = 2.05 \pm 0.27\,\mathrm{nb}$ and for the ratio $BR(W \to \tau\nu_\tau)/BR(W \to e\nu_e) = 0.97 \pm 0.07$ in agreement with the SM expectations assuming lepton universality [210]. Both measurements include statistical and systematic errors.

The same measurements with an integrated luminosity of $18\,\mathrm{pb}^{-1}$ have been accomplished by the D0 Collaboration. They published a cross section of $2.22 \pm 0.09\,(\mathrm{stat.}) \pm 0.1\,(\mathrm{syst.}) \pm 0.1\,(\mathrm{lumi.})\,\mathrm{nb}$ and a ratio of 0.980 ± 0.031 [211]. Similar measurements were also performed by the UA1 and UA2 Collaborations [43, 212].

The $W \to \tau\nu_\tau$ branching ratio was also measured at the LEP collider and deviations from the SM expectations were observed. The four LEP experiments (ALEPH, DELPHI, L3, and OPAL) measured an average branching ratio of $(11.44 \pm 0.19\,(\mathrm{stat.}) \pm 0.2\,(\mathrm{syst.}))\%$ [2–5].[1] Assuming 100% unknown correlation, the systematic uncertainty of the average value is set on 0.2%. The SM expectation lies at 10.83%, which means that the LEP experiments have deviations of approximately 2.2σ, which necessitates the aim of repitition of this measurement at the LHC.

These measurements are repeated with the first LHC data. Chapter 8 covers the $W \to \tau\nu_\tau$ cross section measurement, which was published in [137] and [138].

In this thesis, one focus in the cross section measurement lies on acceptance calculations (see Sec. 8.5 and Sec. 8.6.4). A first estimation of possible results is given by a generator based study [213].[2] A simplified efficiency calculation was done with the following cuts:

- $20\ \mathrm{GeV} \leq p_{\mathrm{T}}(\tau) \leq 60\ \mathrm{GeV}$,

[1] The averaged branching ratio is calculated by arithmetic averaging. The individual branching ratios are: $(11.25 \pm 0.32\,(\mathrm{stat.}) \pm 0.20\,(\mathrm{syst.}))\%$ (ALEPH) [2], $(11.46 \pm 0.39\,(\mathrm{stat.}) \pm 0.19\,(\mathrm{syst.}))\%$ (DELPHI) [3], $(11.89 \pm 0.40\,(\mathrm{stat.}) \pm 0.20\,(\mathrm{syst.}))\%$ (L3) [4], and $(11.14 \pm 0.42\,(\mathrm{stat.}) \pm 0.17\,(\mathrm{syst.}))\%$ (OPAL) [5]. The errors are calculated with usual error propagation of the individual errors from the experiments.

[2] This study was performed in collaboration with Marc Sangel who worked as a summer student at the DESY ATLAS group in summer 2011.

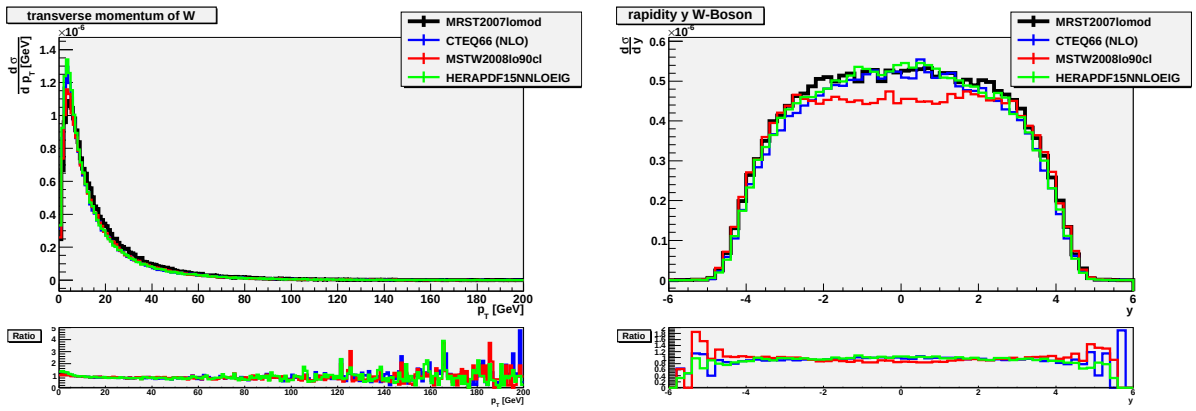

(a) (b)

Figure 7.5: (a) Transverse momentum and (b) rapidity of the W boson in $W \to \tau\nu_\tau$ events [213].

- $|\eta(\tau)| \leq 2.5$ and not in $1.3 \leq |\eta(\tau)| \leq 1.7$,
- $(\sum p^\nu)_T \geq 30$ GeV, and
- $\Delta\phi(p^\tau, \sum p^\nu) \geq 0.5$,

where $p_\mathrm{T}(\tau)$ and $\eta(\tau)$ are the transverse momentum and pseudorapidity of the τ lepton. The term $(\sum p^\nu)_T$ is the transverse part of the sum of the neutrino momenta. The angle $\Delta\phi(p^\tau, \sum p^\nu)$ is the angle between the momentum of the τ lepton and the sum of the neutrino momenta. These cuts are chosen in a way that they are similar to Sec. 8.5 and correspond to the visible part of a reconstructed τ lepton. For an approximation of the efficiency expected in the acceptance calculation of Sec. 8.5, 100 000 $W \to \tau\nu_\tau$ events have been generated with PYTHIA6 for different parton distribution functions (PDFs): CTEQ66 (NLO) [214], MRST2007lomod [201], MSTW2008lo90cl (LO) [22] and HERAPDF15NNLO [29]. The efficiency is defined as

$$\epsilon = \frac{\text{number of all events after cuts}}{\text{number of all generated events}}. \tag{7.4}$$

Results are shown in Figs. 7.5 and 7.6 and Tabs. 7.1, 7.2, and 7.3.

As expected, there are differences in the distributions of the W boson and the τ lepton in Figs. 7.5 and 7.6 for the different PDFs and the distributions which agree with the results in [201] (see Sec. 6.3.4). Table 7.1 shows the number of events after each cut for hadronically and leptonically decaying τ leptons in $W \to \tau\nu_\tau$ events with the corresponding efficiency in Tab. 7.2. The statistical error for the efficiency is calculated with usual error propagation. In order to have an approximation of the efficiency of hadronically decaying τ leptons only, the efficiency of all decaying τ leptons (see Tab. 7.2) is multiplied with the branching ratio of hadronically decaying τ leptons of 0.6479 and gets the efficiency of hadronically decaying τ leptons shown in Tab. 7.3. The differences in the acceptance between this result and what was published in [137] ($(9.75 \pm 0.19)\,\%$) arises due to the use of a different tune. ATLAS uses the AMBT1 LO* tune [176] while in this study the PYTHIA6 standard tune [215] based on Rick Field's tune A was

cut	number of events		error
MRST2007lomod			
without cut	100000	±	316.228
$p_T(\tau)$	77770	±	278.873
$\lvert\eta(\tau)\rvert$	42835	±	206.966
$(\sum p^\nu)_T$	14030	±	118.448
$\Delta\phi(p^\tau, \sum p^\nu)$	13617	±	116.692
CTEQ66 (NLO)			
without cut	100000	±	316.228
$p_T(\tau)$	78182	±	279.61
$\lvert\eta(\tau)\rvert$	44171	±	210.169
$(\sum p^\nu)_T$	13804	±	117.49
$\Delta\phi(p^\tau, \sum p^\nu)$	13482	±	116.112
MSTW2008lo90cl			
without cut	100000	±	316.228
$p_T(\tau)$	78215	±	279.669
$\lvert\eta(\tau)\rvert$	41773	±	204.384
$(\sum p^\nu)_T$	13116	±	114.525
$\Delta\phi(p^\tau, \sum p^\nu)$	12762	±	112.969
HERAPDF15NNLOEIG			
without cut	10000	±	316.228
$p_T(\tau)$	78277	±	279.78
$\lvert\eta(\tau)\rvert$	44714	±	211.457
$(\sum p^\nu)_T$	13752	±	117.269
$\Delta\phi(p^\tau, \sum p^\nu)$	13427	±	115.875

Table 7.1: Number of events after each cut for hadronically and leptonically decaying τ leptons in $W \to \tau\nu_\tau$ events [213].

PDF	efficiency		error
MRST2007lomod	0.13617	±	0.00124
CTEQ66	0.13482	±	0.00124
MSTW2008lo80cl	0.12762	±	0.00120
HERAPDF15NNLOEIG	0.13427	±	0.00123

Table 7.2: Efficiency for hadronically and leptonically decaying τ leptons in $W \to \tau\nu_\tau$ events [213].

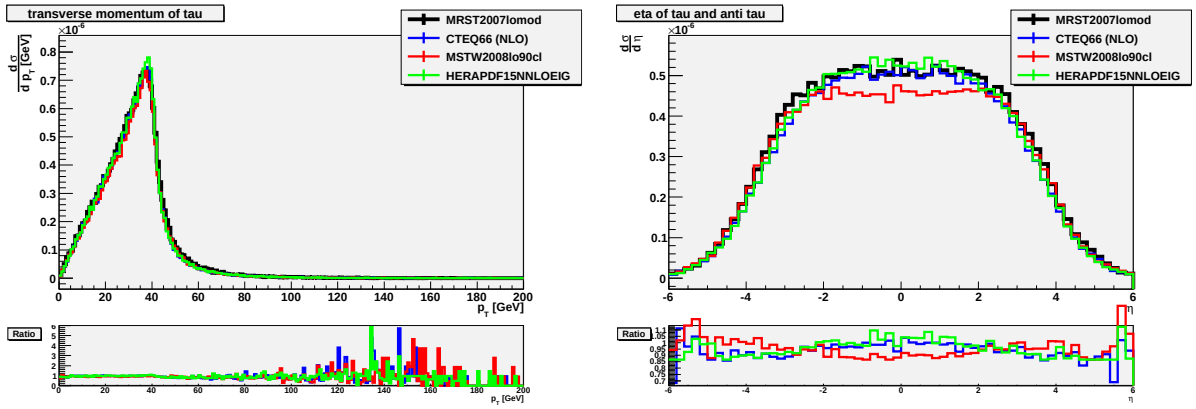

(a) (b)

Figure 7.6: (a) Transverse momentum and (b) rapidity of the τ lepton in $W \to \tau\nu_\tau$ events [213].

PDF	efficiency		error
MRST2007lomod	0.08822	±	0.00081
CTEQ66	0.08735	±	0.00080
MSTW2008lo80cl	0.08269	±	0.00078
HERAPDF15NNLOEIG	0.08699	±	0.00080

Table 7.3: Efficiency for only hadronically decaying τ leptons in $W \to \tau\nu_\tau$ events [213] (modified).

used. Comparisons for different tunes have also been performed with no significant differences.

Several $W \to \tau_\mathrm{h}\nu_\tau$ candidates have already been observed [216]. Figure 7.7 shows the event signature of one of the first candidates observed by the ATLAS experiment. The event was collected on May 24th 2010 and passed the event selection criteria described in [216]. The hadronic τ lepton candidate has a transverse momentum of 29 GeV and has one charged track in its decay (1-prong). The missing transverse momentum in the event is 39 GeV and the angle $\Delta\phi$ between the τ lepton candidate and the missing transverse momentum is 3.1. No electrons, muons, photons, jets or other objects can be found in this event. The top left view is a projection of the event in the x-y plane. The isolated hadronic τ lepton candidate is visualised as an orange line. Its energy depositions in the electromagnetic (green) and hadronic (red) calorimeter can be seen as yellow boxes. The missing transverse energy opposite to the hadronic τ lepton candidate in the x-y plane is a red dotted line. The shape of the energy depositions of the hadronic τ lepton is given in the top right view. These energy depositions (magenta and yellow boxes) in the 3D view denotes that hadronically decaying τ leptons have similar shapes like QCD jets but narrower.

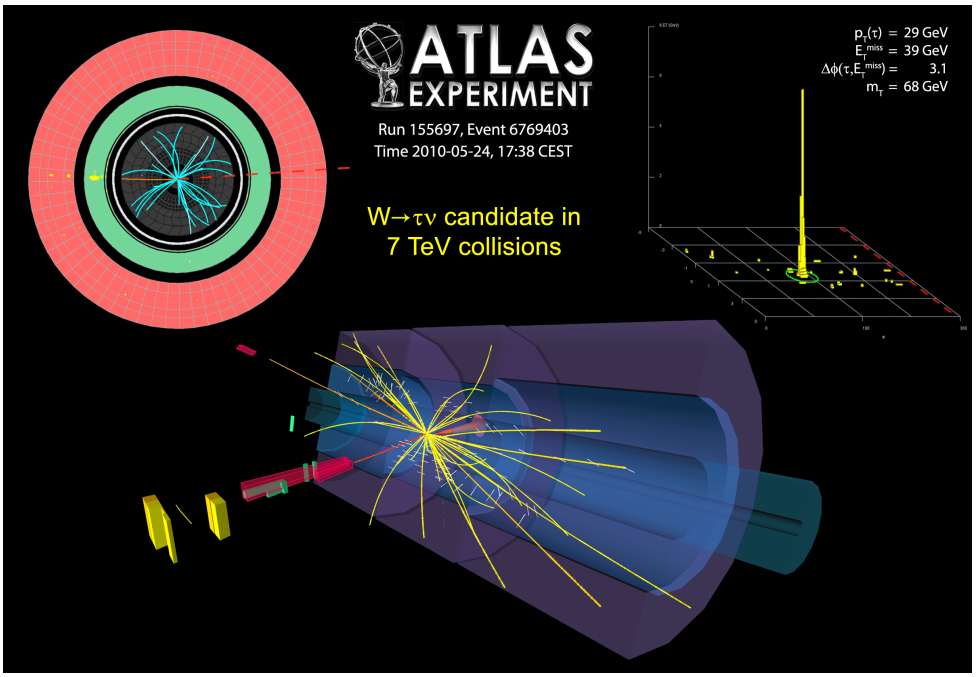

Figure 7.7: Event display of a $W \to \tau_{\mathrm{h}}\nu_\tau$ candidate, collected on May 24th 2010. Event properties: $p_{\mathrm{T}}(\tau) = 29\,\mathrm{GeV}$, $E_{\mathrm{T}}^{\mathrm{miss}} = 39\,\mathrm{GeV}$, $\Delta\phi\left(\tau, E_{\mathrm{T}}^{\mathrm{miss}}\right) = 3.1$ and $m_{\mathrm{T}} = 68\,\mathrm{GeV}$. No additional object (electron, muon or jet) was found in the event [217].

8 Measurement of the $W \rightarrow \tau\nu_\tau$ cross section in proton-proton collisions at $\sqrt{s} = 7\,\text{TeV}$ with the ATLAS experiment

The study of the $W \rightarrow \tau\nu_\tau$ decay in pp collisions is crucial for the physics program using early ATLAS data. It complements the measurement of W boson production decaying into electrons and muons [218, 219]. It is important to rediscover the SM at the LHC experiments as a demonstration of detector understanding and as background for new physics searches. Furthermore, these measurements can improve the precision currently available for many SM parameters. In addition, the $W \rightarrow \tau\nu_\tau$ branching ratio has to be checked, because deviations of approximately 2.2σ from the theoretical prediction have been observed at LEP. A $W \rightarrow \tau\nu_\tau$ branching ratio of 10.83% is expected but a branching ratio of $(11.44 \pm 0.19\,(\text{ stat.}) \pm 0.1\,(\text{ syst.}))\%$, averaged over all LEP experiments, was measured (see Sec. 7.3) [2–5].

Therefore, as one of the starting points, the cross section of $W \rightarrow \tau\nu_\tau$ is determined. As already mentioned in Sec. 7.3, $W \rightarrow \tau\nu_\tau$ events are dominated by low-p_T W bosons decaying into τ leptons with small visible transverse momenta. Due to the neutrinos in the W boson and τ lepton decays, there is large missing transverse momentum in the event. From NNLO calculations, a cross section times branching ratio of $\sigma \times \text{BR} = 10.46 \cdot 10^3\,\text{pb}$ is expected for a center-of-mass energy $\sqrt{s} = 7\,\text{TeV}$ [22, 203, 220].

The entire cross section measurement published in [137] and [138] is described in this chapter. The focus lies on the acceptance calculation and systematic uncertainties of the acceptance. Furthermore, systematic uncertainties of the underlying event modelling are evaluated by using different tunes. For the analysis, the full 2010 data, recorded by the ATLAS experiment, corresponding to an integrated luminosity of $34.3\,\text{pb}^{-1}$ is used. In the following, a hadronically/leptonically decaying τ lepton is denoted as $\tau_\text{h}/\tau_\text{l}$ lepton.

8.1 Data samples

The cross section measurement is performed on the 2010 ATLAS data recorded in proton-proton collisions at a center-of-mass-energy of $\sqrt{s} = 7\,\text{TeV}$. Only data, taken during data taking periods where all relevant subdetector systems were fully operational, is taken into account. Furthermore, only events, which are selected by a combined τ_h lepton and E_T^miss trigger, are used. This results in a total integrated luminosity of $34.3\,\text{pb}^{-1}$. Further cleaning cuts are applied to guarantee that the events come from real collisions, and that all the objects and quantities are correctly reconstructed.

The collected data is compared to ATLAS Monte Carlo samples.

8.1.1 Data samples

The considered data samples are divded into two different periods: Run 158632 – 166658 compose the first period and run 166786 – 167844 the second. For the first period, the

Period	Runs	Integrated luminosity
First period	158632 – 166658	$10.7\,\text{pb}^{-1}$
Second period	166786 – 167844	$23.6\,\text{pb}^{-1}$
Total		$34.3\,\text{pb}^{-1}$

Table 8.1: Run periods and corresponding integrated luminosity for the standard analysis. A loose τ lepton trigger was used in the first period and a medium τ lepton trigger in the second period.

Period	Runs	Integrated luminosity
First period	158632 – 166658	$10.7\,\text{pb}^{-1}$
Second period	166786 – 167844	$5.6\,\text{pb}^{-1}$
Total		$16.3\,\text{pb}^{-1}$

Table 8.2: Run periods and corresponding integrated luminosity for the QCD estimation. In both periods a loose τ lepton trigger is used.

EF_tau12_loose_xe20_noMu trigger is used, and for the second EF_tau16_medium_xe22_noMu. More details on the trigger is given in Sec. 8.2.3. The two periods are chosen to avoid high prescale factors being applied to the triggers, because the trigger used for the first period is highly prescaled in the second period. Due to the fact that the EF trigger was not active in the first runs from 152166 to 158582, these events, with an insignificant integrated luminosity of $77\,\text{nb}^{-1}$, are not used.

For the analysis, centrally produced data samples, which consist of events that are collected by the L1Calo stream, respectively the JetTauEtMiss stream from run 160387 on[1], are used in the D3PD format, created by the TauD3PDMaker [221] (tag 01-00-01-01) [222]. For good data quality, a good run list (GRL) is applied, in which all necessary detector flags for W boson and τ_h lepton physics are combined.[2]

The total integrated luminosity is summarised in Tab. 8.1. It is already corrected by a factor 0.964 from the updated luminosity measurement in ATLAS [224]. The QCD jet background is extracted from data in a control region (see Sec. 8.3). The integrated luminosity of this control region is summarised in Tab. 8.2. A loose τ lepton trigger is used for both data periods, for which reason the integrated luminosity differs from the one in the signal region of Tab. 8.1.

8.1.2 Monte Carlo samples

Monte Carlo (MC) samples are used for comparison between data and theory. The background is evaluated with these Monte Carlo samples. The main background comes from electroweak (EW) processes like W production decaying into an electron or a muon and the corresponding neutrino, or Z production decaying into two leptons. QCD jets are also one of the largest backgrounds and the contribution is estimated from data, due to the limited MC statistic available. Table 8.3 summarises the used MC datasets, with the first part listing the MC datasets used in the analysis, and the other parts those used for systematic studies (e.g. different tunes). These MC datasets are also centrally produced and available in the same format as for real data (D3PDs

[1] The name of the stream changed starting with run 160387.
[2] The GRL can be found at [223].

created with the TauD3PDMaker tag 01-00-01-01, see Sec. 8.1.1). TAUOLA [156] is used for simulating τ lepton decays and PHOTOS [168, 169] for QED radiation in the final state in all samples.

All samples are produced including the pile-up effect with an averaged number of additional vertices of $< n_{\text{additional,vtx}} >= 2$. Each MC sample has to be reweighted with factors calculated separately for each MC sample to account for the pile-up conditions in data. Each event is reweighted in a way that the distributions of the number of reconstructed primary vertices per bunch crossing matches the number measured by ATLAS. The reweighting factors are calculated for events with 1, 2, 3, 4, and ≥ 5 reconstructed vertices after the data quality requirements, the trigger selection and jet cleaning cuts for each of the used triggers in the signal and control regions defined in Sec. 8.3. The reweighting factors can be found in Appendix B.1.

8.2 Event selection

An efficient event selection is needed to select the signal signature $W \rightarrow \tau_{\text{h}}\nu_\tau$ and to suppress the background. This section describes possible background processes, reintroduces the used τ lepton reconstruction algorithm and introduces the event selection.

8.2.1 Background processes

The following background processes, which are normalised to the NNLO cross section given in Tab. 8.3 (except QCD jets, see below), are considered in this analysis:

QCD jets: QCD jet events, where one jet is misidentified as a hadronically decaying τ lepton and with a significant amount of misreconstructed missing transverse momentum, is the dominant background process. The cross section of these background events is several orders of magnitude larger than that of the signal, so that an effective suppression of QCD jet events is crucial for the analysis. Due to limited statistics of QCD jet events in the MC samples, a method to extract this background from data is used (see Sec. 8.3).

$W \rightarrow e\nu_e/\mu\nu_\mu$: This process contributes to the background if the lepton from the W boson decay is misidentified as a hadronically decaying 1-prong τ lepton, which can be suppressed by electron and muon vetoes. It can also contribute to the background if a jet fakes a hadronically decaying τ lepton. To supress these fakes, it is required that no reconstructed electron or muon is in the event, so that there are only fake τ leptons left in events where the electron or muon could not be reconstructed.

$W \rightarrow \tau\nu_\tau \rightarrow e\nu_e/\mu\nu_\mu$: As already mentioned, the decay products from leptonically decaying τ leptons are difficult to distinguish from primary electrons and muons, but this process can nevertheless be suppressed similarly to $W \rightarrow e\nu_e/\mu\nu_\mu$ processes.

$Z \rightarrow ee/\mu\mu$: This process can contribute to the background if one electron or muon is misidentified as a hadronically decaying τ lepton and the other one is lost. This process can be rejected, as with $W \rightarrow e\nu_e/\mu\nu_\mu$ processes by applying electron and muon vetoes.

$Z \rightarrow \tau\tau$: Although the production cross section of $Z \rightarrow \tau\tau$ events is ten times smaller than for $W \rightarrow \tau\nu_\tau$ events, it can contribute to the background, if only one of the τ leptons is reconstructed as a hadronically decaying τ lepton and the other one is lost.

MC DS ID	MC Sample	MC Generator	UE Tune	PileUp	Simulation tag	Events	cross section [nb]
106043	$W \to e\nu_e$	Pythia6	AMBT1	InTime $< 2 >$	e574_s933_s946_r1661_r1700	1.4M	10.46
106044	$W \to \mu\nu_\mu$	Pythia6	AMBT1	InTime $< 2 >$	e574_s933_s946_r1659_r1700	1.4M	10.46
107054	$W \to \tau\nu_\tau$	Pythia6	AMBT1	InTime $< 2 >$	e574_s934_s946_r1660_r2040	1M	10.46
106046	$Z \to ee$	Pythia6	AMBT1	InTime $< 2 >$	e574_s933_s946_r1661_r1700	1M	0.99
106047	$Z \to \mu\mu$	Pythia6	AMBT1	InTime $< 2 >$	e574_s933_s946_r1659_r1700	1M	0.99
106052	$Z \to \tau\tau$	Pythia6	AMBT1	InTime $< 2 >$	e574_s934_s946_r1660_r2040	1M	0.99
105200	$t\bar{t}$ leptonic	MC@NLO	AUET1	InTime $< 2 >$	e598_s933_s946_r1659_r1700	200k	0.144×0.556
105204	$t\bar{t}$ hadronic	MC@NLO	AUET1	InTime $< 2 >$	e598_s933_s946_r1659_r1700	30k	0.144×0.444
107419	$W \to \tau\nu_\tau$	Pythia6	Perugia2010	InTime $< 2 >$	e618_s934_s946_r1660_r2040	500k	10.46
107418	$Z \to \tau\tau$	Pythia6	Perugia2010	InTime $< 2 >$	e618_s934_s946_r1660_r2040	500k	0.99
108328	$W^+ \to \tau^+\nu_\tau$	MC@NLO	AUET1	InTime $< 2 >$	e598_s934_s946_r1660_r1700	200k	6.16
108329	$W^- \to \tau^-\overline{\nu}_\tau$	MC@NLO	AUET1	InTime $< 2 >$	e598_s934_s946_r1660_r1700	200k	4.3

Table 8.3: Monte Carlo datasets (DS) used in the analysis. The cross sections are the NNLO cross sections given in [22, 203, 220].

Signature	Efficiency
EF_tau12_loose_xe20_noMu	(81.3 ± 0.8) %
EF_tau16_medium_xe22_noMu	(62.7 ± 0.7) %

Table 8.4: Trigger efficiencies for the two triggers used [138]. The uncertainties are statistical only.

$t\bar{t}$: The cross section of $t\bar{t}$ events is much smaller than that of the signal, but top quarks decay into a W boson and a bottom quark. This process contributes to the background, if one of the W bosons decays into a hadronically decaying τ lepton or if one of the decay products fakes a hadronically decaying τ lepton.

8.2.2 BDT τ_{h} identification

A boosted decision tree ID is used for the reconstruction and identification of hadronically decaying τ leptons. This method uses eight variables, which are the cluster mass, the track mass, the track radius, the leading track momentum fraction, the electromagnetic radius, the core energy fraction, the electromagnetic fraction, and the transverse flight path significance (see Sec. 4.4.2).

8.2.3 Event selection

The following event selection is performed for both data and MC to suppress the background sources (after applying the GRL in the case of data).

Trigger

Events are selected using triggers at all three ATLAS trigger levels, based on a τ_{h} lepton and missing transverse momentum $E_{\mathrm{T}}^{\mathrm{miss}}$ signatures. As already mentioned in Sec. 8.1, two triggers are used. EF_tau12_loose_xe20_noMu is used for the first data period, in which a loosely identified τ_{h} lepton candidate with a transverse momentum $p_{\mathrm{T},\tau_{\mathrm{h}}} > 12\,\mathrm{GeV}$ (reconstructed at trigger level) and a missing transverse momentum $E_{\mathrm{T}}^{\mathrm{miss}} > 20\,\mathrm{GeV}$ is required. The part 'noMu' refers to the fact that the missing transverse momentum is reconstructed with the calorimeter information only (without the information coming from the muon spectrometer). The trigger for the second data period is the EF_tau16_medium_xe22_noMu trigger, which means that a medium identified τ_{h} lepton candidate with a transverse momentum $p_{\mathrm{T},\tau_{\mathrm{h}}} > 16\,\mathrm{GeV}$ (reconstructed at trigger level) and a missing transverse momentum $E_{\mathrm{T}}^{\mathrm{miss}} > 22\,\mathrm{GeV}$ (reconstructed with the calorimeter information only) is required. A tighter τ lepton selection is needed for the second data period due to increased luminosity. The trigger efficiencies with respect to the offline event selection is summarised in Tab. 8.4.

Collision and jet cleaning

Collision cleaning It is required that there is at least one vertex in the event with three or more ($p_{\mathrm{T}} > 150\,\mathrm{MeV}$) tracks to ensure that the event is a good collision event.

	Loose	Medium = Loose OR	***under discussion*** Tight = Medium OR
HEC spikes	HECf>0.5 && |HECQ|>0.5 or |neg. E|>60GeV	HECf>1-|HECQ|	
EM coherent noise	EMf>0.95 &&|LArQ|>0.8 && |eta|<2.8	EMf>0.9 && |LArQ|>0.8 && |eta|<2.8	|LArQ|>0.95 or EMf>0.98 && |LArQ|>0.05
Non-collision background & Cosmics	|t|>25ns or EMf<0.05 && Chf<0.05 && |eta|<2 or EMf<0.05 && |eta|>=2 or FMax>0.99 && |eta|<2	|t|>10ns or EMf<0.05 && Chf<0.1 && |eta|<2 or EMf>0.95 && Chf<0.05 && |eta|<2	EMf<0.1 && Chf<0.2 && |eta|<2 or EMf<0.1 && |eta|>=2 or EMf>0.9 && Chf<0.02 && |eta|<2

Figure 8.1: Sets of cuts for jet cleaning [138].

Jet cleaning Additional selection cuts are applied to suppress events coming from cosmic rays or events containing jets which were incompletely reconstructed or affected by electronic noise in the calorimeters. A summary of possible sets of cuts for the jet cleaning is given in Fig. 8.1. The loose one is used in this analysis.

The jet cleaning is not applied to MC because some of the cleaning variables are poorly described in MC. The effect of jet cleaning in MC has been checked and was found to be negligible as systematic uncertainty (lower than 0.1% for the loose trigger period, lower than 0.2% for the medium trigger period), because the other systematic uncertainties are much higher [138].

Additional cleaning cuts

In addition to the data quality requirement (GRL) and the collision and jet cleaning cuts, further cleaning cuts are applied.

Jet in crack region Events with at least one jet with $p_{\mathrm{T}} > 20\,\mathrm{GeV}$ are suppressed if a jet or a τ_{h} lepton candidate is found in the crack region, $1.3 < |\eta| < 1.7$, of the ATLAS detector. This transition region between the barrel and the end-cap calorimeter has a lower resolution than in the rest of the calorimeter, which can result in a bad $E_{\mathrm{T}}^{\mathrm{miss}}$ reconstruction.

$\Delta\phi\left(\mathbf{jet}, \boldsymbol{E}_{\mathbf{T}}^{\mathbf{miss}}\right)$ A cut on events on the minimum of $\Delta\phi\left(\mathrm{jet}, E_{\mathrm{T}}^{\mathrm{miss}}\right) > 0.5$ for jets with $p_{\mathrm{T}} > 20\,\mathrm{GeV}$ is required to suppress QCD jet events that are collinear with $\Delta\phi\left(\mathrm{jet}, E_{\mathrm{T}}^{\mathrm{miss}}\right)$.

Event signature

For the signature of $W \to \tau_{\mathrm{h}}\nu_\tau$ processes, further cuts have to be applied, which are described in the following.

$\boldsymbol{E}_{\mathbf{T}}^{\mathbf{miss}}$ cut A minimum missing transverse momentum $E_{\mathrm{T}}^{\mathrm{miss}}$ of 30 GeV is required to reject QCD jets as background. The missing transverse momentum reconstruction method used, MET_LocHadTopo, is based on the reconstruction of $E_{\mathrm{T}}^{\mathrm{miss}}$ using the LCW calibration method (see Sec. 4.4.3).

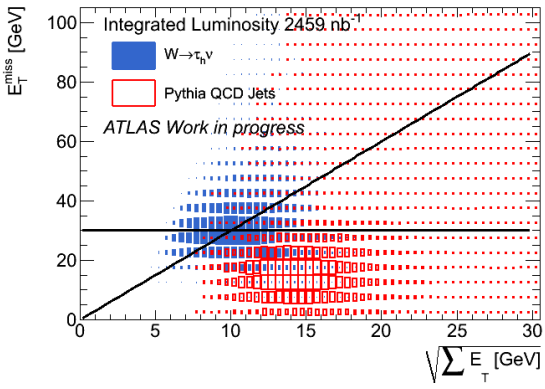

Figure 8.2: Distribution of events in the $E_{\mathrm{T}}^{\mathrm{miss}}$–$\sqrt{\sum E_{\mathrm{T}}}$ plane after the trigger requirement for QCD jet background and the signal $W \to \tau_{\mathrm{h}}\nu_{\tau}$ Monte Carlo samples. Each sample is scaled according to its cross section. The applied $E_{\mathrm{T}}^{\mathrm{miss}}$ and $S_{E_{\mathrm{T}}^{\mathrm{miss}}}$ criteria are shown as solid lines [138].

Tau selection The τ lepton candidate has to pass the medium BDT τ lepton identification for 1-prong τ lepton candidates and the tight BDT τ lepton identification for multi-prong τ lepton candidates. It should also have a transverse momentum between 20 and 60 GeV. Furthermore, only τ lepton candidates with $|\eta| < 2.5$ and not in $1.3 < |\eta| < 1.7$ are considered.

Lepton vetoes Lepton vetoes are needed for the suppression of EW background sources ($W \to e\nu_e$, $W \to \mu\nu_{\mu}$, $W \to \tau_{\mathrm{l}}\nu_{\tau}$, $Z \to ee$, $Z \to \mu\mu$, and $Z \to \tau\tau$), in which a τ_{h} is faked from misidentified electrons or muons, or from additional jets in the event. To supress electrons and muons faking a τ_{h} lepton, a (tight) electron and muon veto provided by the τ_{h} identification algorithm is applied. Events with leptonically decaying W and Z bosons, where the electron or muon is correctly reconstructed and the τ_{h} lepton comes from an additional jet, are rejected by applying a cut on the transverse momentum of the electron or muon at $p_{\mathrm{T}} > 15$ GeV.

Significance of $E_{\mathrm{T}}^{\mathrm{miss}}$ The significance of $E_{\mathrm{T}}^{\mathrm{miss}}$ is defined as:

$$S_{E_{\mathrm{T}}^{\mathrm{miss}}} = \frac{E_{\mathrm{T}}^{\mathrm{miss}}[\mathrm{GeV}]}{0.5\sqrt{\mathrm{GeV}}\sqrt{\sum E_{\mathrm{T}}[\mathrm{GeV}]}}. \tag{8.1}$$

The significance of $E_{\mathrm{T}}^{\mathrm{miss}}$ is a strong variable to suppress QCD background, which has lower $S_{E_{\mathrm{T}}^{\mathrm{miss}}}$ values than for signal $W \to \tau_{\mathrm{h}}\nu_{\tau}$ events as illustrated in Fig. 8.2. Events are rejected if $S_{E_{\mathrm{T}}^{\mathrm{miss}}} < 6$.

8.2.4 Summary of the event selection

To summarise, the following cuts are applied in the event selection:

- Preselection cuts:
  - GRL

  - Trigger: EF_tau12_loose_xe20_noMu for the first and EF_tau16_medium_xe22_noMu for the second data period

- Cleaning cuts:
  - Collision candidate: at least one vertex with $N_{\text{trk}} \geq 3$
  - Jet/$E_{\text{T}}^{\text{miss}}$ cleaning: reject event if there is any loose bad jet with $p_{\text{T}} > 20\,\text{GeV}$
  - Jet in crack region: reject the event if there is a jet with $p_{\text{T}} > 20\,\text{GeV}$ and $1.3 < |\eta| < 1.7$
  - $\Delta\phi\left(\text{jet}, E_{\text{T}}^{\text{miss}}\right)$: reject event if $\min\left(\Delta\phi\left(\text{jet}, E_{\text{T}}^{\text{miss}}\right)\right) < 0.5$ for jets with $p_{\text{T}} > 20\,\text{GeV}$
- Event signature cuts:
  - $E_{\text{T}}^{\text{miss}}$ cut: $E_{\text{T}}^{\text{miss}} > 30\,\text{GeV}$
  - Tau lepton selection: select the τ lepton candidate passing BDT identification (medium for 1-prong and tight for multi-prong candidates):
    - require this candidate to have $20\,\text{GeV} < E_{\text{T}} < 60\,\text{GeV}$
    - require this candidate to have $|\eta| < 2.5$
    - require the candidate not to be in the crack region $1.3 < |\eta| < 1.7$
- Lepton vetoes:
  - require the τ lepton candidate to pass the τ lepton tight electron and muon vetoes
  - electron veto: reject the event, if there is an electron with $p_{\text{T}} > 15\,\text{GeV}$
  - muon veto: reject the event, if there is a muon with $p_{\text{T}} > 15\,\text{GeV}$
- Significance of $E_{\text{T}}^{\text{miss}}$: $S_{E_{\text{T}}^{\text{miss}}} = \frac{E_{\text{T}}^{\text{miss}}}{0.5\sqrt{\sum E_{\text{T}}}} \geq 6$

8.3 Background estimation

8.3.1 Electroweak background estimation

There is a good agreement between data and MC simulation in the W boson cross section measurement at ATLAS, where the W boson decays into an electron or muon [218, 219]. Therefore, the number of signal and EW background events is also extracted from MC simulation here. An embedding technique was used as a cross-check of the results derived from MC. The muon in a high-purity sample of $W \to \mu\nu_\mu$ events is replaced by a simulated τ_{h} lepton. Only the τ lepton decay and its detector response are taken from the simulation. All other properties of the event are extracted from the $W \to \mu\nu_\mu$ data events. Details of the embedding technique used can be found in [138]. Figure 8.3 shows the good agreement of $S_{E_{\text{T}}^{\text{miss}}}$ between the τ_{h}-embedded and a $W \to \tau_{\text{h}}\nu_\tau$ MC sample. This is a good indication that MC simulation can be used reliably to estimate the rate of signal and EW background processes.

8.3.2 QCD jet background estimation

The QCD jet background is estimated with a data driven method, the ABCD method introduced in [216], due to the limited statistics of the available MC samples.[3] For this data driven ABCD

[3] The selection process removes QCD jet backgrounds from MC samples almost completely. The remaining events then have to be scaled by huge factors, resulting in very large uncertainties.

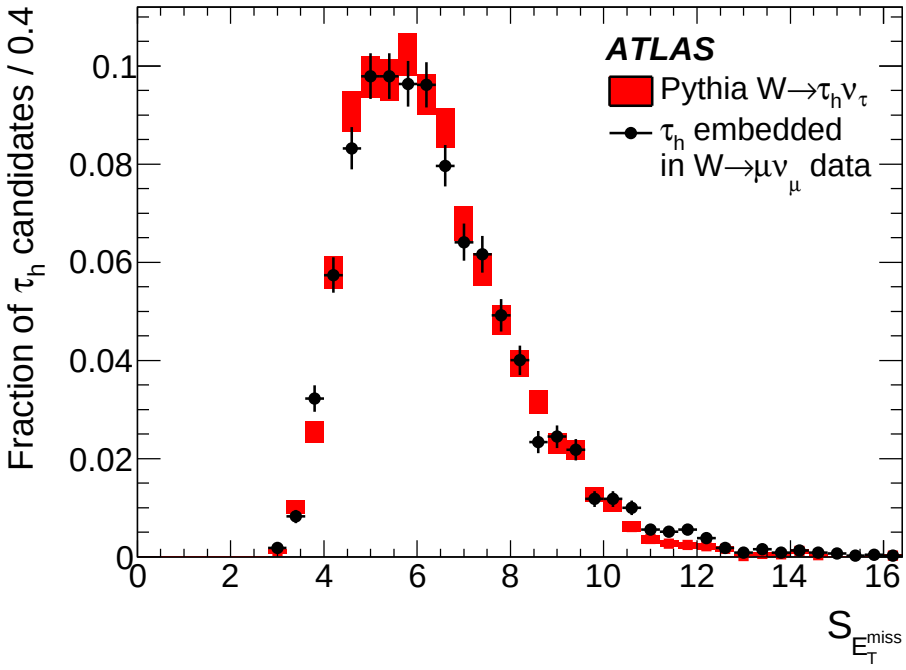

Figure 8.3: Distribution of $S_{E_{\mathrm{T}}^{\mathrm{miss}}}$ for the τ_{h}-embedded $W \to \mu\nu_{\mu}$ data sample (points) and simulated $W \to \tau_{\mathrm{h}}\nu_{\tau}$ events (red boxes), including statistical uncertainties [137].

method, four regions are defined as illustrated in Fig. 8.4: one signal-dominated region (signal region) following the event selection and three background-dominated regions (control regions) defined by inverting the selections on $S_{E_{\mathrm{T}}^{\mathrm{miss}}}$ and/or the τ_{h} lepton identification (ID). This results in these four regions used in this analysis:

- Region A: $S_{E_{\mathrm{T}}^{\mathrm{miss}}} > 6.0$ and τ_{h} lepton candidates satisfying the signal medium/tight τ_{h} lepton ID requirements,
- Region B: $S_{E_{\mathrm{T}}^{\mathrm{miss}}} < 4.5$ and τ_{h} lepton candidates satisfying the signal-region medium/tight τ_{h} lepton ID requirements,
- Region C: $S_{E_{\mathrm{T}}^{\mathrm{miss}}} > 6.0$ and τ_{h} lepton candidates satisfying a looser τ_{h} lepton ID but failing the medium/tight τ_{h} lepton ID requirements of the signal region, and
- Region D: $S_{E_{\mathrm{T}}^{\mathrm{miss}}} < 4.5$ and τ_{h} lepton candidates satisfying a looser τ_{h} lepton ID but failing the medium/tight τ_{h} lepton ID requirements of the signal region

Region A is the signal region and regions B, C, and D control regions. The contamination from signal and EW background processes is too large for the loose BDT τ_{h} lepton identification in the control regions C and D, and so, a looser cut on the BDTJet score[4] is applied (BDTJet score < 0.5 for τ_{h} leptons with one track and BDTJet score < 0.45 for τ_{h} leptons with more than one track).

[4]The BDTJet score corresponds to the jet BDT score defined in Sec. 4.4.2.

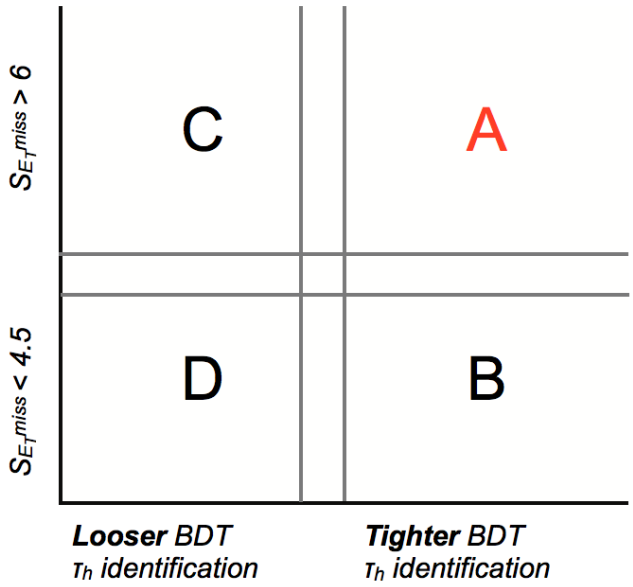

Figure 8.4: QCD jet background estimation: signal region A and the three control regions B,C, and D [138].

The ABCD method used has some assumptions, which are partly fulfilled (see [138]). The signal and EW background contribution in the control regions has to be negligible and the shape of the $S_{E_T^{miss}}$ distribution for the QCD jet background must be independent of the τ_h lepton identification requirements.

The number of QCD jet background events can be calculated as

$$N^A_{QCD} = \frac{N^B N^C}{N^D} \tag{8.2}$$

with N^i as number of observed events in region i. To include the signal and background contaminations in the control regions B, C, and D, N^i has to be corrected

$$N^i \to N^i_{corr} = N^i - c_i(N^A - N^A_{QCD}) \qquad i = B, C, D \tag{8.3}$$

with

$$c_i = \frac{N^i_{sig} + N^i_{EW}}{N^A_{sig} + N^A_{EW}}, \qquad i = B, C, D \tag{8.4}$$

as the ratio of simulated signal and EW background events in the control region i over those in the signal region A. Using Eqs. (8.3) and (8.4), (8.2) becomes

$$N^A_{QCD} = \frac{[N^B - c_B(N^A - N^A_{QCD})][N^C - c_C(N^A - N^A_{QCD})]}{N^D - c_D(N^A - N^A_{QCD})}. \tag{8.5}$$

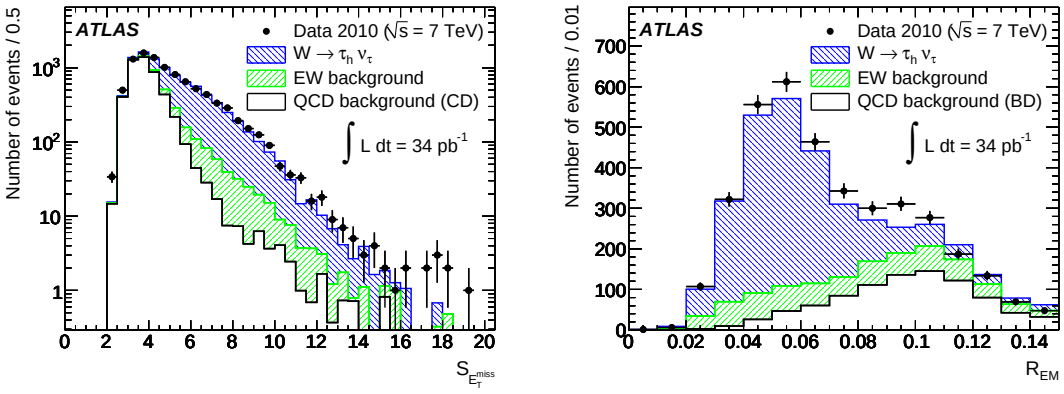

(a) (b)

Figure 8.5: (a) $S_{E_{\mathrm{T}}^{\mathrm{miss}}}$ distribution in the combined region AB, extended over the full $S_{E_{\mathrm{T}}^{\mathrm{miss}}}$ range. The QCD jet background shape was extracted from regions CD. Monte Carlo signal and EW background in regions AB are also shown; (b) the τ_{h} lepton identification variable R_{EM} in the combined region AC. The QCD jet background shape was extracted from regions BD. Monte Carlo signal and EW background in regions AC are also shown [137].

Thereby, the uncertainty of the calculation of the c_i coefficients, due to limited MC statistics, and the statistical uncertainty of the data in the four regions is both included in the statistical error of $N_{\mathrm{QCD}}^{\mathrm{A}}$.

8.4 Results of the event selection

The event selection is applied to data and MC. The results are summarised in Tabs. 8.5 and 8.6. It is transparent out of the cut flow (Tab. 8.5), that 2335 events are selected in data after the event selection, whereby 2095 events are signal (1811) and EW background events according to the MC samples. QCD events are not considered in these numbers. The previously described ABCD method is used for the estimation for the QCD jet background and can estimate 127 QCD events in the signal region A (see Tab. 8.6).

For evaluating the quality of the description of the selected data by the background models, Fig. 8.5 shows the $S_{E_{\mathrm{T}}^{\mathrm{miss}}}$ and R_{EM} distributions for data in comparison to MC simulation and QCD jet background estimation in combined regions of the ABCD method. Characteristic properties of $W \to \tau_{\mathrm{h}}\nu_\tau$ events are given in Fig. 8.6. A good agreement between data and MC predictions can be noticed in all distributions.

8.5 Methodology for cross section measurement

The fiducial cross section is measured in a phase space region determined by the geometrical acceptance of the detector and the kinematic event selection of the analysis:

$$\sigma^{\mathrm{fid}}_{W\to\tau_{\mathrm{h}}\nu_\tau} = \sigma_W \times BR\,(W \to \tau\nu_\tau) \times BR\,(\tau \to \mathrm{had}\nu) = \frac{N_{\mathrm{obs}} - N_{\mathrm{bkg}}}{C_W \mathcal{L}}, \tag{8.6}$$

	Data	$W \to \tau_h \nu_\tau$	$W \to \tau\nu_\tau$	$W \to e\nu_e$	$W \to \mu\nu_\mu$	$Z \to \tau\tau$	$Z \to ee$	$Z \to \mu\mu$	$t\bar{t}$ lep	$t\bar{t}$ had
Events	1919991948	232377	126672	358359	358656	34033.7	34644.3	33917.5	2746.2	2185.9
GRL	165757532	232377	126672	358359	358656	34033.7	34644.3	33917.5	2746.2	2185.9
Trigger	6879843	20110.6±80.8	7507.3±49.6	175936±151.7	5620.4±37.2	2663.7±9.1	2306.1±8.5	707.1±4.8	1304.7±3.4	394.5±5.4
Collision cleaning	6879795	20107.5±80.8	7506.9±49.6	175882±151.7	5620.4±37.2	2663.6±9.1	2306±8.5	707.1±4.8	1304.7±3.4	394.5±5.4
Jet cleaning	6873901	20107.5±80.8	7506.9±49.6	175882±151.7	5620.4±37.2	2663.6±9.1	2306±8.5	707.1±4.8	1304.7±3.4	394.5±5.4
Jet in gap veto	4962570	16372.6±73.6	6123.1±45	143338±148.6	4504.7±33.4	2085.7±8.1	1458.9±6.9	569.6±4.3	673.8±3	175.4±3.8
$\min\left(\Delta\phi\left(\text{jet}, E_{\text{T}}^{\text{miss}}\right)\right) > 0.5$	2421757	15326.5±71.4	5770.8±43.8	137755±147.6	4215.8±32.3	1659.3±7.3	656.4±4.7	526.9±4.2	375.6±2.4	27.2±1.6
$E_{\text{T}}^{\text{miss}} > 30\,\text{GeV}$	350444	11899±63.5	3718±35.5	104857±138.1	3829.4±30.8	1145.2±6.1	19.3±0.8	459±3.9	349.4±2.3	6.5±0.8
$p_{\text{T}}(\tau_h) > 20\,\text{GeV}$	321246	11599.8±62.8	3545.1±34.7	103800±137.7	3760.5±30.6	1122.7±6	18.7±0.8	450.7±3.8	349.2±2.3	6.5±0.8
τ_h identification	62754	5526.4±44.1	1112.4±19.6	23918.8±75.6	662.5±12.9	579.8±4.4	5.2±0.4	124.1±2	120.3±1.4	1.3±0.4
$p_{\text{T}}(\tau_h) < 60\,\text{GeV}$	37199	4789.6±41.1	767.3±16.4	19648±69	280.1±8.4	445.8±3.9	3.2±0.3	54.5±1.4	50.9±0.9	0.1±0.1
τ_h ID ele/mu veto	10199	3975.9±37.5	44±3.9	452.7±10.8	202.1±7.2	347.1±3.4	0.1±0	38.1±1.1	18.2±0.6	0.1±0.1
Electron veto	9912	3959.4±37.5	35.7±3.5	196±7.1	197.7±7.1	344.1±3.4	0±0	36.7±1.1	15±0.5	0.1±0.1
Muon veto	9604	3958.8±37.5	29.4±3.2	195.9±7.1	110.9±5.3	259.4±2.9	0±0	2.9±0.3	10.9±0.4	0.1±0.1
$S_{E_{\text{T}}^{\text{miss}}} > 6$	2335	1811.2±25.4	15.1±2.3	92.5±4.9	56.1±3.8	112.1±1.9	0±0	1.4±0.2	6.4±0.3	0±0

Table 8.5: Cut flow table of the event selection. The MC is normalised to an integrated luminosity of $34.3\,\text{pb}^{-1}$ [138].

	A	B	C	D
N^i (Data)	2335	4796	1577	27636
N^i_{sig} $(W \to \tau_{\text{h}}\nu_\tau)$	1811 ± 25	683 ± 16	269 ± 8	93 ± 5
N^i_{EW}	284 ± 7	118 ± 4	388 ± 9	90 ± 4
c_i		0.38 ± 0.01	0.31 ± 0.01	0.087 ± 0.003
N^i_{QCD}	127 ± 8	3953 ± 75	885 ± 45	27444 ± 166

Table 8.6: Estimated sample compositions and c_i factors (as defined in Eq. (8.4)) in the signal region A and control regions B, C, and D defined in the text [137].

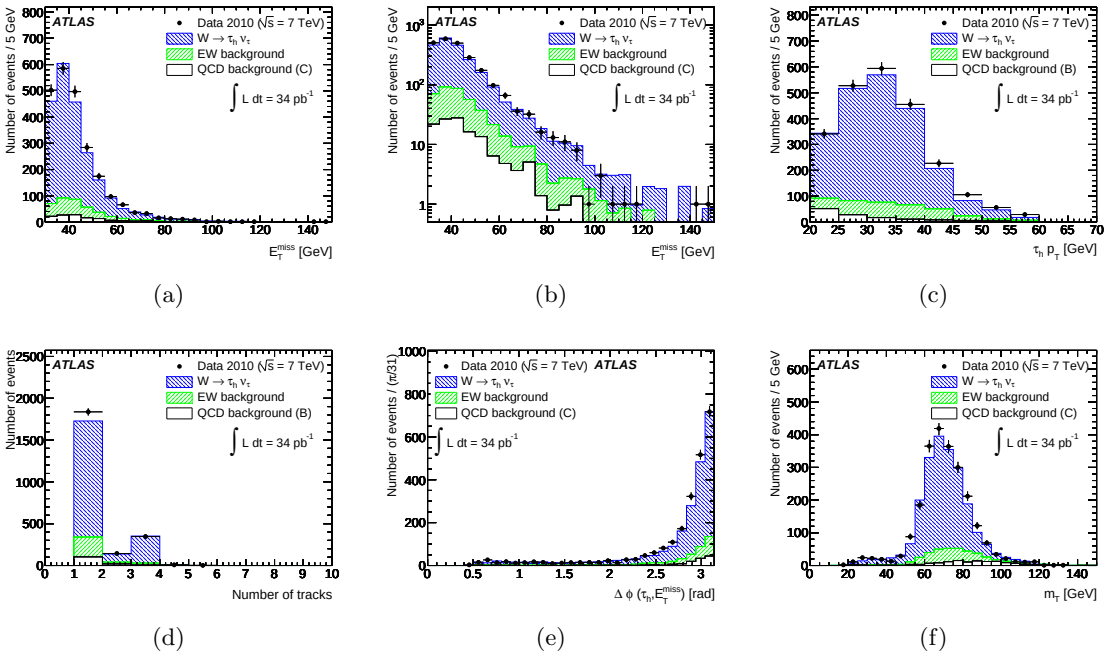

(a) (b) (c)

(d) (e) (f)

Figure 8.6: (a) Distribution of missing transverse energy in signal region A on a linear scale. The QCD background shape was extracted from control region C. (b) Same distribution on a logarithmic scale. (c) Transverse momentum and (d) number of tracks of τ_{h} lepton candidates in signal region A. The QCD jet background shape was extracted from control region B. (e) Distribution of $\Delta\phi\left(\text{jet}, E_{\text{T}}^{\text{miss}}\right)$, and (f) transverse mass $m_{\text{T}} = \sqrt{2 \cdot p_{\text{T}}^{\tau_{\text{h}}} \cdot E_{\text{T}}^{\text{miss}} \cdot \left(1 - \cos\Delta\phi\left(\tau_{\text{h}}, E_{\text{T}}^{\text{miss}}\right)\right)}$ in signal region A. The QCD jet background shape was extracted from control region C. The expectation from Monte Carlo signal and EW background in region A are also shown [137].

where N_{obs} is the number of observed events in data, N_{bkg} the number of estimated (QCD and EW) background events, and $\mathcal{L}$ the integrated luminosity. The factor C_W is a correction factor which takes into account the trigger efficiency, the τ_{h} reconstruction and identification efficiencies, and the efficiency of the selection cuts within the detector acceptance

$$C_W = \frac{N_{\text{reco, all cuts}}}{N_{\text{gen, kin/geom}}}, \tag{8.7}$$

where $N_{\text{reco, all cuts}}$ is the number of fully simulated signal events passing the reconstruction, trigger and selection cuts used in the analysis, and $N_{\text{gen, kin/geom}}$ the number of simulated signal events within the acceptance region.

The acceptance region is defined, based on the decay products of a τ_{h} lepton decay:

- $20\,\text{GeV} < p_{\text{T}}^{\tau_{\text{h,vis}}} < 60\,\text{GeV}$,
- $|\eta^{\tau_{\text{h,vis}}}| < 2.5$, excluding $1.3 < |\tau_{\text{h,vis}}| < 1.7$,
- $(\sum p^{\nu})_{\text{T}} > 30\,\text{GeV}$, and
- $|\Delta\phi\,(\tau_{\text{h,vis}}, \sum \nu)| > 0.5$.

A visible hadronically decaying τ lepton $\tau_{\text{h,vis}}$ is the sum of the four-vectors of the decay products, excluding neutrinos, from a simulated hadronic τ lepton decay. Photons, radiated from the τ_{h} lepton and from its decay products, are considered in the $\tau_{\text{h,vis}}$ lepton if they are within a cone of $\Delta R < 0.4$ with respect to the τ_{h} lepton. The $\sum \nu$ is defined analogously by the sum of the four-vectors of the neutrinos and corresponds to missing energy/momentum in the detector. By this definition, the transverse component of the sum of the simulated neutrino four-vectors $(\sum p^{\nu})_T$ corresponds to the missing transverse momentum $E_{\text{T}}^{\text{miss}}$.

Using the kinematic and geometrical signal acceptance

$$A_W = \frac{N_{\text{gen, kin/geom}}}{N_{\text{gen, all}}}, \tag{8.8}$$

where $N_{\text{gen, all}}$ is the total number of simulated signal events and $N_{\text{gen, kin/geom}}$ is as defined previously in Eq. (8.7), the total cross section can be calculated as follows

$$\sigma^{\text{tot}}_{W\to\tau_{\text{h}}\nu_\tau} = \sigma^{\text{fid}}_{W\to\tau_{\text{h}}\nu_\tau}/A_W = \frac{N_{\text{obs}} - N_{\text{bkg}}}{A_W C_W \mathcal{L}}. \tag{8.9}$$

A_W and C_W are estimated by using a PYTHIA Monte Carlo signal $W \to \tau\nu_\tau$ sample with the dataset identification number 107054, using the AMBT1 tune [176] and PDF set MRST2007lomod/MRSTLO* [201] (see Tab. 8.3). The acceptance is found to be $A_W = 0.0975 \pm 0.0004$ (stat.) and the correction factor $C_W = 0.0799 \pm 0.0011$ (stat.).

In the following, the procedure of the acceptance A_W calculation is described in more detail. The acceptance calculation is restricted to MC generator information only. To use the MC truth particles correctly, one has to pay attention to the particle data group identification numbers (pdgID) [12] and the status code information of the particles. Concerning the HepMC event record (see Sec. 6.1), a status code of 1 means a stable particle, 2 a decaying particle and status codes of 3 and larger are so-called 'documentary' particles, intended for internal use within the generators. In reality, many intermediate particles like the W boson have different status codes

Cut	$W \to \tau_{\mathrm{h}}\nu_\tau$
Events (no cut)	639288.0 ± 799.6
τ_{h} p_{T}	317343.0 ± 563.3
τ_{h} η	204831.0 ± 452.6
$(\sum p^{\nu})_{\mathrm{T}}$	65217.0 ± 255.4
$\lvert\Delta\phi\,(\tau_{\mathrm{h,vis}}, \sum \nu)\rvert$	62333.0 ± 249.7
Acceptance $A_W = \lvert\Delta\phi\,(\tau_{\mathrm{h,vis}}, \sum \nu)\rvert$/Events	0.0975 ± 0.0004

Table 8.7: Number of events (no scaling of the MC) after the acceptance cuts and the resulting acceptance.

in different generators. The challenge in the acceptance calculation is to deal with the status codes and pdgIDs of the particles in the generators. This procedure is summarised in Fig. 8.9 for PYTHIA and MC@NLO/HERWIG (for the determination of systematic uncertainties of A_W, see Sec. 8.6.4), the generators used. For getting a $W \to \tau_{\mathrm{h}}\nu_\tau$ event at generator level in PYTHIA, one has to look for a W boson with status code 3 that can decay into a τ lepton with status code 3 (as 'documentary' particle) and a W boson with status code 2 or 10902.[5] In order to find the $W \to \tau_{\mathrm{h}}\nu_\tau$ decay chain, one has to continue with these W bosons and check their decay particles which must be either photons or τ leptons with status code 2. These τ leptons can radiate photons and decay leptonically, with neutrinos and a lepton in the decay chain, and hadronically, with a neutrino and no other particle or a neutrino and a W boson, which can radiate further in the decay chain. To get the $W \to \tau_{\mathrm{h}}\nu_\tau$ decay, one has to look for the hadronic decay, which means finding a neutrino and no further particle or a neutrino and a W boson in the event. If such an event is detected, one can determine the visible part of the τ_{h} lepton and the sum of the neutrinos $\sum \nu$, the variables for the acceptance calculation, from the particles in this decay chain. All radiated photons found in the event are included in the acceptance calculation as described above. The procedure for MC@NLO/HERWIG is equivalent, using different status codes as given in Fig. 8.9.

A cut flow table for the acceptance calculation is given in Tab. 8.7. The number of events represent the pure MC statistics, they are not scaled to a specific integrated luminosity. Figures 8.7 and 8.8 show variables of the $\tau_{\mathrm{h,vis}}$ lepton and the $\sum \nu$ before any acceptance cut, which look as expected. The corresponding distributions following the defined acceptance cuts are shown in Figs. B.1 – B.8. In total, an acceptance of $A_W = 0.0975 \pm 0.0004$ (stat.) is estimated, as mentioned above.

With the determined acceptance A_W and the correction factor C_W, the measured fiducial cross section of the $W \to \tau_{\mathrm{h}}\nu_\tau$ decay is

$$\sigma^{\mathrm{fid}}_{W\to\tau_{\mathrm{h}}\nu_\tau} = (0.70 \pm 0.02\ (\mathrm{stat.}))\ \mathrm{nb} \tag{8.10}$$

and the total cross section

$$\sigma^{\mathrm{tot}}_{W\to\tau_{\mathrm{h}}\nu_\tau} = (7.2 \pm 0.2\ (\mathrm{stat.}))\ \mathrm{nb}. \tag{8.11}$$

Alternative analyses are performed to confirm these results [138]. For example, the BDT τ_{h}

[5] The status code of the τ leptons changes by PHOTOS if a photon is radiated.

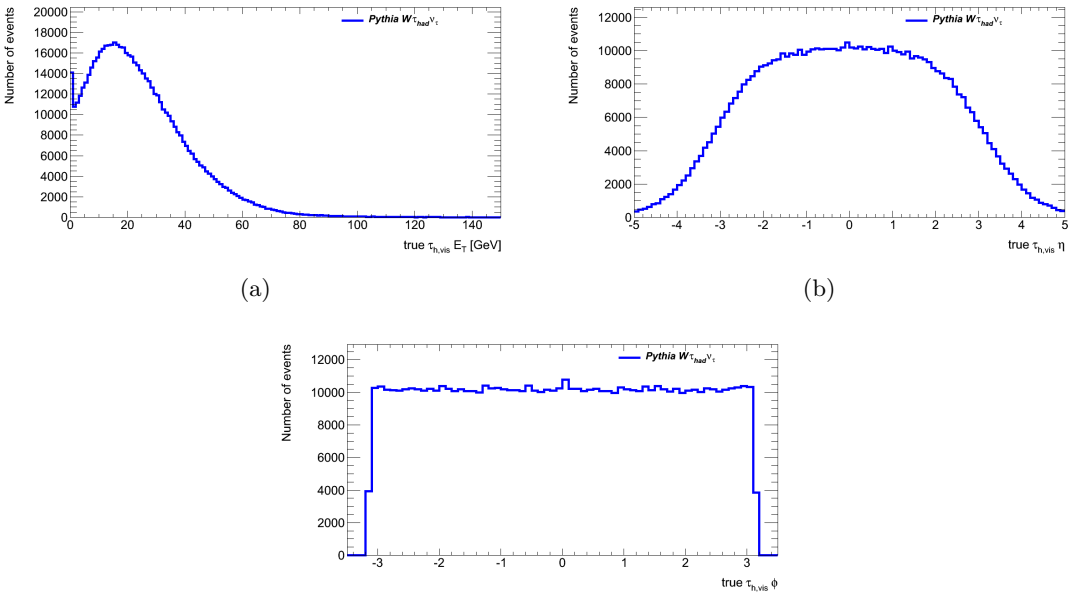

(a) (b)

(c)

Figure 8.7: (a) Visible transverse energy, (b) pseudorapidity η, and (c) angle ϕ of the true $\tau_{\mathrm{h,vis}}$ lepton before any acceptance cut.

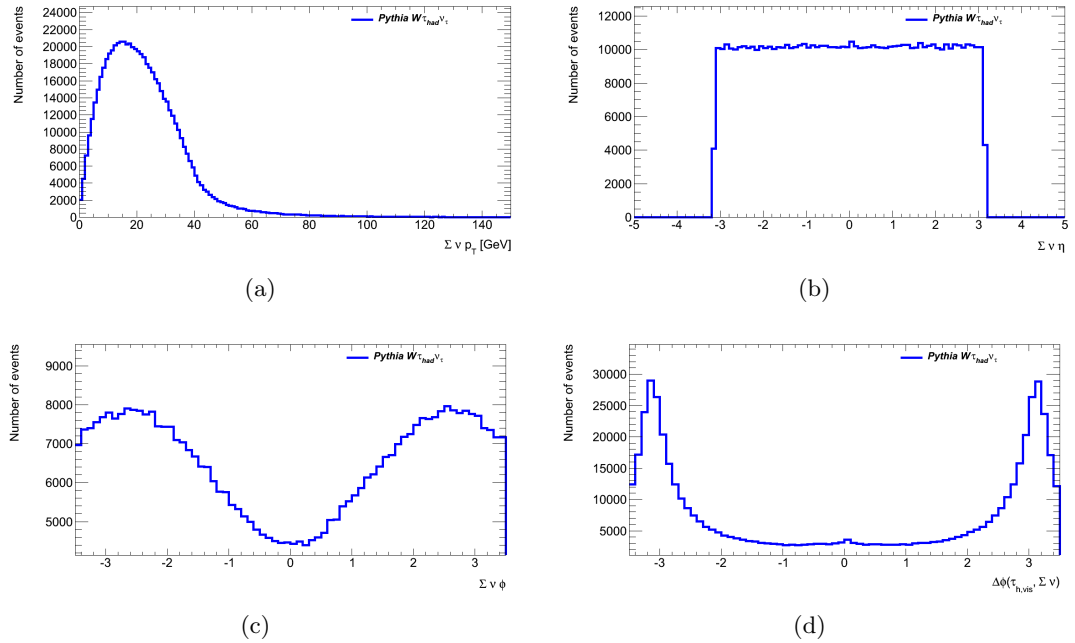

(a) (b)

(c) (d)

Figure 8.8: (a) Transverse momentum, (b) pseudorapidity η, (c) angle ϕ of the sum of the neutrinos $\sum\nu$, and (d) angle $\Delta\phi$ between the true $\tau_{\mathrm{h,vis}}$ lepton and the sum of the neutrinos $\sum\nu$ before any acceptance cut.

lepton identification is replaced by a simple cut based identification (see Sec. 4.4.2). Furthermore, the signal selection is rectricted to events with only one reconstructed vertex to study the influence of the pile-up effect. These alternative studies yield results consistent with those shown here.

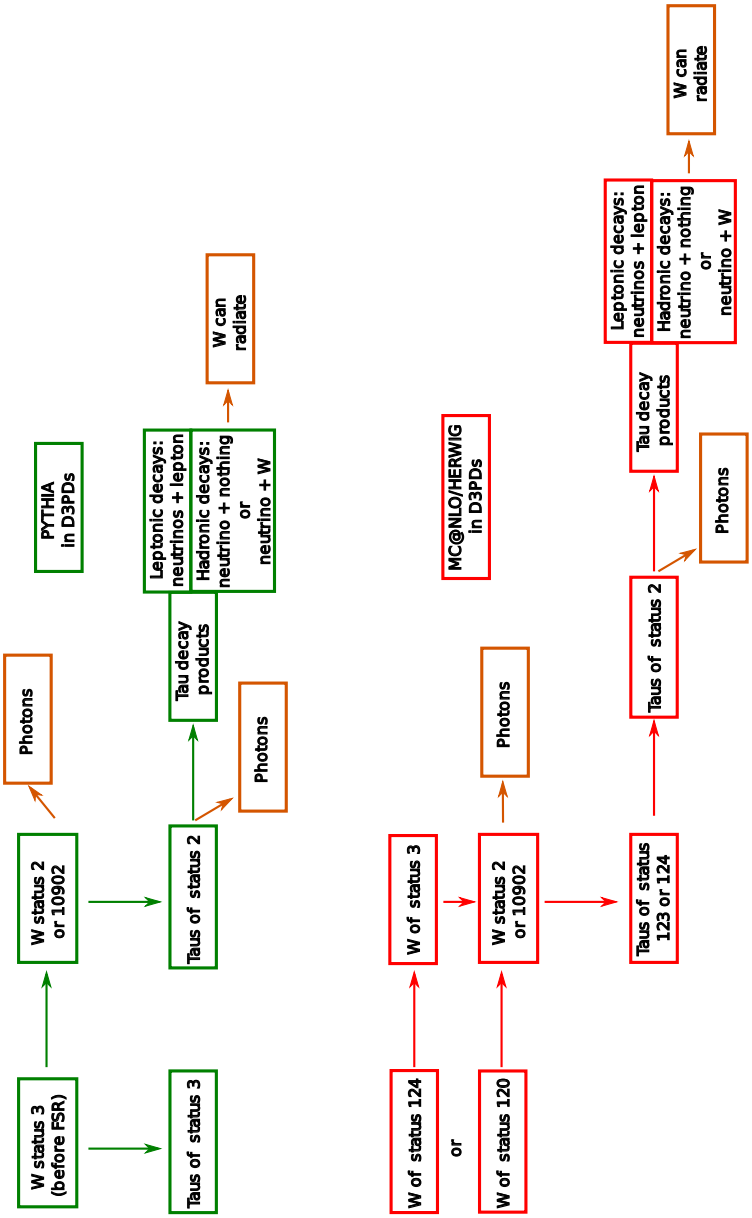

Figure 8.9: Strategy for the acceptance calculation A_W: look for a W boson with the appropriate status and navigate down to the τ lepton decay products (idea from [225]).

Sample	Cross Section	Combination	Reference
$W \to e\nu_e / W \to \mu\nu_\mu$	$(10.391 \pm 0.022(\text{stat.}) \pm 0.238(\text{syst.}) \pm 0.353(\text{lumi.}) \pm 0.312(\text{acc.}))$ nb	3.8%	[203, 218]
$W \to \tau_\text{l}\nu_\tau$	$(10.46 \pm 0.52(\text{ comb.}))$ nb	5%	NNLO [22, 220]
$Z \to ee / Z \to \mu\mu$	$(0.945 \pm 0.006(\text{stat.}) \pm 0.011(\text{syst.}) \pm 0.032(\text{lumi.}) \pm 0.038(\text{acc.}))$ nb	4.2%	[203, 218]
$Z \to \tau\tau$	$(0.99 \pm 0.05(\text{ comb.}))$ nb	5%	NNLO [22, 220]
$t\bar{t}$	$(180 \pm 9(\text{stat.}) \pm 15(\text{syst.}) \pm 6(\text{lumi.}))$ pb	9.7%	[226]

Table 8.8: Cross section of backgrounds as measured by ATLAS [138].

8.6 Systematic uncertainties

This section describes briefly the systematic uncertainties of the $W \to \tau\nu_\tau$ cross section measurement, which are summarised in [137] and [138] in more detail, with focus on uncertainties of the acceptance calculation.

8.6.1 Systematic uncertainties of Monte Carlo predictions

Cross sections

The uncertainty of the cross sections of each of the background processes lies between 3.8% and 9.7%. A summary of these uncertainties is given in Tab. 8.8. The uncertainty is taken from the ATLAS measurement, if a measurement is available [203, 218]. Otherwise, the uncertainty of the theoretical NNLO cross section is used [22, 220].

Luminosity

The uncertainty of the integrated luminosity, taken from the luminosity determination in pp collision at $\sqrt{s} = 7\,\text{TeV}$ at ATLAS [224], is 3.4%.

Pile-up effect

There is also a systematic on the pile-up effect, due to the reweighting procedure in the MC samples. This reweighting procedure itself is limited by the statictical uncertainty of data and MC. The systematic uncertainty from the reweighting factors is evaluated by varying these factors within their statistical uncertainty and comparing the results after the event selection. The systematic uncertainties are 0.4% for $W \to e\nu_e$, 2.3% for $W \to \mu\nu_\mu$, 2.6% for $W \to \tau_\text{l}\nu_\tau$, and 1.2% for $Z \to \tau\tau$ processes.

Trigger efficiency

The trigger efficiency for the combined E_T^miss and τ_h triggers is estimated using only MC. This is because a determination on real data is not possible within the statistics of 2010 ATLAS data. The systematic uncertainty for each of the triggers of the two periods is determined by dividing the combined trigger in its individual trigger parts, E_T^miss and τ_h. On them, a selection of cuts of the event selection, like the cut on BDT τ_h ID, on $\Delta\phi\left(\text{jet}, E_\text{T}^\text{miss}\right)$, and $S_{E_\text{T}^\text{miss}}$, is applied on a pure and unbiased data sample enriched with $W \to \tau_\text{h}\nu_\tau$. The response of the individual trigger part is compared to the response in the MC signal sample. The differences are integrated over the offline τ_h lepton p_T and the E_T^miss range [138]. The uncertainty of the combined trigger is calculated by the square root of the sum of the square of both trigger parts. The combination of the two combined triggers used in the two data periods gives an uncertainty of 6.1%, which is

Signature	Systematic
tau12_loose	6.5 %
xe20_noMu	1.0 %
EF_tau12_loose_xe20_noMu	6.6 %
EF_tau16_medium	5.0 %
xe22_noMu	3.2 %
EF_tau16_medium_xe22_noMu	5.9 %
Combination	6.1 %

Table 8.9: Summary of trigger systematics [138].

calculated by the square root of the sum of the square of both triggers. The individual results are summarised in Tab. 8.9.

Jet cleaning

The systematic effect from the jet cleaning is negligible (see Sec. 8.2.3).

Energy scale and $E_{\mathrm{T}}^{\mathrm{miss}}$ scale

The signal and background efficiencies depend on the energy scale of the calibrated τ_{h} lepton candidates and on the energy scales of the clusters, which are needed for the computation of $E_{\mathrm{T}}^{\mathrm{miss}}$ and $S_{E_{\mathrm{T}}^{\mathrm{miss}}}$. The uncertainty due to the cluster energy within $|\eta| < 3.2$ varies between 3% for high-p_{T} clusters and less than 10% for p_{T} of 500 MeV [96]. In the forward region, $|\eta| > 3.2$, it is 10%. All clusters in the event are scaled corresponding to these uncertainties and $E_{\mathrm{T}}^{\mathrm{miss}}$ and $\sum E_{\mathrm{T}}$ are recalculated to determine the uncertainty of $E_{\mathrm{T}}^{\mathrm{miss}}$ and $S_{E_{\mathrm{T}}^{\mathrm{miss}}}$. Simultaneuosly, the energy scale of the τ_{h} lepton is varied according to its uncertainty [132]. The uncertainty fluctuates between 2.5% and 10%. It depends on the number of tracks of the τ_{h} lepton, its transverse momentum p_{T} and the η range. Additionally, the sensitivity of the signal and background efficiencies to the $E_{\mathrm{T}}^{\mathrm{miss}}$ resolution was studied. It was found that it varies for the signal and EW background between 6.7% and 8.7%, respectively.

Hadronically decaying τ lepton identification efficiency

Hadronically decaying τ lepton candidates are identified using the medium BDT ID for 1-prong τ_{h} leptons and the tight BDT ID for multi-prong τ_{h} leptons. It was found that the reconstruction and identification efficiencies are mainly compromised by the detector geometry, the noise thresholds of calorimeter cells for cluster reconstruction, the underlying event model, and by the hadronic shower model. These uncertainties are evaluated in [132] separately as a function of the τ_{h} lepton p_{T} for 1-prong or multi-prong τ leptons and low or high multiplicity of primary vertices per event. This results in systematic uncertainties in the signal and EW background efficiencies of 9.6% and 4.1%, respectively.

Jet and lepton fake rates of τ_{h} lepton candidates

The τ_{h} lepton missidentification probability from jets are determined by using a selection of $W \to l\nu_l + \text{jets}$ events ($l = e, \mu$) and measuring the fraction of identified to reconstructed τ

lepton candidates in data and MC. This fraction is 31% (28%) for the electron (muon) channel. As systematic uncertainty, the highest value is used, which has to be applied to the fraction of background events, where the lepton is not reconstructed and the τ_{h} lepton candidate is mistaken by a jet. The EW background has an uncertainty of 7.2%.

The τ_{h} lepton fake rate from electrons is determined in $Z \rightarrow ee$ events by a 'tag-and-probe' method [227]. The τ_{h} lepton idenfication and τ_{h} lepton electron veto is applied to one of the electrons. The systematic uncertainty is the difference between the fake rate in data and MC as a function of η and comes up to 4.5% for the EW background.

The missidentification rate from muons is negligible.

Electron and muon reconstruction and identification efficiency

A systematic uncertainty turns up due to the fact that reconstructed electrons/muons passing the electron/muon identification are applied to reject the EW background. The systematic uncertainties on the electron and muon reconstruction and identification efficiencies are rather small and have been determined using a 'tag-and-probe' method on $Z \rightarrow ee$ events, respectively $Z \rightarrow \mu\mu$ events [228–230]. It is 1.2% for the electrons and 0.3% for the muons in each case for the EW background.

Underlying event modelling

In order to study the effect of the underlying event modelling on the signal and background selection, alternative models to the AMBT1 tune [176] used in this thesis are studied. In particular, $E_{\mathrm{T}}^{\mathrm{miss}}$ values are expected to differ. A cut flow table for the available MC samples of the Perugia2010 tune [178] is shown in Tab. 8.10. The deviation after full event selection with respect to the default samples is taken as systematic uncertainties. It amounts to 1.3% for $W \rightarrow \tau_{\mathrm{h}}\nu_{\tau}$ and 1.1% for $Z \rightarrow \tau\tau$, which is applied to all MC background samples.

The reasonability of this systematic uncertainty could be verified with comparisons to an embedding sample (see Sec. 8.3.1). The comparison of $W \rightarrow \mu\nu_{\mu}$ data to $W \rightarrow \mu\nu_{\mu}$ MC events results in a difference of less than 1% [138].

8.6.2 Systematic uncertainties of QCD jet background estimation

The uncertainty of QCD jet background estimation comprehends two different sources, the stability of the ABCD method (see Sec. 8.3.2) and the contamination of signal and EW background events in the control regions.

Variations of $S_{E_{\mathrm{T}}^{\mathrm{miss}}}$ between 4 and 6 tests the two variables, τ_{h} lepton ID and $S_{E_{\mathrm{T}}^{\mathrm{miss}}}$. It also checks the correlation between the two variables and the stability of the ABCD method. The systematic uncertainty of 2.7% is chosen by the largest deviation of the resulting number of background events.

The systematic uncertainty of the signal and EW background contamination is 2.1%. It is estimated by varying the number of events in the four regions (signal and background regions) up and down within the combined systematic and statistical uncertainties of the MC predictions. The result of the again applied ABCD method is taken as systematic.

The combined total uncertainty of the QCD jet background estimation of 3.4% is calculated by the sqare root of the sum of the squared uncertainties.

	$W \to \tau_{\mathrm{h}}\nu\tau$	$W \to \tau_{\mathrm{l}}\nu\tau$	$Z \to \tau\tau$
Events	232946	126925	34095
GRL	232946	126925	34095
Trigger	19442.4±112.7	7152.4±68.7	2603.9±12.7
Collision cleaning	19433.7±112.6	7151.8±68.7	2603.3±12.7
Jet cleaning	19433.7±112.6	7151.8±68.7	2603.3±12.7
Jet in gap veto	15722.9±102.3	5812.1±62.3	2034.9±11.3
$\min\left(\Delta\phi\left(\mathrm{jet}, E_{\mathrm{T}}^{\mathrm{miss}}\right)\right) > 0.5$	14760.4±99.3	5478.4±60.5	1621.9±10.2
$E_{\mathrm{T}}^{\mathrm{miss}} > 30\,\mathrm{GeV}$	11339.1±88	3423.5±48.3	1108.6±8.5
$p_{\mathrm{T}}\left(\tau_{\mathrm{h}}\right) > 20\,\mathrm{GeV}$	11036.4±86.9	3269.2±47.3	1083.6±8.4
τ_{h} identification	5233.5±60.8	1077.6±27.3	551.9±6.1
$p_{\mathrm{T}}\left(\tau_{\mathrm{h}}\right) < 60\,\mathrm{GeV}$	4489±56.4	726.5±22.5	417±5.3
τ_{h} ID ele/mu veto	3773.2±51.8	39.2±5.2	319.2±4.6
Electron veto	3753.3±51.7	29.8±4.5	316.1±4.6
Muon veto	3752.6±51.7	25.1±4.2	241.4±4 1
$S_{E_{\mathrm{T}}^{\mathrm{miss}}} > 6$	1787.7±35.8	15.1±3.2	110.9±2.6

Table 8.10: Cut flow table for PYTHIA Monte Carlo samples with the Perugia2010 tune normalised to an integrated luminosity of $34.3\,\mathrm{pb}^{-1}$.

8.6.3 Systematic uncertainties of C_W

The systematic uncertainty of C_W contains most of the uncertainty in the MC signal prediction described in 8.6.1. Its uncertainty is summarised in Tab. B.11.

8.6.4 Systematic uncertainties of A_W

The theoretical uncertainty on the geometric and kinematic acceptance A_W, defined in Eq. (8.8), is dominated by the limited knowledge of the proton PDFs and the modelling of the W boson production at the LHC. The uncertainty has three components: deviations between different PDF sets, uncertainty within one PDF set, and the uncertainty due to the modelling of the parton shower.

Uncertainty between different PDF sets

The uncertainty due to the choice of the PDF set is determined by reweighting the default signal sample (dataset ID 107054, see Tab. 8.3) with the MRST2007lomod PDF set [201] to different PDF sets, CTEQ6.6 [214] and HERAPDF1.0 [28], and comparing the resulting acceptances from these different PDF sets. The number of events after the defined acceptance cuts and the resulting acceptances can be found in Tab. 8.11. The uncertainty is the maximal deviation between the resulting acceptances of the PDF sets CTEQ6.6 and HERAPDF1.0 compared to the default MRST2007lomod and has a value of 1.6%. This small value is depicted in Figs. 8.10 and 8.11. These figures show typical variables for the acceptance calculation (see. Sec 8.5) and have small deviations.

Cut	MRST2007lomod	CTEQ6.6	HERAPDF1.0
Events (no cut)	639288.0 ± 799.6	613870.5 ± 783.5	630972.3 ± 794.3
τ_{h} p_{T}	317343.0 ± 563.3	304659.0 ± 552.0	313418.7 ± 559.8
τ_{h} η	204831.0 ± 452.6	200277.0 ± 447.5	205760.8 ± 453.6
$(\sum p^{\nu})_{\mathrm{T}}$	65217.0 ± 255.4	63613.8 ± 252.2	65161.4 ± 255.3
$\lvert\Delta\phi\,(\tau_{\mathrm{h,vis}}, \sum \nu)\rvert$	62333.0 ± 249.7	60824.1 ± 246.6	62305.3 ± 249.6
Acceptance $A_W = \lvert\Delta\phi\,(\tau_{\mathrm{h,vis}}, \sum \nu)\rvert$/Events	0.0975 ± 0.0004	0.0991 ± 0.0004	0.0987 ± 0.0004

Table 8.11: Number of events after the acceptance cuts and the resulting acceptance. The error is statistical only. The MC is not scaled, but reweighted from the MRST2007lomod PDF to the corresponding PDF.

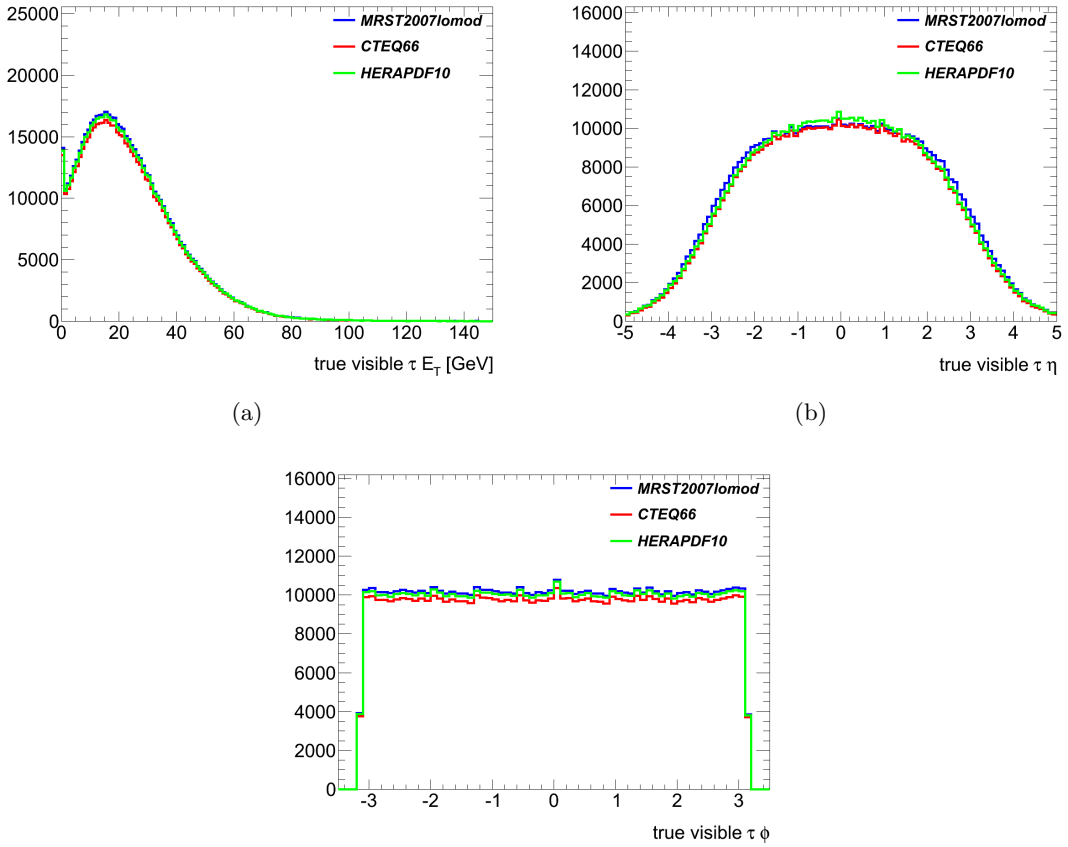

(a) (b)

(c)

Figure 8.10: (a) Visible transverse energy, (b) pseudorapidity η, and (c) angle ϕ of the true $\tau_{\mathrm{h,vis}}$ lepton before any acceptance cut.

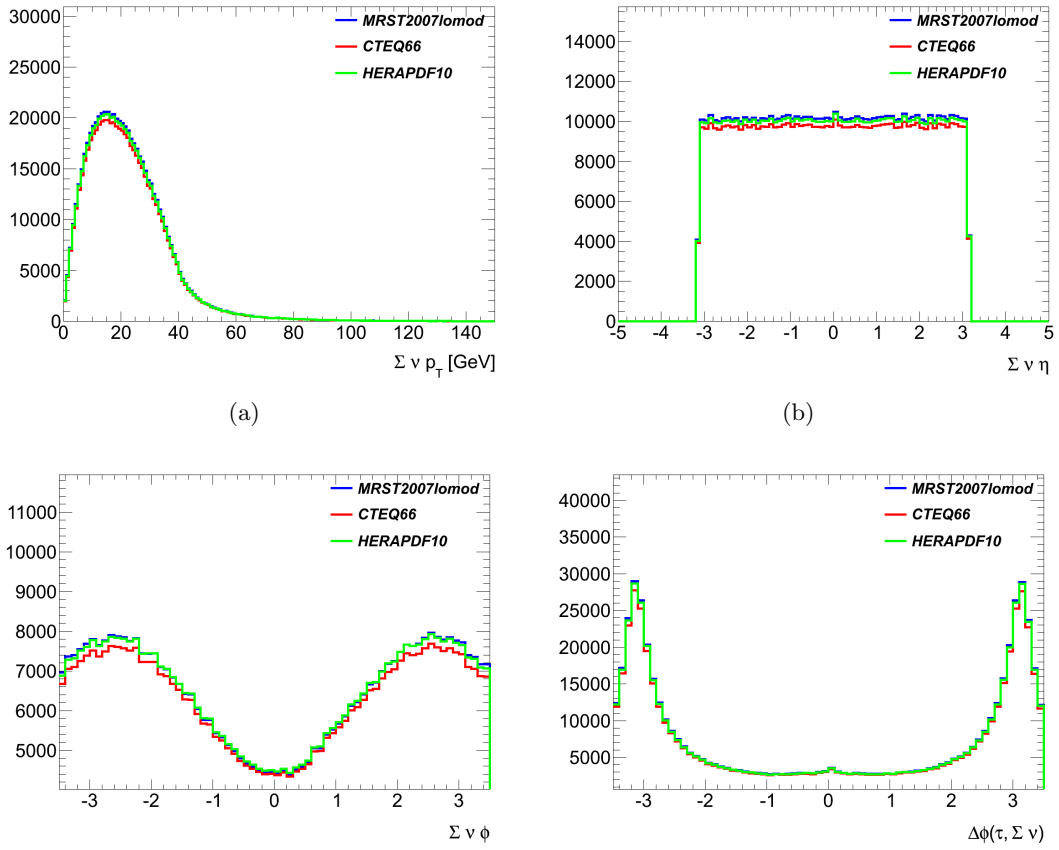

Figure 8.11: (a) Transverse momentum, (b) pseudorapidity η, (c) angle ϕ of the sum of the neutrinos $\sum\nu$, and (d) angle $\Delta\phi$ between the true $\tau_{\mathrm{h,vis}}$ lepton and the sum of the neutrinos $\sum\nu$ before any acceptance cut.

Uncertainty within one PDF set

The uncertainty within one PDF set is estimated by using the 44 error eigenvectors, which are available, for the CTEQ6.6 NLO PDF set [214]. The variations are obtained by reweighting the default sample (MRST2007lomod) to the relevant error eigenvectors of CTEQ6.6. The acceptances A_W^{i+} and A_W^{i-} are calculated from the up and down, respectively odd and even, eigenvector excursion for each eigenvector, which can be found in Tab. B.7. The uncertainty is derived using

$$\Delta A_W = \frac{1}{2}\sqrt{\sum_i \left(A_W^{i+} - A_W^{i-}\right)^2}, \tag{8.12}$$

which gives the error $\Delta A_W = 0.0008$ of the central value (best fit) $A_W = 0.0991$ of the CTEQ6.6 PDF set (see Tab. B.7). The largest deviation from $A_W = 0.0991 \pm 0.0008$ estimates the uncertainty within one PDF set

$$\sigma_{A_{W,\text{one PDF}}} = \frac{A_W \pm \Delta A_W}{A_W}. \tag{8.13}$$

	A_W
Pythia MRST2007lomod	0.0975
Pythia CTEQ6.6	0.0991
Pythia HERAPDF1.0	0.0987
MC@NLO CTEQ6.6	0.1145
MC@NLO spin effect correction	0.0973

Table 8.12: Variation of A_W values using different Monte Carlo configurations.

	A_W
CTEQ 6.6 eignevector set	1.0%
Different PDF sets	1.6%
Model dependence	0.2%
Total systematic	1.9 %
A_W value	0.0975
Stat. error	0.0004
Syst. error	0.019

Table 8.13: Summary table for systematic uncertainties affecting A_W.

The resulting uncertainty is 0.8%. An uncertainty of 1.0% is used in the following (see [137, 138]), which overestimates the uncertainty a bit.

Uncertainty due to the modelling of the parton shower

The uncertainty due to the modelling of the parton shower is estimated using an MC@NLO interfaced with HERWIG MC sample with the CTEQ6.6 PDF set and AUET1 tune [179]. The resulting acceptance has to be corrected because HERWIG in combination with external generators does not handle the τ lepton polarisation correctly. The correction is evaluated using samples with and without τ lepton polarisation effect. The correction factor is 0.8500 ± 0.0002 (stat.).
The uncertainty is the deviation in the corrected acceptance of the MC@NLO sample to the one of the default sample, reweighted to the central value of the CTEQ6.6 PDF set. It amounts 0.2%.

All the individual systematic uncertainties result in a total systematic uncertainty of 1.9%. The overall acceptance is $A_W = 0.0975 \pm 0.0004$ (stat.) $\pm$ 0.019 (syst.). Tables 8.12 and 8.13 summarise the geometric and kinematic acceptance, and the systematic uncertainties of different PDFs and model variations.

8.6.5 Summary on systematic uncertainties

A summary of all systematic effects on the fiducial cross section measurement is given in Tab. 8.14. The systematic uncertainties of the indiviudal electroweak background, N_{EW}, N_{QCD} and C_W are given in Tabs. B.8, B.9, B.10, and B.11. The contribution of the $Z \to ee$, $Z \to \mu\mu$, and the hadronic $t\bar{t}$ background is negligible. The uncertainties of the acceptance calculation can be found in Tab. 8.13.

	$\frac{\delta C_W}{C_W}$	$\frac{\delta N_{\mathrm{EW}}}{N_{\mathrm{EW}}}$	$\frac{\delta N_{\mathrm{QCD}}}{N_{\mathrm{QCD}}}$	$\frac{\delta\sigma^{\mathrm{fid}}_{W\to\tau_{\mathrm{h}}\nu_\tau}}{\sigma^{\mathrm{fid}}_{W\to\tau_{\mathrm{h}}\nu_\tau}}$
Trigger efficiency	6.1%	6.1%	-	7.0%
Energy scale	6.7%	8.7%	-	8.0%
τ_{h} lepton ID efficiency	9.6%	4.1%	-	10.3%
Jet τ_{h} lepton misidentification	-	7.2%	-	1.1%
Electron τ_{h} lepton misidentification	-	4.5%	-	0.7%
Pile-up reweighting	1.4%	1.2%	-	1.6%
Electron reconstruction/identification	-	1.2%	-	0.2%
Muon reconstruction	-	0.3%	-	0.04%
Underlying event modelling	1.3%	1.1%	-	1.5%
Cross section	-	4.5%	-	0.7%
QCD estimation: Stability/correlation	-	-	2.7%	0.2%
QCD estimation: Signal/EW contamination	-	-	2.1%	0.1%
Monte Carlo statistics	1.4%	2.4%	6.0%	1.5%
Total systematic uncertainty	13.4%	15.2%	6.9%	15.1%

Table 8.14: Summary table for systematic uncertainties. For the systematic uncertainty of the fiducial cross section measurement, correlations between the systematics affecting C_W and N_{EW} have been taken into account [137].

As it can be seen from Tabs. 8.13 and 8.14, the main systematic uncertainties come from the trigger efficiency, the energy scale, and the τ_{h} lepton identification efficiency.

8.7 $W \to \tau\nu_\tau$ cross section

The fiducial and inclusive total cross sections of the $W \to \tau\nu_\tau$ decay can be calculated using Eq. (8.6) and Eq. (8.9), and the information given in Tab. 8.15. Their methods used for their determination are described in Sec. 8.5.

The number of observed events ($N_{\mathrm{obs}} = 2335$) in data is determined by counting the number of events after the event selection (see Secs. 8.2 and 8.4). A cut flow table, including MC samples, is given in Tab. 8.5. The number of background events, is given by $N_{\mathrm{bkg}} = N_{\mathrm{QCD}} + N_{\mathrm{EW}}$, where $N_{\mathrm{EW}} = 284 \pm 43$ is the number of EW background events estimated from MC and $N_{\mathrm{QCD}} = 127 \pm 9$ is the number of QCD jet background events estimated from data with the ABCD method (see Sec. 8.3.2). The defined detector acceptance $A_W = 0.0975 \pm 0.0019$ can be estimated using Eq. 8.8, and the correction factor (for the trigger efficiency, τ_{h} lepton reconstruction and identification efficiencies, and the efficiency of all selection cuts within the detector acceptance) $C_W = 0.0799 \pm 0.0107$ by using Eq. 8.7. Systematic uncertainties were studied and are summarised in Tabs. 8.13 and 8.14.

Within the acceptance region the fiducial cross section $\sigma^{\mathrm{fid}}_{W\to\tau_{\mathrm{h}}\nu_\tau}$ is estimated to be

$$\sigma^{\mathrm{fid}}_{W\to\tau_{\mathrm{h}}\nu_\tau} = (0.70 \pm 0.02\ (\mathrm{stat.}) \pm 0.11\ (\mathrm{syst.}) \pm 0.02\ (\mathrm{lumi.}))\ \mathrm{nb} \tag{8.14}$$

and the total cross section $\sigma^{\mathrm{tot}}_{W\to\tau_{\mathrm{h}}\nu_\tau}$ to be

$$\sigma^{\mathrm{tot}}_{W\to\tau_{\mathrm{h}}\nu_\tau} = (7.2 \pm 0.2\ (\mathrm{stat.}) \pm 1.1\ (\mathrm{syst.}) \pm 0.2\ (\mathrm{lumi.}))\ \mathrm{nb}. \tag{8.15}$$

Parameter	Value
N_{obs}	2335
N_{QCD}	127 ± 9
N_{EW}	284 ± 43
A_W	0.0975 ± 0.0019
C_W	0.0799 ± 0.0107

Table 8.15: Input parameters for the cross section calculation. The errors include statistical and systematic uncertainties.

This cross section has to be corrected for the hadronic τ lepton branching ratio $BR(\tau \to \text{had}\nu_\tau) = 0.6479 \pm 0.0007$ [12], which results in an inclusive total cross section $\sigma^{\text{tot}}_{W\to\tau\nu_\tau}$ of

$$\sigma^{\text{tot}}_{W\to\tau\nu_\tau} = (11.1 \pm 0.3\ (\text{stat.}) \pm 1.7\ (\text{syst.}) \pm 0.4\ (\text{lumi.}))\ \text{nb}. \tag{8.16}$$

The result is in good agreement with the measured $W \to e\nu_e$ and $W \to \mu\nu_\mu$ cross sections at ATLAS [218, 219] and with the theoretical NNLO cross section (10.46 ± 0.52) nb [22, 203, 220]. A $W \to \tau\nu_\tau$ branching ratio of $(11.1 \pm 0.3\ (\text{stat.}) \pm 1.8\ (\text{syst.}) \pm 0.4\ (\text{lumi.}))\%$ is evaluated, which agrees with the SM expectation of 10.83%. For the estimation of this branching ratio, a W boson production cross section of 100 nb is used (see Fig. 3.3) [29]. The uncertainty on the W boson production cross section is approximately $\pm 5\%$ and comes mainly from the uncertainty of the PDFs [22, 175, 231]. Its statistical uncertainty and the uncertainty from the luminosity is neglected in the estimation of the $W \to \tau\nu_\tau$ branching ratio.

Figure 8.12 shows the first $W \to \tau\nu_\tau$ cross section measurement at the LHC in comparison to the $W \to e\nu_e$ and $W \to \mu\nu_\mu$ ATLAS cross sections and the theoretical predictions.

8.8 Summary and Outlook

A first measurement of the $W \to \tau\nu_\tau$ cross section at the LHC has been performed. The result for the total inclusive cross section of $\sigma^{\text{tot}}_{W\to\tau\nu_\tau} = (11.1 \pm 0.3\ (\text{stat.}) \pm 1.7\ (\text{syst.}) \pm 0.4\ (\text{lumi.}))$ nb agrees with the SM expectation of 10.46 nb within the error. The estimated $W \to \tau\nu_\tau$ branching ratio of $(11.1 \pm 0.3\ (\text{stat.}) \pm 1.8\ (\text{syst.}) \pm 0.4\ (\text{lumi.}))\%$ is also in accord with the SM expectation of 10.83% within the error. In order to achieve these results, the following tasks were performed. To deal with the effect of pile-up, the MC samples were reweighted such that the distributions of the number of reconstructed primary vertices per bunch crossing agree with those measured. Due to limited MC statistics for the QCD jet background, a data driven method to estimate QCD jet background has been used. Correction factors have to be applied for the calculation of the cross section. Firstly, a factor C_W takes into account the trigger efficiency, the τ_{h} lepton reconstruction and identification efficiencies, and the efficiency of the selection cuts within the detector acceptance. The second factor is the acceptance A_W, which was estimated to be $A_W = 0.0975 \pm 0.0004\ (\text{stat.}) \pm 0.0190\ (\text{syst.})$. The total systematic uncertainty on the acceptance of 1.9% is small in comparison to other uncertainties. The most important systematic uncertainties come from the trigger efficiency, the energy scale of the calibrated τ_{h} lepton and of the clusters in the calorimeter, and the τ_{h} lepton identification efficiency, which have values between 4.1% and 10.3%, as shown in Tab. 8.14.

The $W \to \tau\nu_\tau$ branching ratio estimated in this thesis of $(11.1 \pm 0.3\ (\text{stat.}) \pm 1.8\ (\text{syst.}) \pm 0.4\ (\text{lumi.}))\%$ has higher uncertainties than those mea-

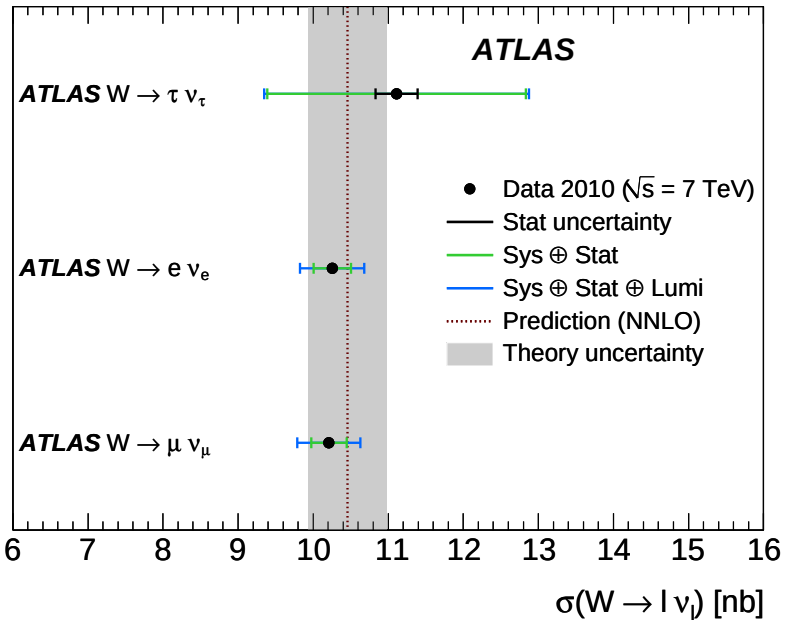

Figure 8.12: Cross sections for the different $W \to l\nu_l$ channels measured in ATLAS with 2010 data (points). Systematic, luminosity and statistical uncertainties are added in quadrature. The theoretical NNLO expectation is also shown (dashed line), together with its uncertainty (filled area) [137].

sured at LEP of $(11.44 \pm 0.19\,(\text{ stat.}) \pm 0.2\,(\text{ syst.}))\%$ (see Sec. 7.3). To obtain the same precision as the LEP experiments of approximately 2%, the precision of around 17% in this measurement has to be improved by a factor of 8.5. This means that the overall uncertainty of 1.87% has to be reduced by a factor of 6.7 to reach the overall uncertainty of 0.28% of the LEP experiments.

The reduction of the statistical uncertainty will come down with the increase of data recorded, but dealing with the triggers relevant for this analysis will be a big challenge in future ATLAS data. The event rate is higher with a higher center-of-mass energy, so the event rate has to be scaled down. This is done by prescale factors in the relevant triggers. The prescale factors of the triggers used in this thesis would be very high so that these triggers are not used anymore. Other unprescaled triggers (or at least triggers with low prescale factors), which are sensitive on τ_h leptons and E_T^miss, are needed. There is still an unprescaled combined τ_h lepton and E_T^miss trigger called EF_tau29_xe35_noMu, but which has higher thresholds on the different objects and would not give the needed statistics, probably.

On the other hand, the systematic uncercainty has to be reduced by a factor of 9 to reach the systematic uncertainty of the LEP measurements. For example, one of the main systematic uncertainties is the energy scale of the calibrated τ_h lepton, which could be reduced by dividing the energy range into smaller bins and providing more correction factors for the calibration. But then, higher statistics will be needed. Other possibilities to reduce the systematic uncertainty would be to improve the trigger efficiency and τ_h lepton identification efficiency.

These are already large challenges in the $W \to \tau_\text{h}\nu_\tau$ analysis and it is unsure if a precision comparable to the LEP precision can be reached in future. For this reason, searches for $W \to \tau_\text{h}\nu_\tau$ decays is being replaced by the search for $W \to \tau_\text{l}\nu_\tau \to l\nu_\text{l}\nu_\tau$ decays at ATLAS [232].

9 Summary

The last few years have been very successful for particle physics. The LHC began operation and probed new energy regions. ATLAS and the other LHC experiments are operating well. Anyway, precise MC simulations are needed in order to check the expectations of what will be measured in the detector and to optimise the detector performance. Sophisticated tools are needed to ensure the functionality and a good quality of the simulations. One of them is the HepMCAnalysis Tool, whose development comprises one part of this thesis.

The HepMCAnalysis Tool is a package for MC generator validation and comparisons offering a stable, easy-to-use, and extendable framework, allowing easy access to MC generator level analysis. It uses the generator independent HepMC event record and contains a class library with different benchmark physics processes, allowing the user to analyse events at generator level and fill the results into histograms. Currently, analysis classes for $b\bar{b}$, $t\bar{t}$, W + Jets, $W \to \tau\nu_\tau$, Z, $Z \to \tau\tau$, and jet events, as well as for the analysis of elastic scattered protons, missing energy, and the underlying event are implemented. Additionally, it contains a user analysis class, in which other generator level analyses can easily be implemented. The HepMCAnalysis Tool provides a software environment with steerable example programs for MC event generation as well as scripts for a web display and comparisons of the histograms, including Kolmogorov-Smirnoff- and χ^2-tests.

The tool is used in a wide range of applications. It is implemented in Athena, the ATLAS software framework. Within ATLAS, the HepMCAnalysis Tool is used for validation and regression tests. It runs in the RunTimeTester for nightly tests and checks the functionality and validity of ATLAS MC production scripts. Several (pre-)validations for a large production of ATLAS MC samples were performed and bugs were discovered early in the production of MC samples. Additionally, it is used in generator level studies and in preparation of analyses inside and outside of ATLAS. A PDF study was presented, which showed the effectiveness of modified leading order PDFs in describing NLO effects. Further applications are its use in MC schools of the Helmholtz alliance 'Physics at the Terascale' and histogram based validation in the Generator Services Project, in which it helped to discover that the internal event record for Z bosons changed in HERWIG++ 2.5.0 with respect to version 2.4.2. For the future, it will run in nightly regression tests of the Generator Services Project.

Due to the successful operation of the ATLAS detector and software, many SM processes have already been rediscovered in 7 TeV data collected in the first year and are used to optimise the detector performance. There is already a first hint for the Higgs boson at a mass range around 126 GeV [1]. A Higgs boson decaying into two photons can be measured very precisely [59], but at such a light Higgs mass, the branching ratio of $H \to \tau\tau$ decays is substantial (see Fig. 2.7). The $H \to \tau\tau$ decay might be the only decay which can be measured directly at this mass range. There is also the $H \to b\bar{b}$ decay, but it is unknown if it can be measured precise enough [56–58]. Furthermore, τ leptons are often produced within decay cascades of many supersymmetric scenarios. Thus, it is important to understand τ leptons from SM processes, like $Z \to \tau\tau$ and $W \to \tau\nu_\tau$, in order to search for physics beyond the SM. Hadronically decaying τ leptons have similar event shapes in the detector as the event shapes of QCD jets, but they are narrower. It

is therefore a challenge to distinguish between hadronically decaying τ leptons and QCD jets, which form a large background for τ lepton physics due to the high QCD jet cross section.

In this thesis, the production of a W boson and its subsequent decay into a τ lepton and a τ neutrino is studied. The cross section of a $W \to \tau\nu_\tau$ decay is ten times larger than the cross section of a $Z \to \tau\tau$ decay leading to a large sample of τ leptons. This decay is similar to the decay of a charged Higgs boson decaying into a τ lepton and the corresponding neutrino ν_τ, as well as to $H \to \tau\tau$ in which one of the τ leptons is not reconstructed. A good understanding of $W \to \tau\nu_\tau$ events is essential for a possible discovery of new physics beyond the SM.

Here, the cross section of $W \to \tau\nu_\tau$ events in proton-proton collisions at a center-of-mass energy of $\sqrt{s} = 7\,\text{TeV}$ at the ATLAS experiment was determined. The main problems for this cross section determination were the pile-up effect and the QCD jet background. Sufficient MC statistics were only available for the electroweak signal and background. A data driven ABCD method was used to determine the QCD jet background. In data, 2335 $W \to \tau\nu_\tau$ events were observed, with 1811 signal and 284 electroweak background events resulting from the MC samples. With the data driven ABCD method, the QCD jet background was estimated to be 127 events.

Another focus was an acceptance calculation (including systematic uncertainties), needed for the cross section calculation, and the underyling event modelling, which was tested by checking different MC tunes. The acceptance was estimated to be $A_W = 0.0975 \pm 0.0004\,(\text{stat.}) \pm 0.0190\,(\text{syst.})$. By using another correction factor $C_W = 0.0799 \pm 0.0107$, which considers the trigger efficiency, the hadronically decaying τ lepton (τ_h) reconstruction and identification efficiency, and the efficiency of the selection cuts within the detector acceptance, the fiducial cross section of $W \to \tau\nu_\tau$ events in proton-proton collisions was calculated to be $\sigma^{\text{fid}}_{W\to\tau_\text{h}\nu_\tau} = (0.70 \pm 0.02\,(\text{stat.}) \pm 0.11\,(\text{syst.}) \pm 0.02\,(\text{lumi.}))\,\text{nb}$ and the total cross section $\sigma^{\text{tot}}_{W\to\tau_\text{h}\nu_\tau} = (7.2 \pm 0.2\,(\text{stat.}) \pm 1.1\,(\text{syst.}) \pm 0.2\,(\text{lumi.}))\,\text{nb}$. A total inclusive cross section of $\sigma^{\text{tot}}_{W\to\tau\nu_\tau} = (11.1 \pm 0.3\,(\text{stat.}) \pm 1.7\,(\text{syst.}) \pm 0.4\,(\text{lumi.}))\,\text{nb}$ was ensued after correcting the hadronic τ lepton branching ratio $BR\,(\tau \to \text{had}\nu_\tau) = 0.6479 \pm 0.0007$. The main sources of systematic uncertainties are the trigger efficiency, the energy scale of the calibrated τ_h lepton and of the clusters in the calorimeter, and the τ_h lepton identification efficiency, which all have values between 4.1% and 10.3%. This cross section measurement is the first measured $W \to \tau\nu_\tau$ cross section at the LHC and is in good agreement with the measured $W \to e\nu_e$ and $W \to \mu\nu_\mu$ cross sections at ATLAS and with the NNLO predictions of $(10.46 \pm 0.52)\,\text{nb}$.

In addition, the $W \to \tau\nu_\tau$ branching ratio was evaluated to be $(11.1 \pm 0.3\,(\text{stat.}) \pm 1.8\,(\text{syst.}) \pm 0.4\,(\text{lumi.}))\%$, using a total W boson production cross section of 100 nb (see Fig. 3.3) [29] with an uncertainty of 5% [22, 175, 231]. This estimated value agrees with the SM expectation of 10.83%.

To summarise, the presented cross section measurement agrees with the SM. It will be a big challenge to improve the precision of more than 15% in this cross section measurement (and approximately 17% in the $W \to \tau\nu_\tau$ branching ratio evaluation) by decreasing the large uncertainties to reach the precision of the LEP experiments of approximately 2% (see Sec. 7.3). Triggering $W \to \tau\nu_\tau$ events is one of the large difficulties in this analysis. One has to find a suitable trigger, where the threshold of the transverse momentum of the τ_h lepton and the missing transverse momentum is not too high, while the trigger should be unprescaled or have a low prescale factor. This is one of the reasons why the focus lies on the search for $W \to \tau_\text{l}\nu_\tau \to l\nu_\text{l}\nu_\tau$ decays at ATLAS in future.

Appendix A

Control histograms and further histograms of the PDF study in Sec. 6.3.4

In this section, control histograms and further histograms of the PDF study presented in Sec. 6.3.4 are given. All histograms are normalised to the corresponding cross section given in Sec. 6.3.4.

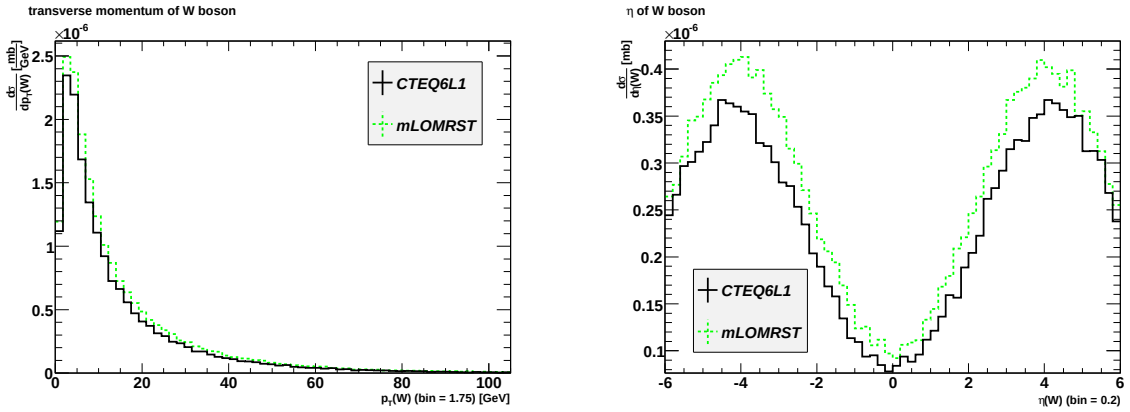

(a) (b)

Figure A.1: (a) Transverse momentum p_{T} and (b) pseudorapidity η of the W boson for the PDFs CTEQ6L1 and MRST2007lomod in $pp \to W \to \mu\nu_{\mu}$ events normalised to the cross section.

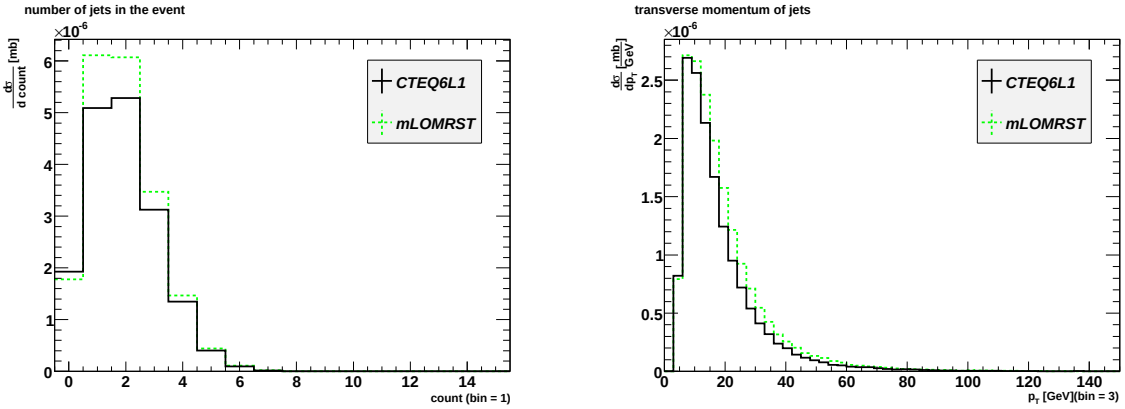

(a) (b)

Figure A.2: (a) Number of jets and (b) transverse momentum p_{T} of jets for the PDFs CTEQ6L1 and MRST2007lomod in $pp \to W \to \mu\nu_\mu$ events normalised to the cross section. The number of jets and the p_{T} in the event is higher for the modLO PDF.

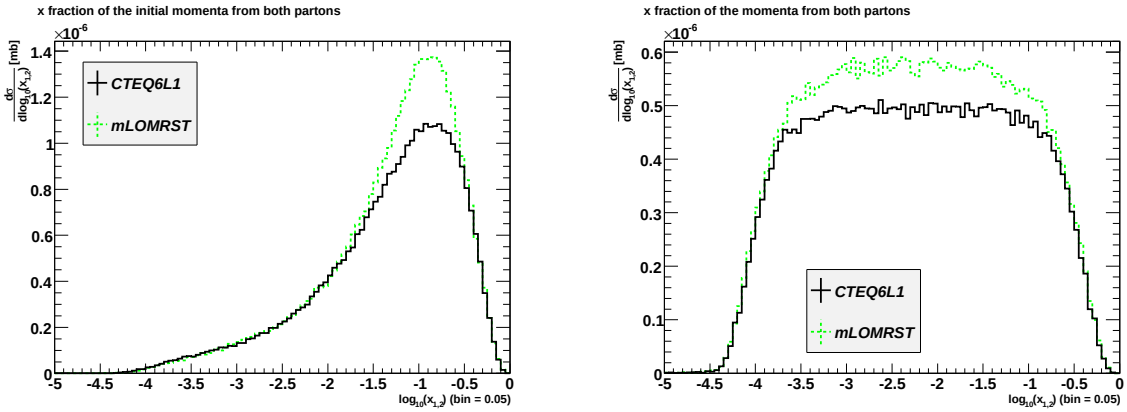

(a) (b)

Figure A.3: Bjorken x of both at the hard process participating partons (a) before gluon radiation and (b) after gluon radiation for the PDFs CTEQ6L1 and MRST2007lomod in $pp \to W \to \mu\nu_\mu$ events normalised to the cross section.

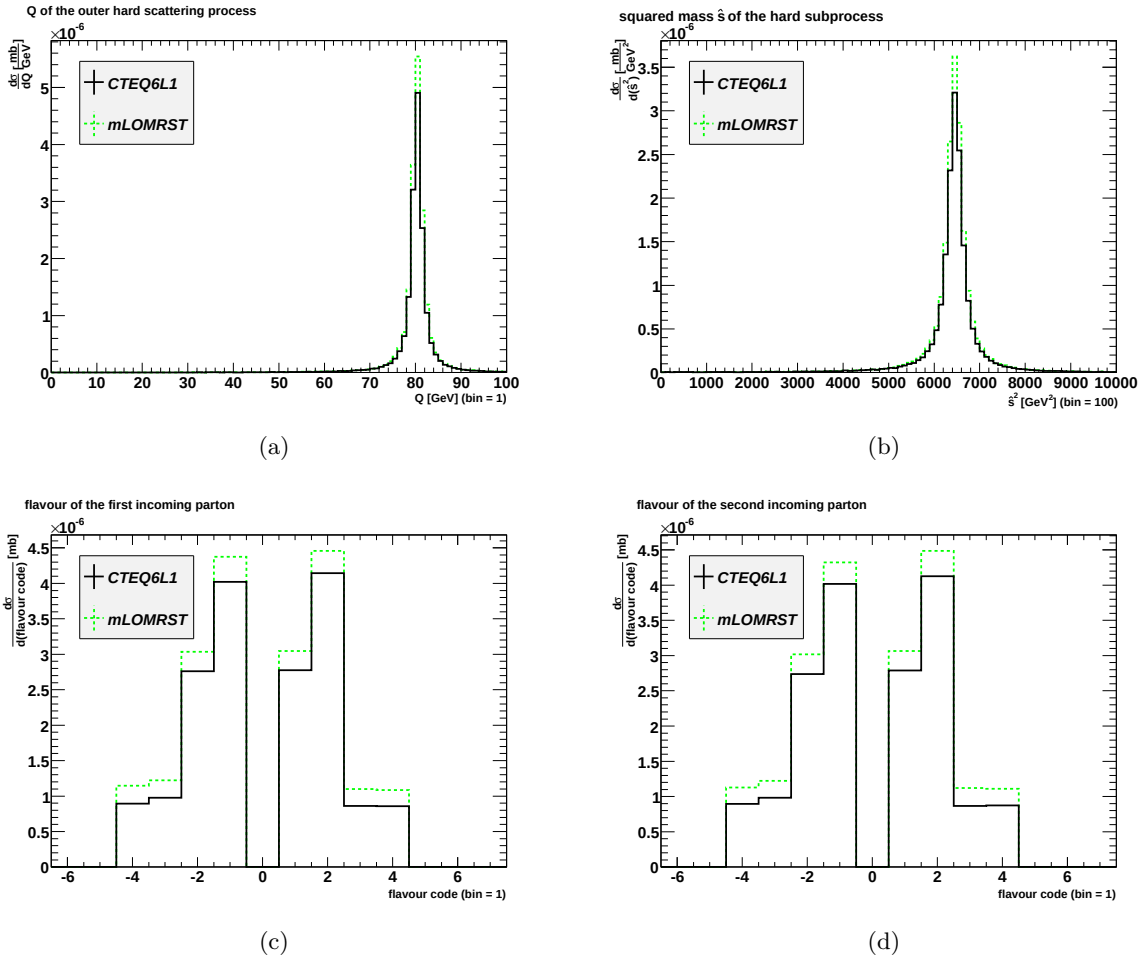

Figure A.4: Control histograms: (a) Q of the outer hard scattering process, (b) squared mass of the hard subprocess, (c) flavour (pdgID) of the first incoming parton, and (d) flavour (pdgID) of the second incoming parton for the PDFs CTEQ6L1 and MRST2007lomod in $pp \to W \to \mu\nu_\mu$ events normalised to the cross section.

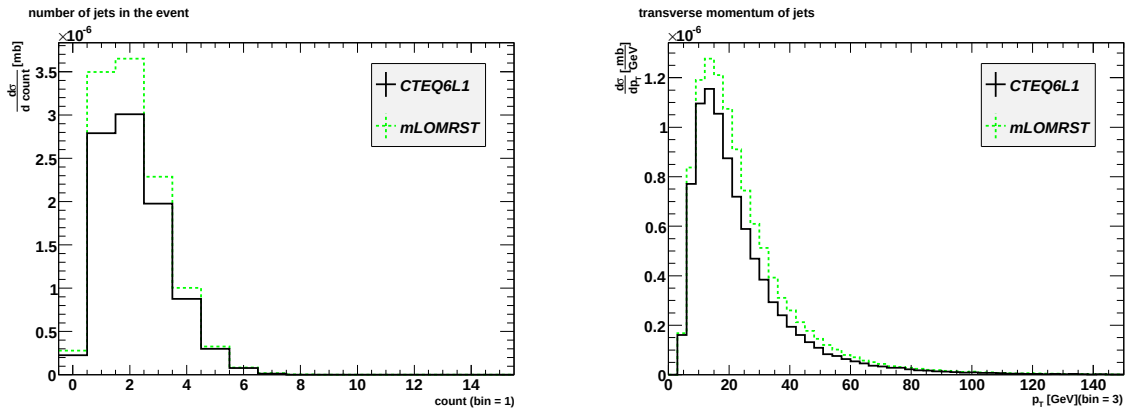

(a) (b)

Figure A.5: (a) Number of jets and (b) transverse momentum p_{T} of jets for the PDFs CTEQ6L1 and MRST2007lomod in $pp \to W +$ jets events normalised to the cross section. Jets with a transverse momentum of $p_{\mathrm{T}} < 15\,\mathrm{GeV}$ are skipped. There are more jets for the modLO PDF in the event.

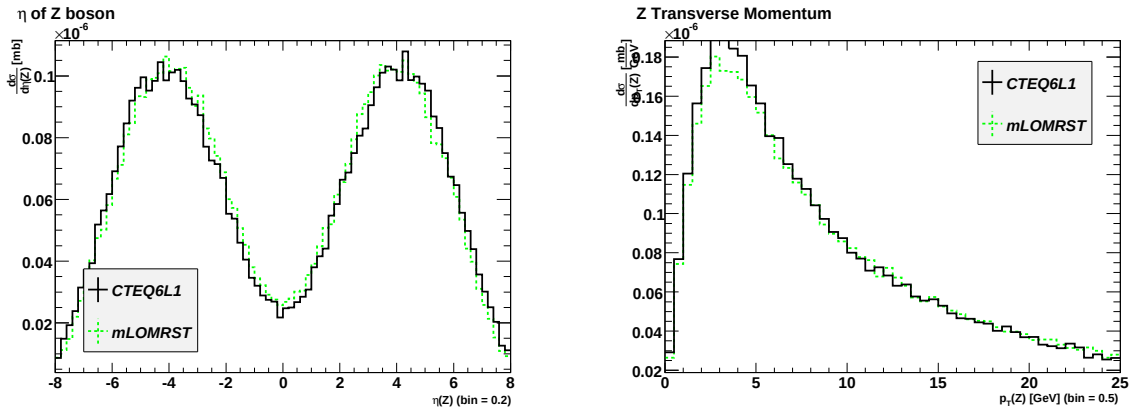

(a)

(b)

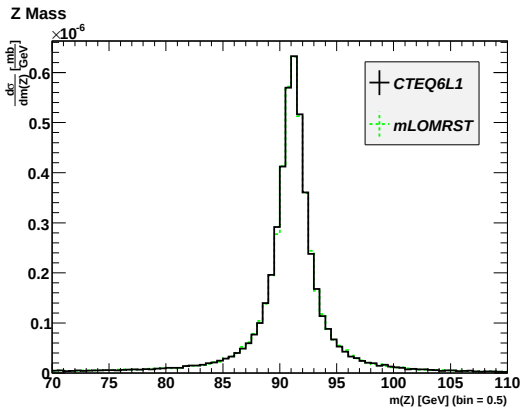

(c)

Figure A.6: (a) η of the Z boson, (b) transverse momentum p_{T} of the Z boson, and (c) the mass of the Z boson in $pp \to Z \to l\nu_l$ events normalised to the cross section. The results of $pp \to W \to \mu\nu_\mu$ events could be repeated for $pp \to Z \to l\nu_l$ events.

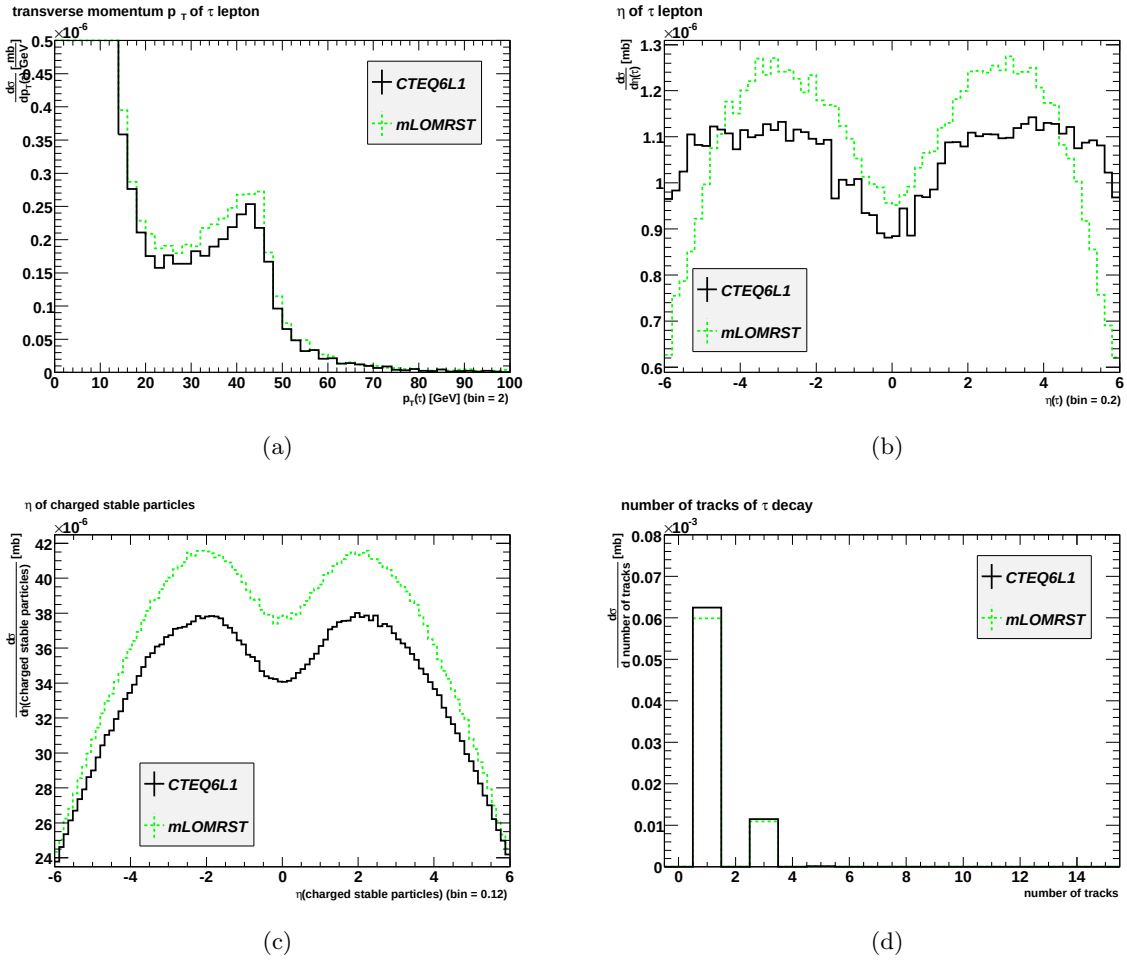

Figure A.7: (a) Transverse momentum p_{T} of the τ lepton, (b) η of the τ lepton, (c) η of charged stable particles, and (d) the number of tracks in the τ lepton decay in $pp \to Z \to \tau\tau$ events normalised to the cross section. The strong failing edge at around 45 GeV in (a) is due to the mass of the Z boson, while the increase below 20 GeV is due to QCD. There are many τ leptons in a range of $-2.5 < \eta < 2.5$. Many charged stable particles coming from the τ lepton decay can be found in the same η-range.

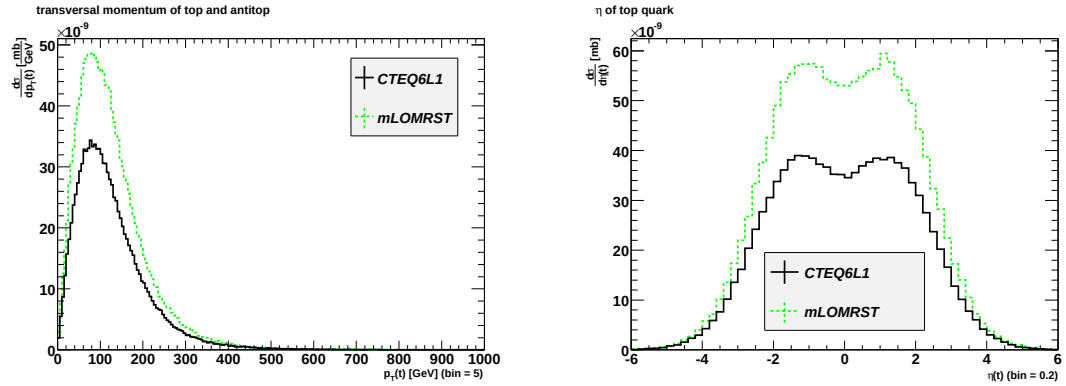

(a)

(b)

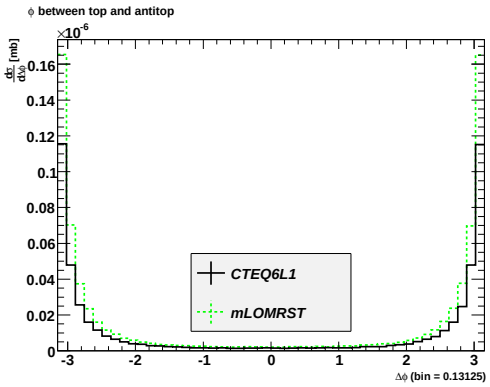

(c)

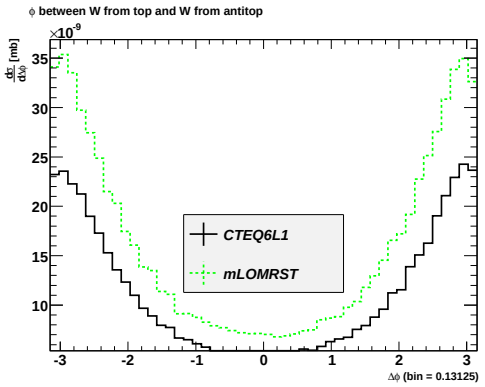

(d)

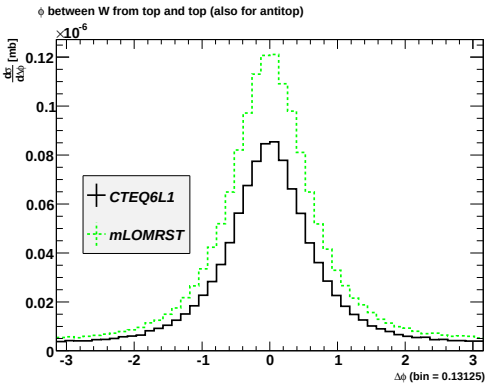

(e)

Figure A.8: (a) Transverse momentum p_{T} of the top quark, (b) η of the top quark, (c) $\Delta\phi$ between the top and antitop quark, (d) $\Delta\phi$ between the W boson coming from the top quark and the W boson coming from the antitop quark, and (e) $\Delta\phi$ between the top quark and the W boson coming from the top quark (for the antitop quark accordingly) in $pp \to t\bar{t}$ events normalised to the cross section. As it can be seen the top and the antitop quark as well as the corresponding W bosons are back to back in ϕ, while the top/antitop quark and the corresponding W boson are in the same ϕ direction.

Appendix B

Additional information for the $W \longrightarrow \tau\nu_\tau$ cross section measurement

This section gives additional information for the measurement of the $W \rightarrow \tau\nu_\tau$ cross section in proton-proton collisions at $\sqrt{s} = 7\,\text{TeV}$ with the ATLAS experiment.

B.1 Vertex reweighting factors for the pile-up treatment

MC DS ID	MC Sample	Number of vertex	Loose trigger	Medium trigger	Control Region loose trigger	Control region medium trigger
106043	$W \to e\nu_e$	1	1.7754	1.14406	1.68806	1.68794
		2	1.12514	0.98859	1.11679	1.12264
		3	0.821507	0.937024	0.841398	0.844769
		4	0.66279	0.950365	0.694241	0.690231
		≥ 5	0.54173	1.0652	0.5881	0.579024
106044	$W \to \mu\nu_\mu$	1	1.79668	1.06468	1.7083	1.67099
		2	1.10945	0.948919	1.10121	1.10363
		3	0.830828	0.942013	0.850945	0.850709
		4	0.655664	1.00305	0.686777	0.704225
		≥ 5	0.547385	1.22131	0.594239	0.586459
107054	$W \to \tau_{\mathrm{h}}\nu_\tau$	1	1.73679	1.12353	1.65135	1.72327
		2	1.14563	0.982599	1.13712	1.12332
		3	0.828194	0.924436	0.848247	0.833403
		4	0.664028	0.967772	0.695539	0.688607
		≥ 5	0.519908	1.12161	0.56441	0.583733
107054	$W \to \tau_{\mathrm{l}}\nu_\tau$	1	1.80445	1.16635	1.71568	1.72451
		2	1.15159	1.00152	1.14304	1.13317
		3	0.810049	0.928691	0.829663	0.84334
		4	0.656711	0.921603	0.687874	0.678062
		≥ 5	0.523152	1.0741	0.567932	0.566071
106046	$Z \to ee$	1	2.02864	1.31533	1.92884	1.95011
		2	1.19411	1.0805	1.18525	1.22224
		3	0.815278	0.929735	0.835018	0.839564
		4	0.622493	0.855854	0.652032	0.627576
		≥ 5	0.445311	0.865003	0.483427	0.467178
106047	$Z \to \mu\mu$	1	1.77221	1.13539	1.68504	1.67296
		2	1.13125	0.976437	1.12285	1.12956
		3	0.809016	0.921017	0.828604	0.8366
		4	0.678903	0.962271	0.71112	0.697388
		≥ 5	0.536725	1.14683	0.582667	0.581839

Table B.1: Vertex reweighting factors for the Monte Carlo datasets (DS) of the signal and the control region for each of the used triggers.

MC DS ID	MC Sample	Number of vertex	Loose trigger	Medium trigger	Control Region loose trigger	Control region medium trigger
106052	$Z \to \tau\tau$	1	1.83938	1.15329	1.74889	1.75725
		2	1.17564	1.00349	1.16692	1.15375
		3	0.819322	0.93673	0.83916	0.837455
		4	0.63552	0.934331	0.665678	0.672087
		≥ 5	0.494792	1.03886	0.537144	0.543927
105200	$t\bar{t}$ leptonic	1	1.7065	1.08633	1.62255	1.62412
		2	1.12614	0.970124	1.11778	1.11015
		3	0.82807	0.948742	0.84812	0.854013
		4	0.683189	0.983546	0.715609	0.707304
		≥ 5	0.535181	1.11513	0.580991	0.591279
105204	$t\bar{t}$ hadronic	1	1.68915	1.02784	1.60606	1.63994
		2	1.13646	1.01731	1.12802	1.13039
		3	0.820538	0.906472	0.840405	0.82323
		4	0.68314	1.00716	0.715557	0.713513
		≥ 5	0.542479	1.16092	0.588912	0.602128
119928	$W \to e\nu_e$	1	1.77564	1.13542	1.68829	1.68493
		2	1.14218	0.986911	1.1337	1.12135
		3	0.819608	0.937321	0.839453	0.844233
		4	0.661769	0.947701	0.693172	0.688726
		≥ 5	0.524326	1.086	0.569206	0.585227
119929	$W \to \mu\nu_\mu$	1	1.86818	1.14534	1.77628	1.69169
		2	1.09704	0.971882	1.0889	1.14229
		3	0.800975	0.940174	0.820368	0.852514
		4	0.69024	0.947258	0.722994	0.664973
		≥ 5	0.544692	1.11272	0.591315	0.570758
107419	$W \to \tau_\mathrm{h}\nu_\tau$	1	1.81308	1.11311	1.72389	1.72417
		2	1.12897	0.962485	1.12059	1.12825
		3	0.823213	0.936121	0.843145	0.834308
		4	0.667797	0.997843	0.699486	0.686039
		≥ 5	0.513103	1.11415	0.557022	0.578136

Table B.2: Vertex reweighting factors for the Monte Carlo datasets (DS) of the signal and the control region for each of the used triggers.

MC DS ID	MC Sample	Number of vertex	Loose trigger	Medium trigger	Control Region loose trigger	Control region medium trigger
107419	$W \to \tau_l\nu_\tau$	1	1.77323	1.14587	1.686	1.75071
		2	1.19563	0.993704	1.18676	1.13847
		3	0.811766	0.937132	0.831421	0.840173
		4	0.647018	0.948745	0.677722	0.681315
		≥ 5	0.495652	1.05025	0.538078	0.549514
113719	$Z \to ee$	1	2.03519	1.26084	1.93507	1.90736
		2	1.21952	1.09583	1.21047	1.22347
		3	0.829007	0.914835	0.849079	0.833635
		4	0.603161	0.886331	0.631783	0.644596
		≥ 5	0.428183	0.865851	0.464834	0.466432
113721	$Z \to \mu\mu$	1	1.85739	1.15698	1.76602	1.68772
		2	1.14806	0.927251	1.13954	1.12252
		3	0.809747	0.965041	0.829353	0.838219
		4	0.624839	0.970641	0.65449	0.697734
		≥ 5	0.549457	1.13433	0.596488	0.581225
107418	$Z \to \tau\tau$	1	1.90607	1.15707	1.81231	1.77187
		2	1.14612	1.00169	1.13762	1.144
		3	0.832525	0.940983	0.852683	0.842352
		4	0.617504	0.93164	0.646806	0.670382
		≥ 5	0.50717	1.03203	0.550581	0.544249
107414	$W \to \tau_h\nu_\tau$	1	1.81005	1.08421	1.72101	1.70482
		2	1.12737	0.97946	1.119	1.12889
		3	0.809719	0.929179	0.829324	0.84109
		4	0.665606	0.998095	0.697191	0.697639
		≥ 5	0.54095	1.12416	0.587253	0.559962
107414	$W \to \tau_l\nu_\tau$	1	1.89442	1.17472	1.80123	1.7456
		2	1.13217	1.05198	1.12377	1.18689
		3	0.824737	0.899659	0.844706	0.805098
		4	0.639233	0.920391	0.669566	0.676141
		≥ 5	0.511548	1.01694	0.555334	0.558899

Table B.3: Vertex reweighting factors for the Monte Carlo datasets (DS) of the signal and the control region for each of the used triggers.

MC DS ID	MC Sample	Number of vertex	Loose trigger	Medium trigger	Control Region loose trigger	Control region medium trigger
107413	$Z \rightarrow \tau\tau$	1	1.86792	1.14591	1.77603	1.7461
		2	1.15636	0.987364	1.14778	1.13882
		3	0.821909	0.955443	0.84181	0.850655
		4	0.638633	0.927115	0.668938	0.672826
		≥ 5	0.498141	1.05501	0.54078	0.544821
108328	$W^+ \rightarrow \tau^+_{\text{had}}\nu_\tau$	1	1.75103	1.08509	1.66489	1.64815
		2	1.12174	0.995058	1.11342	1.1391
		3	0.836589	0.920311	0.856845	0.841599
		4	0.644352	0.974421	0.674929	0.690938
		≥ 5	0.556105	1.14307	0.603706	0.580382
108328	$W^+ \rightarrow \tau^+_{\text{l}}\nu_\tau$	1	1.79689	1.07597	1.70849	1.58843
		2	1.18636	1.05681	1.17755	1.21843
		3	0.844118	0.929576	0.864556	0.839723
		4	0.574221	0.931713	0.601469	0.673759
		≥ 5	0.547232	1.02667	0.594073	0.539344
108329	$W^- \rightarrow \tau^-_{\text{had}}\bar{\nu}_\tau$	1	1.76069	1.106	1.67407	1.74264
		2	1.13637	0.969409	1.12793	1.10697
		3	0.849006	0.952229	0.869563	0.856019
		4	0.634057	0.958568	0.664145	0.685585
		≥ 5	0.526427	1.12105	0.571487	0.563158
108329	$W^- \rightarrow \tau^-_{\text{l}}\bar{\nu}_\tau$	1	1.83585	1.20022	1.74554	1.85031
		2	1.09158	0.973038	1.08347	1.13116
		3	0.826395	0.895434	0.846404	0.818691
		4	0.651299	0.998344	0.682205	0.665939
		≥ 5	0.570743	1.09007	0.619596	0.575733

Table B.4: Vertex reweighting factors for the Monte Carlo datasets (DS) of the signal and the control region for each of the used triggers.

MC DS ID	MC Sample	Number of vertex	Loose trigger	Medium trigger	Control Region loose trigger	Control region medium trigger
107376	$W \to \tau_h\nu_\tau$	1	1.68454	1.09031	1.60168	1.70211
		2	1.23097	0.994063	1.22184	1.11865
		3	0.822308	0.952223	0.842219	0.838876
		4	0.597907	0.888305	0.62628	0.644426
		≥ 5	0.543724	1.2137	0.590264	0.661898
107376	$W \to \tau\nu_\tau$	1	1.82201	1.08278	1.73238	1.62913
		2	1.12361	1.08092	1.11527	1.1642
		3	0.871487	0.89575	0.892588	0.834992
		4	0.60735	0.88729	0.636171	0.662611
		≥ 5	0.521346	1.14806	0.565971	0.607615
107373	$Z \to \tau\tau$	1	1.8996	1.21412	1.80616	1.87343
		2	1.14731	0.952951	1.1388	1.10757
		3	0.835034	0.943984	0.855253	0.859097
		4	0.586062	0.902973	0.613872	0.624763
		≥ 5	0.550114	1.16291	0.597201	0.589577
107377	$W \to \tau_h\nu_\tau$	1	1.84801	1.10862	1.7571	1.74533
		2	1.25199	0.925092	1.2427	1.06959
		3	0.800213	0.979371	0.819588	0.914378
		4	0.598342	0.936854	0.626736	0.634064
		≥ 5	0.492214	1.24974	0.534345	0.59816
107377	$W \to \tau\nu_\tau$	1	1.80623	1.13506	1.71738	1.67571
		2	1.06867	1.01872	1.06074	1.16777
		3	0.911579	0.917215	0.933651	0.760584
		4	0.598305	0.935445	0.626696	0.72804
		≥ 5	0.560848	1.07533	0.608854	0.647836

Table B.5: Vertex reweighting factors for the Monte Carlo datasets (DS) of the signal and the control region for each of the used triggers.

MC DS ID	MC Sample	Number of vertex	Loose trigger	Medium trigger	Control Region loose trigger	Control region medium trigger
107374	$Z \to \tau\tau$	1	1.90356	1.08247	1.80992	1.7005
		2	1.20118	0.974249	1.19227	1.16471
		3	0.70418	0.935788	0.72123	0.830501
		4	0.765161	1.03946	0.801471	0.652289
		≥ 5	0.517232	1.05755	0.561504	0.593626
107378	$W \to \tau_{\mathrm{h}}\nu_\tau$	1	1.79353	1.16882	1.70531	1.79561
		2	1.09222	1.00573	1.08411	1.14331
		3	0.807793	0.906348	0.827351	0.861466
		4	0.717876	0.919692	0.751941	0.615631
		≥ 5	0.538577	1.13473	0.584677	0.581642
107378	$W \to \tau_{\mathrm{l}}\nu_\tau$	1	1.54507	1.45982	1.46906	1.78614
		2	1.22454	0.978942	1.21545	1.14815
		3	0.82488	0.921742	0.844853	0.860635
		4	0.602094	0.942451	0.630666	0.654048
		≥ 5	0.623758	0.868843	0.677149	0.527026
107375	$Z \to \tau\tau$	1	1.98452	1.19723	1.8869	1.84716
		2	1.12694	0.975245	1.11857	1.11286
		3	0.809167	0.897231	0.828759	0.806152
		4	0.689574	0.964119	0.722297	0.695897
		≥ 5	0.461333	1.14148	0.500821	0.586609

Table B.6: Vertex reweighting factors for the Monte Carlo datasets (DS) of the signal and the control region for each of the used triggers.

B.2 Histograms for the acceptance calculation after acceptance cuts

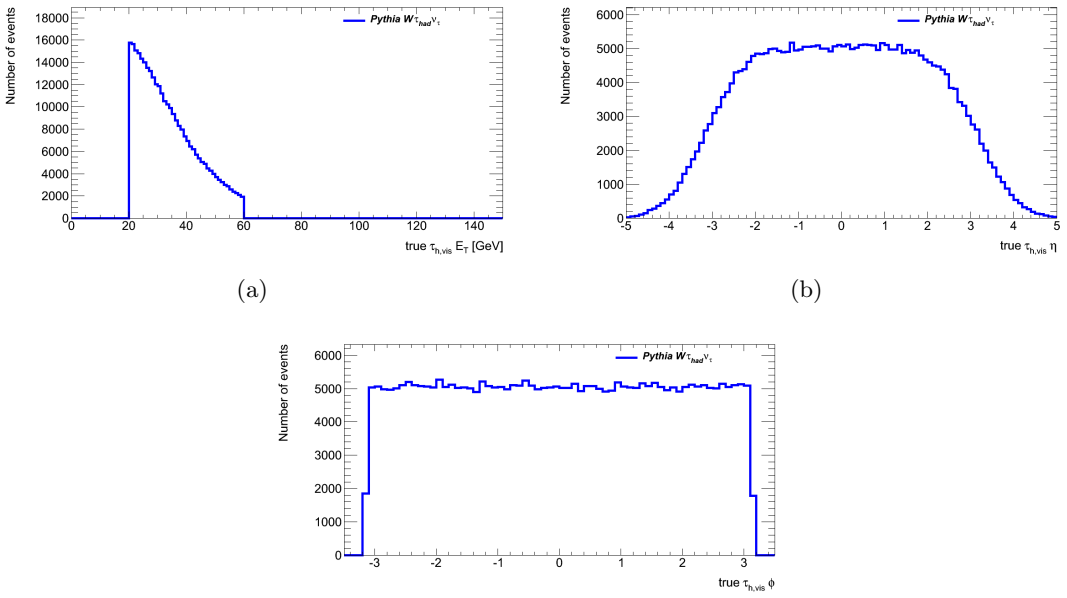

(a) (b)

(c)

Figure B.1: (a) Visible transverse energy, (b) pseudorapidity η, and (c) angle ϕ of the true $\tau_{\mathrm{h,vis}}$ lepton after the cut on the transverse momentum p_{T} of the true $\tau_{\mathrm{h,vis}}$ lepton.

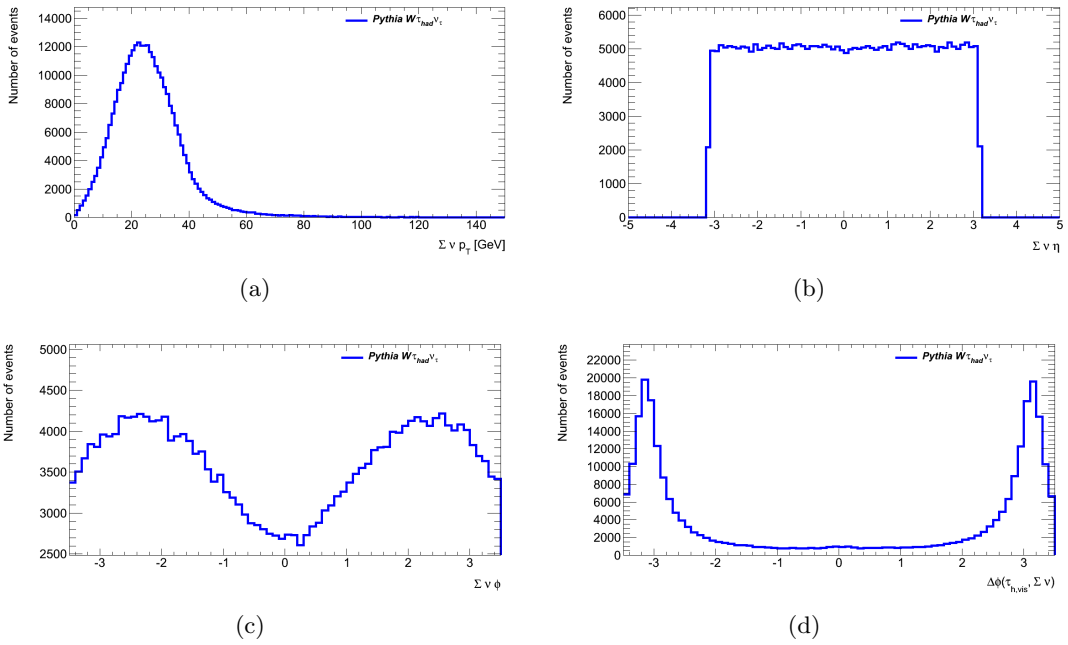

(a) (b) (c) (d)

Figure B.2: (a) Transverse momentum, (b) pseudorapidity η, (c) angle ϕ of the sum of the neutrinos $\sum \nu$, and (d) angle $\Delta\phi$ between the true $\tau_{\mathrm{h,vis}}$ lepton and the sum of the neutrinos $\sum \nu$ after the cut on the transverse momentum p_{T} of the true $\tau_{\mathrm{h,vis}}$ lepton.

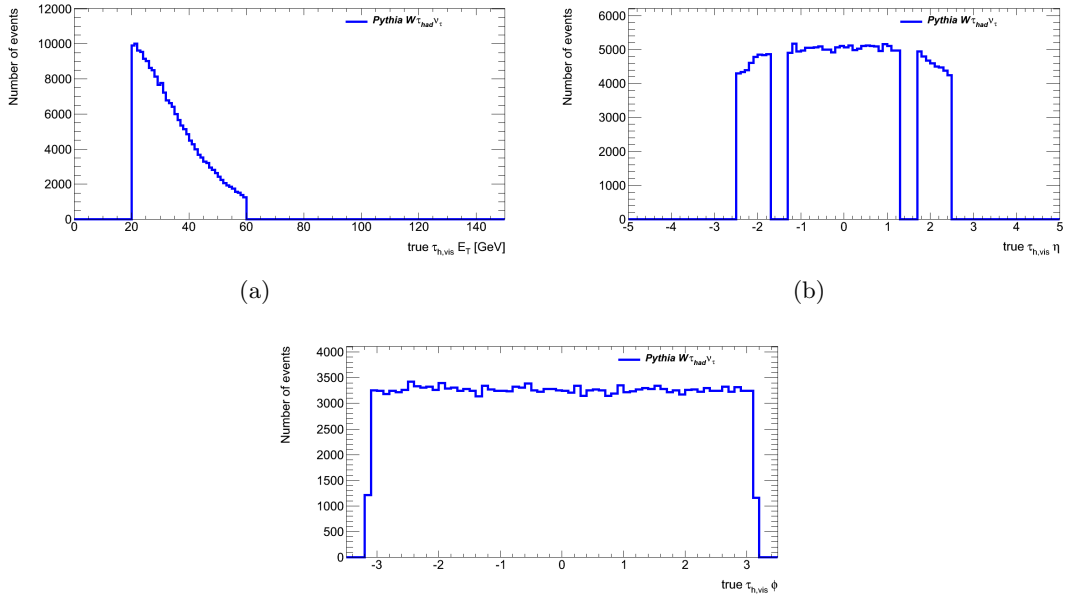

(a) (b) (c)

Figure B.3: (a) Visible transverse energy, (b) pseudorapidity η, and (c) angle ϕ of the true $\tau_{\mathrm{h,vis}}$ lepton after the cuts on the transverse momentum p_{T} and the pseudorapidity η of the true $\tau_{\mathrm{h,vis}}$ lepton.

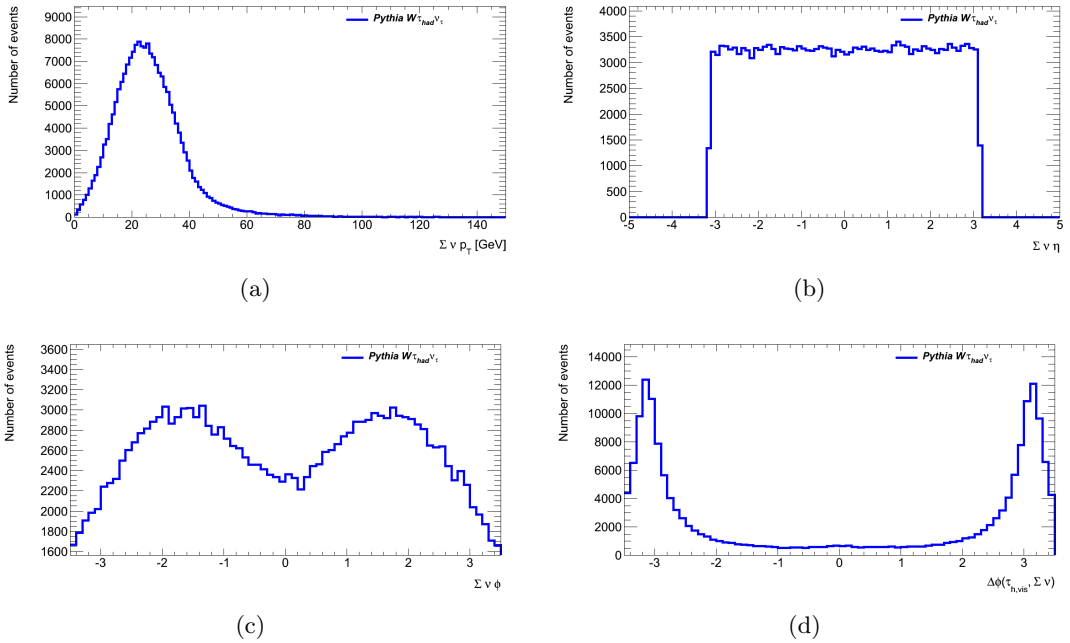

Figure B.4: (a) Transverse momentum, (b) pseudorapidity η, (c) angle ϕ of the sum of the neutrinos $\sum \nu$, and (d) angle $\Delta\phi$ between the true $\tau_{\mathrm{h,vis}}$ lepton and the sum of the neutrinos $\sum \nu$ after the cuts on the transverse momentum p_{T} and the pseudorapidity η of the true $\tau_{\mathrm{h,vis}}$ lepton.

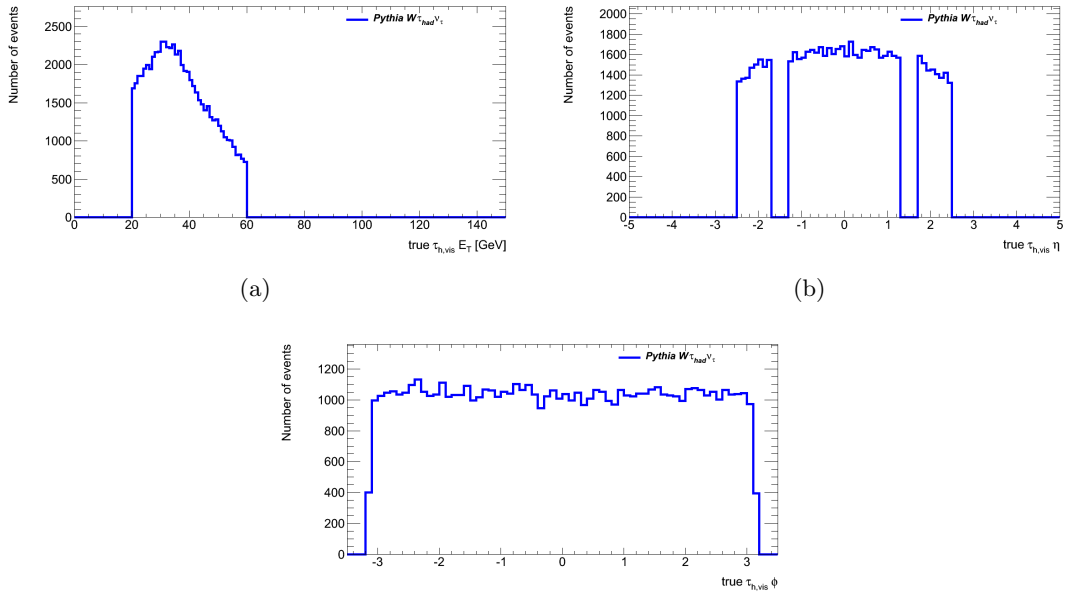

Figure B.5: (a) Visible transverse energy, (b) pseudorapidity η, and (c) angle ϕ of the true $\tau_{\mathrm{h,vis}}$ lepton after the cuts on the transverse momentum p_{T} and the pseudorapidity η of the true $\tau_{\mathrm{h,vis}}$ lepton and the transverse momentum of the sum of the neutrino $(\sum p^{\nu})_{\mathrm{T}}$.

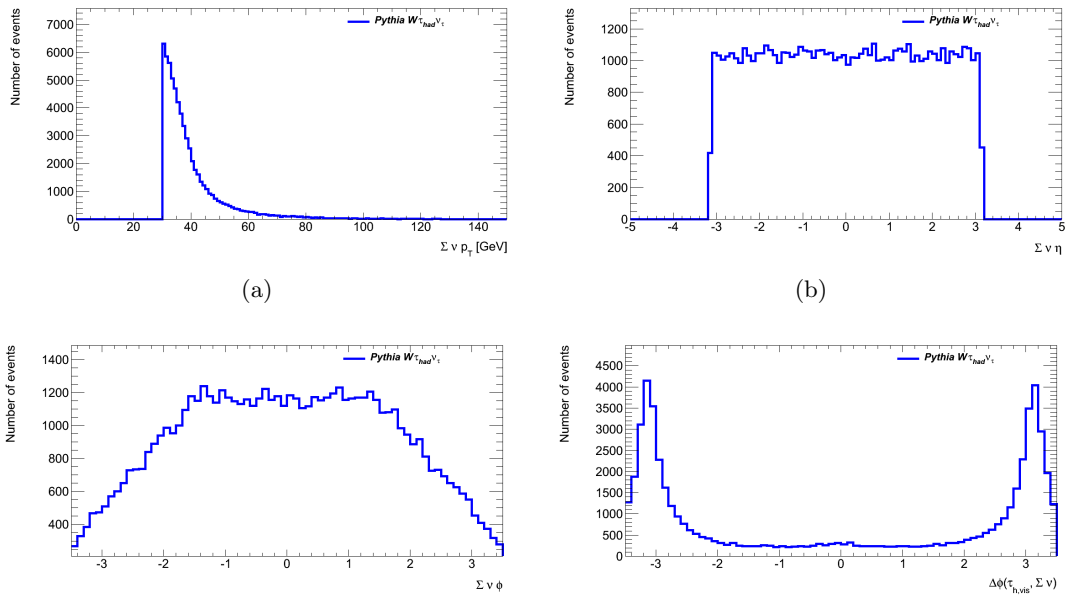

Figure B.6: (a) Transverse momentum, (b) pseudorapidity η, (c) angle ϕ of the sum of the neutrinos $\sum \nu$, and (d) angle $\Delta\phi$ between the true $\tau_{\mathrm{h,vis}}$ lepton and the sum of the neutrinos $\sum \nu$ after the cuts on the transverse momentum p_{T} and the pseudorapidity η of the true $\tau_{\mathrm{h,vis}}$ lepton and the transverse momentum of the sum of the neutrino $(\sum p^{\nu})_{\mathrm{T}}$.

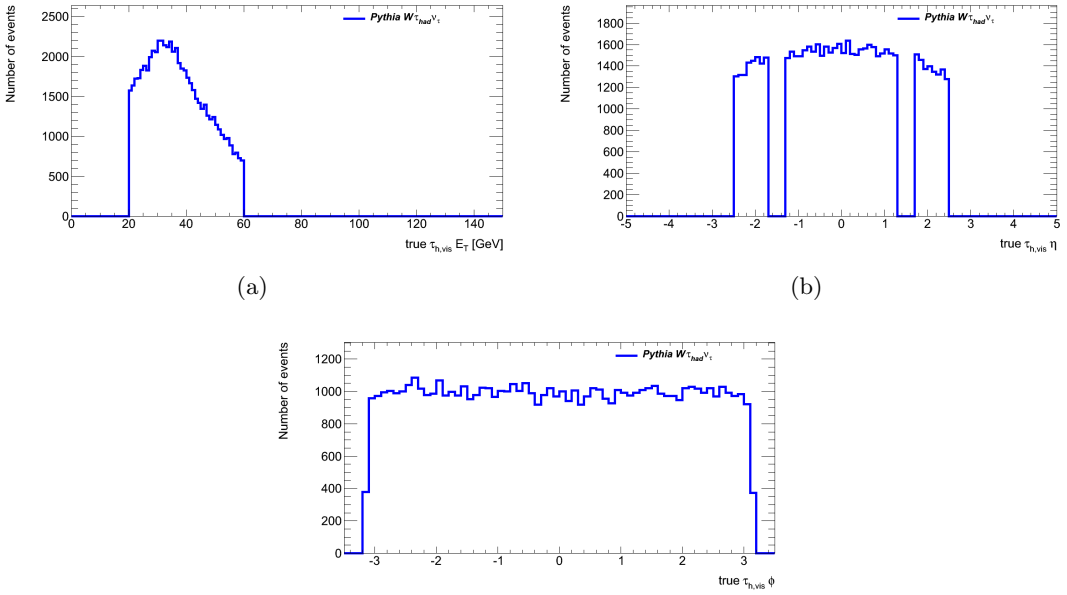

Figure B.7: (a) Visible transverse energy, (b) pseudorapidity η, and (c) angle ϕ of the true $\tau_{\mathrm{h,vis}}$ lepton after all cuts on the transverse momentum p_{T} and the pseudorapidity η of the true $\tau_{\mathrm{h,vis}}$ lepton, the transverse momentum of the sum of the neutrino $(\sum p^{\nu})_{\mathrm{T}}$ and the $|\Delta\phi\,(\tau_{\mathrm{h,vis}}, \sum \nu)|$.

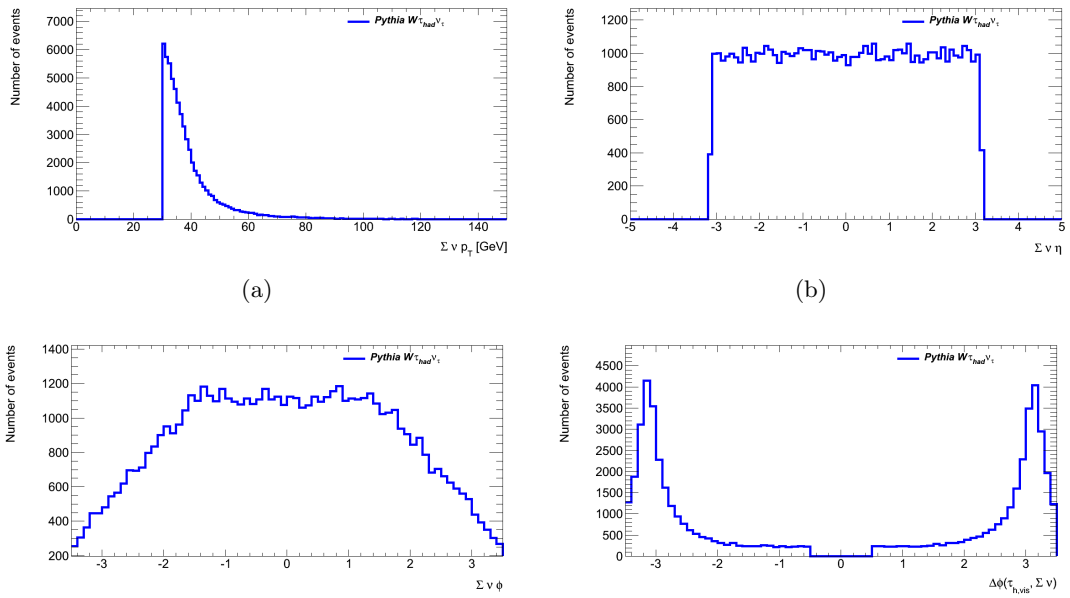

(a) (b) (c) (d)

Figure B.8: (a) Transverse momentum, (b) pseudorapidity η, (c) angle ϕ of the sum of the neutrinos $\sum \nu$, and (d) angle $\Delta\phi$ between the true $\tau_{\mathrm{h,vis}}$ lepton and the sum of the neutrinos $\sum \nu$ after all cuts on the transverse momentum p_{T} and the pseudorapidity η of the true $\tau_{\mathrm{h,vis}}$ lepton, the transverse momentum of the sum of the neutrino $(\sum p^{\nu})_{\mathrm{T}}$ and the $|\Delta\phi\,(\tau_{\mathrm{h,vis}}, \sum \nu)|$.

B.3 Cut flow table of error eigenvectors within one PDF set for the acceptance calculation

Eigenvector \ Cut	Events (no cut)	$\tau_{\mathrm{h}}\ p_{\mathrm{T}}$	$\tau_{\mathrm{h}}\ \eta$	$(\sum p^{\nu})_{\mathrm{T}}$	$\lvert\Delta\phi\left(\tau_{\mathrm{h,vis}}, \sum\nu\right)\rvert$	$A_W = \lvert\Delta\phi\left(\tau_{\mathrm{h,vis}}, \sum\nu\right)\rvert$/Events
central value 0	613870.5 ± 783.5	304659.0 ± 552.0	200277.0 ± 447.5	63613.8 ± 252.2	60824.1 ± 246.6	0.0991 ± 0.0004
eigenvector set 1	607092.8 ± 779.2	301309.9 ± 548.9	197695.3 ± 444.6	62784.0 ± 250.6	60023.3 ± 245.0	0.0989 ± 0.0004
eigenvector set 2	620840.1 ± 787.9	308102.7 ± 555.1	202933.7 ± 450.5	64467.8 ± 253.9	61648.2 ± 248.3	0.0993 ± 0.0004
eigenvector set 3	609378.0 ± 780.6	302446.3 ± 550.0	198999.5 ± 446.1	63242.2 ± 251.5	60474.1 ± 245.9	0.0992 ± 0.0004
eigenvector set 4	618366.3 ± 786.4	306872.0 ± 554.0	201536.1 ± 448.9	63979.4 ± 252.9	61168.0 ± 247.3	0.0989 ± 0.0004
eigenvector set 5	613370.7 ± 783.2	304407.2 ± 551.7	199946.0 ± 447.2	63533.5 ± 252.1	60749.5 ± 246.5	0.0990 ± 0.0004
eigenvector set 6	614349.2 ± 783.8	304901.0 ± 552.2	200613.2 ± 447.9	63693.2 ± 252.4	60897.5 ± 246.8	0.0991 ± 0.0004
eigenvector set 7	610339.3 ± 781.2	302895.3 ± 550.4	199220.9 ± 446.3	63272.1 ± 251.5	60495.6 ± 246.0	0.0991 ± 0.0004
eigenvector set 8	617375.6 ± 785.7	306411.0 ± 553.5	201314.1 ± 448.7	63949.7 ± 252.9	61147.0 ± 247.3	0.0990 ± 0.0004
eigenvector set 9	607805.3 ± 779.6	301664.7 ± 549.2	198308.4 ± 445.3	62984.8 ± 251.0	60223.6 ± 245.4	0.0991 ± 0.0004
eigenvector set 10	620271.2 ± 787.6	307816.1 ± 554.8	202292.7 ± 449.8	64257.4 ± 253.5	61437.6 ± 247.9	0.0990 ± 0.0004
eigenvector set 11	603249.7 ± 776.7	299431.3 ± 547.2	197408.6 ± 444.3	62686.6 ± 250.4	59942.2 ± 244.8	0.0994 ± 0.0004
eigenvector set 12	625100.9 ± 790.6	310178.2 ± 556.9	203133.6 ± 450.7	64532.9 ± 254.0	61695.4 ± 248.4	0.0987 ± 0.0004
eigenvector set 13	616397.0 ± 785.1	305907.0 ± 553.1	200625.6 ± 447.9	63748.6 ± 252.5	60954.5 ± 246.9	0.0989 ± 0.0004
eigenvector set 14	611027.0 ± 781.7	303254.6 ± 550.7	199797.4 ± 447.0	63436.0 ± 251.9	60652.1 ± 246.3	0.0993 ± 0.0004
eigenvector set 15	613827.1 ± 783.5	304632.8 ± 551.9	200030.9 ± 447.2	63567.7 ± 252.1	60783.1 ± 246.5	0.0990 ± 0.0004
eigenvector set 16	613791.6 ± 783.4	304627.1 ± 551.9	200527.8 ± 447.8	63651.3 ± 252.3	60855.8 ± 246.7	0.0991 ± 0.0004
eigenvector set 17	617414.2 ± 785.8	306436.3 ± 553.6	201907.0 ± 449.3	64138.9 ± 253.3	61337.2 ± 247.7	0.0993 ± 0.0004
eigenvector set 18	610717.2 ± 781.5	303075.0 ± 550.5	198792.2 ± 445.9	63134.9 ± 251.3	60355.5 ± 245.7	0.0988 ± 0.0004
eigenvector set 19	609433.9 ± 780.7	302427.9 ± 549.9	198397.2 ± 445.4	63067.5 ± 251.1	60299.7 ± 245.6	0.0989 ± 0.0004
eigenvector set 20	619057.8 ± 786.8	307263.2 ± 554.3	202435.6 ± 449.9	64247.3 ± 253.5	61432.4 ± 247.9	0.0992 ± 0.0004
eigenvector set 21	604633.2 ± 777.6	300080.0 ± 547.8	196225.2 ± 443.0	62317.9 ± 249.6	59573.4 ± 244.1	0.0985 ± 0.0004
eigenvector set 22	620108.2 ± 787.5	307751.5 ± 554.8	203163.7 ± 450.7	64536.3 ± 254.0	61715.3 ± 248.4	0.0995 ± 0.0004
eigenvector set 23	611459.0 ± 782.0	303435.7 ± 550.9	199292.2 ± 446.4	63328.6 ± 251.7	60548.7 ± 246.1	0.0990 ± 0.0004
eigenvector set 24	615151.8 ± 784.3	305325.6 ± 552.6	200863.9 ± 448.2	63772.1 ± 252.5	60977.1 ± 246.9	0.0991 ± 0.0004
eigenvector set 25	614411.2 ± 783.8	304897.6 ± 552.2	200777.6 ± 448.1	63848.4 ± 252.7	61053.6 ± 247.1	0.0994 ± 0.0004
eigenvector set 26	612011.1 ± 782.3	303762.8 ± 551.1	199314.0 ± 446.4	63240.5 ± 251.5	60461.6 ± 245.9	0.0988 ± 0.0004
eigenvector set 27	612866.7 ± 782.9	304114.4 ± 551.5	200011.4 ± 447.2	63580.7 ± 252.2	60791.2 ± 246.6	0.0992 ± 0.0004
eigenvector set 28	615208.9 ± 784.4	305362.3 ± 552.6	200707.2 ± 448.0	63700.6 ± 252.4	60908.1 ± 246.8	0.0990 ± 0.0004
eigenvector set 29	613549.1 ± 783.3	304501.3 ± 551.8	200167.1 ± 447.4	63559.9 ± 252.1	60766.9 ± 246.5	0.0990 ± 0.0004
eigenvector set 30	614786.5 ± 784.1	305119.7 ± 552.4	200772.5 ± 448.1	63763.2 ± 252.5	60971.5 ± 246.9	0.0992 ± 0.0004
eigenvector set 31	607357.2 ± 779.3	301434.8 ± 549.0	197923.0 ± 444.9	62845.5 ± 250.7	60084.9 ± 245.1	0.0989 ± 0.0004
eigenvector set 32	616744.9 ± 785.3	306088.4 ± 553.3	201284.4 ± 448.6	63945.6 ± 252.9	61143.8 ± 247.3	0.0991 ± 0.0004
eigenvector set 33	613366.9 ± 783.2	304444.1 ± 551.8	200466.7 ± 447.7	63636.4 ± 252.3	60845.6 ± 246.7	0.0992 ± 0.0004
eigenvector set 34	613900.8 ± 783.5	304647.7 ± 551.9	200052.5 ± 447.3	63541.7 ± 252.1	60751.6 ± 246.5	0.0990 ± 0.0004
eigenvector set 35	615161.3 ± 784.3	305303.6 ± 552.5	200906.5 ± 448.2	63769.9 ± 252.5	60969.5 ± 246.9	0.0991 ± 0.0004
eigenvector set 36	614415.4 ± 783.8	304935.6 ± 552.2	200639.1 ± 447.9	63716.4 ± 252.4	60922.6 ± 246.8	0.0992 ± 0.0004
eigenvector set 37	614276.0 ± 783.8	304865.4 ± 552.1	200556.9 ± 447.8	63671.1 ± 252.3	60876.2 ± 246.7	0.0991 ± 0.0004
eigenvector set 38	611962.3 ± 782.3	303723.8 ± 551.1	199694.1 ± 446.9	63404.3 ± 251.8	60621.0 ± 246.2	0.0991 ± 0.0004
eigenvector set 39	615894.1 ± 784.8	305676.0 ± 552.9	201126.8 ± 448.5	63841.2 ± 252.7	61038.6 ± 247.1	0.0991 ± 0.0004
eigenvector set 40	611828.4 ± 782.2	303646.5 ± 551.0	199674.3 ± 446.8	63406.4 ± 251.8	60623.5 ± 246.2	0.0991 ± 0.0004

Table B.7: Number of events after the acceptance cuts and resulting acceptances of the central value and all 44 error eigenvectors of the PDF set CTEQ6.6. The MC is not scaled, but reweighted from the MRST2007lomod PDF to the corresponding eigenvector of CTEQ6.6.

B.4 Summary tables for systematic uncertainties of the indiviudal electroweak background, N_{EW}, N_{QCD} and C_W

	$W \to e\nu_e$	$W \to \mu\nu_\mu$	$W \to \tau_{\mathrm{l}}\nu_\tau$	$Z \to \tau\tau$	$t\bar{t}$ lep
Trigger efficiency	6.1%	6.1%	6.1%	6.1%	6.1%
Energy scale	14.1%	5.8%	9.6%	6.2%	-
τ_{h} identification	-	-	-	9.8%	10.3%
Jet τ_{h} misidentification	9%	13%	31%	-	-
Electron τ_{h} misidentification	13.8%	-	-	-	-
Pile-up reweighting	0.4%	2.3%	2.6%	1.2%	1.6%
Electron reconstruction/identification	3.5%	-	1.2%	0	0.5%
Muon reconstruction	-	0.8%	0	0.3%	0.4%
Jet cleaning	-	-	-	-	-
Underlying event modeling	1.1%	1.1%	1.1%	1.1%	1.1%
Cross section	3.8%	3.8%	5.0%	5.0%	9.7%

Table B.8: Summary table for systematic uncertainties affecting the individual EW backgrounds [138].

	EW Sum
Trigger efficiency	6.1%
Energy scale	8.7%
τ_{h} identification	4.1%
Jet τ_{h} misidentification	7.2%
Electrob τ_{h} misidentification	4.5%
Pile-up reweighting	1.2%
Electron reconstruction/identification	1.2%
Muon reconstruction	0.3%
Jet cleaning	-
Underlying event modelling	1.1%
Cross section	4.5%
Total systematic	15.0%
Number of events	283.6
Stat.	6.9
Syst.	42.6

Table B.9: Summary table for systematic uncertainties affecting N_{EW} [138].

	QCD
QCD estimation: Stability/correlation	2.7%
QCD estimation: Signal/EW contamination	2.1%
Total systematic	3.4%
Number of events	127
Stat.	8
Syst.	4.3

Table B.10: Summary table for systematic uncertainties affecting N_{QCD} [138].

	C_W
Trigger efficiency	6.1%
Energy scale	6.7%
τ_{h} identification	9.6%
Pile-up reweighting	1.4%
Underlying event modelling	1.3%
Jet cleaning	-
Total systematic	13.3%
C_W value	0.0799
Stat. error	0.0011
Syst. error	0.0107

Table B.11: Summary table for systematic uncertainties affecting C_W [138].

List of Figures

List of Tables

Bibliography

[1] Combination of Higgs Boson Searches with up to 4.9 fb^{-1} of pp Collisions Data Taken at a center-of-mass energy of 7 TeV with the ATLAS Experiment at the LHC. (ATLAS-CONF-2011-163), Dec 2011.

[2] A. Heister et al. Measurement of W-pair production in e^+e^- collisions at centre-of-mass energies from 183 GeV to 209 GeV. *Eur.Phys.J.*, C38:147–160, 2004.

[3] J. Abdallah et al. Measurement of the W pair production cross-section and W branching ratios in e^+e^- collisions at $\sqrt{s} = 161$ GeV to 209 GeV. *Eur.Phys.J.*, C34:127–144, 2004.

[4] P. Achard et al. Measurement of the cross section of W-boson pair production at LEP. *Phys.Lett.*, B600:22–40, 2004.

[5] G. Abbiendi et al. Measurement of the $e^+e^- \to W^+W^-$ cross section and W decay branching fractions at LEP. *Eur.Phys.J.*, C52:767–785, 2007. This paper is dedicated to the memory of Ben Shen.

[6] Steven Weinberg. A Model of Leptons. *Phys. Rev. Lett.*, 19:1264–1266, 1967.

[7] S. L. Glashow. Partial Symmetries of Weak Interactions. *Nucl. Phys.*, 22:579–588, 1961.

[8] Abdus Salam. Weak and Electromagnetic Interactions. Originally printed in *Svartholm: Elementary Particle Theory, Proceedings of the Nobel Symposium Held 1968 at Lerum, Sweden*, Stockholm 1968, 367-377.

[9] H. Fritzsch, Murray Gell-Mann, and H. Leutwyler. Advantages of the Color Octet Gluon Picture. *Phys. Lett.*, B47:365–368, 1973.

[10] Marciano, William J. Elementary Particle Theory. *AIP Conf.Proc.*, 127:731–792, 1985.

[11] DESY - Media Database. *Website*. Available online at `http://bilder.desy.de:9080/DESYmediabank//ConvertAssets/Vereinigung_der_Kraefte_eng.jpg`; visited on December 9th 2011.

[12] K. Nakamura et al. Review of particle physics. *J. Phys.*, G37:075021, 2010.

[13] Berger, Christoph. Elementarteilchenphysik - Von den Grundlagen zu den modernen Experimenten. *Springer*, 2002.

[14] Julian Schwinger. On quantum-electrodynamics and the magnetic moment of the electron. *Phys. Rev.*, 73:416–417, Feb 1948.

[15] R. P. Feynman. Mathematical formulation of the quantum theory of electromagnetic interaction. *Phys. Rev.*, 80:440–457, Nov 1950.

[16] F. Englert and R. Brout. Broken symmetry and the mass of gauge vector mesons. *Phys. Rev. Lett.*, 13:321–323, Aug 1964.

[17] Peter W. Higgs. Broken symmetries and the masses of gauge bosons. *Phys. Rev. Lett.*, 13:508–509, Oct 1964.

[18] CERN Press Office. ATLAS and CMS experiments present Higgs search status. *Website.* Available online at `http://press.web.cern.ch/press/pressreleases/releases2011/PR25.11E.html`; visited on December 16th 2011.

[19] M. Baak, M. Goebel, J. Haller, A. Hoecker, D. Ludwig, et al. Updated Status of the Global Electroweak Fit and Constraints on New Physics. 2011.

[20] Daniel Stump, Joey Huston, Jon Pumplin, Wu-Ki Tung, H.L. Lai, et al. Inclusive jet production, parton distributions, and the search for new physics. *JHEP*, 0310:046, 2003.

[21] A.D. Martin, R.G. Roberts, W.J. Stirling, and R.S. Thorne. Physical gluons and high E_T jets. *Phys.Lett.*, B604:61–68, 2004.

[22] A.D. Martin, W.J. Stirling, R.S. Thorne, and G. Watt. Parton distributions for the LHC. *Eur.Phys.J.*, C63:189–285, 2009.

[23] S. Alekhin. Parton distribution functions from the precise NNLO QCD fit. *JETP Lett.*, 82:628–631, 2005.

[24] C. Adloff et al. Deep inelastic inclusive *ep* scattering at low x and a determination of alpha(s). *Eur.Phys.J.*, C21:33–61, 2001.

[25] C. Adloff et al. Measurement and QCD analysis of neutral and charged current cross-sections at HERA. *Eur.Phys.J.*, C30:1–32, 2003.

[26] S. Chekanov et al. A ZEUS next-to-leading-order QCD analysis of data on deep inelastic scattering. *Phys.Rev.*, D67:012007, 2003.

[27] S. Chekanov et al. An NLO QCD analysis of inclusive cross-section and jet-production data from the ZEUS experiment. *Eur.Phys.J.*, C42:1–16, 2005.

[28] F.D. Aaron et al. Combined Measurement and QCD Analysis of the Inclusive $e^{\pm}p$ Scattering Cross Sections at HERA. *JHEP*, 1001:109, 2010.

[29] Campbell, John M. and Huston, J. W. and Stirling, W. J. Hard Interactions of Quarks and Gluons: A Primer for LHC Physics. *Rept. Prog. Phys.*, 70:89, 2007.

[30] S.D. Drell and Tung-Mow Yan. Partons and their Applications at High-Energies. *Annals Phys.*, 66:578, 1971.

[31] L.N. Lipatov. The parton model and perturbation theory. *Sov.J.Nucl.Phys.*, 20:94–102, 1975.

[32] Vladimir Naumovich Gribov and L N Lipatov. Deep inelastic *ep* scattering in perturbation theory. *Sov. J. Nucl. Phys.*, 15(4):438–450, 1972.

[33] Guido Altarelli and G. Parisi. Asymptotic Freedom in Parton Language. *Nucl.Phys.*, B126:298, 1977.

[34] Yuri L. Dokshitzer. Calculation of the Structure Functions for Deep Inelastic Scattering and e^+e^- Annihilation by Perturbation Theory in Quantum Chromodynamics. *Sov. Phys. JETP*, 46:641–653, 1977.

[35] I.I. Balitsky and L.N. Lipatov. The Pomeranchuk Singularity in Quantum Chromodynamics. *Sov.J.Nucl.Phys.*, 28:822–829, 1978.

[36] Victor S. Fadin, E.A. Kuraev, and L.N. Lipatov. On the Pomeranchuk Singularity in Asymptotically Free Theories. *Phys.Lett.*, B60:50–52, 1975.

[37] E.A. Kuraev, L.N. Lipatov, and Victor S. Fadin. Multi - Reggeon Processes in the Yang-Mills Theory. *Sov.Phys.JETP*, 44:443–450, 1976.

[38] E.A. Kuraev, L.N. Lipatov, and Victor S. Fadin. The Pomeranchuk Singularity in Non-abelian Gauge Theories. *Sov.Phys.JETP*, 45:199–204, 1977.

[39] Marcello Ciafaloni. Coherence effects in initial jets at small Q^2/s. oai:cds.cern.ch:176717. *Nucl. Phys. B*, 296(CERN-TH-4672-87):49–74. 37 p, Mar 1987.

[40] S. Catani, F. Fiorani, and G. Marchesini. QCD Coherence in Initial State Radiation. *Phys.Lett.*, B234:339, 1990.

[41] Martin L. Perl et al. Evidence for anomalous lepton production in e^+e^- annihilation. *Phys. Rev. Lett.*, 35:1489–1492, 1975.

[42] K. Kodama et al. Observation of tau neutrino interactions. *Phys.Lett.*, B504:218–224, 2001. Press release available at `http://www.fnal.gov/pub/presspass/press_releases/donut.html`.

[43] C. Albajar et al. Studies of Intermediate Vector Boson Production and Decay in UA1 at the CERN Proton - Antiproton Collider. *Z. Phys.*, C44:15–61, 1989.

[44] J. Alitti et al. A Measurement of the W and Z production cross-sections and a determination of Gamma (W) at the CERN $\bar{p}p$ collider. *Phys.Lett.*, B276:365–374, 1992.

[45] J. Alcaraz et al. Precision Electroweak Measurements and Constraints on the Standard Model. 2007.

[46] H. Georgi and S.L. Glashow. Unity of All Elementary Particle Forces. *Phys.Rev.Lett.*, 32:438–441, 1974.

[47] Stephen P. Martin. A Supersymmetry primer. 1997.

[48] Howard E. Haber and Gordon L. Kane. The Search for Supersymmetry: Probing Physics Beyond the Standard Model. *Phys.Rept.*, 117:75–263, 1985.

[49] Hans Peter Nilles. Supersymmetry, Supergravity and Particle Physics. *Phys.Rept.*, 110:1–162, 1984.

[50] E. Komatsu et al. Five-Year Wilkinson Microwave Anisotropy Probe (WMAP) Observations: Cosmological Interpretation. *Astrophys.J.Suppl.*, 180:330–376, 2009.

[51] A.D. Sakharov. Violation of CP Invariance, c Asymmetry, and Baryon Asymmetry of the Universe. *Pisma Zh.Eksp.Teor.Fiz.*, 5:32–35, 1967. Reprinted in *Kolb, E.W. (ed.), Turner, M.S. (ed.): The early universe* 371-373, and in *Lindley, D. (ed.) et al.: Cosmology and particle physics* 106-109, and in Sov. Phys. Usp. 34 (1991) 392-393 [Usp. Fiz. Nauk 161 (1991) No. 5 61-64].

[52] Andrew G. Cohen, D.B. Kaplan, and A.E. Nelson. Progress in electroweak baryogenesis. *Ann.Rev.Nucl.Part.Sci.*, 43:27–70, 1993.

[53] M.B. Gavela, P. Hernandez, J. Orloff, O. Pene, and C. Quimbay. Standard model CP violation and baryon asymmetry. Part 2: Finite temperature. *Nucl.Phys.*, B430:382–426, 1994.

[54] Howard E. Haber. The Status of the minimal supersymmetric standard model and beyond. *Nucl.Phys.Proc.Suppl.*, 62:469–484, 1998.

[55] D.I. Kazakov. Beyond the standard model: In search of supersymmetry. pages 125–199, 2000.

[56] Search for the Standard Model Higgs boson produced in association with a vector boson and decaying to a b-quark pair with the ATLAS detector at the LHC. (ATLAS-CONF-2011-103), Jul 2011.

[57] G Aad et al. Expected performance of the ATLAS experiment: detector, trigger and physics. 2009.

[58] Aad, G. and others. The ATLAS Experiment at the CERN Large Hadron Collider. *JINST*, 3:S08003, 2008.

[59] ATLAS Collaboration. Search for the Standard Model Higgs boson in the diphoton decay channel with 4.9 fb^{-1} of pp collisions at $\sqrt{s} = 7$ TeV with ATLAS. 2012.

[60] LHC Higgs Cross Section Working Group, S. Dittmaier, C. Mariotti, G. Passarino, and R. Tanaka (Eds.). Handbook of LHC Higgs Cross Sections: 1. Inclusive Observables. *CERN-2011-002*, CERN, Geneva, 2011.

[61] Andre Sopczak. Cross-sections and branching ratios for charged Higgs searches. *PoS*, CHARGED2008:023, 2008.

[62] Stephen Godfrey and Ken Moats. Exploring Higgs Triplet Models via Vector Boson Scattering at the LHC. *Phys.Rev.*, D81:075026, 2010.

[63] Eri Asakawa, Shinya Kanemura, and Junichi Kanzaki. Potential for measuring the $H^{\pm}$ $W^{\mp}$ Z^0 vertex from WZ fusion at the Large Hadron Collider. *Phys.Rev.*, D75:075022, 2007.

[64] (ed.) Evans, Lyndon and (ed.) Bryant, Philip. LHC Machine. *JINST*, 3:S08001, 2008.

[65] Lyndon Evans. The LHC machine. *PoS*, EPS-HEP2009:004, 2009.

[66] CERN Press Office. LHC progress report, week 1. *Website*. Available online at `http://lhc-first-beam.web.cern.ch/lhc-first-beam/News/lhc_080918.html`; visited on October 10th 2011.

[67] CERN Press Office. Incident in LHC sector 3-4. *Website*. Available online at `http://press.web.cern.ch/press/PressReleases/Releases2008/PR09.08E.html`; visited on October 10th 2011.

[68] CERN Press Office. CERN releases analysis of LHC incident. *Website*. Available online at `http://press.web.cern.ch/press/PressReleases/Releases2008/PR14.08E.html`; visited on October 10th 2011.

[69] CERN Press Office. The LHC is back. *Website*. Available online at `http://press.web.cern.ch/press/PressReleases/Releases2009/PR16.09E.html`; visited on October 10th 2011.

[70] CERN Press Office. Two circulating beams bring first collisions in the LHC. *Website*. Available online at `http://press.web.cern.ch/press/PressReleases/Releases2009/PR17.09E.html`; visited on October 10th 2011.

[71] CERN Press Office. LHC research programme gets underway. *Website*. Available online at `http://press.web.cern.ch/press/PressReleases/Releases2010/PR07.10E.html`; visited on October 10th 2011.

[72] CERN Press Office. CERN completes transition to lead-ion running at the LHC. *Website*. Available online at `http://press.web.cern.ch/press/PressReleases/Releases2010/PR21.10E.html`; visited on October 11th 2011.

[73] CERN Press Office. CERN announces LHC to run in 2012. *Website*. Available online at `http://press.web.cern.ch/press/pressreleases/Releases2011/PR01.11E.html`; visited on October 11th 2011.

[74] The accelerator complex. *Website*. Available online at `http://public.web.cern.ch/public/en/Research/AccelComplex-en.html`; visited on September 28th 2011.

[75] Etienvre, A. I. Top mass measurement at LHC. *PoS*, TOP2006:023, 2006.

[76] Patrick Reichart. Relativistische Kinematik - Formelsammlung. *Website*. Available online at `http://www.e12.physik.tu-muenchen.de/stud/vorlesungen/misc/relkin.pdf`; visited on November 3rd 2011.

[77] ATLAS collaboration. ATLAS magnet system: Technical Design Report, 1. 1997.

[78] ATLAS collaboration. ATLAS central solenoid: Technical Design Report. 1997. Electronic version not available.

[79] A. Yamamoto, Y. Doi, Y. Makida, K. Tanaka, T. Haruyama, H. Yamaoka, T. Kondo, S. Mizumaki, S. Mine, K. Wada, S. Meguro, T. Sotoki, K. Kikuchi, and H. H. J. ten Kate. Progress in ATLAS central solenoid magnet. *IEEE Trans. Appl. Supercond.*, 10(1):353–6, 2000.

[80] J. P. Badiou, J. Beltramelli, J. M. Maze, and J. Belorgey. ATLAS barrel toroid: Technical Design Report. 1997. Electronic version not available.

[81] ATLAS collaboration. ATLAS end-cap toroids: Technical Design Report. 1997. Electronic version not available.

[82] ATLAS collaboration. ATLAS inner detector: Technical Design Report, 1. 1997.

[83] N. Wermes and G. Hallewel. ATLAS pixel detector: Technical Design Report. 1998.

[84] Ahmad, A. et al. The Silicon Microstrip Sensors of the ATLAS SemiConductor Tracker. oai:cds.cern.ch:1019885. (ATL-INDET-PUB-2007-007. ATL-COM-INDET-2007-008. CERN-ATL-COM-INDET-2007-008. 1), Mar 2007.

[85] E. Abat et al. The ATLAS Transition Radiation Tracker (TRT) proportional drift tube: Design and performance. *JINST*, 3:P02013, 2008.

[86] ATLAS collaboration. ATLAS liquid-argon calorimeter: Technical Design Report. 1996.

[87] ATLAS collaboration. ATLAS tile calorimeter: Technical Design Report. 1996.

[88] ATLAS collaboration. ATLAS muon spectrometer: Technical Design Report. 1997. distribution.

[89] ATLAS collaboration. ATLAS level-1 trigger: Technical Design Report. 1998.

[90] Mogens Dam. The ATLAS tau trigger. *J.Phys.Conf.Ser.*, 219:032006, 2010.

[91] J Garvey et al. Use of an FPGA to identify electromagnetic clusters and isolated hadrons in the ATLAS level-1 calorimeter trigger. oai:cds.cern.ch:725122. (ATL-DAQ-2004-008), Dec 2003.

[92] Pierre-Hugues Beauchemin. Performance of the ATLAS missing E_{T} trigger with first $\sqrt{s}$ = 7 TeV data. *J.Phys.Conf.Ser.*, 293:012015, 2011.

[93] Tau Reconstruction and Identification Performance in ATLAS. (ATLAS-CONF-2010-086), Oct 2010.

[94] Reconstruction of hadronic tau candidates in QCD events at ATLAS with 7 TeV proton-proton collisions. (ATLAS-CONF-2010-059), Jul 2010.

[95] Performance of the Missing Transverse Energy Reconstruction and Calibration in Proton-Proton Collisions at a Center-of-Mass Energy of 7 TeV with the ATLAS Detector. (ATLAS-CONF-2010-057), Jul 2010.

[96] Reconstruction and Calibration of Missing Transverse Energy and Performance in Z and W events in ATLAS Proton-Proton Collisions at 7 TeV. (ATLAS-CONF-2011-080), Jun 2011.

[97] G Aad et al. Performance of the ATLAS Detector using First Collision Data. *JHEP*, 09:056, 2010.

[98] ATLAS Computing: technical design report. (ATLAS-TDR-017, CERN-LHCc-2005-022), 2005.

[99] ATLAS Collaboration. ATLAS Experiment - Public Results - Luminosity Public Results. *Website*. Available online at `https://twiki.cern.ch/twiki/bin/view/AtlasPublic/LuminosityPublicResults`; visited on November 13th 2011.

[100] Luminosity Determination Using the ATLAS Detector. (ATLAS-CONF-2010-060), Jul 2010.

[101] Aad, Georges et al. Luminosity Determination in pp Collisions at $\sqrt{s} = 7$ TeV using the ATLAS Detector at the LHC. oai:cds.cern.ch:1323586. *Eur. Phys. J. C*, 71(arXiv:1101.2185. CERN-PH-EP-2010-069):1630. 61 p, Jan 2011. Comments: 24 pages plus author list (36 pages total). 9 Figures, 10 Tables, submitted to Journal EPJC.

[102] ATLAS Collaboration. DataPeriods. *Website*. Available online at `https://twiki.cern.ch/twiki/bin/view/AtlasProtected/DataPeriods`; visited on November 14th 2011.

[103] ATLAS Collaboration. Datasets Selection - Display an existing Period. *Website*. Available online at `https://ami.in2p3.fr/AMI/servlet/net.hep.atlas.Database.Bookkeeping.AMI.Servlet.Command`; visited on November 13th 2011.

[104] ATLAS Collaboration. COMA Period Documentation Menu. *Website*. Available online at `https://atlas-tagservices.cern.ch/tagservices/RunBrowser/runBrowserReport/rBR_Period_Report.php`; visited on November 14th 2011.

[105] G. Barrand et al. GAUDI - A software architecture and framework for building HEP data processing applications. *Comput. Phys. Commun.*, 140:45–55, 2001.

[106] Marco Clemencic et al. Recent developments in the LHCb software framework Gaudi. *J. Phys. Conf. Ser.*, 219:042006, 2010.

[107] Jr. Alves, A.Augusto et al. The LHCb Detector at the LHC. *JINST*, 3:S08005, 2008.

[108] Georges Aad et al. The ATLAS Simulation Infrastructure. *Eur. Phys. J.*, C70:823–874, 2010.

[109] Matt Dobbs and Jorgen Beck Hansen. The HepMC C++ Monte Carlo event record for High Energy Physics. *Comput. Phys. Commun.*, 134:41–46, 2001.

[110] Matt Dobbs, Jorgen Beck Hansen, Lynn Garren, and Lars Sonnenschein. HepMC 2 - a C++ Event Record for Monte Carlo Generators. 2009. Available online at `http://lcgapp.cern.ch/project/simu/HepMC/20400/HepMC2_user_manual.pdf` ; visited on November 14th 2011.

[111] S. Agostinelli et al. GEANT4: A simulation toolkit. *Nucl. Inst. and Meth.*, A506:250–303, 2003.

[112] John Allison et al. Geant4 developments and applications. *IEEE Trans. Nucl. Sci.*, 53:270, 2006.

[113] K. S. Cranmer. The ATLAS analysis architecture. *Nucl. Phys. Proc. Suppl.*, 177-178:126–130, 2008.

[114] Karsten Koeneke. A new data format for the commissioning phase of the ATLAS detector. *J.Phys.Conf.Ser.*, 219:032047, 2010.

[115] LHC Computing Grid Project. POOL - Persistency Framework - Pool Of persistent Objects for LHC. *Website*. Available online at `http://pool.cern.ch/`; visited on November 14th 2011.

[116] ROOT. *Website*. Available online at `http://root.cern.ch/drupal/`; visited on November 14th 2011.

[117] Bird, I. , (ed.) and others. LHC computing Grid. Technical design report. CERN-LHCC-2005-024.

[118] Miguel Branco et al. Managing ATLAS data on a petabyte-scale with DQ2. *J.Phys.Conf.Ser.*, 119:062017, 2008.

[119] Torbjorn Sjostrand. Monte Carlo Generators. 2006.

[120] M. A. Dobbs et al. Les Houches guidebook to Monte Carlo generators for hadron collider physics. 2004.

[121] Generator Services Project. *Website*. Available online at `http://sftweb.cern.ch/generators/`; visited on November 15th 2011.

[122] Calorimetry and Jets – Journal Club WS 2009. *Website*. Available online at `http://www.kip.uni-heidelberg.de/atlas/seminars/WS2009_JC/`; visited on November 17th 2011.

[123] Asquith, L. et al. Performance of Jet Algorithms in the ATLAS Detector. *ATLAS note*, 2010.

[124] Jet Algorithms. *Website*. Available online at `https://twiki.cern.ch/twiki/bin/view/AtlasProtected/JetAlgorithms`; visited on November 17th 2011.

[125] Gregory Soyez. The SISCone and anti-kt jet algorithms. 2008.

[126] Stephen D. Ellis. Implementing jet algorithms: A practical jet primer. *Talk*. Available online at `http://particle.physics.ucdavis.edu/seminars/data/media/2006/dec/ellis.pdf`; visited on November 18th 2011.

[127] Matteo Cacciari, Gavin P. Salam, and Gregory Soyez. The Anti-k(t) jet clustering algorithm. *JHEP*, 0804:063, 2008.

[128] Matteo Cacciari and Gavin P. Salam. Dispelling the N^3 myth for the k_t jet-finder. *Phys.Lett.*, B641:57–61, 2006.

[129] Stephen D. Ellis and Davison E. Soper. Successive combination jet algorithm for hadron collisions. *Phys.Rev.*, D48:3160–3166, 1993.

[130] Jet energy scale and its systematic uncertainty in proton-proton collisions at $\sqrt{s} = 7$ TeV in ATLAS 2010 data. (ATLAS-CONF-2011-032), Mar 2011.

[131] Public:Tau project. *Website*. Available online at `https://wiki.nbi.ku.dk/hep/Public:Tau_project`; visited on November 20th 2011.

[132] Reconstruction, Energy Calibration, and Identification of Hadronically Decaying Tau Leptons. (ATLAS-CONF-2011-077), May 2011.

[133] Cut based identification of hadronic tau decays. (ATL-PHYS-PUB-2010-001), Jan 2010.

[134] L. Breiman, J. Friedman, C.J. Stone, and R.A. Olshen. Classification and Regression Trees. 1984.

[135] Data Mining Server. Decision Trees. *Website*. Available online at `http://dms.irb.hr/tutorial/tut_dtrees.php`; visited on November 22nd 2011.

[136] Yoav Freund and Robert E. Schapire. Experiments with a new boosting algorithm, 1996.

[137] Aad, Georges and others. Measurement of the $W \to \tau\nu_\tau$ Cross Section in pp Collisions at $\sqrt{s} = 7$ TeV with the ATLAS experiment. *Phys. Lett. B*, 706:276–294, 2012.

[138] A. Andreazza, L. Dell'Asta, J. Kraus, J. Kroseberg, P. Bechtle, C. Cuenca Almenar, N. Dawe, S. Johnert, J. Liebal, R. Mazini, Z. Meng, G. Nunes Hanninger, D. O'Neil, M. Uhlenbrock, E. von Toerne, M. Wolter, and S. Xella. Measurement of the $W \to \tau\nu$ Cross Section in pp Collisions at $\sqrt{s} = 7$ TeV with the ATLAS Experiment. (ATL-COM-PHYS-2011-637), May 2011.

[139] Atlas Toronto. Accessing Missing Et Objects For Analysis. *Website*. Available online at `http://hep-twiki.physics.utoronto.ca/bin/view/AtlasToronto/EtMiss`; visited on November 22rd 2011.

[140] Torbjorn Sjostrand, Stephen Mrenna, and Peter Z. Skands. PYTHIA 6.4 Physics and Manual. *JHEP*, 0605:026, 2006.

[141] G. Corcella, I.G. Knowles, G. Marchesini, S. Moretti, K. Odagiri, et al. HERWIG 6: An Event generator for hadron emission reactions with interfering gluons (including supersymmetric processes). *JHEP*, 0101:010, 2001.

[142] G. Corcella, I.G. Knowles, G. Marchesini, S. Moretti, K. Odagiri, et al. HERWIG 6.5 release note. 2002.

[143] Torbjorn Sjostrand, Stephen Mrenna, and Peter Z. Skands. A Brief Introduction to PYTHIA 8.1. *Comput.Phys.Commun.*, 178:852–867, 2008.

[144] M. Bahr, S. Gieseke, M.A. Gigg, D. Grellscheid, K. Hamilton, et al. Herwig++ Physics and Manual. *Eur.Phys.J.*, C58:639–707, 2008.

[145] Bo Andersson, G. Gustafson, G. Ingelman, and T. Sjostrand. Parton Fragmentation and String Dynamics. *Phys.Rept.*, 97:31–145, 1983.

[146] Bo Andersson. The Lund model. *Camb.Monogr.Part.Phys.Nucl.Phys.Cosmol.*, 7:1–471, 1997.

[147] Torbjorn Sjostrand. Status of Fragmentation Models. *Int. J. Mod. Phys.*, A3:751, 1988.

[148] Bryan R Webber. A QCD model for jet fragmentation including soft gluon interference. oai:cds.cern.ch:147786. *Nucl. Phys. B*, 238(CERN-TH-3713):492–528. 53 p, Sep 1983.

[149] G Marchesini and Bryan R Webber. Simulation of QCD jets including soft gluon interference. oai:cds.cern.ch:143716. *Nucl. Phys. B*, 238(CERN-TH-3525):1–29. 39 p, Feb 1983.

[150] G. Marchesini and B.R. Webber. Monte Carlo Simulation of General Hard Processes with Coherent QCD Radiation. *Nucl.Phys.*, B310:461, 1988.

[151] T. Sjostrand and P. Skands. Multiple interactions and the structure of beam remnants. *JHEP*, 0403:053, 2004.

[152] Michelangelo L. Mangano, Mauro Moretti, Fulvio Piccinini, Roberto Pittau, and Antonio D. Polosa. ALPGEN, a generator for hard multiparton processes in hadronic collisions. *JHEP*, 0307:001, 2003.

[153] Tanju Gleisberg, Stefan Hoeche, Frank Krauss, Andreas Schalicke, Steffen Schumann, et al. SHERPA 1. alpha: A Proof of concept version. *JHEP*, 0402:056, 2004.

[154] T. Gleisberg, Stefan. Hoeche, F. Krauss, M. Schonherr, S. Schumann, et al. Event generation with SHERPA 1.1. *JHEP*, 0902:007, 2009.

[155] H. Jung et al. The CCFM Monte Carlo generator CASCADE 2.2.0. *Eur. Phys. J.*, C70:1237–1249, 2010.

[156] Stanislaw Jadach, Johann H. Kuhn, and Zbigniew Was. TAUOLA: A Library of Monte Carlo programs to simulate decays of polarized tau leptons. *Comput.Phys.Commun.*, 64:275–299, 1990.

[157] E. Boos, M. Dobbs, W. Giele, I. Hinchliffe, J. Huston, et al. Generic user process interface for event generators. 2001.

[158] G. J. Alner et al. The UA5 High-Energy anti-p p Simulation Program. *Nucl. Phys.*, B291:445, 1987.

[159] J. M. Butterworth, Jeffrey R. Forshaw, and M. H. Seymour. Multiparton interactions in photoproduction at HERA. *Z. Phys.*, C72:637–646, 1996.

[160] J.M. Butterworth and Jeffrey R. Forshaw. Photoproduction of multi - jet events at HERA: A Monte Carlo simulation. *J.Phys.G*, G19:1657–1663, 1993.

[161] ThePEG - Toolkit for High Energy Physics Event Generation. *Website*. Available online at `http://home.thep.lu.se/ThePEG/`; visited on January 05th 2012.

[162] Leif Lonnblad. CLHEP: A project for designing a C++ class library for high-energy physics. *Comput.Phys.Commun.*, 84:307–316, 1994.

[163] Borut Paul Kersevan and Elzbieta Richter-Was. The Monte Carlo event generator AcerMC version 2.0 with interfaces to PYTHIA 6.2 and HERWIG 6.5. 2004.

[164] Borut Paul Kersevan and Elzbieta Richter-Was. AcerMC Monte-Carlo Generator. *Website*. Available online at `http://borut.home.cern.ch/borut/`; visited on January 05th 2012.

[165] M. R. Whalley, D. Bourilkov, and R. C. Group. The Les Houches Accord PDFs (LHAPDF) and Lhaglue. 2005.

[166] E. Boos et al. CompHEP 4.4: Automatic computations from Lagrangians to events. *Nucl.Instrum.Meth.*, A534:250–259, 2004.

[167] Stefano Frixione and Bryan R. Webber. Matching NLO QCD computations and parton shower simulations. *JHEP*, 0206:029, 2002.

[168] Elisabetta Barberio and Zbigniew Was. PHOTOS: A Universal Monte Carlo for QED radiative corrections. Version 2.0. *Comput.Phys.Commun.*, 79:291–308, 1994.

[169] Piotr Golonka and Zbigniew Was. PHOTOS Monte Carlo: A Precision tool for QED corrections in Z and W decays. *Eur.Phys.J.*, C45:97–107, 2006.

[170] Paolo Nason. A New method for combining NLO QCD with shower Monte Carlo algorithms. *JHEP*, 0411:040, 2004.

[171] Stefano Frixione, Paolo Nason, and Carlo Oleari. Matching NLO QCD computations with Parton Shower simulations: the POWHEG method. *JHEP*, 0711:070, 2007.

[172] Simone Alioli, Paolo Nason, Carlo Oleari, and Emanuele Re. A general framework for implementing NLO calculations in shower Monte Carlo programs: the POWHEG BOX. *JHEP*, 1006:043, 2010.

[173] S. Catani, F. Krauss, R. Kuhn, and B.R. Webber. QCD matrix elements + parton showers. *JHEP*, 0111:063, 2001.

[174] Adam Bailey. Boson Production at the LHC: Monte Carlo Comparisons of Transverse Momentum and Jet Production. 2011. Summer student report of the DESY summer student programme 2011, supervised by S. Johnert and J. Katzy, available online at `http://www.desy.de/f/students/2011/reports/bailey.pdf`; visited on January 07th 2012.

[175] J. Pumplin, D.R. Stump, J. Huston, H.L. Lai, Pavel M. Nadolsky, et al. New generation of parton distributions with uncertainties from global QCD analysis. *JHEP*, 0207:012, 2002.

[176] Charged particle multiplicities in pp interactions at $\sqrt{s} = 0.9$ and 7 TeV in a diffractive limited phase-space measured with the ATLAS detector at the LHC and new PYTHIA6 tune. (ATLAS-CONF-2010-031), Jul 2010.

[177] Rick Field. Min-Bias and the Underlying Event at the LHC. 2011.

[178] Peter Zeiler Skands. Tuning Monte Carlo Generators: The Perugia Tunes. *Phys.Rev.*, D82:074018, 2010.

[179] ATLAS Collaboration. First tuning of HERWIG/JIMMY to ATLAS data. (ATL-PHYS-PUB-2010-014), Oct 2010.

[180] Andy Buckley, Hendrik Hoeth, Heiko Lacker, Holger Schulz, and Jan Eike von Seggern. Systematic event generator tuning for the LHC. *Eur.Phys.J.*, C65:331–357, 2010.

[181] Andy Buckley, Jonathan Butterworth, Leif Lonnblad, Hendrik Hoeth, James Monk, et al. Rivet user manual. 2010.

[182] (Ed.) Altarelli, G., (Ed.) Kleiss, R., and (Ed.) Verzegnassi, C. Z physics at LEP-1. Proceedings, Workshop, Geneva, Switzerland, September 4-5, 1989. VOL. 3: Event Generators and Software. 1989.

[183] Particle Data Group. The review of particle physics. *Website*. Available online at `http://pdg.lbl.gov/`; visited on November 26th 2011.

[184] C. Ay, S. Johnert, J. Katzy, and Zhong-Hua Qin. HepMCAnalyser: A tool for Monte Carlo generator validation. *J.Phys.Conf.Ser.*, 219:032029, 2010.

[185] Johnert, S. et al. HepMCAnalysis Tool. *Website*. Available online at `http://hepmcanalysistool.desy.de/`; visited on November 27th 2011.

[186] Matteo Cacciari, Gavin P. Salam, and Gregory Soyez. FastJet user manual. 2011. * Temporary entry *.

[187] Johnert, S. et al. HepMCAnalysisInterface. *Website*. Available online at `https://twiki.cern.ch/twiki/bin/viewauth/AtlasProtected/HepMCAnalysisInterface`; visited on November 28th 2011.

[188] Leggett, C. et al. THistSvc. *Website*. Available online at `https://twiki.cern.ch/twiki/bin/viewauth/Atlas/THistSvc`; visited on November 28th 2011.

[189] Terascale MC School 2009. *Website*. Available online at `https://indico.desy.de/conferenceDisplay.py?confId=1583`; visited on November 28th 2011.

[190] Terascale Monte Carlo School 2011. *Website*. Available online at `https://indico.desy.de/conferenceDisplay.py?confId=3246`; visited on November 28th 2011.

[191] Physics at the Terascale - Helmholtz Alliance. *Website*. Available online at `http://www.terascale.de/`; visited on November 28th 2011.

[192] DESY - Deutsches Elektronen-Synchrotron. *Website*. Available online at `http://www.desy.de/`; visited on November 28th 2011.

[193] LHC Computing Grid Project. HepMCAnalysis tool - validation plots for pythia6 426 generator. *Website*. Available online at `http://sftweb.cern.ch/generators/files/generator/hvalidation/pythia6/426/_Wtaunu~Wtaunu/index.html`; visited on November 28th 2011.

[194] Judith Katzy, Anton Pytel et al., private/email communication, May 17th 2011 and the following days.

[195] Judith Katzy, private communication.

[196] Johnert, S. et al. GeneratorsRTT. *Website*. Available online at `https://twiki.cern.ch/twiki/bin/view/AtlasProtected/GeneratorsRTT`; visited on November 28th 2011.

[197] The RunTimeTester User Guide. *Website*. Available online at `https://atlasrtt.cern.ch/docs/site/guide`; visited on November 29th 2011.

[198] Query RTT. *Website*. Available online at `https://atlasrtt.cern.ch/rtt/query.php`; visited on November 29th 2011.

[199] DCube Documentation. *Website*. Available online at `https://twiki.cern.ch/twiki/bin/view/Sandbox/DCubeDoc`; visited on November 29th 2011.

[200] DCube integration within RTT framework. *Website*. Available online at `https://twiki.cern.ch/twiki/bin/view/Sandbox/RTTAndDCube`; visited on November 29th 2011.

[201] A. Sherstnev and R.S. Thorne. Parton Distributions for LO Generators. *Eur.Phys.J.*, C55:553–575, 2008.

[202] A.D. Martin, R.G. Roberts, W.J. Stirling, and R.S. Thorne. NNLO global parton analysis. *Phys.Lett.*, B531:216–224, 2002.

[203] Georges Aad et al. Measurement of the $W \to l\nu$ and $Z/\gamma^* \to ll$ production cross sections in proton-proton collisions at $\sqrt{s} = 7$ TeV with the ATLAS detector. *JHEP*, 1012:060, 2010.

[204] F. Abe et al. Measurement of the lepton charge asymmetry in W-boson decays produced in $p\overline{p}$ collisions. *Phys. Rev. Lett.*, 81:5754–5759, Dec 1998.

[205] D. Acosta and The CDF Collaboration. Measurement of the Forward-Backward Charge Asymmetry from $W \to e\nu$ Production in p anti-p Collisions at $\sqrt{s} = 1.96$ TeV. *PHYS.REV.D*, 71:051104, 2005.

[206] V.M. Abazov et al. Measurement of the electron charge asymmetry in $p\bar{p} \to W + X \to e\nu + X$ events at $\sqrt{s} = 1.96$-TeV. *Phys.Rev.Lett.*, 101:211801, 2008.

[207] V.M. Abazov et al. Measurement of the muon charge asymmetry from W boson decays. *Phys.Rev.*, D77:011106, 2008.

[208] D. Decamp et al. Measurement of the polarization of tau leptons produced in Z decays. *Phys. Lett.*, B265:430–444, 1991.

[209] B.K. Bullock, Kaoru Hagiwara, and Alan D. Martin. Tau polarization and its correlations as a probe of new physics. *Nucl.Phys.*, B395:499–533, 1993.

[210] Abe, F. and others. Measurement of the ratio $B(W \to \tau\nu)/B(W \to e\nu)$ in $p\overline{p}$ collisions at $\sqrt{s} = 1.8$ TeV. *Phys. Rev. Lett.*, 68:3398–3402, Jun 1992.

[211] B. Abbott et al. A measurement of the $W \to \tau\nu$ production cross section in $p\bar{p}$ collisions at $\sqrt{s} = 1.8$ TeV. *Phys.Rev.Lett.*, 84:5710–5715, 2000.

[212] J. Alitti et al. A Search for charged Higgs from top quark decay at the CERN $\bar{p}p$ collider. *Phys.Lett.*, B280:137–145, 1992.

[213] Marc Sangel. Analysing $pp \to W \to \tau\nu_\tau$ events using HepMCAnalysis Tool for different PDFs, Tunes and Generators. 2011. Summer student report of the DESY summer student programme 2011, supervised by S. Johnert, available online at `http://www.desy.de/f/students/2011/reports/sangel.pdf`; visited on January 07th 2012.

[214] Pavel M. Nadolsky, Hung-Liang Lai, Qing-Hong Cao, Joey Huston, Jon Pumplin, et al. Implications of CTEQ global analysis for collider observables. *Phys.Rev.*, D78:013004, 2008.

[215] R. Field. Min-Bias and the Underlying Event in Run 2 at CDF. *Acta Physica Polonica B*, 36:167, February 2005.

[216] Observation of $W \to \tau\nu_\tau$ Decays with the ATLAS Experiment. (ATLAS-CONF-2010-097), Nov 2010.

[217] ATLAS Collaboration. ATLAS Event Displays from 2010 and 2011 Collision Data. *Website*. Available online at `https://twiki.cern.ch/twiki/bin/view/AtlasPublic/EventDisplayPublicResults`; visited on January 17th 2012.

[218] A measurement of the total $W^\pm$ and Z/γ^* cross sections in the e and μ decay channels and of their ratios in pp collisions at $\sqrt{s} = 7$ TeV with the ATLAS detector. (ATLAS-CONF-2011-041), Mar 2011.

[219] Georges Aad et al. Measurement of the inclusive $W^{\pm}$ and Z/γ^* cross sections in the e and μ decay channels in pp collisions at $\sqrt{s} = 7$ TeV with the ATLAS detector. 2011.

[220] Charalampos Anastasiou, Lance J. Dixon, Kirill Melnikov, and Frank Petriello. High precision QCD at hadron colliders: Electroweak gauge boson rapidity distributions at NNLO. *Phys.Rev.*, D69:094008, 2004.

[221] ATLAS Collaboration. How to Make D3PDs for the Tau Group. *Website*. Available online at `https://twiki.cern.ch/twiki/bin/viewauth/AtlasProtected/TauD3PDMaker`; visited on January 20th 2012.

[222] ATLAS Collaboration. Centrally Produced D3PDs for the TauWG. *Website*. Available online at `https://twiki.cern.ch/twiki/bin/viewauth/AtlasProtected/TauWGDPDs`; visited on January 20th 2012.

[223] ATLAS Collaboration. Index of /atlasdqm/grlgen/CombinedPerf/Tau/Tau_h_v01. *Website*. Available online at `http://atlasdqm.web.cern.ch/atlasdqm/grlgen/CombinedPerf/Tau/Tau_h_v01/`; visited on January 21st 2012.

[224] Updated Luminosity Determination in pp Collisions at $\sqrt{s} = 7$ TeV using the ATLAS Detector. (ATLAS-CONF-2011-011), Mar 2011.

[225] S. Consonni. $Z \to \tau\tau$ cross section first studies. *$Z \to \tau\tau$ Analysis Informal Meeting, Talk*. Available online at `https://indico.cern.ch/conferenceDisplay.py?confId=129192`; visited on January 29th 2012.

[226] A combined measurement of the top quark pair production cross-section using dilepton and single-lepton final states. (ATLAS-CONF-2011-040), Mar 2011.

[227] Measurement of the Mis-identification Probability of τ Leptons from Hadronic Jets and from Electrons. (ATLAS-CONF-2011-113), Aug 2011.

[228] Georges Aad et al. Electron performance measurements with the ATLAS detector using the 2010 LHC proton-proton collision data. 2011. Long author list - awaiting processing.

[229] O Arnaez et al. Electron efficiency measurements using ATLAS 2010 data at $\sqrt{s} = 7$ TeV: Supporting note for the 2010 egamma paper. (ATL-COM-PHYS-2011-322), Mar 2011.

[230] Determination of the muon reconstruction efficiency in ATLAS at the Z resonance in proton-proton collisons at $\sqrt{s} = 7$ TeV. (ATLAS-CONF-2011-008), Feb 2011.

[231] Alan D. Martin, R.G. Roberts, W.James Stirling, and R.S. Thorne. Parton distributions and the LHC: W and Z production. *Eur.Phys.J.*, C14:133–145, 2000.

[232] Klaus Desch, Philip Bechtle, Mathias Uhlenbrock, private communication, February 8th 2012.

Acknowledgement

For the success of this thesis, I have to thank a number of people to whom I want to express my gratitude here.

First of all, there is Dr. Philip Bechtle, my supervisor, who gave me the opportunity to work in his group and the ATLAS collaboration. Many thanks for all your engagement, suggestions, ideas, and for all your patience. Furthermore, I would like to thank Prof. Dr. Johannes Haller, Prof. Dr. Peter Schleper, and Dr. Michael Martins for being the referees for the dissertation, the thesis defense, and the chairman of the examination board.

I want to thank also Dr. Judith Katzy for the supervision during the development of the HepMCAnalysis Tool. For this purpose, many thanks to Dr. Jan Kotanski and Dr. Sebastian Piec for continuing all the work on the HepMCAnalysis Tool when I started to write up my thesis.

I am also thankful to Dr. Jürgen Kroseberg, Jana Kraus, and Dr. Lidia Dell'Asta for a nice and pleasant working athmosphere in the $W \to \tau\nu_\tau$ subgroup and for all your help in the $W \to \tau\nu_\tau$ analysis. Thank you for the interesting discussions.

Many thanks go to the summer students Chris-Malena Delitzsch for the development of a $W \to \tau\nu_\tau$ analysis class of the HepMCAnalysis Tool, as well as Marc Sangel and Adam Bailey for working with the tool and providing results concerning $W \to \tau\nu_\tau$ decays at generator level and tuning of generators.

If there were any computing problems, I could go to Dr. Wolfgang Ehrenfeld and Jörgen Samson, who helped to solve these problems. Thank you for all your help.

Especially for the end of my thesis time, I would like to thank Dr. Nicholas Styles, Dr. Tiago Perez, James Dassoulas, Dr. Judith Katzy, Dr. Mark Terwort, Dr. Jan Kotanski, Dr. Gordon Fischer, Milan Zvolskỳ, Dr. Wolfgang Ehrenfeld, and Björn Sarrazin for reading parts of the thesis and providing comments. Special thanks to Dr. Nicholas Styles and Dr. Tiago Perez, who read a lot and stayed so friendly because I know that I required a lot of you shortly before the end. And many thanks to all the people who joined my rehearsals and provided me a lot of comments.

I would like to thank the whole DESY ATLAS group for the kind and pleasant atmosphere.

Last but not least, I would like to thank my family and friends, from whom I have always gotten help, especially in difficult times.